Diss. ETH No. 18732

Gain and waveguide engineering in mid-infrared quantum cascade lasers

A dissertation submitted to
ETH ZÜRICH

for the degree of
Doctor of Sciences

presented by
TOBIAS GRESCH
Dipl. Phys.-El., University of Neuchâtel
born on November 3, 1977
citizen of Freienbach, SZ – Switzerland

accepted on the recommendation of
Prof. Dr. Jérôme Faist, examiner
Prof. Dr. Carlo Sirtori, co-examiner

2009

Abstract

Quantum cascade lasers are unipolar semiconductor lasers that, due to the generality of the principles they are based on and the flexibility of the underlying technology, allow to fabricate sources of coherent light from the mid-infrared down to the frequencies of the terahertz. In this work we present different approaches in the domains of active region and waveguide engineering of mid-infrared quantum cascade lasers.

The quantum cascade lasers with large optical cavities presented in this work allow to obtain an optical mode with a quasi-rectangular intensity profile. We show that devices based this principle reduce the effects of vertical spatial hole burning in the waveguide core and thus achieve an optimal slope efficiency. We also show that the introduction of passive layers in the waveguide core stabilizes the electric field in the latter and enhances its thermal conductivity. Moreover, due to the large spatial extension of the optical mode, the devices exhibit a much narrower farfield than devices with standard waveguides. Despite limitations encountered due to the use of non-optimized active regions and old-school device processing we could demonstrate devices that exhibit more than 14 W of peak power and 34 % slope efficiency at $\lambda \approx 5\,\mu$m in pulsed operation (1 % duty-cycle) at cryogenic temperatures. Devices emitting at $\lambda \approx 10.5\,\mu$m and fabricated with more advanced techniques attained a peak power of 4.7 W and slope efficiencies up to 1.6 W/A in pulsed operation (1 % duty-cycle) at room temperature.

Strain-compensated active regions developed more than 10 years ago and based on the GaInAs and AlInAs materials and grown on InP substrates have shown to be the best way to obtain high power quantum cascade lasers emitting in the first mid-infrared atmospheric window (3.5-5.0 μm). After introducing the framework (including surface segregation) that allows us to quantitatively simulate the performances of our devices and to correctly predict their emission wavelength at different temperatures we present a “spiked” active region design. With this design structures are grown with a small amount of strain (±0.5 %) and AlAs and InAs spikes with sub-monolayer thicknesses are added in the barriers and wells, respectively, that are situated around the wells hosting the lasing transition. Devices based on this design and emitting at $\lambda \approx 4.5\,\mu$m and $\lambda \approx 4.8\,\mu$m worked in continuous-wave operation up to room temperature and a maximal average power of 200 mW was observed at 303 K.

Furthermore we present a multi-section cavity gain measurement technique that allows to measure the gain of a quantum cascade laser structure in waveguide configuration. The self-aligned technique yields a direct and quantitative measurement of the gain and the waveguide losses and, due to its pulsed operation, can be performed at high temperatures and for high current densities. Using this technique we measured the gain of devices based on a single-quantum-well active region and that operate in a regime of very low to vanishing population inversion. The measured gain shows a dispersive lineshape for low population inversion between the upper and lower subband of the lasing transition and recovers a more Lorentzian-shaped gain for increasing population of the upper subband. This evolution of the gain shape is predicted by a model that includes scattering-assisted transitions between the two subbands.

Resumé

Des lasers à cascade quantique sont des lasers unipolaires qui, grâce à la flexibilité des principes et de la technologie sur lesquels ils sont basés, permettent de réaliser des sources de lumière cohérente qui émettent des longueurs d'ondes dans l'infrarouge moyen jusqu'aux fréquences theraherz. Dans ce travail, nous allons présenter des approches différentes dans le domaine de l'ingénieurie des régions actives d'une part et des guides d'onde d'autre part pour des lasers à cascade quantique qui émettent dans l'infrarouge moyen.

Les lasers à cascade quantique avec des cavités optiques que nous présentons dans ce travail permettent de réaliser des modes optiques avec un profile d'intensité quasi rectiligne. Nous montrons que des lasers basés sur ce principe réduisent les effets du hole-burning spatial dans la direction de croissance et permettent d'obtenir une pente différentielle optimale. Nous montrons aussi que l'incorporation de couches passives dans le coeur du guide d'onde stabilise le champ électrique et améliore la conduction thermique du dispositif. De plus, l'extension spatiale large du mode optique dans le guide résulte dans un champ lointain étroit ce qui facilite la collection de la lumière avec des dispositifs optiques. Malgré les limitations que nous avons rencontrés dû à l'emploi de régions actives non-optimisées montrant des courants de seuil importants d'une part et une fabrication simpliste des echantillons d'autre part, nous avons pu démontrer des dispositifs qui émettent plus de 14 W de puissance de crête et une efficacité de 34 % à une longeur d'onde de $\lambda \approx 5\,\mu$m à température cryogénique. Un échantillon émettant à $\lambda \approx 10.5\,\mu$m et fabriqué avec une technologie plus avancée a atteint une puissance de crête de 4.7 W et une pente différentielle jusqu'à 1.6 W/A à température ambiante en mode pulsé.

Des régions actives avec contrainte compensée ont été developpé il y a dix ans. Les lasers basés sur les matériaux GaInAs et AlInAs et crûs sur un substrat de InP ont montré que ceci est la meilleure méthode pour fabriquer des lasers à cascade quantique qui émettent dans la première fenêtre transparente de l'infrarouge moyen qui se trouve entre 3.5 et 5.0 μm. Après la présentation des bases (en incluant la ségrégation à la surface des matériaux volatiles)

qui nous permet de faire une simulation quantitative des performances des échantillons et de prédire correctement leur longueur d'onde d'émission en fonction de la température, nous présentons une région active qui contient des pics. Cette région active a été crû avec relativement peu de contrainte ($\pm 0.5\,\%$), mais des couches fines de InAs et de AlAs avec une épaisseur plus fine qu'une couche atomique ont été introduites dans les puits et barrières proches de la transition optique. Des échantillons basés sur ce principe et qui émettent à $\lambda \approx 4.5\,\mu$m et $\lambda \approx 4.8\,\mu$m ont fonctionné jusqu'à température ambiante en mode continu et ont atteint une puissance maximale de 200 mW à la même température.

De plus, nous présentons une technique basée sur un guide d'onde divisé en plusieurs sections qui permet de mesurer le gain d'une structure à cascade quantique. Ceci est une technique auto-alignée qui permet de faire une mesure directe et quantitative du gain et des pertes de guide et qui, grâce au mode d'opération pulsé, permet aussi de faire les mesures à haute température et avec des densités de courant importantes. En utilisant cette technique, nous avons mesuré le gain d'échantillons basés sur une région active contenant un simple puits quantique. Ces échantillons travaillent dans un régime d'inversion de population faible. Le gain mesuré montre une forme dispersive quand l'inversion de population est très faible et devient de plus en plus symétrique lorsqu'on augmente le courant et donc l'inversion de population. Cette évolution de la forme de gain est prévue par un modèle qui tient compte de transitions du deuxième ordre entre des sous-bandes.

Contents

List of Tables

List of Figures

Chapter 1

Introduction

1.1 Organization of this work

This work describes some of the work performed by the author, first at the University of Neuchâtel and later at ETH Zürich under the supervision of Prof. Dr. J. Faist and treats several aspects of waveguide and gain medium engineering in the domain of mid-infrared quantum cascade lasers. In this introduction we start with a brief historical overview of the ideas and discoveries that led to the experimental demonstration of the quantum cascade laser in 1994. Then we will briefly discuss the major milestones achieved in the quantum cascade laser community in the quest to extend the operation wavelength range of these devices as well as for high power and high temperature operation. But the best quantum cascade laser has little value if there is no use for it. Therefore, in section 1.5, we present a selection of applications for quantum cascade lasers as sources of coherent light in the mid-infrared and far-infrared (treated only superficially) wavelength range. In chapter 2 we briefly introduce some of the basic theory behind intersubband transitions and quantum cascade lasers and present some of the models that allow to describe the characteristics of the devices. It starts with a short summary of intersubband physics in semiconductor materials. Then we introduce the model of resonant tunneling between subbands developed by Kazarinov and Suris in the seventies. It follows a discussion of the rate-equation model that allows to describe the most important characteristics of a laser device, like threshold current and slope efficiency and more fundamental parameters. At the end of the chapter we will define the term "waveguide losses" and briefly discuss the contributing mechanisms.

Technical aspects like sample fabrication and measurement techniques are treated in chapter 3. The chapter terminates with a discussion of multi-section cavity gain measurements. A technique that we improved and used to measure the modal gain in quantum cascade laser structures with high and low electron population inversion.[1, 2, 3]

Chapter 4 talks about waveguides of mid-infrared quantum cascade lasers and our experiments with large optical cavity waveguides that allow to achieve very high peak powers and slope efficiency. Unfortunately they are strongly limited in average emission power due to the bad thermal conductance of the devices.[4, 5]

In chapter 5 we discuss the material systems and some of their particularities more closely and present the results we obtained with lasers emitting around $\lambda \approx 4.6\,\mu$m and that are based on a strain-compensated AlInAs/GaInAs design with sub-monolayer thick AlAs and InAs spikes in the active region.[3, 6]

The last chapter is dedicated to gain measurements on quantum cascade lasers based on a single quantum well active region.[2, 1] These measurements were used to validate an enhanced model unifying the description of gain in quantum cascade lasers and superlattices and that takes into account second-order scattering processes.[1, 7]

1.2 Early developments

The concept to amplify light by stimulated emission of radiation dates back to 1958 when Schawlow[1] and Townes[2] published their seminal paper where they extended the concept of the MASER to electromagnetic radiation with infrared and optical wavelengths.[8] It was five years before that Townes and co-workers at Columbia University built the first MASER,[8] based on downward transitions of excited ammonia molecules.[3] A first operating laser was demonstrated two years later, in May 1960, by Maiman at Hughes Research Laboratories in Malibu, California.[10] It was a solid-state laser based on a ruby rod as active medium. The first gas laser (based on HeNe) followed in December of the same year.[11]

The first proposals to use semiconductors in amplifiers for microwave and optical frequencies date back to the late-fifties with Krömer's proposal of a negative-mass microwave amplifier[12] and B. Lax who was investigating cyclotron resonance in semiconductors. Lax suggested to use transitions

---

[1] A. L. Schawlow was awarded the Nobel Prize in Physics in 1981 for his contribution to the development of laser spectroscopy.

[2] C. H. Townes was awarded the Nobel Prize in Physics in 1964 for fundamental work in the field of quantum electronics.

[3] We refer to [9] for a textbook description of the ammonia two-level system.

of holes between non-equidistant Landau levels in order to obtain "quantum amplifiers and oscillators".[13] With the feasibility of solid-state and gas lasers demonstrated in 1960 and the rapidly growing interest in these new sources for coherent light, the possibility of stimulated emission in semiconductor materials became more attractive. Indeed, two years later several groups reported lasing action in semiconductors.[14, 15, 16] The breakthrough for semiconductor interband lasers came with the development of the double-heterostructure laser that helped to dramatically reduce the threshold current of these devices and converted them from a laboratory curiosity to a practical, compact and coherent light source with many applications. Although the idea of double-heterostructure lasers was already stated independently by Krömer and Kazarinov and Alferov[4] in 1963, it took until 1969 that a device that worked in pulsed mode at room temperature could be demonstrated.[17, 18] The difficulties encountered were related to the growth of the heterostructures as the two different semiconductors needed a careful matching of the lattice constants and the epitaxial growth techniques needed to be improved until material with sufficiently high quality could be grown.

It was Esaki[5] and Tsu's idea of using advanced thin film growth techniques to fabricate simple double-barrier structures first and a series of barriers (a superlattice) later, that enabled a new area of interdisciplinary research: quantum engineering. They predicted that, if the electron mean free path was longer than the superlattice period, the electron system would exhibit

---

[4] Z. I. Alferow and H. Krömer were awarded the Nobel Prize in Physics in 2000 for developing semiconductor heterostructures.

[5] L. Esaki was awarded the Nobel Prize in Physics in 1973 for his experimental discoveries regarding tunneling phenomena in semiconductors.

quantum mechanical effects and that the electrons would show unusual transport properties including a negative differential resistance. Their new idea of “do-it-yourself quantum mechanics” had a difficult standing in the beginning. Indeed, the first version of their paper was rejected by the reviewer of *Physical Review* for being “too speculative” and the lack of new physics. Despite this initial setback the new field emerged rapidly and research was carried out with these structures in all aspects of physics, material research and devices.

In 1971 Kazarinov and Suris showed how to obtain a population inversion between electronic subbands in semiconductor superlattices and proposed to use intersubband transitions in a biased superlattice for light amplification.[19, 20] A — at a first sight — completely different and intriguing way to obtain gain in superlattices was proposed in the same year by Ktitorov *et al.*[21] and later by Ignatov and Romanov.[22] Based on semi-classical arguments they predicted optical gain despite a missing population inversion due to Bloch oscillations.

In the following years superlattices and resonant tunneling through double-barrier heterostructures were studied extensively. Esaki and Tsu presented calculations of resonant tunneling transport through finite superlattices in 1973 and shortly after they reported together with Chang on the observation of resonant tunneling through a double-barrier heterostructure.[23, 24] It followed the discovery of oscillatory behavior (due to domain formation) of the differential conductance of a superlattice with respect to the applied voltage by Esaki and Chang[25] and the introduction of “hopping-transport”, or phonon-assisted tunneling, by Tsu and Döhler.[26] At around the same time, Dingle *et al.* used absorption measurements to prove the existence of discrete energy levels inside thin semiconductor quantum wells.[27] After a slow-down in the field of resonant tunneling and superlattices in the late seventies, this research area got new momentum once material with sufficiently high quality could be grown. Initiated by the microwave experiments by Sollner *et al.*[28] resonant tunneling and superlattices were re-visited by numerous experimental [29, 30, 31, 28, 32] and theoretical [33, 34, 35] investigations.

All these experiments were made possible thanks to the introduction of a new epitaxial growth technique with unprecedented flexibility in terms of material composition, thickness control, uniformity and very high material quality: molecular beam epitaxy (MBE).[36] The technique as we know it today was pioneered at AT&T Bell Labs by Arthur and Cho.[37] Arthur showed in 1968 that it was possible to obtain epitaxial growth on a heated GaAs substrate wafer by pointing beams of Ga atoms and As molecules on the latter in a metal vacuum system without heated walls. Cho brought the technology to its maturity while, at that time, mostly working with the GaAs-$Al_xGa_{1-x}As$ material system. In molecular beam epitaxy, compared to liquid phase (LPE) and vapor phase epitaxy (VPE) that were the most common epitaxial growth techniques at that time, the growth happened under ultra-high vacuum conditions. A heated substrate wafer was placed in front of several effusion ovens (typically six) that had an orifice pointing to the substrate. The crucibles were filled with material of the constituting elements of the crystal layer that was to be grown. The intensity of the beams and their relative composition was regulated by the temperature of the effusion ovens whereas the composition of the to-be-grown material could be changed rapidly by opening and closing shutters that were placed in the beams. The relatively slow growth rate around 1 μm/h and the possibility to analyze the state of the growing surface by electron diffraction allowed to control the growth process with the precision of a crystal mono-layer. Additionally, the doping profile could be controlled in the same manner what enabled the possibility to grow very complex doping profiles.[38]

Intersubband transitions were first demonstrated by Kamgar *et al.*[39] in the inversion layer of metal-oxide-semiconductor capacitor devices where resonant absorption was observed. Two years later Gornik *et al.* reported on the far-infrared emission from silicon inversion layers in metal-oxide-semiconductor field-effect transistors.[40] In case of intersubband transitions in quantum wells it was Pinczuk *et al.*[41] who first observed the discrete energy levels by Raman spectroscopy and later West and Eglash were able to observe resonant absorption between the ground state and the first excited state of the electron wave function. Harwitt and Harris calculated the eigenstates of quantum well superlattices in an applied electric field and were able to correctly predict the Stark shift of the intersubband transitions with applied electric field.[42, 43] Another breakthrough followed in 1989 when Helm *et al.* were the first to report infrared light emission from intersubband transitions in superlattices.[44]

According to Ref. [45], Capasso, Cho and co-workers at AT&T Bell Labs initiated research on resonant tunneling in 1985. They first focused on AlInAs/GaInAs in their quest for new high-performance electronic and photonic devices. In 1986 they observed sequential resonant tunneling between the ground and excited states of adjacent quantum wells[46] and about one year later Levine *et al.* demonstrated the first quantum well infrared photodetector[47] (QWIP) where resonant photons excite electrons from the ground state of quantum wells to the first excited state or the continuum.[48]

It was also at that time that the first practical suggestions for quantum cascade lasers were made by Capasso *et al.*[49] and later by Liu.[50] These proposals contained some key-notions of quantum cascade lasers like using intersubband transitions between energy states that arise due to the confinement of the electrons in heterostructure quantum wells, the engineering of the state lifetimes in order to obtain population inversion as suggested by Kazarinov and Suris, electrical injection of the carriers and also the cascading of subsequent periods. However these design suggestions had the problem that population inversion was achieved at an unstable point of the current-voltage curve.

1.3 Advent of the quantum cascade laser

Jérôme Faist joined Capasso's group at AT&T Bell Labs in 1991. At the end of 1993 Faist *et al.* demonstrated electroluminescence in a coupled quantum well using a graded-gap electron injector.[51] It followed the realization that the intersubband electroluminescent spectrum could be considerably narrowed when the doping was set back from the active region.[52] Consequently an electric field narrowing of the electroluminescent spectrum down to a width of 21 meV was observed at cryogenic temperatures. Finally, eight years after the proposal by Capasso *et al.*[49] and more than twenty years after the initial proposal by Kazarinov and Suris,[19, 20] the first quantum cascade laser could be demonstrated at AT&T Bell Labs in 1994.[53] The structure was grown with the $Al_{0.48}In_{0.52}As/Ga_{0.47}In_{0.53}As$ material system lattice matched to InP and devices emitted at $\lambda \approx 4.2\,\mu$m with a threshold current density of $11\,\mathrm{kA\,cm^{-2}}$ for a $720\,\mu$m long device at 10 K heat sink temperature.

In the following years people working at AT&T Bell Labs set the foundation of quantum cascade laser research in the domains of the device physics, crystal growth and processing techniques. With a three-quantum-well design optimized for high temperature operation Faist *et al.* could demonstrate pulsed operation of a quantum cascade laser emitting at $\lambda \approx 5.2\,\mu$m above room temperature.[54] In this vertical transition active region the width of the funnel injector has been increased to prevent electron back-filling into the lower lasing state. Moreover, a narrow well was added after the injection barrier that selectively enhanced the overlap of the upper lasing state with the ground state of the injector and thus increased injection efficiency. The active region core also was overgrown by InP as the top cladding layer instead of $Al_{0.48}In_{0.52}As$ for improved thermal conductivity of the device. This waveguide design became the standard waveguide design for mid-infrared quantum cascade lasers (see chapter 4). Quantum cascade lasers emitting at longer wavelengths were also demonstrated during this period.[55, 56, 57] Scaling the quantum cascade laser technology to longer wavelengths and other material systems stressed the importance of low waveguide losses that finally were obtained by sophisticated waveguide design.[58, 57] We will discuss waveguides more closely in chapter 4.

The first distributed feedback quantum cascade lasers were demonstrated in 1997 by Faist *et al.* and they were based on loss-coupling by etching the first-order grating into the plasmon-confining layer.[59] Index-coupled distributed feedback quantum cascade lasers where were developed at about the same time.[60] In these devices the grating was etched into a $\mathrm{Ga_{0.47}In_{0.53}As}$ cap layer that was grown on top of the active region and that was overgrown with InP.

Also in 1997 an intersubband laser was demonstrated by Scamarcio *et al.* where lasing was achieved between minibands of a strongly coupled superlattice, taking advantage of the of the high oscillator strength of this transition at the mini-boundary of the Brillouin zone.[61] However, the active region had to be highly doped in order to render the miniband flat what strongly increased the waveguide losses. This design was later improved by Tredicucci *et al.* who introduced the chirped superlattice to obtain a flat miniband under applied electric field without additional doping.[62, 63] This design achieved room temperature operation, high peak powers (0.5 W at 325 K) and the the lowest threshold current density ($5.2\,\mathrm{kA\,cm^{-2}}$ at 295 K) at the time.

In 1998 the first quantum cascade laser grown with the $\mathrm{GaAs/Al_{x}Ga_{1-x}As}$ material system was realized by Sirtori *et al.*[64] demonstrating experimentally that the established principles of quantum cascade lasers were general and could be applied to other material systems. In the same year Faist *et al.* reported on the realization of a quantum cascade laser emitting at $\lambda \approx 3.4\,\mu\mathrm{m}$ and based on a strain-compensated $\mathrm{Ga_{0.3}In_{0.7}As/Al_{0.6}In_{0.4}As}$ active region where strain was introduced in the layers in order to increase the conduction band discontinuity.[65] These lasers held the short-wavelength record for 10 years.

In 2002 the *IEEE Journal of Quantum Electronics* published a feature issue on mid-infrared quantum cascade lasers [66] with many contributions of the researchers working in this field, covering history and highlights of quantum cascade lasers [45], general discussion including physics, designs, technology and future prospects of quantum cascade lasers [67, 68], device physics and technology[69, 70] and applications.[71] In the same year Beck *et al.* demonstrated a $\lambda \approx 9\,\mu$m quantum cascade laser that operated in continuous-wave up to a heat sink temperature of 312 K.[72] Although the threshold current density in pulsed operation at 300 K was still relatively high (3.1 kA cm^{-2}) continuous-wave operation at room temperature could be achieved by burying the ridge waveguide in undoped InP for increased thermal conductance and epi-down mounting on a diamond heat spreader. Also in this year the first far-infrared quantum cascade laser was demonstrated by Köhler *et al.*[73]. The device lased at a frequency of ≈4.4 THz ($\lambda \approx 67\,\mu$m) and worked in pulsed operation up to a temperature of 50 K. Although quantum cascade laser structures exhibiting gain in the far-infrared region already existed before,[74] only the invention of a double surface plasmon waveguide where the guided mode is totally contained between two metallic cladding layers and that allows to obtain a low-loss TM mode with a high overlap factor made this breakthrough possible.

Due to intersubband transition selection rules and the resulting TM polarization of the optical mode quantum cascade laser devices were conceived as facet-emitters. However, in 2003 Colombelli *et al.* demonstrated a surface emitting photonic crystal laser where they combined a deeply etched, high index contrast two-dimensional photonic crystal micro-resonator with a quantum cascade laser gain medium designed for a wavelength of $\lambda \approx 8\,\mu$m.[75]

1.4 Reaching maturity

Further developments up to present will be grouped in different sections. On one hand there has been a tremendous progress in the performances of quantum cascade lasers based on the GaInAs/AlInAs/InP material system. This was achieved by optimizing structure design and doping level, crystal growth, waveguide design and doping, device processing and heat sinking (including mounting). On the other hand intersubband structures and lasers have been obtained in new material systems for example to realize short-wavelength quantum cascade lasers. Applications requiring sources that are tunable over a wide range fructified the development of broadband gain media and different technologies to obtain broadly tunable quantum cascade laser sources. Last but not least there has been a lot of progress in the understanding of the physics of these devices and measurement techniques that give clearer insight in their working.

There also has been a tremendous progress in the research of quantum cascade lasers emitting in the far-infrared region. However, we will not go into it as this subject is beyond of the scope of this work.

1.4.1 GaInAs/AlInAs-based quantum cascade lasers

Another milestone in the development of GaInAs/AlInAs/InP-based mid-infrared quantum cascade lasers was the results by Evans *et al.* that reported on a quantum cascade laser emitting at $\lambda \approx 4.8\,\mu$m and operating

Table 1.1: Mid-infrared quantum cascade lasers from Northwestern University

λ [μm]	$T_{\max}$ [K]	$J_{\mathrm{th}}^{\mathrm{RT}}$ [kA cm^{-2}]	Power [W]	Year	Ref.
4.8	$323^{a,c}$	$1.7^{a,c}$	$0.04^{a,c}$ (323 K) $0.6^{b,c}$ (RT, 50 %)	2004	[76]
4.3	$313^{a,c}$	$1.5^{a,c}$	$0.17^{a,c}$ (298 K)	2005	[77]
3.8	$318^{a,c}$	$1.5^{a,c}$	$0.14^{a,c}$ (RT)	2006	[78]
5.3	$363^{a,c}$	$1.4^{a,c}$	$0.5^{a,c}$ (RT)	2006	[79]
9.5	$318^{a,c}$	$1.6^{a,c}$	$0.02^{a,c}$ (318 K)	2006	[80]
4.7	$358^{a,c}$	$1.2^{a,c}$	$0.68^{a,c}$ (RT)	2007	[81]
10.6	$358^{a,c}$	$0.8^{a,c}$	$0.15^{a,c}$ (RT)	2007	[82]
4.6	378+	$1.7^{a,c}$	$1.3^{a,c}$ (RT)	2008	[83]

[a] continuous-wave operation
[b] pulsed operation
[c] highly-reflective coating

in continuous-wave operation up to 323 K with 38 mW of power at that temperature.[76] In pulsed operation with 50 % duty-cycle they obtained 600 mW of average power at room temperature. Since then the Northwestern University group reports on state-of-the-art quantum cascade lasers emitting between 3.8 and 10.6 μm with impressive continuity and performance improvements. A summary is given in Tab. (1.1). Their outstanding results can be attributed to a complete mastering of the growth of strained

AlInAs/GaInAs material and optimization of both, structure designs and technology. Structures are grown by gas-source molecular beam epitaxy that – we believe – could have some advantages compared to a solid arsenic source for the growth of highly strained materials (see chapter 5). With their continuing optimizations also the wall plug efficiency was continuously improved. Recently, Bai *et al.* reported on a quantum cascade laser emitting at $\lambda \approx 4.6\,\mu$m that achieved 12.5 % wall plug efficiency for continuous-wave operation at room temperature.[84]

Excellent results were also obtained by Agilent Technologies[6] who grew their structures by metal-organic chemical vapor deposition and fabricated devices with a buried-heterostructure process. Diehl *et al.* reported on devices emitting at $\lambda \approx 5.3\,\mu$m that operated up to 370 K in continuous-wave operation with 312 mW of power at 300 K.[85] Other devices with a two-phonon resonance active region, emitting at $\lambda \approx 8.4\,\mu$m they obtained continuous-wave operation at more than 400 K with 204 mW power at room temperature.[86]

As mid-infrared quantum cascade lasers reach maturity more and more companies working in the domain of molecular spectroscopy are interested in this technology. As an example we would like to mention Pranalytica that reported on buried-heterostructure quantum cascade lasers emitting at $\lambda \approx 4.6\,\mu$m with 1.6 W continuous-wave power at 300 K and the threshold current density of the device was 1.1 kA cm^{-2} and the maximal wall plug efficiency 8.8 %.

---

[6] Before they decided to spin-off their semiconductor branch that is called Avago Technologies now.

1.4.2 Alternative material systems

GaAs/$\mathbf{Al_xGa_{1-x}As}$

This is a closely matched material system due to the similar lattice constants of GaAs (5.65 Å) and AlAs (5.66 Å). Therefore the aluminum content (and thus the conduction band discontinuity) in the barrier can be varied over a large range without having to worry about a buildup of large strain in the layers. After the demonstration of the first GaAs/AlGaAs-based quantum cascade laser in 1998 many more structures have been developed. We refer to the publication of Sirtori *et al.*[68] for an overview of the research that has been performed with this material system for lasers emitting in the mid-infrared region. Although the performances of these devices could not compete with devices realized with the AlInAs/GaInAs material system for emission in the mid-infrared, it became material system of choice for quantum cascade lasers emitting in the far-infrared.

GaInAs/Al(Ga)AsSb grown on InP

Quantum cascade lasers based on AlAsSb as barrier and GaInAs as well material and grown on InP substrates were developed in the group of J. W. Cockburn at University of Sheffield and at the Fraunhofer Institute for Applied Solid State Physics in Freiburg, Germany. This material system was considered as a promising candidate for obtaining high performance quantum cascade lasers that emit in the wavelength region between 3 and 5 μm because of the large Γ-valley conduction band offset of ≈1.6 eV.

Drawbacks are that the underlying technology is less mature than for the well known and mastered GaInAs/AlInAs material system and the epitaxial growth of AlAsSb needs to be performed within the miscibility gap and therefore is very difficult.[87, 88] First laser devices, emitting at approximately 4.3 μm, were demonstrated in 2004 and lattice-matched compositions $Ga_{0.47}In_{0.53}As$ and $AlAs_{0.56}Sb_{0.44}$ were used as well and barrier material, respectively.[89, 90] However, the barrier material is an indirect semiconductor with the X-valley energy position approximately 0.7 eV lower than the one of the Γ-valley as shown in Fig. 1.1(a). Yang *et al.* scaled their initial active region design emitting at 4.5 μm down to 3.9 μm where the upper lasing state is almost aligned with the energy position of the X-valley and noticed that the threshold current was about a factor of two higher than calculations predicted.[91] They attributed this discrepancy to the scattering of electrons into the X-valley and thus reducing the population inversion between the lasing states. Femtosecond pump-probe experiments were performed in order to better understand the influence of Γ-X-scattering on the performance of quantum cascade lasers.[92, 93, 94] These experiments have shown that inter-valley scattering of high-energy electrons located above or close to indirect minima in the barrier material have little effect on the relaxation times. However, the experiments also have shown that care must be taken when designing structures as in one sample, carriers leaked into the barrier where metastable states at X-minimum existed due to doping of the former. Indeed, lasers could be demonstrated with wavelengths down to 3.05 μm, although working only at low temperatures.[95] Much better results were obtained using strain compensated GaInAs/AlAsSb quantum cascade lasers.[96] Zhang *et al.* recently demonstrated quantum cascade lasers emitting at 3.1 μm up to room temperature and based on $Ga_{0.33}In_{0.67}As/AlAs_{0.8}Sb_{0.2}$ grown on InP substrates.[97] However, the threshold current density of $19.2\,\mathrm{kA\,cm^{-2}}$ at $295\,\mathrm{K}$ is still very high and prohibits the use of such devices in continuous-wave operation on a thermoelectric cooler.

Another development in this category of material systems was the replacement of the ternary AlAsSb material in the barriers by the quaternary AlGaAsSb material.[98] By adding gallium to the barrier the conduction band discontinuity is decreased to approximately $1\,\mathrm{eV}$ that is still sufficient to realize quantum cascade lasers that emit down to $\lambda \approx 3.7\,\mu\mathrm{m}$. Since the barrier height is reduced, thicker and therefore better thickness-controllable barriers can be used while still maintaining a high tunneling probability between the lower injector and the upper lasing state. Additionally, a smaller aluminum content in the barriers can have beneficial effects on the device lifetime as the likelihood of facet oxidation is reduced. Using this technique, lasers emitting at $3.6\,\mu\mathrm{m}$ at $77\,\mathrm{K}$ and $3.8\,\mu\mathrm{m}$ at $300\,\mathrm{K}$ were demonstrated.[99] Although these samples represented a big improvement with respect to earlier designs the performances are still below the results obtained with strain-compensated GaInAs/AlInAs quantum cascade lasers at similar wavelength.[78]

InAs/(Ga)AlSb grown on InAs

Even higher conduction band discontinuity is obtained with the InAs/AlSb heterojunction, as shown in Fig. 1.1(b). These materials are easier to grow than AlAsSb from a metallurgical point of view but other difficulties arise from the fact that no common element is present across interfaces. Since both of the group *III* and group *V* elements change between the materials,

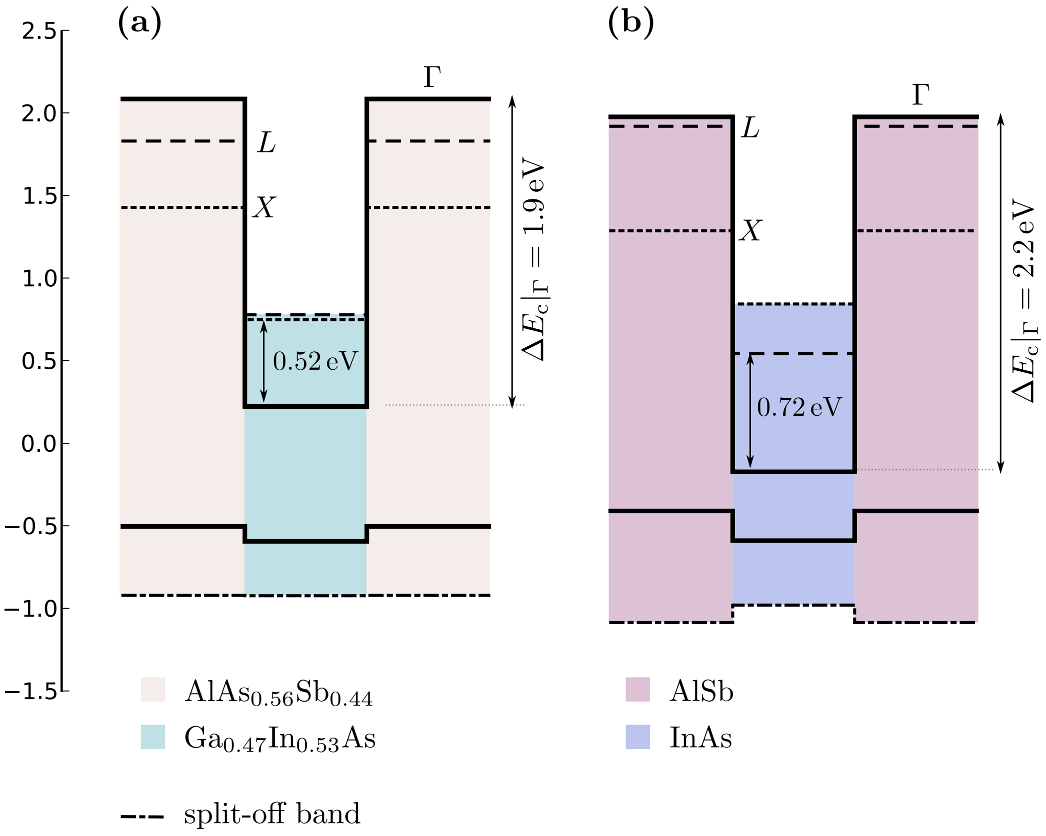

Figure 1.1: Antimony containing heterojunctions

Heterojunction between $AlAs_{0.56}Sb_{0.44}$ *and* $Ga_{0.47}In_{0.53}As$ *(a) and heterojunction between AlSb and InAs (b). The black, bold line represents the profile of the conduction band and the heavy and light hole valence bands (degenerate) The split-off valence band is shown as the mixed line. Positions of the X and L-valley minima are shown as dotted and dashed lines, respectively. The energy scale (in eV) is with respect to the conduction band lineup of InSb. Values were calculated using the parameters compiled in the publication by Vurgaftman.[100] Effects of strain were not taken into account.*

two different types of interfaces can be grown: AlAs-like and InSb-like. The electronic and optical properties of quantum wells grown in this material system depend strongly on the interfaces present and therefore, the need of interface control makes the grown more difficult.[101, 102] Additionally, the indium in the wells tends to segregate into the barriers, changing the composition profiles.[103]

The Γ-valley conduction band discontinuity for this material system is 2.1-2.2 eV. The heterojunction is shown in Fig. 1.1(b) together with the position of X and L-valley minima. As the figure shows the energy difference between the lowest lateral valley and the conduction band of InAs is $\approx$0.72 eV. When designing quantum cascade structures with such high conduction band discontinuities the barriers must be kept very thin in order to maintain a strong coupling. Also, higher order states may still be confined and therefore must be pushed to high energies in order to prevent resonant intersubband absorption.

The first InAs/AlSb quantum cascade lasers were demonstrated around 2003 but were emitting at relatively long wavelength of 10 μm, respectively 6.7 μm.[104, 105] A year later a quantum cascade laser emitting near 4.5 μm with a threshold current density of 1.5 kA cm^{-2} at 80 and 9 kA cm^{-2} at 300 K were demonstrated.[106] Further development to shorter wavelength was hampered by the lack of a suitable waveguide. Once the waveguide as described in section 4.2.4 of chapter 4 was developed quantum cascade lasers emitting close to and below 3 μm could be demonstrated.[107, 108]

For reasons of the waveguide the AlSb/InAs structures are usually grown on InAs substrates. This implies that the AlSb material with a larger lattice constant inevitably introduces compressive strain to the layers, reducing the maximal growth thickness of the structure. Therefore Marcadet *et al.* proposed to add some aluminum to the barriers in order to reduce the strain.[109] Their devices emitted in pulsed operation at 300 K at a wavelength of 3.5 μm and with a threshold current density of $\approx$8 kA cm^{-2}.

Others

Silicon is by far the most used semiconductor in technology today due to many reasons like material cost, possibility to grow huge ingots with almost perfect crystalline structure and its mechanical properties. Unfortunately no diode lasers can be fabricated based on silicon as it is an indirect semiconductor but many applications like optical interconnects on chips would exist. Therefore, people started working on the realization of intersubband devices in the Si/SiGe material system. Indeed, intersubband electroluminescence was observed in p-type structures designed in the valence band for emission at $\lambda \approx 10\,\mu$m in 2000.[110] However, no silicon based quantum cascade laser could be demonstrated up to now.

Intersubband devices are also very interesting for applications in the telecom wavelengths at 1.3 μm and 1.55 μm. Material systems that provide enough band offset include GaN/AlGaN and also II-VI semiconductors like the ZnSe/BeTe system,[111] but we consider them to be too far from the subject of this work to discuss them in detail.

1.4.3 Wavelength tunability

Wavelength tunability is a requirement for spectroscopic applications and the wider the frequency of a given source can be tuned, the more molecules and wider absorption features of a sample can be analyzed.

The center wavelength of a Fabry-Pérot quantum cascade laser inherently tunes with temperature due to the temperature induced change of the refractive index and band parameters. However, multi-mode spectra are not desired for most applications and therefore distributed feedback gratings are often used to achieve single-mode operation. Their frequency can be tuned continuously by a heat-induced change of the refractive index over a wavelength range of typically $\Delta\lambda/\lambda \sim 0.5-1\,\%$. Tuning coefficients (in wavenumbers) are in the order of $\Delta\nu/\Delta T = -0.1\,\mathrm{cm}^{-1}\,\mathrm{K}^{-1}$ for changing of the heat sink temperature and $\Delta\nu/\Delta I = -0.02\,\mathrm{cm}^{-1}\,\mathrm{mA}^{-1}$ for self-induced current heating.

The first distributed feedback quantum cascade laser working in continuous-wave operation on a thermoelectric cooler was reported in 2003 by Aellen *et al.*[112]. Devices were fabricated using a buried-heterostructure process and were mounted junction-down on diamond heat spreaders. Emission was at $\lambda \approx 9\,\mu\mathrm{m}$ and tuning range of $5\,\mathrm{cm}^{-1}$ between 200 and 245 K was achieved and maximum operating temperature was 260 K.

Up to today mid-infrared distributed feedback quantum cascade lasers have been demonstrated for many different wavelengths. For example the group at Northwestern University demonstrated distributed feedback quantum cascade lasers at 4.8, 7.8, 9.6 μm and all these devices work above room temperature in continuous-wave operation.[113, 114, 115] The same group also develops photonic-crystal distributed feedback quantum cascade lasers that are strictly single mode and produce a diffraction limited farfield. Recently, Bai reported on such a laser emitting at $\lambda \approx 4.7\,\mu$m with a peak output power of 6 W (per facet) at 300 K with 1 % duty-cycle.[116] Distributed feedback quantum cascade lasers are also developed in our group. Recently, Wittmann *et al.* managed to operate a device emitting at $\lambda \approx 9\,\mu$m up to 423 K in continuous-wave operation. On another structure Wittmann *et al.* used photolithography to define distributed feedback gratings with different periodicities on the same mask. With this technique lasers emitting between 7.7 and 8.3 μm and based on the same bound-to-continuum active region design and fabricated in the same process could be fabricated. The lasers worked in continuous-wave operation above room temperature and in the center of the gain an operation temperature of 63 ℃ was attained. In this approach the devices were still separated and tested individually. Lee *et al.* went a step further and build a widely tunable single-mode source where an array of 32 waveguide ridges with individual gratings were monolithically integrated on one chip. They achieved a tuning range between 8.7 and 9.4 μm and used the device in a proof-of-concept spectrometer for spectroscopy of liquids.[117] Using a heterogeneous active region based on two bound-to-continuum designs centered at 8.4 and 9.6 μm, respectively, they recently demonstrated a laser array covering over 220 cm^{-1} and centered at 9 μm in pulsed operation.[118]

For even wider tuning range a gain medium with larger gain is required. Thanks to its flexibility the quantum cascade laser technology provides many possibilities to achieve that. In 2002 Gmachl *et al.* reported on a ultra-broadband, supercontinuum quantum cascade laser that simultaneously emitted between 6 and 8 μm at cryogenic temperatures.[119] The waveguide core was based on 36 active/injection region pairs with dissimilar optical transitions and the electroluminescence spectrum at cryogenic temperature showed a full-width at half-maximum of 93 meV.

Maulini *et al.* chose an approach where two quantum cascade laser designs with overlapping gain curve are stacked one on the other in a waveguide core ("heterogeneous cascade").[120] Their two designs were centered at 8.4 and 9.6 μm, respectively, and 20 stages were grown of each. The electroluminescence spectrum showed a full-width at half-maximum of 350 cm^{-1} at 300 K and they could tune the laser emission from 8.16 to 10.41 μm (265 cm^{-1}, $\Delta\lambda/\lambda \sim 0.24$) in their external-cavity setup with a grating in Littrow configuration. With a similar gain chip with buried heterostructure process and mounting on a diamond heat spreader Wittmann *et al.* achieved a tuning range of 201 cm^{-1} $\Delta\lambda/\lambda \sim 0.18$) in continuous-wave operation at 15 ℃. Widely tunable quantum cascade lasers were also developed at shorter wavelength. Recently, Maulini *et al.* reported on a grating-coupled external cavity quantum cascade laser that is tunable over a range of 160 cm^{-1} around the center wavelength 4.6 μm in continuous-wave operation at room temperature.[121]

1.5 Applications

1.5.1 Infrared spectroscopy

The by far most important application of quantum cascade lasers that emit in the mid-infrared wavelength region is infrared spectroscopy. In infrared spectroscopy a beam of infrared light is passed through a sample and it is measured how much of light is absorbed at a given energy. The resulting transmittance or absorbance spectrum then gives information about the molecular structure of the sample. Although infrared spectroscopy is also performed in the far- and near-infrared wavelength ranges, the mid-infrared spectral region is of particular interest because it contains the fundamental vibrations and associated rotational-vibrational structure of a large number of molecules of interest for environmental monitoring and pollution control, detection of water and soil contaminants, industrial process monitoring and non-invasive disease diagnosis through breath analysis. As an illustration absorption lines of the H_2O-molecule in the spectral range between 400 and $4000\,\mathrm{cm}^{-1}$ and for a selection of molecules in the two infrared atmospheric windows are shown in Fig. 1.2.

However, conventional solid-state lasers are mainly limited to wavelengths below $\lambda \approx 3\,\mu$m due to the lack of suitable crystalline laser gain materials at longer wavelengths. Therefore, a large number of alternative technologies to generate coherent mid-infrared radiation have been developed in the past and present, driven by advances in material science, crystal growth and semiconductor material processing. For an overview of these technologies and their applications we refer to the book edited by Sorokina and Vodopyanov[123]

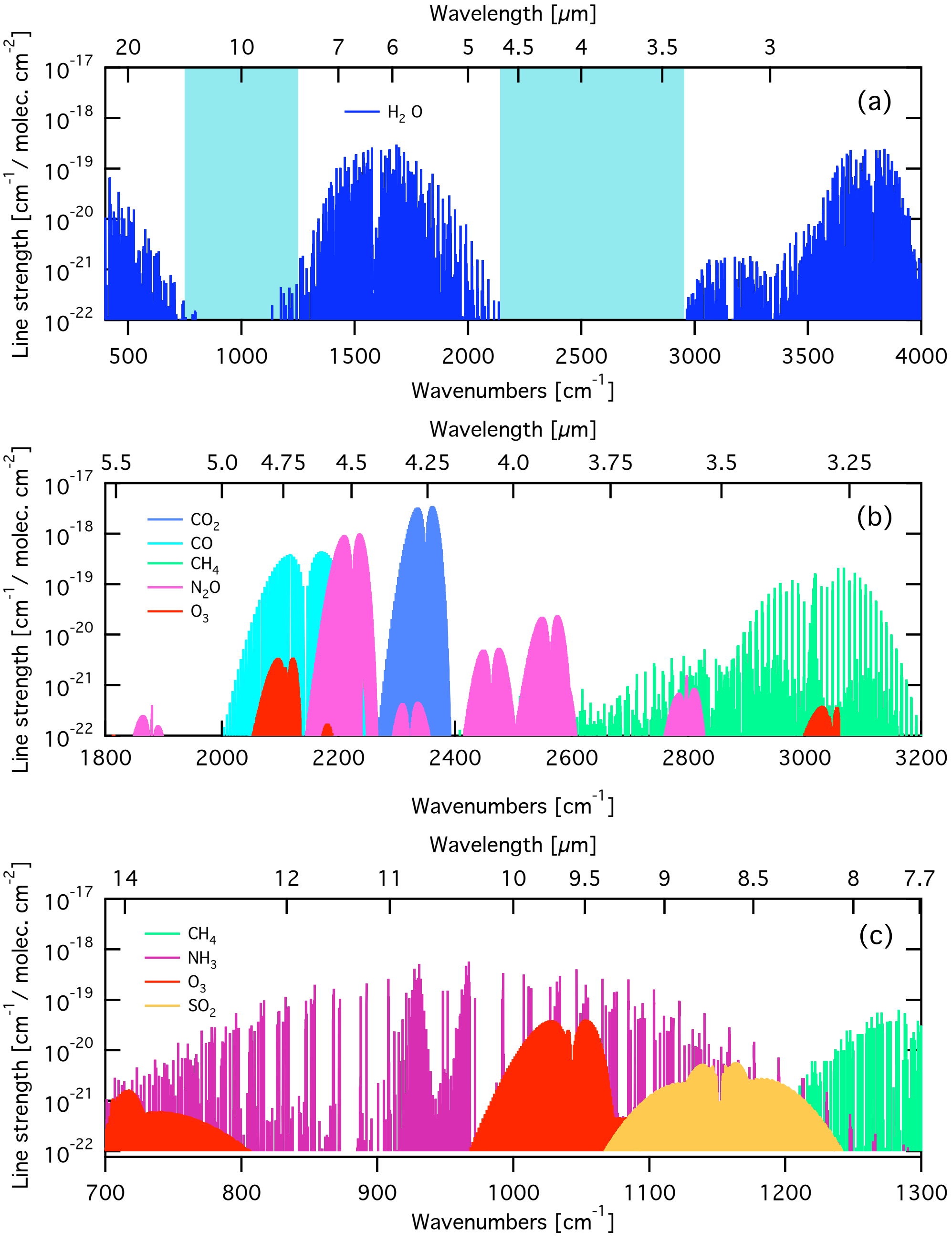

Figure 1.2: Mid-infrared absorption lines

(a) Absorption lines of the H_2O-molecule between 400 and 4000 cm^{-1}. The two infrared atmospheric windows are marked in light blue. Absorption lines of a selection of molecules in the first atmospheric window are shown in (b) and in the second atmospheric window in (c). Data was compiled using the HITRAN04 database.[122]

and its successor edited by Ebrahim-Zadeh and Sorokina[124].

As we have seen in the previous sections, quantum cascade lasers have made a huge progress in the last years in terms of continuous-wave operation, emitted power and wavelength tunability. This makes them an ideal source for many applications in the mid-infrared range that require relatively high power, small package footprint and low power consumption. An excellent overview of the use of quantum cascade lasers as light source for trace gas analysis and commonly used absorption spectroscopy techniques are given in the publication by Kosterev *et al.*[125]. As another example we also would like to mention the work performed by Tuzson *et al.* at EMPA[7] who used a quantum cascade laser operated spectrometer to perform continuous and simultaneous measurements of $^{12}CO_2$, $^{13}CO_2$ and $^{16}O\,^{12}C\,^{18}O$ isotopic species during six days in the field.[126, 127]

1.5.2 Free-space telecommunication

With the deployment of large computer networks in companies and the advent of bandwidth hungry streaming applications, quantum cascade lasers were also considered as light sources in optical point-to-point links for data communication, e.g. between neighboring corporate buildings or for bridging the "last mile" link in high bandwidth telecommunication infrastructure. Although such systems existed already using superluminescent light diodes or lasers that emit in the visible or NIR region, quantum cascade lasers are considered as a superior light source for several reasons. The ultrafast carrier relaxation lifetime and the absence of relaxation oscillation resonance would

---

[7] Swiss Federal Laboratories for Materials Testing and Research

allow a very fast modulation of the device.[128, 129] Additional to that, a wavelength can be chosen that lies in the highly transmissive windows of the atmosphere between 3.3 and 4.2 μm or between 8 and 13 μm. Free-space optical transmission in these windows is limited by the atmospheric transmission losses that are dominated by light scattering and scintillation effects. All these effects have a strong dependence on wavelength and are much more favorable for longer wavelength. For example, attenuation due to Rayleigh scattering has a λ^{-4}-dependence, and taking into account all these effects, researchers in Ref. [45] estimate that for a free-space optical link working in the second atmospheric transmission window in clear weather conditions, atmospheric absorption losses would be about a factor 100 lower than for one working in the NIR region.

Free-space optical communication experiments with quantum cascade lasers have been performed at University of Neuchâtel, at AT&T Bell Labs and also elsewhere.[130, 131, 132, 133] In an experiment at AT&T Bell Labs, two laser beams at $\lambda = 8.1\,\mu$m and $\lambda = 850\,$nm were combined using a beam splitter and sent over the same optical path of about 200 m in open-air and the signal transmission was measured.[45] Although they clearly demonstrated the superior signal transmission for the long wavelength beam in foggy conditions, the long wavelength did not prevent the connection from dropping when the fog was very dense.

The reasons why quantum cascade laser-based free-space optical links did not find their way into the telecommunication infrastructure are probably manifold: The lack of cheap quantum cascade laser sources and detectors, the high cost of the required optics and the incapability to guarantee the connection in strong fog and thus requiring a backup solution that further increases the cost of the system. It also has to be noted that in the last 10 years many radio-based telecommunication systems working in the ISM bands have been developed that are easy to use and, due to high-volume production, are cheap. Therefore free-space optical links are only considered for niche applications where a very high bandwidth is required (>1 Gb/s) and no fiber or copper connection can be constructed or is too expensive.

1.5.3 Countermeasures

Countermeasures represent a true niche application for quantum cascade lasers. However, we believe that it is worth mentioning because military agencies were among the first to realize the big potential of quantum cascade lasers as a bright and powerful source of mid-infrared light. Therefore, these agencies helped financing the pre-industrial development of quantum cascade lasers at universities and that at that time only private company fabricating quantum cascade lasers.

Since the fifties man-portable air-defense systems (MANPADS) have been developed to protect ground forces from enemy aircraft. Many of these systems employ missiles that use an IR sensor to home in on a heat source on an aircraft, typically the engine exhaust plume, and detonate a warhead in or close to the aircraft. These infrared-guided missiles are feared not only by military but also by civil airlines as terrorists can buy them relatively cheap on the black market and no special training is required to launch them. Indeed, in the last fifteen years several incidents have been reported where cargo and civil airplanes have been attacked by terrorists. Therefore, a broad spectrum of countermeasure devices have been developed and high-power quantum cascade lasers, due to their brightness, small size and efficient generation of IR light, are considered to be an ideal source to produce an infrared beam that can be used to disturb the guidance system of an infrared-guided missile.

Another countermeasure scenario using quantum cascade lasers consists in using high power quantum cascade laser sources in the form of laser pointers to disturb highly sensitive thermal cameras that are used in military equipment like tanks and helicopters for vision during night.

1.5.4 Others

Another niche, but nevertheless very important application of quantum cascade lasers, is to use them as local oscillators in heterodyne detection systems for the far- and mid-infrared region.[134, 135, 136, 137, 138] Sonnabend *et al.* for example used a quantum cascade laser emitting at $\lambda \approx 10\,\mu$m as local oscillator for their tunable heterodyne infrared spectrometer and were able to measure Mars zonal winds with unprecedented spatial resolution.[137, 139] In another experiment Weidmann *et al.* used a quantum cascade laser heterodyne radiometer to measure atmospheric ozone profiles with high spectral resolution and unprecedented vertical resolution.[140, 138] The $1\,\%$ tunability around the center frequency of the used distributed feedback quantum cascade laser emitting at $\lambda \approx 10\,\mu$m allowed them to sweep the frequency of the local oscillator and perform spectral analysis without the need of any IF signal, and thus with a much less complex system.

An application that is reserved to quantum cascade lasers emitting in the far-infrared is terahertz imaging[141] for biomedical, industrial and homeland security applications.[142, 143, 144, 145] Light in this wavelength range is non-ionizing and has the advantage of having a wavelength long enough to penetrate most non-metallic materials and short enough to provide good spatial resolution. Many possibilities exist to generate terahertz radiation but quantum cascade lasers are seen as an ideal source for these applications because of power, efficiency and small footprint. However, direct generation of terahertz radiation by a quantum cascade laser operated on a thermoelectric cooler is unfortunately still not possible and therefore more expensive and bulkier cooling has to be provided.

Chapter 2

Theory

The goal of this chapter is to give a short summary on the device physics and underlying models that are used to understand and predict the characteristics of our structures.

2.1 Intersubband physics

2.1.1 Electronic states in heterostructures

Envelope function formalism

For a detailed derivation of the envelope function formalism we refer to the textbook by Rosencher and Vinter.[146]

Let us consider a semiconductor whose potential is composed of a periodic part $V_c(\mathbf{r})$ for the crystal lattice and a slowly varying part $V(\mathbf{r})$ with respect to the lattice spacing. The Hamiltonian for an electron moving in the conduction band of this semiconductor is:

$$\mathcal{H} \;=\; \frac{p^2}{2m_0} + V_\mathrm{c}(\mathbf{r}) + V(\mathbf{r}) \tag{2.1}$$

and it can be shown that for $V(\mathbf{r})=0$ the solution to Schrödinger's equation are the Bloch wavefunctions:

$$\psi_{n\mathbf{k}}(\mathbf{r}) \;=\; \frac{1}{\sqrt{\Omega}} e^{i\,\mathbf{k}\cdot\mathbf{r}}\, u_{n\mathbf{k}}(\mathbf{r}) \tag{2.2}$$

where Ω is the crystal volume and n is the band index. The functions $u_{n\mathbf{k}}(\mathbf{r})$ have the periodicity of the lattice and the corresponding energy is $\varepsilon_{n\mathbf{k}}$. For $V(\mathbf{r}) \neq 0$ an envelope function $\zeta_N(\mathbf{r}) = \sum_{\mathbf{K}} a_{N\mathbf{K}}\, e^{i\,\mathbf{K}\cdot\mathbf{r}}$ is introduced and the Schrödinger equation for this envelope function writes:[146]

$$\left[-\nabla \frac{\hbar^2}{2m^*_N(\mathbf{r})} \nabla + V(\mathbf{r})\right] \zeta_N(\mathbf{r}) \;=\; (E - \varepsilon_{N\mathbf{0}})\, \zeta_N(\mathbf{r}) \tag{2.3}$$

where the energy $\varepsilon_{N\mathbf{0}}$ of the Nth band at $\mathbf{K} = 0$ and the effective mass m^*_N take into account *all* influence of the material. Equ. (2.3) already assures the conservation of the probability flux across an interface between two semiconductors. Additionally, wavefunctions must be continuous across the interface.

Quantum well

In a heterostructure quantum well electrons can move freely in the plane perpendicular to the growth direction z and effective mass and potential only depend on z. Therefore the envelope function can be written:

$$\zeta(\mathbf{r}) \;=\; \zeta_{n\mathbf{K}}(z)\,\exp(i\,\mathbf{K}\cdot\mathbf{R}) \quad \text{with } \mathbf{R}=(x,y) \text{ and } \mathbf{K}=(k_x,k_y) \tag{2.4}$$

and the Schrödinger equation becomes:

$$\left[-\frac{d}{dz}\,\frac{\hbar^2}{2m^*(z)}\,\frac{d}{dz} \;+\; \left(V(z)+\frac{\hbar^2\mathbf{K}^2}{2m^*(z)}\right)\right]\zeta_{n\mathbf{K}}(z) \;=\; E\,\zeta_{n\mathbf{K}}(z) \tag{2.5}$$

For small values of K the K-dependence of $\zeta_{n\mathbf{K}}(z)$ (due to the variation of the effective mass) can be dropped and Equ. (2.5) simplifies to:

$$\left[-\frac{d}{dz}\,\frac{\hbar^2}{2m^*(z)}\,\frac{d}{dz}+V(z)\right]\zeta_n(z) \;=\; \varepsilon_n\,\zeta_n(z)\;,\;\varepsilon_n=E_n-\frac{\hbar^2\mathbf{K}^2}{2m_{\mathrm{w}}} \tag{2.6}$$

where w_{b} is the effective mass in the well. Solution of Equ. (2.6) yields stationary states $|n\mathbf{K}\rangle$ with energies $E_{n\mathbf{K}}=\varepsilon_n+\frac{\hbar^2\mathbf{K}^2}{2m_{\mathrm{w}}}$ where ε_n are discrete energies and solutions to Equ. (2.6). The states form subbands as shown in Fig. 2.1. Electrons occupying such a subband[1] have the same quantized motion in the growth direction and continuously varying $\mathbf{K}$ as they can move freely in the other two directions.

For complex heterostructures solutions are determined numerically, for example by a transfer-matrix method.[43]

Multi-band and non-parabolicity

In practice the precision obtained by solving Schrödinger's equation in a one-band model (except for energy levels close to the bottom of the wells) is not

---

[1] Also called two-dimensional electron gas.

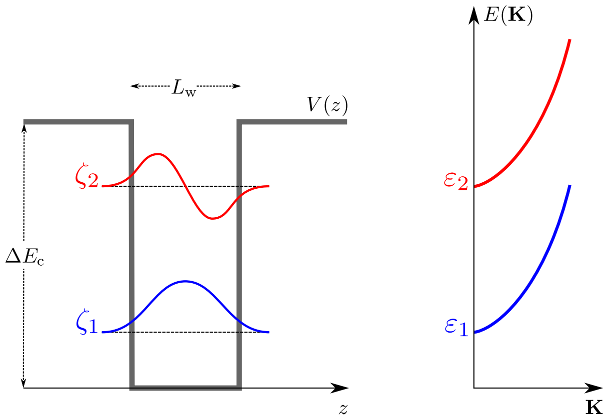

Figure 2.1: Subband states in a quantum well

sufficient and the influence of the full conduction and valence band structure needs to be taken into account. A more precise, but computationally much more intensive, approximation is obtained with the Kane model where conduction, heavy-hole, light-hole and spin-orbit split-off bands are taken into account.[147]

However, in the case where only electronic states in the conduction band are considered, the four-band Kane model (8×8 reduced by spin degeneracy) can be reduced to an "effective" two-band model by assuming that the in-plane momentum vanishes, and thus decoupling the heavy-hole band, and replacing the light-hole and split-off band band by a virtual valence band.[148] This "effective" two-band model can then be recast into a one-band model through an energy-dependent effective mass.[149] In this model the energy-dependent effective mass in the well and barrier material, respectively are given by:

$$m_\mathrm{w}^*(E) = m_\mathrm{w}^* \left(1 + \frac{E}{E_\mathrm{w}^\mathrm{eff}}\right) , \quad m_\mathrm{b}^*(E) = m_\mathrm{w}^* \left(1 - \frac{V - E}{E_\mathrm{b}^\mathrm{eff}}\right) \tag{2.7}$$

where V is the barrier height and m_i^* and E_i^{eff} are empirical parameters for effective masses and effective gaps, respectively. The nonparabolicity parameter γ that describes nonparabolicity in the neighborhood of energy-band extrema according to the dispersion relation

$$E = \frac{\hbar^2 \mathbf{K}^2}{2m^*}\left(1 - \gamma \mathbf{K}^2\right) \tag{2.8}$$

is related to effective energy gap and mass by:

$$\gamma_i = \frac{\hbar^2}{2m_i^* \, E_i^{\mathrm{eff}}} \,, \quad (i = \mathrm{w}, \mathrm{b}) \tag{2.9}$$

These properties on both sides of the interfaces are linked by the expressions:

$$m_{\mathrm{w}}^*/m_{\mathrm{b}}^* = E_{\mathrm{w}}^{\mathrm{eff}}/E_{\mathrm{b}}^{\mathrm{eff}} \tag{2.10}$$

$$\gamma_{\mathrm{w}}/\gamma_{\mathrm{b}} = \left(m_{\mathrm{b}}^*/m_{\mathrm{w}}^*\right)^2 \tag{2.11}$$

The effective gaps can then be determined for example using measured bulk effective masses and a measured or calculated nonparabolicity parameter.

Charge distribution

In our structures carriers are provided by doping a region in the injector with a donor material (typically Si) and a bias voltage is applied to the structure in order to pass current through it. The final potential $V(z)$ is therefore composed of the band-edge profile V^{mat} that arises from epitaxially growing layers of alternating materials with a conduction band offset ΔE_{c} (see Fig. 2.1), a homogeneous potential due to the applied bias voltage and the Hartree potential due to the charge distribution in the structure:

$$V(z) \;=\; V^{\mathrm{mat}}(z) + V^{\mathrm{bias}}(z) + V^{\mathrm{Hartree}}(z) \tag{2.12}$$

The Hartree potential is calculated by solving Poisson's equation

$$\frac{\partial^2 V^{\mathrm{Hartree}}(z)}{\partial z^2} \;=\; -\frac{\rho(z)}{\epsilon\epsilon_0} \tag{2.13}$$

where ϵ_0 is the vacuum permittivity, ϵ is the material dielectric constant and $\rho(z)$ is the local charge density that is calculated from the profile of ionized donors $N_{\mathrm{D}}(z)$ and the carrier distribution in the subbands:

$$\rho(z) \;=\; q\left[N_{\mathrm{D}}(z) - \sum_i n_i |\zeta_i(z)|^2\right] \tag{2.14}$$

The subband population n_i is either determined by transport computations or can be approximated by distributing the carriers thermally in the subbands assuming a common chemical potential μ and charge neutrality:

$$\sum_i n_i = \sum_i \left[\int_E \mathcal{D}_i(E)\mathcal{F}(E)dE\right] \;=\; \int_{\text{period}} N_{\mathrm{D}}(z)dz = n_{\mathrm{s}} \tag{2.15}$$

with

$$\mathcal{D}_i(E) = \frac{m^*(E)}{\pi\hbar^2}\,\Theta(E - E_i) \quad \text{and } \mathcal{F}(E) = \frac{1}{e^{(E-\mu)/k_{\mathrm{B}}T} + 1}$$

where $\mathcal{D}_i(E)$ is the density of states in the *ith* subband, $\mathcal{F}(E)$ is the Fermi-Dirac distribution, Θ the Heavyside function and n_{s} is the total sheet carrier density.

Schrödinger and Poisson equation are coupled together by the potential and the subband populations, respectively. Therefore, they are solved iteratively until convergence is found.

2.1.2 Optical transitions

Transitions between different states in a quantum well are now examined under the influence of a electromagnetic wave that is treated like a sinusoidally time-varying perturbation. There are three types of possible transitions:

- Interband transition where an electron in a valence subband band is excited to a conduction subband.
- Intersubband transition where an electron makes a transition from one subband to another while remaining in the same band.
- Intrasubband transition where an electron remains in the same subband but changes its **K**-state.

We will focus our summary here on intersubband transitions as they are the ones providing the gain in our structures. Intrasubband transitions are briefly treated in the next section on scattering processes. For a discussion on interband transitions we refer to the book by Rosencher and Vinter.[146]

Let us consider a wave $\mathbf{E}(\mathbf{r}, t) = \mathbf{E_q} \cos(\mathbf{q} \cdot \mathbf{r} - \omega t)$ that travels across the quantum well. Due to the localized nature of the electronic states in the well we choose an approach based on the electric dipole Hamiltonian $\mathcal{D} \cdot \mathcal{E}$ where the electric dipole interaction potential with the quantum well electron writes:

$$V_{\mathbf{q}}(\mathbf{r},t) = -q\,\mathbf{E}\cdot\mathbf{r} = -\frac{q}{2}\mathbf{E}_{\mathbf{q}}\cdot\mathbf{r}\,e^{i\,(\mathbf{q}\cdot\mathbf{r}-\omega t)+\text{c.c.}} \tag{2.16}$$

Initial and final states of the quantum well electron are given by:

$$\psi_{n\mathbf{K}} \;=\; \frac{1}{\sqrt{A}}\zeta_n(z)\,e^{i\,\mathbf{K}\cdot\mathbf{R}}\,u_{c\mathbf{0}}(\mathbf{r}) \quad \text{and} \quad \psi_{m\mathbf{K}'} \;=\; \frac{1}{\sqrt{A}}\zeta_m(z)\,e^{i\,\mathbf{K}'\cdot\mathbf{R}}\,u_{c\mathbf{0}}(\mathbf{r}) \tag{2.17}$$

Fermi's golden rule is then used to calculate the rate of transitions induced by the electromagnetic field:

$$S(n\mathbf{K}\to m\mathbf{K}') \;=\; \frac{\pi q^2}{2\hbar}\left|\langle m\mathbf{K}'|\mathbf{E}_{\mathbf{q}}\cdot\mathbf{r}|n\mathbf{K}\rangle\right|^2\,\delta(E_{m\mathbf{K}'}-E_{n\mathbf{K}}\mp\hbar\omega) \tag{2.18}$$

where the "−" in the Dirac function stands for absorption and the "+" for emission. Using the fact that the envelope function varies slowly in comparison with the lattice spacing and furthermore assuming conservation of the parallel component of the momentum[2] the transition rate can be rewritten as:

$$S(n\mathbf{K}\to m\mathbf{K}') \;=\; \frac{\pi q^2}{2\hbar}\left|E_{\mathbf{q}z}\right|^2\,\left|\langle m|z|n\rangle\right|^2\,\delta(\varepsilon_m-\varepsilon_n\mp\hbar\omega)\,\Delta_{\mathbf{K},\mathbf{K}'} \tag{2.19}$$

where $\Delta_{\mathbf{K},\mathbf{K}'}$ is the Krönecker delta function. We note that the orthogonality of the envelope functions induces an intersubband selection rule that states that transitions couple only to the z-component of the electric field and the parabolicity of the subbands removes the $\mathbf{K}$-dependence in the Dirac function. Taking into account the subband populations and summing over

---

[2] Light wavevector $\mathbf{q}$ is negligible in comparison with electronic wavevectors $\mathbf{K}$ and $\mathbf{K}'$.

K yields for the net transition rate (excitation+relaxation) from state n:

$$R_{\text{net}} = \left(\frac{dn_n}{dt}\right)_{\text{net}} = \frac{\pi q^2}{2\hbar}\,|E_{\mathbf{q}z}|^2 \sum_m |\langle m|z|n\rangle|^2\;\delta(\varepsilon_m - \varepsilon_n - \hbar\omega)\,(n_n - n_m) \tag{2.20}$$

where $\langle m|z|n\rangle = z_{mn}$ is the dipole matrix element between states m and n with respective population densities n_m and n_n.

Each optical transition corresponds to an absorption or emission of a photon between two resonant subbands. Knowing the transition rate between two subbands n and m with respective population n_n and n_m and separated by the energy $E_{nm} = \hbar\omega_{nm}$ the gain[3] can be calculated and and is given by:[150]

$$G(\hbar\omega) = \frac{\pi q^2 |z_{nm}|^2\,\omega_{nm}}{\varepsilon_0\,n_{\text{eff}}\,c\,L_{\text{p}}}\,\Delta n\,\frac{(\gamma_{nm}/\pi)}{[\hbar(\omega-\omega_{nm})]^2+\gamma_{nm}^2} \tag{2.21}$$

where $\Delta n = (n_n - n_m)$ is the electron population difference and the last term represents the Lorentzian lineshape function with half-width at half-maximum (HWHM) of γ_{nm} and that replaces the Dirac function in Equ. (2.20). The peak gain/absorption is obtained where the photon is resonant with the intersubband transition between levels n and m and writes:

$$G_{\text{p}}(\hbar\omega) = \frac{2q^2|z_{nm}|^2\omega_{nm}}{\varepsilon_0\,n_{\text{eff}}\,c\,L_{\text{p}}}\,\frac{1}{2\gamma_{nm}}\,\Delta n \tag{2.22}$$

with $2\gamma_{nm}$ the full-width at half-maximum (FWHM) of the transition.

As the active region material only “sees” a part of the optical mode a confinement factor Γ needs to be introduced (see section 4.2.1 in chapter 4) and thus the modal gain writes $G_{\text{m}} = G_{\text{p}} \cdot \Gamma$. The gain cross section g_{c} that

---

[3] Corresponds to negative absorption.

we will encounter in section 2.4 below is given by $g_\mathrm{c} = G_\mathrm{m}/\Delta n$.

2.1.3 Spontaneous emission

The spontaneous emission over all spatial directions for a quantum transition between states $|i\rangle$ and $|f\rangle$ with energy E_i–$E_f = \hbar\omega_0$ and in an optical medium with refractive index n_eff is derived in the book by Rosencher and Vinter,[146] or also in Ref. [151], and is given by:

$$\frac{1}{\tau_\mathrm{sp}} = \frac{q^2|z_{if}|^2\omega_0^3\, n_\mathrm{eff}}{3\pi c^3\hbar\varepsilon_0} = \frac{q^2\omega_0^2\, n_\mathrm{eff}}{6\pi c^3\varepsilon_0 m}\,|f_{i\to f}| \qquad (2.23)$$

where

$$f_{i\to f} \;=\; \frac{2m(E_f - E_i)}{\hbar^2}\,|z_{if}|^2 \qquad (2.24)$$

is the oscillator strength and obeys the Thomas-Reiche-Kuhn sum rule.[4] The oscillator strength is a dimensionless quantity and can be interpreted as a measure of the spontaneous emission rate of transition $i \to f$ over the decay rate of a classical Hertzian dipole oscillating at identical frequency.

With the inclusion of an energy-dependent effective mass to take into account of nonparabolicity and of other bands Equ. (2.6) does no longer guarantee completeness nor orthogonality of its eigenfunction set $\zeta_n(z)$. The publication by Sirtori *et al.*[148] shows how oscillator strength and sum rules need to be modified and how the wavefunctions need to be normalized due to energy-dependent effective mass.

---

[4] See complement 3.D in Ref. [146] for a derivation.

2.2 Scattering mechanisms

2.2.1 Fröhlich interaction

Phonons are vibrational waves travelling through a crystal lattice and present a time-dependent perturbation to the periodic crystal potential that determines the electron states in the bands. Additional to the deformation potential that is proportional to the relative displacement of the lattice atoms, in polar semiconductors additional interactions need to be taken into account due to the fact that phonons create polarization and electrostatic fields. The electrostatic field induced interaction caused by optical phonons is called Fröhlich interaction and has a much stronger effect than the deformation potential. For a detailed treatment of phonons and Fröhlich interaction we refer to the book by Rosencher and Vinter.[146]

Using Fermi's golden rule the transition rate for the absorption/emission of a phonon writes:[146]

$$S(\mathbf{k}\!\rightarrow\!\mathbf{k}') \;=\; \frac{2\pi}{\hbar}\,\left|\langle\mathbf{k}| - qV_{\mathbf{q}}|\mathbf{k}'\rangle\right|^2\,\delta\left[E(\mathbf{k}') - E(\mathbf{k}) \mp \hbar\omega_{\mathbf{q}}\right] \qquad (2.25)$$

where $V_{\mathbf{q}}$ is the interaction potential with a phonon of wavevector $\mathbf{q}$ and "$-$" stands for absorption and "$+$" for emission of a phonon. The total scattering rate, given by the sum of scattering rates of absorption and stimulated and spontaneous emission, writes:

$$\begin{aligned}
\lambda[E(\mathbf{k})] &= \sum_{\mathbf{k}'} S_{\mathrm{abs}}(\mathbf{k}\to\mathbf{k}') + \sum_{\mathbf{k}'} S_{\mathrm{em}}(\mathbf{k}\to\mathbf{k}') \\
&= \frac{q^2\hbar\omega_{\mathrm{LO}}\, m^*}{4\pi\varepsilon_0\varepsilon_{\mathrm{st}}\hbar^2\sqrt{2m^*E}}\left(\frac{\varepsilon_{\mathrm{st}}}{\varepsilon_\infty}-1\right) \qquad (2.26)\\
\cdots\times &\left[n_{\mathbf{q}} \ln\left|\frac{\sqrt{E+\hbar\omega_{\mathrm{LO}}}+\sqrt{E}}{\sqrt{E+\hbar\omega_{\mathrm{LO}}}-\sqrt{E}}\right| + (n_{\mathbf{q}}+1)\ \ln\left|\frac{\sqrt{E}+\sqrt{E-\hbar\omega_{\mathrm{LO}}}}{\sqrt{E}-\sqrt{E-\hbar\omega_{\mathrm{LO}}}}\right|\right]
\end{aligned}$$

where $n_{\mathbf{q}}$ is determined by the Bose-Einstein distribution:

$$n_{\mathbf{q}} = \frac{1}{e^{\hbar\omega_{\mathbf{q}}/k_{\mathrm{B}}T}-1} \qquad (2.27)$$

As an example we show in Fig. 2.2 calculated LO-phonon emission and absorption rates for $\mathrm{Ga}_{0.47}\mathrm{In}_{0.53}\mathrm{As}$ at 50 and 300 K. It can be seen that the electron must have an energy larger than $\hbar\omega_{\mathrm{LO}}$ in order to be able to emit a phonon and after this "threshold" the scattering rate changes little with energy. Therefore emission of LO-phonons is a very efficient process for the electron to dissipate excess energy with a timescale in the order of 100 fs.

2.2.2 Impurity scattering

Impurity scattering is generally dominated by the doping introduced in the semiconductor in order to provide the carriers. In a typical quantum cascade laser structure the donors are therefore added within a narrow region in the injector in order to prevent the impurities from influencing the optical transition.[52] Impurity scattering does however influence the transport properties of the quantum cascade laser structures and can be in the order of the other mayor scattering mechanisms.

Impurities are treated as a point charge Zq that is screened by free electrons in the crystal over the Debye screening length $\lambda_\mathrm{D} = 1/q_\mathrm{D}$ where q_D is the Debye wavevector and is given by:

$$q_\mathrm{D} \;=\; q\sqrt{\frac{n_0}{\varepsilon\, k_\mathrm{B}T}} \tag{2.28}$$

where $\varepsilon = \varepsilon_\mathrm{r}\varepsilon_0$ is the permittivity of the medium and n_0 is the is the average electron density. Calculated Debye screening length in $\mathrm{Ga_{0.47}In_{0.53}As}$ and as a function of electron density is shown in Fig. 2.3(a) for temperatures between 50 and 300 K. The scattering rate for an electron in an isotropic, parabolic band and having an effective mass m^* is calculated in chapter 6 of the book by Rosencher and Vinter and is given by:

$$\frac{1}{\tau_\mathrm{imp}(k)} = n_\mathrm{imp}\frac{Z^2q^4}{\varepsilon^2}\frac{m^*}{8\pi\hbar^3k^3}\left\{\ln\left[1+\left(\frac{2k}{q_\mathrm{D}}\right)^2\right] - \frac{(2k/q_\mathrm{D})^2}{1+(2k/q_\mathrm{D})^2}\right\} \tag{2.29}$$

where $n_\mathrm{imp} = N_\mathrm{imp}/V$ is the impurity density. Fig. 2.3(b) shows the calculated impurity scattering rate in $\mathrm{Ga_{0.47}In_{0.53}As}$ as a function of energy and for impurity densities between 10^{15} and $10^{17}\,\mathrm{cm^{-3}}$ and temperatures 50 and 300 K. For the calculation we assumed that the impurity density is equal to the average electron density ($n_\mathrm{imp} = n_0$). As Fig. 2.3(b) shows impurity scattering is very efficient at low energies and large impurity densities around $10^{17}\,\mathrm{cm^{-3}}$ that are typically present in the doped region of a quantum cascade laser.

Scattering times for impurity scattering in different heterostructures have

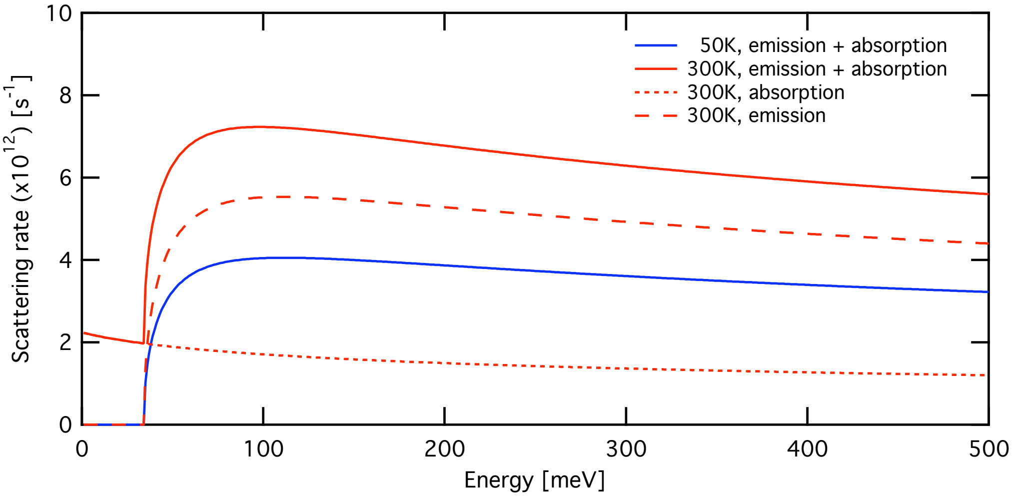

Figure 2.2: Scattering rate for LO-phonon scattering in GaInAs

Scattering rates for LO-phonon absorption and emission at 50 and 300 K in bulk $Ga_{0.47}In_{0.53}As$*. Absorption rate at 50 K is omitted because it is almost three orders of magnitude lower. For the calculation values* $\hbar\omega_{\mathrm{LO}} = 34\,meV$*,* $\varepsilon_\infty = 11.6$*,* $\varepsilon_{\mathrm{st}} = 13.9$ *and* $m^* = 0.043\,m_0$ *were assumed.*

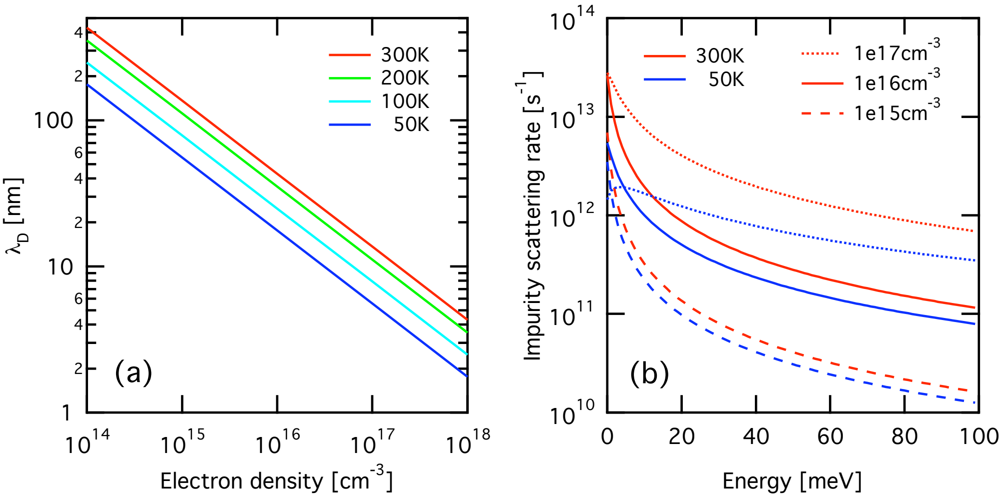

Figure 2.3: Debye screening length and impurity scattering rate

(a) Debye screening length in $Ga_{0.47}In_{0.53}As$ *as a function of average electron density for temperatures between 50 and 300 K. (b) Impurity scattering rate in* $Ga_{0.47}In_{0.53}As$ *as a function of energy and for temperatures 50 K and 300 K and for different impurity densities that are assumed to be equal to the electron densities* $(n_{\mathrm{imp}} = n_0)$*.*

been calculated by Ferreira *et al.*[152] for the case where ionized impurities are located in the vicinity of the interface.

2.2.3 Other scattering mechanisms

LA-phonon scattering

The interaction between electrons and LA-phonons can be calculated using a deformation potential approximation.[152] However, this scattering mechanism is very inefficient compared to others and therefore is usually neglected.

Interface roughness and alloy disorder scattering

Magneto-spectroscopic experiments that have been performed by Sirtori's group in Paris have shown that interface roughness and alloy disorder scattering play a significant role in the depopulation of the upper lasing state.[153, 154] Typically, these elastic scattering mechanisms have been neglected in electron lifetime calculations for the different states. However, Vasanelli *et al.*[154] show with magneto-spectroscopic measurements performed on $\mathrm{Ga_{0.47}In_{0.53}As/Al_{0.48}In_{0.52}As/InP}$-based quantum cascade lasers that at 80 K these mechanisms contribute up to 40 % to the total relaxation rate of the upper lasing state.

Electron-electron scattering

Electron-electron scattering plays an important role in the thermalization of hot carriers in the injection region. But the computation of scattering rates is very tedious and intensive and therefore we do not take into account of electron-electron scattering in our models.

Electron-electron scattering events are named with four indices $ij \rightarrow fg$ to denote the initial and final states of the two electrons with their respective in-plane momenta $k_\kappa = |\mathbf{K}_\kappa|,\ \kappa \in \{i, j, f, g\}$. Roughly speaking the scattering events can be splitted in two categories: “symmetrical” and “Auger” events.[155] In “symmetrical” events both electrons change up or down by one subband (*e.g.* $22 \rightarrow 11$) and in “Auger” events only one electron changes up or down whereas the other electron stays in the same subband. These “Auger” processes are forbidden in symmetric quantum wells due to selection rules.

The most important process is by far $22 \rightarrow 11$ and scattering rates have been calculated by Smet *et al.*[151]. They show that even for carrier concentrations exceeding $10^{12}\,\mathrm{cm}^{-2}$, electron-electron scattering is less important than LO-phonon scattering for intersubband energies larger than 200 meV.

2.3 Resonant tunneling

Resonant tunneling controls the injection of the carriers from the ground state of the injector into the upper lasing state and is also responsible to a large extent for the transport characteristics of our structures. Kazarinov and Suris described sequential resonant tunneling in a tight-binding approximation and calculated the tunneling current in a density-matrix formalism.[19, 20] The current between two subbands coupled via a tunneling barrier and coupling

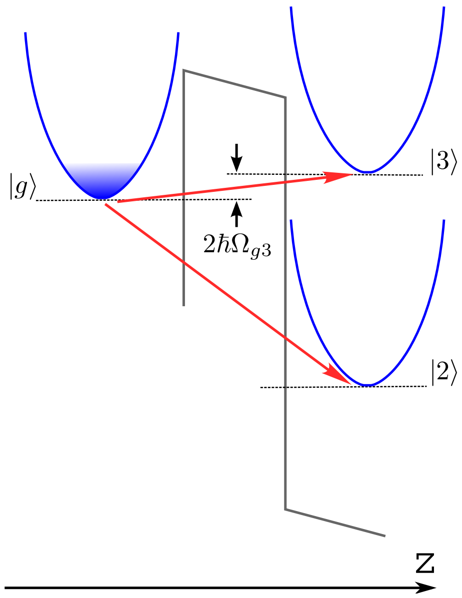

Figure 2.4: Resonant tunneling

energy $2\hbar|\Omega_{g3}|$ is given by:

$$J \;=\; q\,n_{\mathrm{s}}\frac{2|\Omega_{g3}|^2\,\tau_\perp}{1+\Delta^2\,\tau_\perp^2+4|\Omega_{g3}|^2\tau_\perp\tau_3}\;, \qquad \hbar\Delta = E_g - E_3 \tag{2.30}$$

where τ_3 is the upper state lifetime, $\tau_\perp$ is the in-plane dephasing time (~ 0.1 ps) and $\hbar\Delta$ is the energy detuning from resonance that can also be written as $qd(F - F_{\mathrm{R}})$ where d is the distance between the centroids of the two electron probability distributions and F and F_{R} are the applied and resonant fields, respectively. This is illustrated in Fig. 2.4 where the ground state of the injector $|g\rangle$ is shown on the left side of the injection barrier and upper and lower lasing states on the right. If an electric field is applied the detuning energy decreases until it reaches zero where states $|g\rangle$ and $|3\rangle$ form a doublet with anti-crossing energy $2\hbar|\Omega_{g3}|$. In this case the current is maximal and is given by:

$$J_{\mathrm{max}} = q\,n_{\mathrm{s}}\frac{2|\Omega_{g3}|^2\,\tau_{\perp}}{1+4|\Omega_{g3}|^2\tau_{\perp}\tau_3}$$

Depending on the value of $4|\Omega_{g3}|^2\tau_{\perp}\tau_3$ we now distinguish between two regimes:

$$4|\Omega_{g3}|^2\tau_{\perp}\tau_3 : \begin{cases} \ll 1, \quad J_{\mathrm{max}} = 2q\,n_{\mathrm{s}}|\Omega_{g3}|^2\,\tau_{\perp} & \text{(weak coupling)} \\ \gg 1, \quad J_{\mathrm{max}} = q\,n_{\mathrm{s}}/2\tau_3 & \text{(strong coupling)} \end{cases}$$

The weak coupling regime is obtained when the two times are in the same order of magnitude and at the same time are much smaller than $1/|\Omega|$. In that case the maximal current is limited by scattering. The desirable regime for quantum cascade lasers is the strong coupling regime where the current is limited by the upper state lifetime and the electron injection into the upper lasing state is very fast. In that case a quasi-equilibrium is reached between injector and upper lasing state that is characterized by a common quasi-Fermi level. Electron injection is optimal when $J = J_{\mathrm{max}}$ and $2\hbar|\Omega_{g3}|$ is comparable to $\hbar/\tau_{\perp}$.[156]

2.4 Rate equations

Macroscopic device characteristics like threshold current density J_{th} and slope-efficiency dP/dI are developed using a rate-equation approach within a three-level system. We consider three-level system as schematically drawn in Fig. 2.5 consisting in the three electronic states $|3\rangle$, $|2\rangle$ and $|1\rangle$ that are populated by electrons with population densities n_i (in units of cm^2). Electrons are injected from the ground state $|\mathrm{g}\rangle$ with an injection efficiency η

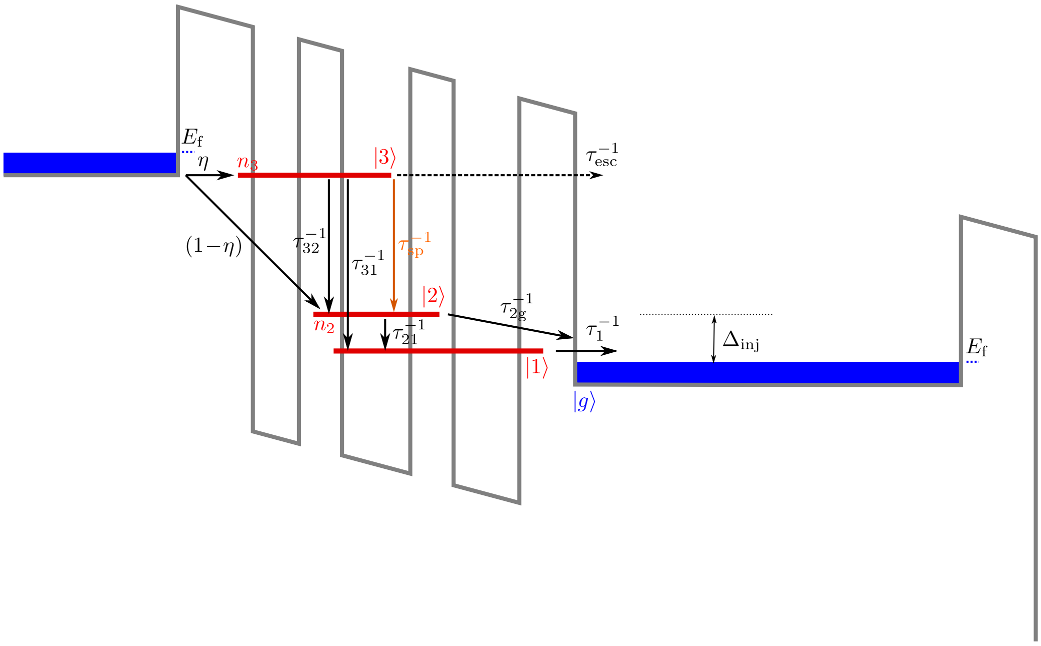

Figure 2.5: Three-level system

into the upper lasing state $|3\rangle$ whereas the remaining electrons are assumed to scatter directly into state $|2\rangle$. The total rates out of levels 3 and 2 are given by individual contributions of individual processes:[157]

$$\tau_3^{-1} = \tau_{32}^{-1} + \tau_{31}^{-1} + \tau_\mathrm{esc}^{-1} \tag{2.31a}$$

$$\tau_2^{-1} = \tau_{21}^{-1} + \tau_\mathrm{2g}^{-1} \tag{2.31b}$$

where τ_{ij} are the respective tunnel rates between levels i and j by non-radiative, optical-phonon scattering and τ_esc^{-1} is the rate of electrons escaping into the continuum. For reasons of simplicity, and without loss of the validity of the model, level 1 is merged with the injector. A set of equations can now be written that relate the change in the carrier density of states 3 and 2 and the change of the photon flux S in the cavity (per period, in units of [cm^{-1} s^{-1}]):

$$\frac{dn_3}{dt} = \eta\frac{J}{q} - \frac{n_3}{\tau_3} - g_c S\,(n_3 - n_2) \tag{2.32a}$$

$$\frac{dn_2}{dt} = (1-\eta)\,\frac{J}{q} + \frac{n_3}{\tau_{32}} + g_c S\,(n_3 - n_2) - \frac{n_2 - n_2^{\mathrm{th}}}{\tau_2} \tag{2.32b}$$

$$\frac{dS}{dt} = \frac{c}{n_{\mathrm{eff}}}\left[\left[g_c\,(n_3 - n_2) - \alpha_{\mathrm{tot}}^{\mathrm{opt}}\right]\cdot S + \beta\frac{n_3}{\tau_{\mathrm{sp}}}\right] \tag{2.32c}$$

were J is the current density injected into the system, q is the electron charge, g_c is the gain cross section (in [cm]), c/n_{eff} is the speed of light in the material and $\alpha_{\mathrm{tot}}^{\mathrm{opt}}$ is the total optical loss in the cavity and is further discussed in section 2.5 of this chapter. A term n_2 has been introduced in Equ. (2.32b) to take into account electrons populating state 2 due to thermal back-filling from the injector with sheet carrier density n_s and whose density is given by $n_2^{\mathrm{th}} = n_s \exp(-\Delta_{\mathrm{inj}}/k_B T)$ with Δ_{inj} the energy difference between level 2 and the injector's quasi Fermi energy (see Fig. 2.5), k_B Boltzmann's constant and T the temperature characterizing the injector. The last term in Equ. (2.32c) stands for the spontaneous emission with $\beta \sim 0.001$ the fraction of light emitted in the lasing mode and τ_{sp}^{-1} the emission rate. However, this term will be neglected because it is much smaller than τ_3^{-1} in the wavelengths we are considering (see 2.1.3). We also note that the rate of stimulated emission is given by $\tau_{\mathrm{stim}}^{-1} = S\,g_c$, resulting in a clamped population inversion between levels 3 and 2 above threshold.

2.4.1 Threshold current density

In order to calculate the threshold current density we set the derivatives with respect to time and S in the rate equations to zero. From Equ. (2.32a) we get an expression for n_3 that is then introduced into Equ. (2.32b) where n_2 is replaced by the expression $n_3 - \Delta n$ with Δn the population inversion and that is then expressed by:

$$\Delta n = \frac{J}{q}\left[\eta\,\tau_{\text{eff}} - (1-\eta)\,\tau_2\right] - n_2^{\text{th}} \tag{2.33}$$

where

$$\tau_{\text{eff}} = \tau_3\left(1 - \frac{\tau_2}{\tau_{32}}\right) \tag{2.34}$$

is the effective upper state lifetime. At threshold the gain equals the losses (Equ. (2.32c)) and the threshold current density is therefore given by:

$$J_{\text{th}} = \frac{q\left(\alpha_{\text{tot}}^{\text{opt}}/g_{\text{c}} + n_2^{\text{th}}\right)}{\tau_{\text{eff}}\,\eta - \tau_2\,(1-\eta)} \underset{\eta=1}{\Longrightarrow} J_{\text{th}} = \frac{q\left(\alpha_{\text{tot}}^{\text{opt}}/g_{\text{c}} + n_2^{\text{th}}\right)}{\tau_{\text{eff}}} \tag{2.35}$$

We note that before reaching threshold the current needs to compensate not only for the losses in the cavity but also for the electrons populating level 2 due to thermal back-filling. This term also introduces a strong temperature dependency of the threshold current if its value is in the order of $\alpha_{\text{tot}}^{\text{opt}}/g_{\text{c}}$. Therefore a high activation energy Δ_{inj} should be chosen in order to minimize n_2^{th} as much as possible. However, a too large value will negatively affect the wall plug efficiency as we will see in section 2.4.3. The term n_2^{th} can also be replaced by an effective loss term that is given by $\alpha_{\text{bf}} = g_{\text{c}}\,n_2^{\text{th}}$. Equ. (2.35) also reveals a very strong dependence of the threshold current with non-unity injection efficiency. In order to obtain a small threshold current it is therefore also crucial to reach an injection efficiency as close to unity as possible and to have a short τ_2.

2.4.2 Slope efficiency

Above threshold the photon flux in the cavity is no longer zero. Equ. (2.32a) is now combined with Equ. (2.32c) to yield an expression for n_3. This equation is then combined with Equ. (2.32b) to yield the photon flux as a function of current:

$$S = \frac{(J - J_{\text{th}})\,[\tau_{\text{eff}}\,\eta - \tau_2\,(1-\eta)]}{q\,\alpha_{\text{tot}}^{\text{opt}}\,(\tau_2 + \tau_{\text{eff}})} \quad \underset{\eta=1}{\Longrightarrow} \quad S = \frac{(J - J_{\text{th}})\,\tau_{\text{eff}}}{q\,\alpha_{\text{tot}}^{\text{opt}}\,(\tau_2 + \tau_{\text{eff}})} \tag{2.36}$$

And the slope efficiency (per facet) is given by:

$$\frac{dP}{dI} = \frac{1}{2}\frac{\hbar\omega}{q} N_{\text{p}} \underbrace{\frac{\alpha_{\text{m}}}{\alpha_{\text{tot}}^{\text{opt}}}}_{\eta_{\text{ext}}} \underbrace{\frac{\tau_{\text{eff}}\,\eta - \tau_2\,(1-\eta)}{\tau_2 + \tau_{\text{eff}}}}_{\eta_{\text{int}}} \tag{2.37}$$

where N_{p} is the number of periods, α_{m} is the mirror loss and η_{ext} and η_{int} are the external and internal quantum efficiencies, respectively.

2.4.3 Wall plug efficiency

A very crude upper bound for the wall plug efficiency can be determined assuming that in the aligned structure the voltage drop U_{p} over one period is given by the sum of the voltage drop over the optical transition (U_{act}) and the injection region (U_{inj}). The wall plug efficiency is then given by:

$$\eta_{\mathrm{wp}} = \frac{P_{\mathrm{opt}}}{P_{\mathrm{el}}} = \frac{I\,U_{\mathrm{act}}}{I\,(U_{\mathrm{act}}+U_{\mathrm{inj}})} = \frac{1}{1+\frac{U_{\mathrm{inj}}}{U_{\mathrm{act}}}} \approx \frac{1}{1+\frac{\Delta_{\mathrm{inj}}}{\hbar\omega}} \qquad (2.38)$$

Inserting the numbers for a transition energy of 250 meV and an injector width of 150 meV yields a maximal wall plug efficiency of 62 %.

A more sophisticated and therefore more precise model was developed by Faist.[158] The wall plug efficiency can also be expressed as:

$$\eta_{\mathrm{wp}} = \frac{(J_{\mathrm{max}}-J_{\mathrm{th}})}{J_{\mathrm{max}}}\frac{dP/dI}{U} \qquad (2.39)$$

where U is the voltage drop on the aligned structure and J_{max} is the maximal current that is proportional to the sheet carrier density and is given by $J_{\mathrm{max}} = n_{\mathrm{s}}\,q/\tau_{\mathrm{trans}}$ with τ_{trans} the global transit time that the electron spends in one period. Expliciting the variables in Equ. (2.39) using the equations developed in previous sections yields:

$$\eta_{\mathrm{wp}} = \eta_{\mathrm{int}}\,\frac{\alpha_{\mathrm{m}}}{\alpha_{\mathrm{tot}}^{\mathrm{opt}}}\,\frac{1}{1+\frac{\Delta_{\mathrm{inj}}}{\hbar\omega}}\left[1-\frac{\tau_{\mathrm{trans}}}{\tau_{\mathrm{eff}}}\left(\frac{\alpha_{\mathrm{tot}}^{\mathrm{opt}}}{n_{\mathrm{s}}\,g_{\mathrm{c}}}+\frac{n_2^{\mathrm{th}}}{n_{\mathrm{s}}}\right)\right] \qquad (2.40)$$

It is then assumed that the total optical losses are given by $\alpha_{\mathrm{tot}}^{\mathrm{opt}} = \alpha_{\mathrm{m}} + \alpha_{\mathrm{w}}$. For simplicity of the model and because we are interested in the maximum value of the wall plug efficiency the total waveguide losses are only expressed as a function of free-carrier absorption and other contributions are neglected (see section 2.5 of this chapter):

$$\alpha_{\mathrm{w}} = g_{\mathrm{fc}}\,n_{\mathrm{s}} \qquad (2.41)$$

where g_{fc} is the free-carrier absorption cross section. A maximal value for the wall plug efficiency at optimal mirror loss can then be derived and is given by:

$$\eta_{\mathrm{wp}}^{\max} = \eta_{\mathrm{int}} \frac{1}{1+\frac{\Delta_{\mathrm{inj}}}{\hbar\omega}} \left[\frac{\sqrt{g^{*}\,\tau^{*}}-1}{\sqrt{g^{*}\,\tau^{*}}}\right]^{2} \tag{2.42}$$

where dimensionless upper state lifetime $\tau^{*} = \tau_{\mathrm{eff}}/\tau_{\mathrm{trans}}$ and cross section $g^{*} = g_{\mathrm{c}}/g_{\mathrm{fc}}$ have been introduced. For a throughout discussion of this formula we refer to the publication by Faist.[158] In general, it can be said that in order to obtain a maximum wall plug efficiency the internal efficiency η_{int} and the term $\sqrt{g^{*}\,\tau^{*}}$ must be maximized. A large value for τ^{*} is obtained in a design where the transport across the injector is fast and where the electrons spend most of the time in the upper lasing state. It also can be shown that the term g^{*} introduces a strong wavelength dependency ($g^{*} \propto \omega^{2}$), making it more difficult to obtain a large wall plug efficiency at longer wavelengths.

2.5 Waveguide losses

Waveguide losses are a very important property of a quantum cascade laser as they have a strong influence on the threshold current and slope efficiency of a device (see sections 2.4.1 and 2.4.2 of this chapter).

The threshold condition for lasers states that at threshold the gain in the cavity must compensate the losses:

$$g\,\Gamma\,J_{\mathrm{th}} = \alpha_{\mathrm{tot}} \tag{2.43}$$

where $g\,\Gamma$ is the modal gain coefficient, J_{th} is the threshold current density and α_{tot} are the total losses. Supposing that the devices do not have electrical leaks due to fabrication problems, the total losses can be split in two parts: Mirror loss $\alpha_{\mathrm{m}}(L)$ that has a dependence on cavity length L and total waveguide losses α_{w} that are composed of various contributing terms that are detailed later in this section and that are constant:

$$g\,\Gamma\,J_{\mathrm{th}} \;=\; \alpha_{\mathrm{m}}(L) + \alpha_{\mathrm{w}} \tag{2.44}$$

Mirror loss is given by:

$$\alpha_{\mathrm{m}} \;=\; \frac{1}{2L}\ln\left(\frac{1}{R_1 R_2}\right)$$

where R_1 and R_2 are the power-reflectivities of the front and back facet, respectively. A commonly used technique to determine the total waveguide losses is to measure the threshold current density of laser devices with different lengths (and thus varying the mirror loss) whereas the total wavguide loss stays constant. This technique is discussed in section 3.4.3 of chapter 3.

Looking at Equ. (2.35) that describes the threshold current in the rate-equation model we can further explicit the waveguide losses:

$$g\,\Gamma\,J_{\mathrm{th}} \;=\; \underbrace{\alpha_{\mathrm{m}}(L) + \Gamma\,\alpha_{\mathrm{n-r}} + (1-\Gamma)\,\alpha_{\mathrm{fc}} + \alpha_{\mathrm{de}} + \alpha_{\mathrm{scatt}}}_{\alpha_{\mathrm{tot}}^{\mathrm{opt}}} + \alpha_{\mathrm{bf}}(T) \tag{2.45}$$

where the individual loss contributions are:

- **Non-resonant losses ($\alpha_{\mathrm{n-r}}$):**

  The absorption spectrum of a mid-infrared quantum cascade laser structure is complex and strongly depends on the design. An illustration of such an absorption spectrum is shown in the figure below.

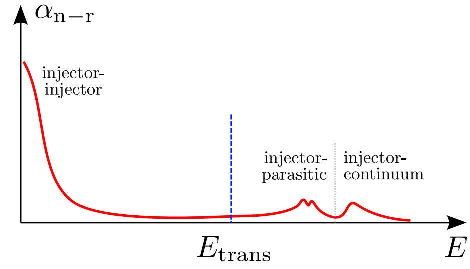

Intersubband transitions between subband states in the injection region typically leads to a strong absorption at low energies. Transitions between subband states in the injector to parasitic states that lie above the injector or continuum states cause absorption features at high energies. The energy of the lasing transition lies somewhere in between (shown by the blue dashed line). Because the features of this absorption lie at energies other than the lasing transition we call it “non-resonant absorption”.

- **Free-carrier absorption** (α_{fc}):

  Arises from the interaction between free electrons in the cladding layers and possible passive bulk layers in the waveguide core (multi-stack wavguides) and the optical mode in the cavity. We further discuss free-carrier absorption in section 4.2.3 of chapter 4.

- **Scattering losses** (α_{scatt}):

  Arise from light-scattering processes in the cavity for example due to material defects or sidewall roughness.[159]

- **Absorption in lossy insulating layer (α_{de}):**

  Standard Fabry-Pérot ridge waveguides as we used for this work are isolated from the top contact metal layer by a thin dielectric layer (typically $\mathrm{Si_x\,N_y}$ or $\mathrm{Si\,O_x}$). These materials have strong characteristic absorption peaks that, depending on the wavelength of the optical mode in the cavity and its overlap with the dielectric layer may cause absorption losses (see section 3.4.1 in chapter 3). These losses can be reduced by sophisticated waveguide design (see section 4.3.4 in chapter 4),[5] or by omitting the layer and burying the waveguide ridge in electrically insulating InP (buried-heterostructure process).[72]

- **Back-filling loss (α_{bf}):**

  The effective loss term α_{bf} is due to thermally-activated back-filling of electrons from the ground state of the injector to the lower state of the lasing transition. This term is given by

  $$\alpha_{\mathrm{bf}} \;=\; g_{\mathrm{c}}\, n_2^{\mathrm{th}} \;=\; n_{\mathrm{s}}\, \exp(-\Delta_{\mathrm{inj}}/k_{\mathrm{B}}T) \qquad (2.46)$$

  and was discussed in more detail in section 2.4 of this chapter.

The total optical losses $\alpha_{\mathrm{tot}}^{\mathrm{opt}}$ that are given by the sum of the terms in Equ. (2.45) with exception of the back-filling loss can be determined using the ratio of the slope efficiencies of an uncoated/coated device. This method is described in section 3.4.3 of chapter 3.

Chapter 3

Measurement techniques

3.1 Introduction

The development of a quantum cascade laser for a commercial application can be very expensive and may require several optimization iterations, depending on the tightness of the specifications. Therefore it is important to have reliable tools at hand that allow to obtain information on the characteristics and performance of the structure very early in the development process in order to make it as efficient as possible. In basic QCL research, the development process may be much shorter and, for example, just require a simple Fabry-Pérot process. However, the need for reliable tools that allow to obtain as much information as soon as possible in the process remains. For the development of interband lasers there exist tools that can be used immediately after growth of the structure and that yield crucial information about material quality, growth homogeneity, emission wavelength and threshold current:

- A photoluminescence mapper can measure photoluminescence spectra as a function of position on the wafer. The position of the exciton peak in the spectrum yields the center of the emission wavelength and their width gives an indication about the quality of the grown material. With quantum cascade laser structures this is not possible for several reasons: The intersubband polarization rule together with the low radiative efficiency for spontaneous emission in the MIR wavelength region would result in an extremely weak emission perpendicular to the wafer surface that would be very difficult to detect. Also, it makes little sense to measure photoluminescence spectra of a QCL structure at zero bias if one wants to get information about its lasing characteristics as lasing only occurs when the band structure is aligned.

- In order to test the threshold current density of interband lasers, often it is sufficient to cleave a small laser bar from the wafer and define a contact stripe where the current is injected. In QCL development this in impracticable due to the much higher threshold current density.

In this chapter we will discuss some of the techniques that are used to characterize the QCL structures as well as the fabrication of the devices.

3.2 Post-growth inspection

The first characterization tool after epitaxial growth is visual inspection under a microscope. An ideal epilayer surface is perfectly flat with no defects. However in reality different kinds of defects can be visible on the surface, depending on the surface quality and cleanliness of the substrate, the state of the epitaxy equipment including calibration and possible disturbances during growth. The structures we refer to in this dissertation were typically grown on half or quarter 2-inch wafers using molecular beam epitaxy. This implies that the epi-ready InP substrates had to be cleaved and mounted on a substrate in a gray room. The indium that was used to glue the wafer on the substrate holder had to be removed again before the wafer was transferred to a MOVPE reactor for InP overgrowth of the cladding layer as our growth equipment had no phosphorus source. All these additional steps are potential sources for surface contamination and therefore local defects. The density of these defects will negatively affect the yield of the fabrication process and may as well lower the performance of an individual device if the defect density is high. Lattice mismatch between grown layers can result in dislocations inside the crystal lattice and a sub-optimal ratio between III/V fluxes can result in a milky surface. X-ray diffraction measurements are performed systematically on all grown structures in order to measure the error of the structure periodicity. This value is then used as a feedback to correct the fluxes for subsequent growths. An error in the structure periodicity causes a shift of the emission wavelength that depends strongly on the width of the active region quantum wells. The width of the XRD peaks and comparison with a simulated X-ray diffraction pattern yields information on the homogeneity of the structure and the quality of the grown material.

Post-growth inspection provides an almost immediate feedback after growth. However, beside the error of the structure periodicity, the information is qualitative at most and not conclusive. Lasers fabricated from a wafer with a milky surface or dislocations may perform very well and the influence of defects on the laser performance depends on their nature and where they are located in the structure.

3.3 Electroluminescence measurements

In electroluminescence measurements a spectrally resolved measurement of the spontaneous emission is performed while a bias is applied to the structure. These measurements are mainly used as a fast feedback for the designer of the structure to verify that the grown wafer emits at the desired wavelength. Otherwise electroluminescence measurements are performed when a structure does not behave as expected. Identifying different transitions in the electroluminescence spectrum shows the relevant radiative channels and the width of the peaks yields information about material quality and interface roughness. Other uses are the determination of the stopband width in distributed feedback quantum cascade lasers or multi-section cavity gain measurements as discussed in section 3.6 of this chapter are a sophisticated type of electroluminescence measurements.

3.3.1 Sample preparation

The simplest way to fabricate a sample for EL measurements is to cleave a small ($500 \times 500\,\mu$m) piece of the wafer and to provide it with electrical contacts. To that end the sample is pressed into a sheet of pure indium on a copper mount and for the top contact a small piece of indium approximately $100 \times 100\,\mu$m in size is pressed on the epilayer. Then the mount is heated on a hot plate to melt the indium and diffuse it slightly across the oxide into the semiconductor and improve the electrical contact. Finally a gold wire is fixated on a gold plated contact pad by thermo compression bonding and cut and pressed into the indium ball of the top contact. A schematic drawing of such a sample is shown in Fig. 3.1(a) and the inset shows a sample spectrum. Although these samples are easy and fast to fabricate the measured spectra are of limited use beyond finding the center of the emission wavelength because the surface where the light is emitted is badly defined. This makes the optical alignment difficult. Additionally, the inhomogeneous electrical contact leads to the formation of field domains that broaden the spectrum and enhance tails on both sides of the center wavelength.

Better spectra are obtained from samples with small mesa structures or specially cleaved ridge waveguides. In order to measure the spontaneous emission, spectrum narrowing effects due to an optical cavity need to be suppressed. This can be obtained by cleaving a very short sample from a Fabry-Pérot laser process as shown in Fig. 3.1(b). The cavity needs to be short enough that no significant amplification occurs along the path to the facet. The maximum length depends on the gain of the structure and waveguide losses and is typically between 100 and 300 μm. Alternatively a ridge waveguide can be cleaved along the direction of the facet emission and mounted 90° rotated as shown in (c) 3.1. This ensures that the path along which amplification could occur is short enough and also suppresses the back facet mirror. Another feature of this method is that with a sufficiently long device stimulated emission can be observed at the same time. However, these samples are difficult to fabricate as the waveguide ridges of mid-infrared

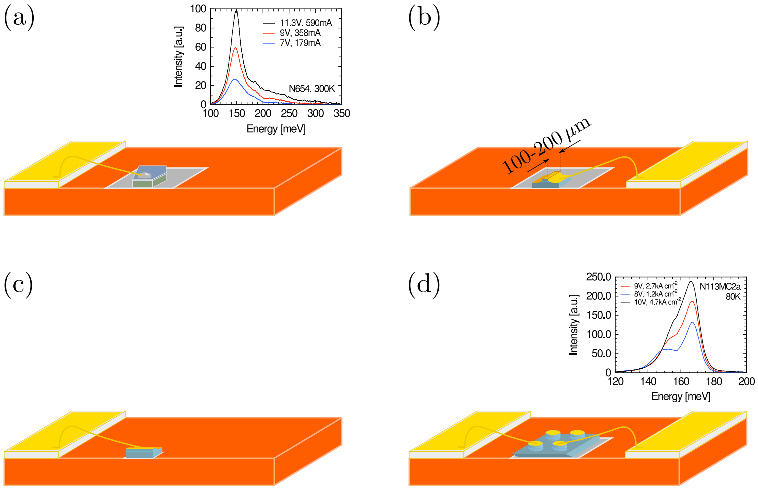

Figure 3.1: Samples suitable for EL measurements
(a) Drawing of a sample with fast electroluminescence process and the inset shows an example spectrum of device N654 at 300 K for voltages between 7 and 11.3 V. The tail on the high-energy side of the peak at 150 meV is an artifact due to inhomogeneous contact. A ridge waveguide sample with a very short cavity is shown in (b) and a sample based on a waveguide cleaved along the emission direction and mounted sideways in (c). (d) Sample with circular mesa structures and in the figure inset an example spectrum of device N113MC2a is shown, measured at 80 K between 8 and 10 V.

quantum cascade lasers are typically 5 to 20 μm wide and therefore difficult to cleave. This is not true for quantum cascade lasers where the waveguide ridge has been embedded in InP by an overgrowth (buried-heterostructure).[72] In this case the light can be collected directly from the side of the sample as the overgrown material is transparent in the mid-infrared.

Similar results can be obtained with circular mesa structures. A schematic drawing of such a sample is shown in Fig. 3.1(d) with an example spectrum in the inset and Fig. 3.2 illustrates how circular mesas are fabricated using planar technology for III-V semiconductors. First a small piece is cleaved from the grown wafer and rinsed in trichloroethylene (TCE), acetone (ACT), isopropanol (IPA) and at last deionized (DI) water as shown in Fig. 3.2 (a).

Then a thin layer of positive photoresist is spin coated onto the surface (b) and the mesa pattern on the photo-mask is transferred onto the resist layer after exposure with UV light (c) and development (d). Material not protected by the photoresist pattern is removed with aged $HBr:HNO_3:H_2O$ (1:1:10) etching solution until the InP of the substrate is revealed (e). After etching the remaining photoresist is stripped (f) and the sample cleaned as described in (a). Another photolithography is performed to define the geometry of the top contact (g)-(i) and Ti/Ge/Au/Ti/Au (1/12/27/10/200 nm) is evaporated on the surface by electron beam evaporation. The thin titanium layer enhances the adhesion of the contact on the semiconductor while the subsequent germanium and gold layers are in the ratio to form an eutectic alloy at 633 K. A second titanium layer acts as diffusion barrier and the thick gold layer is necessary to fixate the gold contact wires by thermo compression bonding. Then the metal that was evaporated on the photoresist is removed by lift-off technique (k), a back contact with the same materials is evaporated on the sample backside. A 45 ° wedge is polished at a sample sidewall in order to improve the light extraction (l). Finally, the sample is heated on a hot plate to 365 ℃ to form the eutectic Au/Ge alloy and diffuse the germanium slightly into the semiconductor to reduce the Schottky barrier. After cleaving the chip is indium-soldered on a copper mount, contacted by wire bonding and is the ready to be measured.

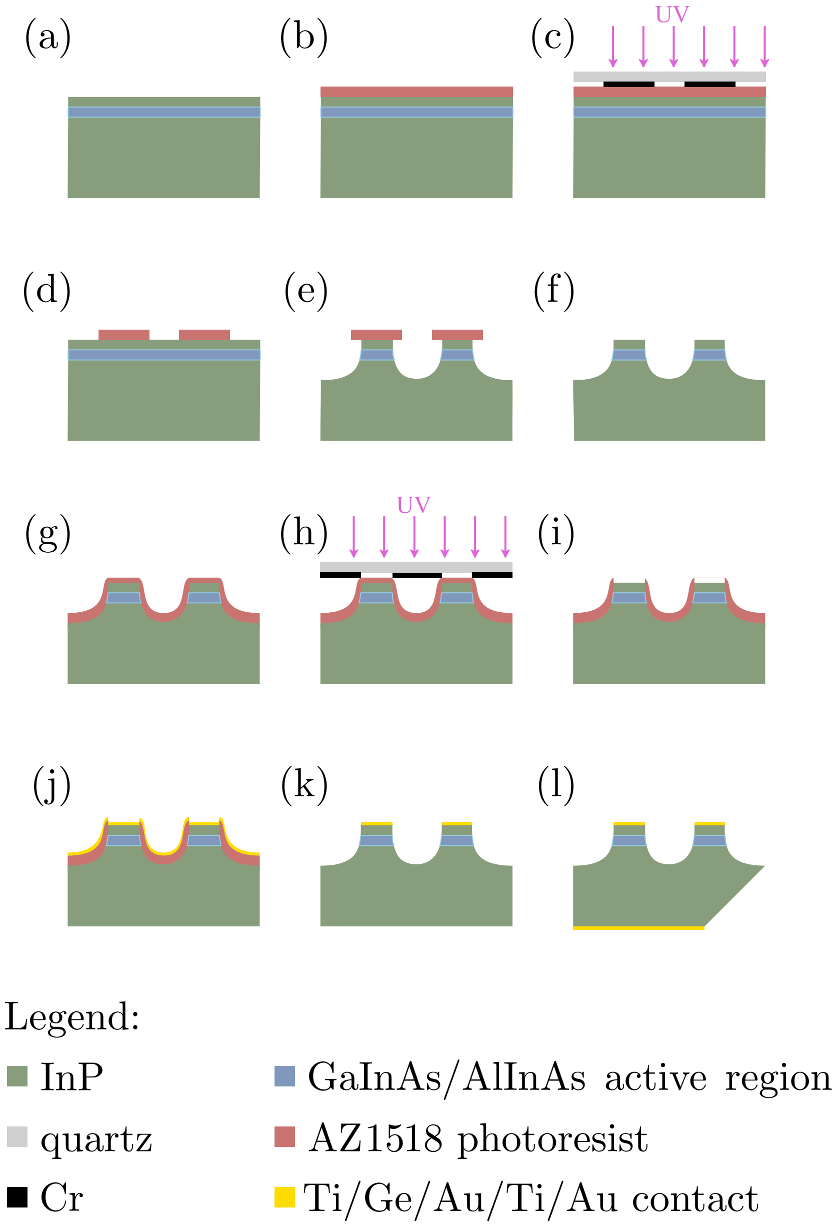

Figure 3.2: Fabrication of circular mesa structures

(a)-(l) Schematic description of the fabrication process for circular mesa structures using III-V semiconductor planar technology. The process requires two photolithographies, one wet-etching step and deposition of the top and back contact by electron beam evaporation. A 45° wedged facet is polished in order to improve light extraction.

3.3.2 Measurement setup

Electroluminescence spectra are measured with the experimental setup schematically shown in Fig. 3.2. A very sensitive measurement technique is required because spontaneous emission in the mid-infrared region is extremely inefficient and the blackbody radiation of the environment, peaking around 9 μm wavelength at room temperature, makes a strong background. Therefore a step-scan measurement is performed with a Fourier-transform spectrometer and highly sensitive detectors and the pulsed signal is then recovered from the noisy background using lock-in detection.

The sample is mounted on a continuous flow cryostat where the temperature can be regulated between 4 and 325 K with a Lakeshore TC330 temperature controller. For measurement temperatures below the dew point the sample is held under vacuum. Emitted light is collected by a $f/0.8$ BBAR-coated aspheric germanium lens that is directly mounted on the case of a Bruker IFS66/S Fourier-transform spectrometer. The interior of the latter is purged by N_2 and the asymmetric Michelson interferometer is equipped with a KBr beam splitter and allows a maximal resolution of $0.112\,\text{cm}^{-1}$. Two liquid nitrogen cooled detectors are available: A photovoltaic HgCdTe detector is installed at an exit port of the spectrometer where a $f/1.5$ BBAR-coated aspheric ZnSe lens is used to focus the beam on the photo-diode surface with a diameter of 100 μm. Alternatively a photoconductive HgCdTe detector can be chosen that is installed after the sample compartment of the spectrometer. Specifications of these two detectors are listed in the appendix. The photovoltaic HgCdTe detector is used for multi-section cavity gain measurements

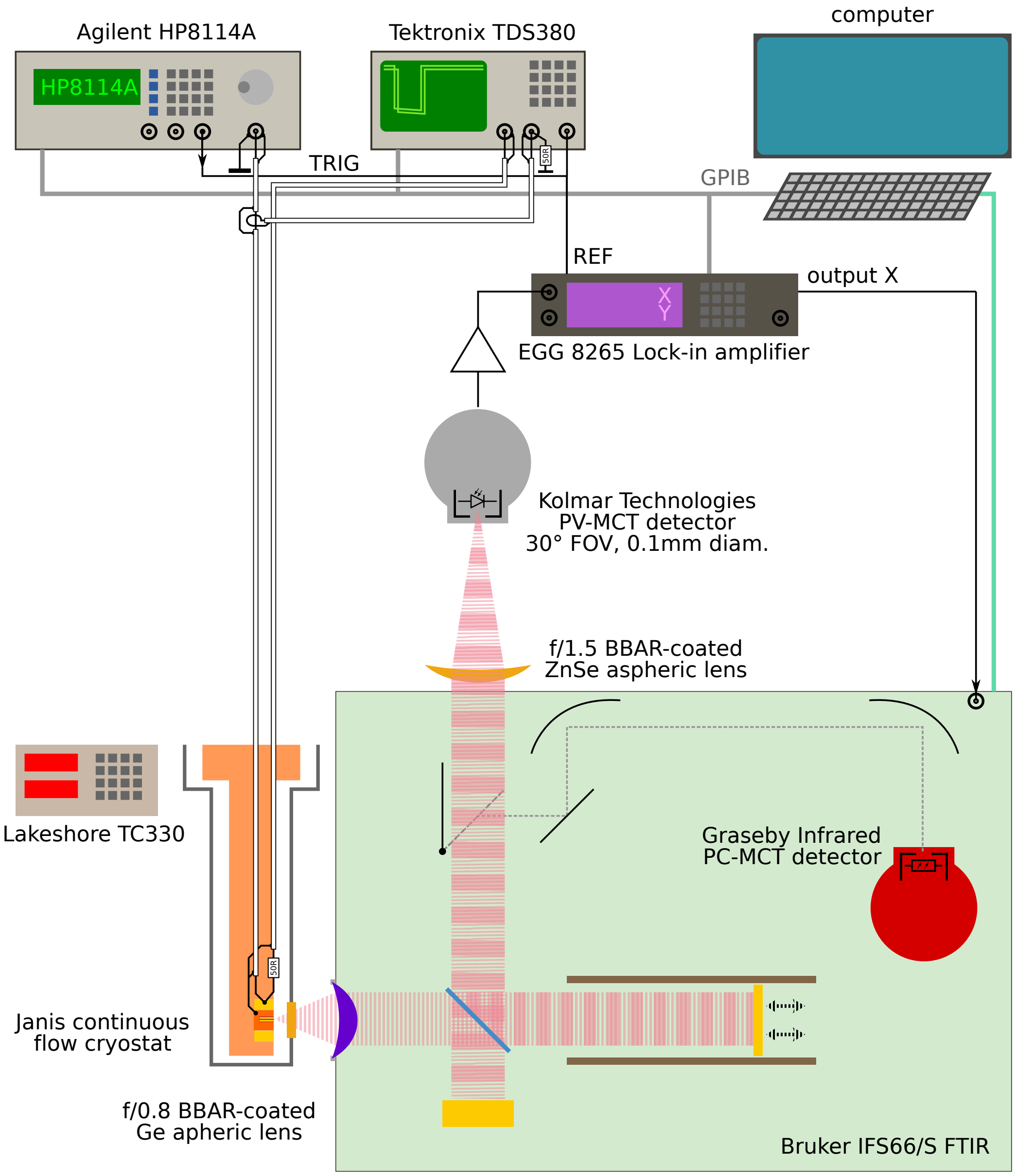

Figure 3.3: Electroluminescence measurement setup

Schematic drawing of the setup used for electroluminescence measurements. The sample is mounted on a continuous flow cryostat where its temperature can be controlled between 4 and 325 K and the spectrum is measured with a Fourier-transform spectrometer using lock-in signal filtering. (The beam path in the spectrometer is only for illustration and does not correspond to the real layout.)

that are discussed in section 3.6 of this chapter. For standard electroluminescence spectrum measurements the photoconductive HgCdTe detector is preferred because the alignment is easier and the signal-to-noise ratio is better.

The pre-amplified detector signal is connected to the input of an EGG7265 DSP lock-in amplifier whose reference is synchronized with the trigger signal of the pulse generator. Its integration time constant is adjusted to the dwell time of the step-scan (typically 200 ms) and for the sensitivity setting a value is chosen that is approximately twice the value of the signal when the spectrometer mirror is far away from the zero-path-difference point (ZPD). After signal processing the in-phase signal is sent to a DAC output of the lock-in amplifier and fed-back to a DC-coupled detector input of the spectrometer whose control software OPUS handles the data acquisition. Typically double-sided interferograms with 3554 points are acquired, resulting in $16\,\mathrm{cm}^{-1}$ spectral resolution. Interferograms are apodized with a Blackman-Harris or Happ-Genzel window and a power spectrum is calculated.

Current pulses are supplied by an Agilent HP8114A pulse generator and their intensity is measured with a wide band current probe that is connected to a Tektronix TDS380 oscilloscope. The acquisition is triggered by the pulse generator and the second channel is used for the measurement of the voltage drop on the device. Typically 2-8 sequential acquisitions are averaged and displayed on the scope. Voltage and current are then determined by averaging the points that are between the gating cursors of the oscilloscope. These gating cursors need to be readjusted each time the pulse width is changed such that they delimit the pulse plateau. For each channel the smallest possible input range is chosen where no clipping of the pulse occurs to minimize the digitizing error. With a 4:1 impedance transformer currents up to 3.5 A (depending on the impedance of the device) can be reached. When even higher currents are needed the HP8114A pulse generator is replaced by an Avtech pulse generator with a maximal pulse width of 100 ns and 5 kHz repetition rate.

Specifications and details on a selection of equipment can be found in appendix A and a step-by-step description of the measurement procedure in appendix B.1.

3.4 LIV characterization

Measurement of the power-current-voltage characteristics is the most important characterization of for a laser device. It reveals essential device characteristics like threshold current density, peak power and slope efficiency. Comparing the dependence of the threshold current density with inverse cavity length yields an estimation of the waveguide losses. Increasing the heat sink temperature of the laser device results in an exponential increase of the threshold current density according to the empirical law $J_{\mathrm{th}} = J_0 \exp(T/T_0)$ where T_0 is a characteristic temperature of the device (T-not) that allows to make predictions for the high-temperature operation of a device.

3.4.1 Sample fabrication

In this section the simplest process to fabricate GaInAs/AlInAs-based Fabry-Pérot lasers with ridge waveguides will be discussed. However, no details are given for the specific process steps as implementations vary between cleanrooms and operators. Schematic illustrations of the process steps are shown in Fig. 3.4.

The starting point is a piece of a wafer with a surface of approximately $1\,\text{cm}^2$ where a QCL structure has been grown on top of a InP substrate by MBE and/or MOVPE.[1] The surface is terminated by a highly doped (Si: $n > 2 \times 10^{19}\text{cm}^{-3}$) $\text{Ga}_{0.47}\text{In}_{0.53}\text{As}$ contact layer and if indium was used to make a homogeneous thermal contact between the substrate and the holder in the MBE, it has to be completely removed.

In a first step waveguide ridges are fabricated in the same way as described in section 3.3.1, Figs. 3.2 (a)-(f) for the fabrication of circular mesa structures. Special attention needs to be attributed to the etching step as the waveguide cross section and the sidewall surface roughness influence the current distribution across the active region and waveguide losses of the device. An ideal waveguide has vertical sidewalls with a surface roughness that is much smaller than the wavelength in the material to minimize scattering effects. After etching the sample is cleaned with solvents and O_2 plasma ashing to remove all remainders of photoresist and other organic material. Then a dielectric material is deposited (b) by PECVD to isolate the active region from the top contact that will be deposited in the following steps. With standard PECVD deposition equipment the choice is typically between silicon nitride and silicon dioxide and typical film thickness is 300 nm. While silicon nitride is preferred due to its ≈20 times higher thermal conductiv-

---

[1] In cleanrooms where the process steps are well mastered tendency is to process entire 1/4 wafers to increase the yield.

ity and better photoresist adhesion, a strong absorption band of SiN_x:H at $2155\,\mathrm{cm}^{-1}$ (Si-H stretching) prohibits its use for lasers emitting below $5\,\mu$m. In terms on thermal conductivity silicon carbide with a thermal conductivity ($120\,\mathrm{W\,m^{-1}\,K^{-1}}$) that is four times higher than for silicon nitride would be even a better choice. However, due to the presence of carbon, it is much more difficult to obtain highly resistive films that are needed to prevent leaking currents. Another photolithography step [Figs. 3.4 (c) and (d)] and dry-etching in a RIE chamber (e) is used to open the dielectric layer on top of the waveguide ridge. Optionally, the same photoresist mask can then be used to deposit an alloyed Ti/Ge/Au (1/12/17 nm) contact by electron beam evaporation (f). After stripping of the resist or lift-off of the superfluous metal layer and proper cleaning a new photolithography is performed to define the geometry of the extended contact [Figs. 3.4 (g) and (h)]. This contact is then deposited by electron beam evaporation [Ti/Au (10/200 nm)] and the metal between the contact pads is removed by lift-off technique. If improved heat sinking is desired, a 4-5 μm thick gold layer is deposited on top of the extended contact by electroplating (j). The substrate is then lapped down to a thickness of 100-150 μm to reduce its thermal resistance and a Ti/Ge/Au/Ti/Au (1/12/27/10/200 nm) contact is deposited on the backside of the sample (k) that then is alloyed at 365 ℃ for five minutes.

The fabrication of the lasers is now completed and the wafer piece is cleaved along crystallographic planes into laser bars with one or several ridges and the bars are indium-soldered on a copper mount that has been cleaned and degreased beforehand. As a last step gold-plated ceramic pads are glued on the copper mount and the waveguide ridges are contacted with

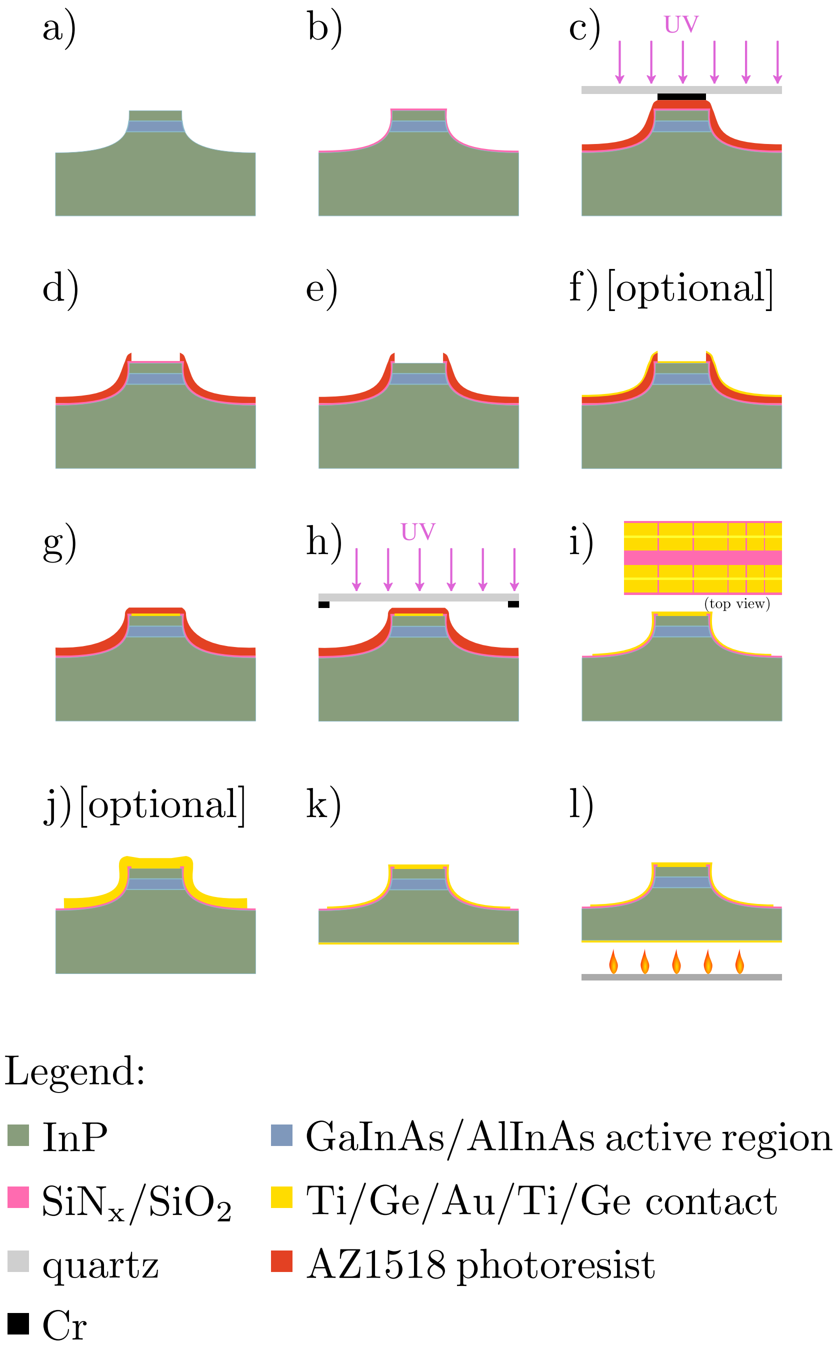

Figure 3.4: Ridge waveguide fabrication

(a)-(l) Schematic step-by-step illustration of the fabrication of ridge waveguide QC lasers. After etching of the waveguide ridge (a) major steps include deposition and patterning of an insulating dielectric layer and fabrication of the expanded top contact and back contact.

gold wires by thermo compression bonding. Sample mounting is a crucial step for high-performance operation of quantum cascade lasers. Therefore more sophisticated mounting is used for high-performance QCLs to improve the operating temperature for continuous-wave operation. Best device thermal conductances are obtained by burying the waveguide ridge in Fe-doped InP (buried-heterostructure process) and mounting the chips epi side down on diamond heat spreaders. However, for the devices mentioned in this work only standard mounting procedures were used.

The sample names we refer to in this work follow a well defined naming-scheme that allows to identify each mesa on a chip and that provides the required flexibility for the work in a research group. The first part in the name is the name of the grown epilayer and it depends on the terminology used by the growth facility. For the samples grown by MBE in Neuchâtel this can be for example N258 meaning the 258^{up} layer grown in the machine in Neuchâtel. It follows a term identifying the process and, if applicable, additional sub-processes (*e.g.* Aa and Ab for samples without and with electroplated gold, respectively). Each mounted sample receives a unique number, starting from one, and each mesa on the chip gets a letter as identifier. Looking at the top of the sample with the emitting facet pointing to the right, the ridge on top is ridge “a”. Thus, sample N808A5b-c stands for the second ridge of the fifth sample that has been mounted from the first process of layer N808 and the suffix “-c” means that ridge has a highly-reflective coating on the back facet.

3.4.2 Measurement setups

Pulsed measurements in cryostat

Fig. 3.5 shows a schematic of our measurement setup that is used for standard current-power-voltage characterization in pulsed-mode operation and for heat sink temperatures between 4 and 325 K. The basic equipment is the same as for electroluminescence spectrum measurements described in section 3.3.2. Instead of sending the beam into a Fourier-transform spectrometer a $f/1.5$ BBAR-coated aspheric ZnSe lens focuses it on a calibrated thermopile detector head that measures the average power. Its signal is read by a Ophir LaserStar display and the values are read by the acquisition software over a GPIB instrumentation bus. The acquisition software ramps the output voltage of the HP8114A pulse generator up to a maximal voltage setting. After the setpoint voltage is set a delay between 0.5 and 1 s is waited in order to give the scope the time to average the required number of acquisitions and the power meter to settle. Then the voltage drop on the device and the current are measured as described in section 3.3.2 and the average power is read from the power meter. The channel scales of the scope are either dynamically adjusted by software or the smallest range is chosen where no clipping occurs at maximum current. Dynamically adjusting the ranges increases the measurement precision in the low-current region of the measurement but range changes cause steps in the resulting current-voltage characteristics due to offset errors of the individual ranges. At the end of a measurement cycle the data is saved to a file for further treatment.

The collection efficiency of this experimental setup is between 70 and 80 %

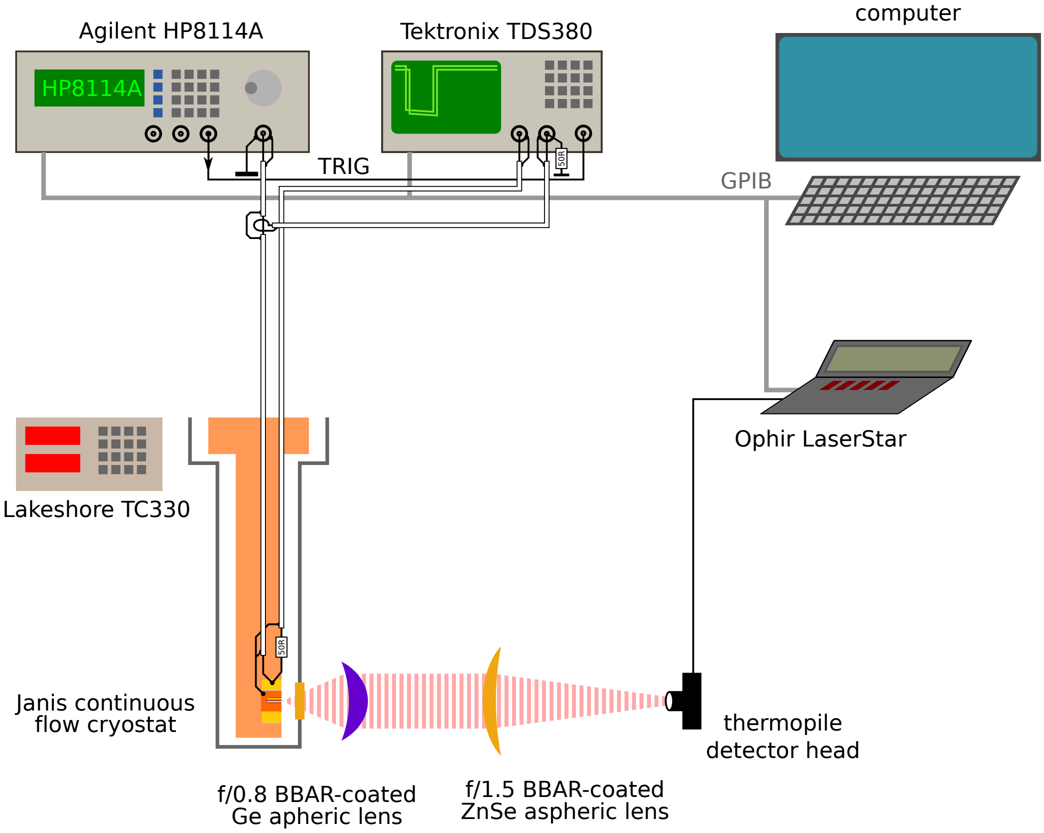

Figure 3.5: Measurement setup for pulsed LIV characterization

Standard setup that is used for LIV measurements in pulsed operation between 4 and 325 K. The sample is mounted on a continuous flow cryostat and the average power of the emitted light is measured with a thermopile detector head. Pulses are supplied by a HP8114A pulse generator and current and voltage drop on the device are measured with a TDS380 scope. The devices are controlled by the acquisition software over GPIB bus.

depending on the optical alignment of the sample and its far-field emission pattern. For measurements where the heat sink temperature is above the dew point in the laboratory the sample enclosure can be removed and the power meter placed directly in front of the laser facet. In this configuration a collection efficiency close to 100 % is obtained.

For measurements at low duty-cycle where the precision of the thermopile detector head is not sufficient the latter is replaced by a fast calibrated room-temperature HgCdTe detector. The detector signal is boxcar-averaged and the resulting DC voltage read through an auxiliary ADC channel of an EGG7265 lock-in amplifier.

Pulsed measurements in LLH100 laser housing

For samples with a large cross section the maximal current that the HP8114A pulse generator can provide (approximately 3.5 A) is not sufficient. In that case, a setup that corresponds to the "Starter Kit" that is sold by Alpes-Lasers SA, is used. The laser is mounted in a LLH100 laser housing with a BBAR-coated ZnSe window in front. The sub-mount temperature is controlled by a thermoelectric cooler that is connected to a TCU151 temperature controller and the extracted heat is removed by a water cooling circuit. A low-impedance connection conducts the current pulses to the laser and the current pulses are switched by a LDD100 driver that is connected to a variable power supply that is controlled by an acquisition program over GPIB instrumentation bus. The pulse shape is provided by a HP8114 pulse generator.

With this setup currents up to 10 A and high duty-cycles can easily be obtained. However, it lacks an accurate current and voltage measurement. Attempts were made to determine the current by measuring the voltage drop on a shunt resistance but the accuracy was not sufficient. The preferred solution is to measure the current with a current probe, as in the other setup, but in that case the current needs to pass through a wire that is inserted into the low-impedance line, resulting in a large impedance mismatch as the impedance of the wire segment is much higher. For technical reasons, instead of measuring the voltage drop on the device, the voltage of the variable power supply is measured. Therefore the voltage drop in the connection and on the power MOSFET in the driver are not taken into account, resulting in an over-estimation of the voltage.

These inaccuracies prohibit the use of this setup to measure reliable power-current-voltage characteristics but it is very well suited for measurements where the maximum average power and duty-cycle are determined.

Continuous-wave measurements

Continuous-wave measurements are performed with a Keithley 2420 sourcemeter as power supply and the optical power is measured with a calibrated thermopile detector head. Basically there are two methods how a power-current-voltage curve can be acquired. The first, we call it the "adiabatic" mode, is the one that was used at the beginning of continuous-wave operating quantum cascade lasers when the devices dissipated 20 to 30 W of electrical power and the heat sink did not provide enough cooling power to stabilize the temperature. In that mode the drive current is ramped-up in a fast way from zero to some limiting value and acquiring approximately 100 data points. In that way the measurement is terminated after a couple of seconds. The temperature is measured at the heat sink. However, the temperature of the chip and especially the active region increases with increasing dissipated power during current ramping. An example of such a “adiabatic” measurement where the temperature of the chip has been measured at the same time is discussed in section 3.5 and results are shown in Fig. 3.8. Because the acquisition is fast and the thermopile detector head has a slow response time, the power measurement usually lags behind and therefore the discontinuity of the differential resistance is used to determine accurately the position of the laser threshold. The second method is the “isothermal” method where the temperature of the sample is measured on the chip itself and is used as a feedback for a control loop that stabilizes the chip temperature to the setpoint. The current is ramped-up much slower such that the temperature control loop is able to follow with the temperature stabilization. As the temperature reported is closer to the actual active region temperature than in the “adiabatic” measurement, not only the reported performances are better but also the measurement is more precise as it is acquired in equilibrium conditions for the heat flow. However, the method requires that the thermoelectric cooler can provide enough cooling power to stabilize the heat sink temperature over the whole current range and the a thermometer needs to be fixated on the chip and close to the laser. Alternatively one could think of a temperature measurement as described in section 3.5 where a second laser on the chip is used as thermometer but in that case individual calibration would be required.

3.4.3 1/L-measurement

A relatively fast and easy way to determine gain and waveguide losses of a processed layer is to study the dependence of the threshold current density with the cavity length. The technique is based on the threshold condition for a laser that states that at threshold the gain in the structure equals the losses:

$$g\Gamma \cdot J_{\mathrm{th}} = \alpha_{\mathrm{m}} + \alpha_{\mathrm{w}} \tag{3.1}$$

Where $g\Gamma$ is the modal differential gain and α_{m} and α_{w} are mirror and waveguide losses of the lasing mode (see section 2.5 in chapter 2). Waveguide losses are assumed to be constant and because they usually depend on the waveguide width, only samples with similar ridge widths should be used for a 1/L-measurement. Mirror losses depend on the cavity length and are determined by

$$\alpha_{\mathrm{m}} = \frac{1}{2L} \ln\left(\frac{1}{R_1 R_2}\right) \tag{3.2}$$

where L is the cavity length and R_1 and R_2 are the power-reflectivities of the front and back facet mirrors that can be calculated in a first approximation with the simple formula

$$R \; = \; \frac{(n_{\mathrm{eff}} - n_0)^2}{(n_{\mathrm{eff}} + n_0)^2} \tag{3.3}$$

with n_{eff} the effective refractive index of the waveguide for the optical mode and $n_0 = 1$ the refractive index of air. For a more precise calculation of the facet reflectivity also higher order modes need to be taken into account.[160, 161]

A series of samples with similar ridge widths are now measured at constant temperature, yielding the threshold current density J_{th} as a function of cavity length. Then for each sample the mirror losses are calculated according to Equ. (3.2) and the threshold current density is plotted as a function of mirror losses. A line ($y = a + bx$) is then fitted to the data points by the least-squares method and the gain coefficient and waveguide losses are calculated from the fitting parameters according to

$$g\Gamma = \frac{1}{b}\ , \qquad \alpha_{\mathrm{w}} = g\Gamma \cdot a = \frac{a}{b} \tag{3.4}$$

where a is the offset of the fitted line and b the slope.

Although $1/L$ studies are often included in publications on MIR-QCLs, a discussion on the uncertainty associated to the reported values is often omitted. A conservative estimation of these uncertainties can be calculated using error propagation, but first it needs to be discussed where the errors come from. As we said before the threshold current density is plotted on the ordinate and each value has an associated uncertainty that strongly depends on the measurement setup and the measurement conditions. Error propagation yields

$$\Delta J_{\mathrm{th}} = J_{\mathrm{th}} \left[\frac{\Delta I_{\mathrm{th}}}{I_{\mathrm{th}}} + \frac{\Delta W}{W} + \frac{\Delta L}{L} \right] \tag{3.5}$$

with ΔI_{th}, ΔW and ΔL the uncertainties or errors of threshold current values, the active region width and the cavity length, respectively. The cavity length is measured with an optical microscope with integrated scale and the measurement precision with 5× or 10× magnification is typically $10\,\mu$m. For a 3 mm long device this yields a relative error of 0.3 %. A much higher error is attributed to the width of the active region that is also measured with an optical microscope and the measurement error is typically between 0.5 and 1 μm. However, if the active region was etched with wet-etching, the latter often has a trapezoidal shape and one needs to define a rule where the active region width is measured. In general we measure the width at the top of the active region. Other uncertainties arise from possible slow modulations of the active region width due to inhomogeneous etching. Considering that typical active region widths vary between 5 and 20 μm, the relative error can reach more than 10 %. Fortunately there is often another way to determine the active region width if the geometric measurement is not precise enough. The current density J_{NDR} at which the negative differential resistance (NDR) sets on is a constant and depends on the active region design and the doping.[162] This current density can be measured on a device where the active region cross section is known precisely and the value can be used to determine the width of the device under test. However, the onset of the NDR region is not always well defined or the required current density not accessible with the current source or if the processed samples are leaking. The uncertainty on the threshold current is composed of the one on the current measurement itself and the determination of the position of the threshold. The latter is determined by fitting a line to the linear part of the power-current curve just after threshold and calculating the zero-crossing. One exception are continuous-wave measurements as described above where the position of the step in the device's differential resistance is determined. The precision with which the threshold is determined depends on the quality of the measurements and cannot be generalized and the precision of the current measurement itself depends on the measurement setup. A very high precision is achieved in continuous-wave measurements where the current is measured with a Keithley 2420 sourcemeter. Pulsed measurements as described in sections 3.3.2 and 3.4.2 are more complex and less accurate. In that case the current is measured with a current probe that has a specified accuracy of ±2 % (see appendix A.1). Systematic errors are introduced by the $50\,\Omega$ load resistance and channel offset of the oscilloscope. The accuracy of the oscilloscope depends on the settings and can vary considerably between models. For example the TDS380 oscilloscope has a vertical accuracy of 2 %. The accuracy of the measurement also deteriorates if the shape of the current pulse is bad due to impedance mismatch between the pulse generator and the the sample. Uncertainties associated with the mirror losses are determined by

$$\Delta\alpha_{\mathrm{m}} = \frac{1}{L}\left[\alpha_{\mathrm{m}} \cdot \Delta L + \frac{1}{2}\left(\frac{\Delta R_1}{R_1} + \frac{\Delta R_2}{R_2}\right)\right] \tag{3.6}$$

where ΔR_1 and ΔR_2 are the uncertainties on the power reflectivities of the facets. The power reflectivity of an uncoated facet for a laser in the mid-infrared region is typically 26-27 % and can be calculated when the effective refractive index of the mode and the emission wavelength is known. Less well known is the power reflectivity of a facet with a metallic highly-reflective coating. Reported values range between 95 and 97 %. Once the error bars for each measurement have been determined, two "extreme" lines can than be placed on the graph is such a way that 2/3 of the points (with error bars) touch the line. These two lines yield maximum and minimum values for the slope b and the offset a and their difference yields the uncertainties Δb and Δa associated with the two parameters. Finally, the uncertainties of the gain coefficient and the waveguide losses are calculated:

$$\Delta(g\Gamma) = (g\Gamma)\,\frac{\Delta b}{b}\ , \qquad \Delta\alpha_\mathrm{w} = \alpha_\mathrm{w}\left[\frac{\Delta b}{b} + \frac{\Delta a}{a}\right] \tag{3.7}$$

In cases where a lot of lasers are measured and the measurements can be considered independent, the standard deviations of the fitting parameters can be used:

$$\Delta(g\Gamma) = (g\Gamma)\,\frac{\sigma_b}{b}\ , \qquad \Delta\alpha_\mathrm{w} = \alpha_\mathrm{w}\sqrt{\left(\frac{\sigma_a}{a}\right)^2 + \left(\frac{\sigma_b}{b}\right)^2} \tag{3.8}$$

where σ_a and σ_b are the standard deviation of the offset and the slope parameter, determined by the least-square method.

If one is interested in the total optical losses $\alpha_\mathrm{tot}^\mathrm{opt}$ only (and thus neglecting back-filling) another technique can be used: First the power-current characteristics of an uncoated laser are measured. Then a highly-reflective coating is deposited on one of the facets and the power-current characteristics are measured again. The ratio of the slope efficiencies in both cases yields:[82]

$$\frac{\eta_\mathrm{c}}{\eta_\mathrm{u}} = \frac{-2\ln(R_\mathrm{u}) + 2L\cdot\alpha_\mathrm{tot}^\mathrm{opt}}{-\ln(R_\mathrm{u}R_\mathrm{c}) + 2L\cdot\alpha_\mathrm{tot}^\mathrm{opt}} \tag{3.9}$$

Where η_u and η_c are the measured slope efficiencies before and after depositing the highly-reflective coating, R_u and R_c are the power reflectivities of the uncoated and coated facet, $\alpha_\mathrm{tot}^\mathrm{opt}$ are the cavity losses and L is the cavity length. Solving Equ. (3.9) for $\alpha_\mathrm{tot}^\mathrm{opt}$ yields

$$\alpha_\mathrm{tot}^\mathrm{opt} = \frac{-2\ln(R_\mathrm{u}) + \ln(R_\mathrm{u}R_\mathrm{c})\cdot\eta_\mathrm{c/u}}{2L(\eta_\mathrm{c/u} - 1)} \tag{3.10}$$

where $\eta_{\mathrm{c/u}} \equiv \frac{1}{\eta_{\mathrm{u/c}}} \equiv \frac{\eta_{\mathrm{c}}}{\eta_{\mathrm{u}}}$ is the ratio of the slope efficiencies. The advantage of this method is that the power reflectivity of the uncoated facet can be calculated precisely. A larger uncertainty exists for the power reflectivity of a facet with an $\mathrm{Al_2O_3/Au/Al_2O_3}$ (300/100/100 nm) or similar highly-reflective coating. Reported values vary between 95 and 97 %.[82, 163] However, the technique requires that the slope efficiencies can be measured with high reproducibility. Absolute values of the slope efficiencies are not important and systematic errors are canceled-out since the ratio of the slope efficiencies is used. A measurement setup with high collection efficiency and where the power meter aperture is placed immediately after the emitting facet should be used because no tedious alignment is involved. An experimental setup as described in section 3.4.2 is not well suited as its collection efficiency depends strongly on the optical alignment. The analysis of the uncertainty associated with the resulting cavity losses by error propagation shows that also with this method it is difficult to determine precise values. Error propagation yields:

$$\begin{aligned}\Delta\alpha_{\mathrm{tot}}^{\mathrm{opt}} &= \alpha_{\mathrm{tot}}^{\mathrm{opt}} \cdot \frac{\Delta L}{L} + \frac{1}{2L(1-\eta_{\mathrm{u/c}})} \times \dots \\ &\dots \left[\left|1 - 2\eta_{\mathrm{u/c}}\right| \frac{\Delta R_{\mathrm{u}}}{R_{\mathrm{u}}} + \frac{\Delta R_{\mathrm{c}}}{R_{\mathrm{c}}} + \frac{\ln\left(\frac{R_{\mathrm{c}}}{R_{\mathrm{u}}}\right)}{(\eta_{\mathrm{c/u}} - 1)} \frac{\Delta\eta_{\mathrm{c/u}}}{\eta_{\mathrm{c/u}}} \right] \qquad (3.11)\end{aligned}$$

Assuming power reflectivities $R_{\mathrm{u}} = 0.27 \pm 0.005$ and $R_{\mathrm{c}} = 0.96 \pm 0.01$ and inserting the numbers for a hypothetical laser with a $[3 \pm 0.005]$ mm long cavity and waveguide losses of $4\,\mathrm{cm^{-1}}$, a slope-efficiency ratio $\eta_{\mathrm{c/u}} = 1.33$ is obtained. Further assuming that the relative error associated with the ratio of slope efficiencies is $\Delta\eta_{\mathrm{c/u}}/\eta_{\mathrm{c/u}} = 0.02$, the relative error on the waveguide losses, calculated by Equ. (3.11), is: $\Delta\alpha_{\mathrm{tot}}^{\mathrm{opt}}/\alpha_{\mathrm{tot}}^{\mathrm{opt}} = 20\,\%$.

3.5 LIVT measurement

A very specific application for a quantum cascade laser with its characteristics of a diode is to use it as a thermometer. Obviously, this makes no sense for standalone thermometers as there are a plethora of calibrated thermometers on the market, but one can imagine scenarios where in an application a chip with two lasers is mounted and the better performing laser is used as light source and the other one as thermometer. The advantage of such a solution would be that the thermometer is intrinsically mounted on the same chip, it is very close to the heat source (the other laser ridge) and the fast response time because the thermal mass of the chip is small. A drawback is that the system needs to be calibrated in order to measure the absolute chip temperature precisely. Fig. 3.6 shows with a schematic illustration how the chip temperature can be measured simultaneously with the laser emission from the second waveguide ridge. The ridge serving as thermometer is biased with a constant current, in this setup coming from a Keithley 2400 sourcemeter, and the voltage drop over the sample is measured. With suitable calibration data one can than determine the chip temperature. To acquire the calibration data, first a probing current must be chosen (typically 0.5-1 mA). Then the temperature controller is set to the highest possible temperature and an acquisition program is started that reads the heat sink temperature and the corresponding voltage drop on the device in regular intervals. Once this routine is running the temperature of the heat sink is slowly ramped down

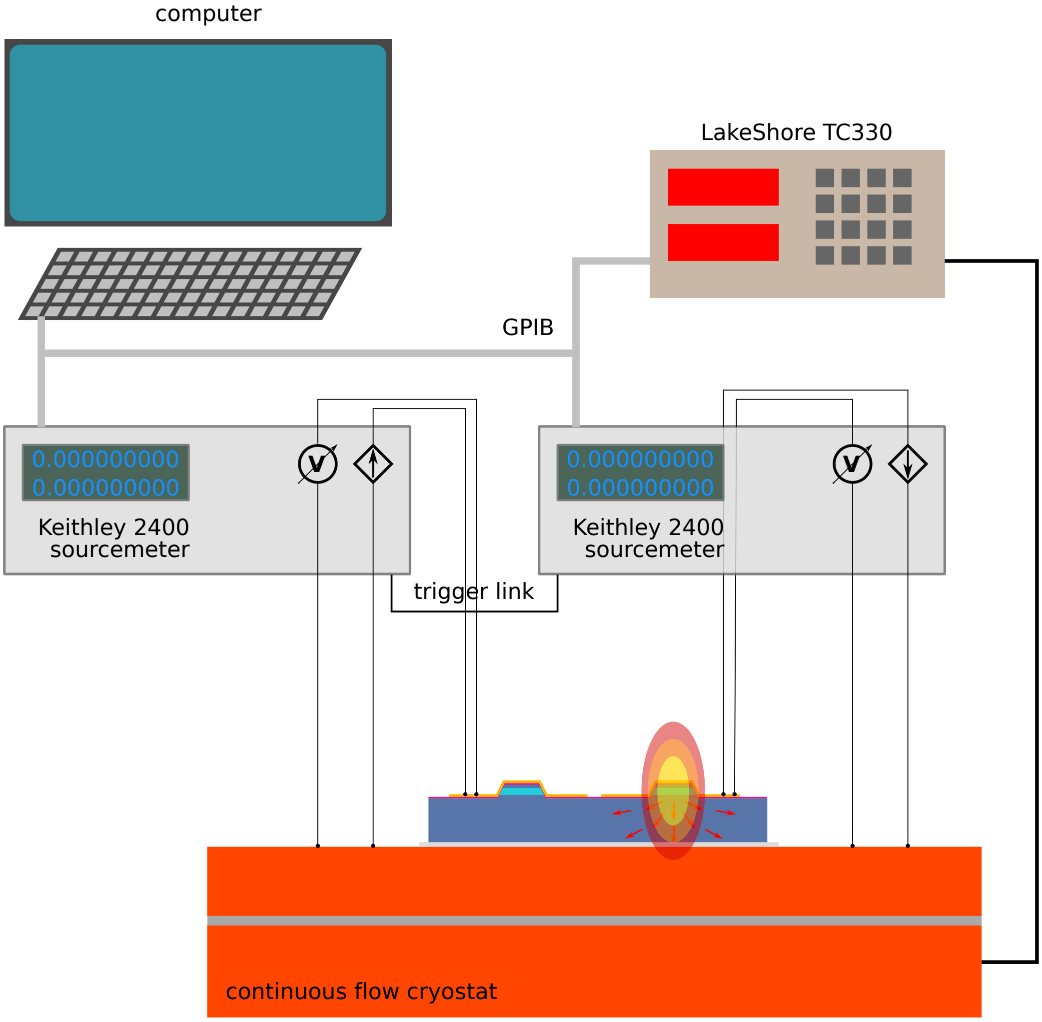

Figure 3.6: Experimental setup for LIVT measurements

Schematic illustration showing how the chip temperature can be measured simultaneously with the laser emission from the second waveguide ridge.

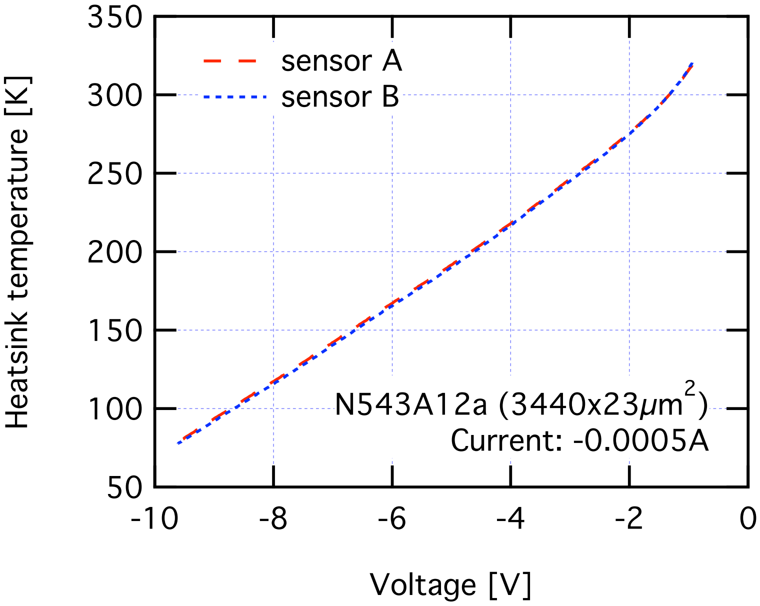

Figure 3.7: Temperature calibration data
Measured calibration data for sample N543A12a with a biasing current of -0.5 mA. The two curves represent the heat sink temperature readings of sensors A and B on the Lakeshore TC330 temperature controller. For the calibration curve the mean temperature is calculated.

to the minimal temperature of interest or below. Example calibration data for sample N543A12a is shown in Fig. 3.7. The acquisition of the power-current-voltage characteristics is then synchronized with the measurement of the voltage drop on the second waveguide ridge on the chip. An example of such a measurement in continuous-wave operation with device N543A12a at 78 K heat sink temperature is shown in Fig. 3.8. In graph (a) the voltage and the emitted power (one facet) is shown as a function of current. A more detailed characterization of this device will follow in section 4.3 of chapter 4 where quantum cascade lasers with large optical cavities are discussed. Here we concentrate on the measurement of the chip temperature that is shown as the red curve in Fig. 3.8 (b). In the same graph the electrical power that is dissipated in the device is shown as the blue curve. At the end of the measurement ($1.9\,\mathrm{kA\,cm^{-2}}$) the dissipated electrical power reaches 19.5 W, the power meter measures 0.9 W of optical power and the chip reaches a temperature of 104 K: 26 K above heat sink temperature. At threshold a kink can be observed in the temperature curve. This is further emphasized in Fig. 3.8 (c) where its derivative versus current (red) is shown together with the differential resistance (blue). Whereas the discontinuity of the differential resistance at threshold is expected, the kink in the temperature curve was a surprise, although easy to explain: below threshold the electrical energy dissipated in the device exclusively contributes to the heating of the sample because the spontaneous emission in the mid-infrared region is very inefficient. At threshold, when the device starts to lase, a fraction of the electrical energy is converted into electromagnetic radiation and emitted from the device. Thus, above threshold less electrical energy is used to heat up the sample and therefore the kink in the curve for the chip temperature.

The temperature measurement can even be used to indirectly determine the emitted optical power of the device as it is shown in Fig. 3.8 (a) by the dashed line. Using a very simplistic thermal impedance model neglecting heat convection (sample in vacuum) and blackbody radiation, we can write the heat exchange balance

$$IV = \begin{cases} \frac{\Delta T}{Z_\mathrm{T}} & I < I_\mathrm{th} \\ \frac{\Delta T}{Z_\mathrm{T}} + Q_\mathrm{rad} & I \geq I_\mathrm{th} \end{cases} \tag{3.12}$$

where I is the current flowing through the device, V is the voltage, ΔT is

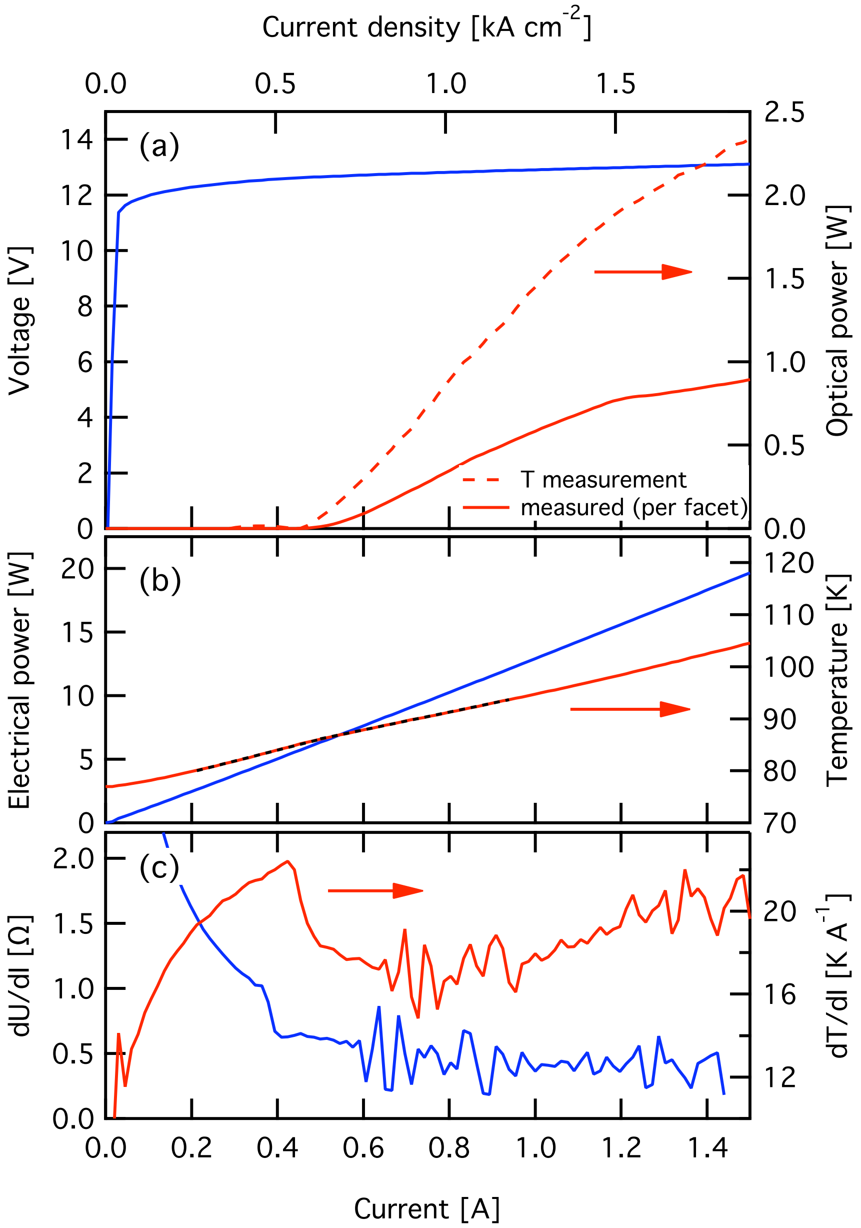

Figure 3.8: LIVT measurement with sample N543A12a at 78 K

(a) Continuous-wave power-current-voltage characterization of device N543A12a with a 3.44 mm long and 23 µm wide waveguide ridge. The dashed line shows the radiated optical power that has been indirectly determined by the chip temperature measurement as described in the text. (b) Dissipated electrical power (blue) and chip temperature (red) as a function of current. The heat sink temperature is 78 K. (c) Differential resistance (blue) and derivative of the chip temperature versus current (red). Both curves show a discontinuity at the laser threshold.

the change in temperature and Z_T is the thermal impedance. The thermal impedance depends on the sample geometry and where the temperature is measured and needs to be determined for each device using the slopes of the power and temperature data below threshold:

$$Z_\mathrm{T} = \frac{\Delta T}{\Delta(IV)} = \frac{\Delta T/\Delta I\Big|_{I<I_\mathrm{th}}}{\Delta(IV)/\Delta I\Big|_{I<I_\mathrm{th}}} \tag{3.13}$$

The example shown in Fig. 3.8 yields Z_T=1.63 K/W. Finally, the radiated power can be determined from Equ. (3.12):

$$Q_\mathrm{rad} = IV - \frac{\Delta T}{Z_\mathrm{T}} \tag{3.14}$$

The curve obtained in Equ. (3.14) is offset but knowing that the radiated power at threshold is zero, this offset can be subtracted. The result is shown in Fig. 3.8 (a) and it agrees well with the measured data. The slope efficiency determined by the temperature measurement is 3 W/A (both facets) and the one measured with the power meter is 1.25 W/A per facet. Making a ratio of the two we find a setup collection efficiency of 83 % that is close to the 70-80 % that we determined with other methods for the same setup.

After discussion with C. Sirtori we were pointed to the publications of Pipe *et al.* who applied the same method to interband laser diodes emitting in the near-infrared region.[164] They used micro-thermocouples, 25×25 μm in size, to measure the temperature on top of the waveguide ridge and the substrate, and they used the technique to quantify their heat exchange model for a laser diode. In their publication they state that convection should not be neglected in thermal models; although that does not apply to our case as the sample was held under vacuum.

We believe that this method is nice from a conceptual point-of-view because of the simplicity of its assumptions, but probably it is of little interest for laser characterization as a direct measurement for the optical power should be preferred. However, the possibility to measure the chip temperature with a second ridge could be interesting for quantum cascade laser systems where a fast and precise temperature control is needed. Or, imagining the opposite case, a second waveguide ridge could be used as a heating element with a fast response time in order to tune DFB quantum cascade lasers over a larger wavelength range.

3.6 Multi-section cavity gain measurements

3.6.1 Gain measurements in quantum cascade lasers

As we have seen in section 3.4.3 measurements of the laser threshold current as a function of cavity length can yield an estimation of the modal gain coefficient of a quantum cascade laser structure. But the method lacks spectral resolution as only the lasing mode is probed. The first spatially resolved gain measurements on quantum cascade lasers were performed by Faist *et al.*[165] soon after the demonstration of the first quantum cascade laser using a technique developed by Hakki and Paoli for interband laser diodes.[166, 167]

Hakki-Paoli method

The Hakki-Paoli method consists in measuring the electroluminescence spectrum of a gain medium in a short Fabry-Pérot waveguide and the gain is directly calculated from the modulation depth of the Fabry-Pérot fringes. But as Cassidy pointed out, this method requires a spectrometer with high resolution to resolve well the fringes and the result has a strong dependency on the instrument response function. He therefore suggested to use a method where the intensity is averaged over the free spectral range of the cavity instead of the peak maximum.[168] A further improvement was suggested by Hofstetter and Faist where Fourier analysis is performed on the emission spectra.[169] This method has the advantage that the interferograms include information on shape and contrast of the Fabry-Pérot fringes and, as the spectrum of mid-infrared lasers is usually measured with a Fourier-transform spectrometer, the raw measurement data has the form of an interferogram that is used directly as input for the absorption/gain calculation. The Hakki-Paoli method is a self-aligned technique yielding absolute results. However, the spectral width is very limited and, for technical reasons, only current densities below threshold are accessible. Measurements in pulsed-mode operation have been performed but are more difficult to do and less accurate because the signal is weaker and the frequency chirp “washes-out” the fringes. Other difficulties arise from the necessity to only support one transverse mode in the waveguide. If other transverse modes exist the fringe patterns are superposed and the fringe-contrast measurement gets very inaccurate. Also, special care needs to be taken that no unguided light, traveling through the substrate is collected with the lens as it would decrease the fringe contrast. This problem is partly remedied by choosing a collection lens with long focal distance and very careful alignment. In the field of quantum cascade laser research the Hakki-Paoli technique was used extensively for gain, waveguide absorption or refractive index dispersion measurements in mid-infrared,[165, 170, 171, 172] and also far-infrared quantum cascade lasers.[173]

Waveguide transmission measurements

A somewhat related technique consists in measuring the transmission of a Fabry-Pérot waveguide. Revin *et al.* used the light of a He-Ne laser with emission at $3.39\,\mu$m and measured the transmission while the temperature of the sample was changed.[174] The waveguide absorption was then determined using the contrast of the resulting fringes. A study on intersubband absorption in a GaInAs/AlAsSb quantum cascade laser using a pure Fourier-transform spectrometer transmission measurement has also been published by the Sheffield group.[175] Peter *et al.* used the broadband blackbody emission of the internal source of a Fourier-transform spectrometer and measured the transmission spectrum of a GaInAs/AlInAs quantum cascade laser emitting at $5.4\,\mu$m.[176] The waveguide optical properties were then determined by Fourier analysis. [177, 169]

These techniques may have the advantage that, depending on the light source, one can measure the optical properties on a wide spectral range and also for empty waveguides without active medium. However, compared to the Hakki-Paoli technique they loose the advantage of being self-aligned and since the transmission is measured, it is very difficult to obtain quantitative results for absorption and gain, respectively. Also, relatively wide waveguide ridges have to be chosen in order to be able to couple enough light into the waveguide. This sets strong constraints on the maximal measurement temperature and driving current density as continuous-wave operation is often necessary to obtain a sufficient signal-to-noise ratio.

A new type of transmission measurements emerged in the last years when the generation of ultrafast light pulses was combined with electro-optical sampling to perform time-resolved transmission measurements, first in the far-infrared and later the mid-infrared region.[178, 179] This method allows to measure time resolved amplitude and phase of a light pulse after propagating through a quantum cascade laser waveguide and due to its inherently high time resolution it allows to observe processes in the laser cavity on a sub-picosecond timescale. The method has been used to investigate absorption and gain processes in far-infrared[180, 178] as well as mid-infrared[179, 181] quantum cascade lasers and also to measure the complex valued refractive index of a mid-infrared quantum cascade laser.[182] Obviously, this is an extremely powerful method and despite its recentness it already allowed to observe phenomena that would not have been possible to observe with the standard time-averaging intensity measurements. However, it needs a dedicated experimental setup that is very expensive and requires the know-how of time-domain spectroscopy. So far, measurements only have been performed at low temperature but it is only a matter of time until measurements will also be performed at high temperature, at least in the mid-infrared region.

Multi-section cavity gain measurements

Multi-section cavity gain measurements are a development of interband diode laser research where monolithic mode-locking semiconductor lasers were fabricated. For that purpose a short section of the waveguide was reverse biased and thus acted as the required saturable absorber. McDougall and Ironside realized that, by measuring emission spectra from these multi-section lasers under specific biasing conditions, they could measure the absorption and the gain in the semiconductor laser material.[183] Later Barbieri *et al.* adopted the technique to measure the gain in GaAs-based quantum cascade lasers and Rochat *et al.* used a related method to measure the waveguide losses of a far-infrared double-plasmon waveguide.[184, 185]

We started to experiment with this measurement technique when we were looking for a way to investigate the gain of special QCL structures that were based on a single quantum well active region and that were designed to operate in a regime with very low population inversion. These structures turned out to be particularly difficult to measure and thus we continued to improve this technique until satisfactory results were obtained and we could experimentally verify an enhanced model for the gain in intersubband transitions.[1] These measurements will be discussed in chapter 6.

The multi-section cavity technique allows to measure the spectrally resolved modal gain and waveguide losses of a structure in the vicinity of the center of the emission wavelength. Although the spectral window is limited by the width of the structure's spontaneous emission, the method has the advantage that the measurements are performed in pulsed operation that allows to pump the structure under test at high current densities and temperature. It also is a self-aligned technique, meaning that no external beam needs to be coupled into the waveguide, and it inherently yields quantitative results. In this technique the ridge waveguide is divided into multiple sections that are optically coupled but can be independently driven. Electrical isolation between the sections is obtained by etching the highly doped contact and plasmon layers between them or by cutting trenches into the top cladding layer by focused ion beam. The first section is grounded and used as an absorber to kill optical feedback from the backfacet and prevent the device from lasing. Light emitted from section $\mathcal{A}$ and amplified (or attenuated) by section $\mathcal{B}$ is collected at the sample facet and measured in a Fourier-transform spectrometer. The gain measurements require that the emission from section $\mathcal{A}$ can be measured without amplification from section $\mathcal{B}$,[184] but the bias of latter needs to be sufficiently high in order to get a measurable signal. Therefore, in a first step, a biasing current J_{bl} for section $\mathcal{B}$ is determined where the structure has no significant gain, the spontaneous emission is negligible and the resonant absorption inside the active region is small. Because this "baseline" is applied as a DC voltage in our setup, the current also has to be small in order to prevent the sample from heating excessively. An optimal "baseline" voltage is determined by making a first series measurements that determine the absorption of section $\mathcal{B}$ as a function of this "baseline" and a value is chosen where the absorption is sufficiently small and the current is not too high. Then the differential gain with respect to the chosen baseline is measured as a function of the current injected into section $\mathcal{B}$ and finally the spectra of the modal gain are calculated by subtracting the baseline absorption from the measurements of the differential gain.

3.6.2 Theory

We look at a multi-section cavity sample with geometry and terminology as shown in Fig. 3.9(a) and for the moment we assume that there are no coupling losses and absorption between the sections.

Baseline absorption

For absorption measurements samples are required where sections $\mathcal{A}$ and $\mathcal{B}$ have the same length. Now we assume that section $\mathcal{A}$ is pumped with a probe current J_p and a small current J_bl is injected into section $\mathcal{B}$ in order to bias it at the baseline voltage. The optical intensity $S'_\mathrm{A}(J_\mathrm{p}, J_\mathrm{bl}, \lambda)$ at the facet is:

$$S'_\mathrm{A}(J_\mathrm{p}, J_\mathrm{bl}, \lambda) = (1 - R) \cdot S_\mathrm{A}(J_\mathrm{p}, \lambda) \cdot e^{-\alpha_\mathrm{B}(J_\mathrm{bl}, \lambda) \cdot L_\mathrm{B}} \tag{3.15}$$

where R is the facet power reflectivity, $S_\mathrm{A}(J_\mathrm{p}, \lambda)$ is the optical intensity at the end of section $\mathcal{A}$ and $\alpha_\mathrm{B}(J_\mathrm{bl}, \lambda)$ is the absorption and L_B the length of section $\mathcal{B}$. When the same probe current is applied to section $\mathcal{B}$ the optical intensity at the facet ($S'_\mathrm{B}(J_\mathrm{p}, \lambda)$) is:

$$S'_\mathrm{B}(J_\mathrm{B}, \lambda) = (1 - R) \cdot S_\mathrm{B}(J_\mathrm{p}, \lambda) \tag{3.16}$$

where $S_{\mathrm{B}}(J_{\mathrm{p}}, \lambda)$ is the optical intensity after section $\mathcal{B}$ (before partial reflection). Because sections $\mathcal{A}$ and $\mathcal{B}$ are identical we have

$$S_{\mathrm{A}}(J_{\mathrm{p}}, \lambda) \equiv S_{\mathrm{B}}(J_{\mathrm{p}}, \lambda) \tag{3.17}$$

and therefore, using equations (3.15) and (3.16), the baseline absorption of section $\mathcal{B}$ can be isolated:

$$\alpha_{\mathrm{B}}(J_{\mathrm{bl}}, \lambda) = \frac{1}{L_{\mathrm{B}}} \ln\left(\frac{S'_{\mathrm{B}}(J_{\mathrm{B}}, \lambda)}{S'_{\mathrm{A}}(J_{\mathrm{p}}, J_{\mathrm{bl}}, \lambda)}\right) = \frac{1}{L_{\mathrm{B}}} \ln\left(\frac{S^{\mathrm{B}=J_{\mathrm{p}}}_{\mathrm{A}=J_{\mathrm{bl}}}(\lambda)}{S^{\mathrm{B}=J_{\mathrm{bl}}}_{\mathrm{A}=J_{\mathrm{p}}}(\lambda)}\right) \tag{3.18}$$

We prefer the notation $S^{\mathrm{B}=J_{\mathrm{B}}}_{\mathrm{A}=J_{\mathrm{A}}}(\lambda)$ that represents the intensity measured at the facet when section $\mathcal{A}$ is pumped with current J_{A} and section $\mathcal{B}$ with current J_{B}.

As the lengths of sections and the intensities of the spectra can only be measured up to a certain precision, the uncertainty on the baseline absorption is calculated by error-propagation and yields:

$$\Delta\alpha_{\mathrm{B}}(J_{\mathrm{bl}}, \lambda) = \frac{1}{L_{\mathrm{B}}}\left[\alpha_{\mathrm{B}}(J_{\mathrm{bl}}, \lambda)\Delta L_{\mathrm{B}} + \frac{\Delta S^{\mathrm{B}=J_{\mathrm{p}}}_{\mathrm{A}=J_{\mathrm{bl}}}(\lambda)}{S^{\mathrm{B}=J_{\mathrm{p}}}_{\mathrm{A}=J_{\mathrm{bl}}}(\lambda)} + \frac{\Delta S^{\mathrm{B}=J_{\mathrm{bl}}}_{\mathrm{A}=J_{\mathrm{p}}}(\lambda)}{S^{\mathrm{B}=J_{\mathrm{bl}}}_{\mathrm{A}=J_{\mathrm{p}}}(\lambda)}\right] \tag{3.19}$$

where ΔL_{B} is the uncertainty associated with the length of section $\mathcal{B}$ and $\Delta S^{\mathrm{B}=J_{\mathrm{p}}}_{\mathrm{A}=J_{\mathrm{bl}}}(\lambda)$ and $\Delta S^{\mathrm{B}=J_{\mathrm{bl}}}_{\mathrm{A}=J_{\mathrm{p}}}(\lambda)$ are the uncertainties associated with the measurement of the spectra. For these values we take the peak values of the noise floor as it is illustrated in Fig. 3.10.

Depending on how the multi-section cavity samples are fabricated, the isolation between the sections cannot be treated as ideal and coupling losses and the absorption of this intermediate section needs to be taken into account. If

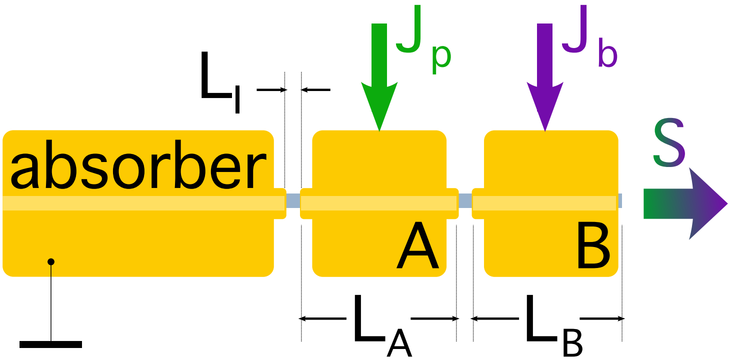

Figure 3.9: Multi-section cavity sample geometry and terminology

Geometry and terminology of a multi-section cavity sample. The first section is connected to ground and acts as an absorber to prevent optical feedback from the backfacet. It follows section $\mathcal{A}$, *or the "light-bulb" section, with length* L_{A} *where the probe pulse is generated by injecting a current* J_{p}. *The generated light is then amplified or attenuated by* section $\mathcal{B}$ *(or amplifier section) with length* L_{B}, *depending on the intensity of the biasing current* J_{b} *and light emitted from the facet at the end of* section $\mathcal{B}$ *is measured. Sections are separated by an unbiased segment with length* L_{I}.

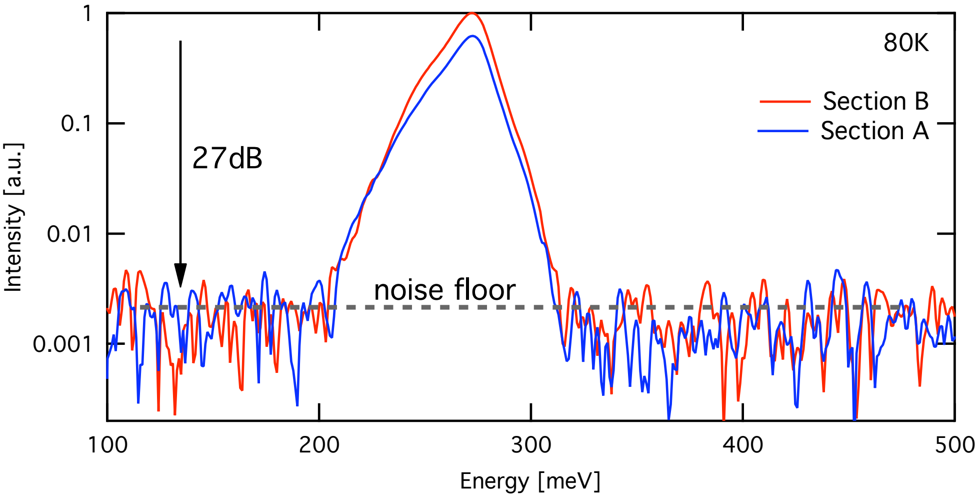

Figure 3.10: Absorption measurement noise floor

Spectra of sections $\mathcal{A}$ and $\mathcal{B}$ *after an absorption measurement at 80 K heat sink temperature. The bias voltage applied to the sections was 11 V and a baseline voltage of 7 V was used. Uncertainty is determined through the RMS value of the noise floor.*

C is the ratio of the light that is lost by coupling-losses and $\alpha_\mathrm{I}(J_\mathrm{I},\lambda)$ is the absorption of the intermediate section (length L_I) that separates sections $\mathcal{A}$ and $\mathcal{B}$, the baseline absorption writes:

$$\alpha(J_\mathrm{bl},\lambda)=\frac{1}{L_\mathrm{B}}\ln\left(\frac{S^{\mathrm{B}=J_\mathrm{p}}_{\mathrm{A}=J_\mathrm{bl}}(\lambda)}{S^{\mathrm{B}=J_\mathrm{bl}}_{\mathrm{A}=J_\mathrm{p}}(\lambda)}\right)-\alpha_\mathrm{I}(J_\mathrm{I},\lambda)\frac{L_\mathrm{I}}{L_\mathrm{B}}+\underbrace{\frac{\ln(1-C)}{L_\mathrm{B}}}_{\mathrm{const}} \tag{3.20}$$

Equation (3.20) shows that these effects appear as an offset in the absorption measurement and their influence can be reduced by choosing long sections.

Differential gain

When a current J_b much higher than the baseline current is applied to section $\mathcal{B}$ such that the section now exhibits gain, Equ. (3.15) writes:

$$S^{\mathrm{B}=J_\mathrm{b}}_{\mathrm{A}=J_\mathrm{p}}(\lambda)=(1-R)\left[S_\mathrm{A}(J_\mathrm{p},\lambda)\cdot e^{-\alpha_\mathrm{B}(J_\mathrm{b},\lambda)\cdot L_\mathrm{B}}+S_\mathrm{B}(J_\mathrm{b},\lambda)\right] \tag{3.21}$$

Subtracting the spontaneous emission of section $\mathcal{B}$ from Equ. (3.21) and dividing by the emission spectrum when section $\mathcal{A}$ is pumped and section $\mathcal{B}$ is at baseline yields:

$$\begin{aligned}\frac{1}{L_\mathrm{B}}\ln\left(\frac{S^{\mathrm{B}=J_\mathrm{b}}_{\mathrm{A}=J_\mathrm{p}}(\lambda)-S^{\mathrm{B}=J_\mathrm{b}}_{\mathrm{A}=J_\mathrm{bl}}(\lambda)}{S^{\mathrm{B}=J_\mathrm{bl}}_{\mathrm{A}=J_\mathrm{p}}(\lambda)}\right) &= \alpha_\mathrm{B}(J_\mathrm{bl},\lambda)-\alpha_\mathrm{B}(J_\mathrm{b},\lambda)\\ &= -\left[\alpha_\mathrm{B}(J_\mathrm{b},\lambda)-\alpha_\mathrm{B}(J_\mathrm{bl},\lambda)\right]\\ &= \delta g(J_\mathrm{b},J_\mathrm{bl},\lambda) \qquad (3.22)\end{aligned}$$

where $\delta g(J_\mathrm{b},J_\mathrm{bl},\lambda)$ is the differential modal gain with respect to the baseline when a current J_b is injected into section $\mathcal{B}$. Analog to Equ. (3.19) the uncertainty associated with with the differential gain is:

$$\begin{aligned}\Delta\left[\delta g(J_\mathrm{b},J_\mathrm{bl},\lambda)\right] &= \frac{1}{L_\mathrm{B}}\left[\delta g(J_\mathrm{b},J_\mathrm{bl},\lambda)\Delta L_\mathrm{B}+\frac{\Delta\left[S^{\mathrm{B}=J_\mathrm{bl}}_{\mathrm{A}=J_\mathrm{p}}(\lambda)\right]}{\left[S^{\mathrm{B}=J_\mathrm{bl}}_{\mathrm{A}=J_\mathrm{p}}(\lambda)\right]}+\cdots\right.\\ &\left.\frac{\Delta\left[S^{\mathrm{B}=J_\mathrm{b}}_{\mathrm{A}=J_\mathrm{p}}(\lambda)-S^{\mathrm{B}=J_\mathrm{b}}_{\mathrm{A}=J_\mathrm{bl}}(\lambda)\right]}{\left[S^{\mathrm{B}=J_\mathrm{b}}_{\mathrm{A}=J_\mathrm{p}}(\lambda)-S^{\mathrm{B}=J_\mathrm{b}}_{\mathrm{A}=J_\mathrm{bl}}(\lambda)\right]}\right]\end{aligned}\tag{3.23}$$

where the uncertainties $\Delta\ldots$ are determined as shown in the case of the baseline absorption measurement.

Modal gain spectrum

The spectrum of the modal gain is finally calculated by subtracting the baseline absorption from the differential gain:

$$g(J_\mathrm{b},\lambda)=\delta g(J_\mathrm{b},J_\mathrm{bl},\lambda)-\alpha_\mathrm{B}(J_\mathrm{bl},\lambda)\tag{3.24}$$

3.6.3 Sample preparation

Choice of section length

Whereas sections of samples for baseline absorption measurements needs to be of the same length, samples where the differential gain has to be measured do not have this restriction. However, it is convenient to use the same sample (with equal section lengths) for both measurements. The choice of the section length depends on the waveguide losses and the gain exhibited by the structure. During gain measurements, a too long section will require a too high dynamic range of the setup and will saturate the measurement. On the other hand in an absorption measurement the signal when the emission of section $\mathcal{A}$ is measured can be very small. Too short sections will negatively affect the accuracy of the measurement due to shorter interaction length. In our experiments we found that 300-400 μm long sections yield good results.

Electrical insulation of sections

In order to be able to drive the sections independently they need to be electrically isolated from each other. Our first samples were fabricated using wet etching to remove the highly doped contact and cap layers on top of the waveguide ridge. To that end standard Fabry-Pérot lasers were fabricated as described in section 3.4.1 but no thick gold was deposited on the top contacts. For easier cleaving of the device the masks were designed in a way that many contact pads of different lengths were aligned along a laser stripe and they were separated by 20 μm wide, gold free sections (see Fig. 3.9 for example). We then proceeded by protecting the sample surface with photoresist and opening this layer on top of the ridge where the semiconductor was directly visible. The $Ga_{0.47}In_{0.53}As$ contact and cap layers were then removed with HBr:HNO_3:H_2O (1:1:10) etchant, resulting in inter-section resistances between 100 and 150 Ω. However, this process was not very reproducible and the yield of working samples was low. Better reproducibility was achieved using dry etching with a methane-based plasma in our reactive-ion-etching equipment but the additional fabrication steps were still tedious and error prone.

A much better and more convenient way to isolate the sections was found later after the group moved to ETH Zürich. Focused-ion-beam is a very

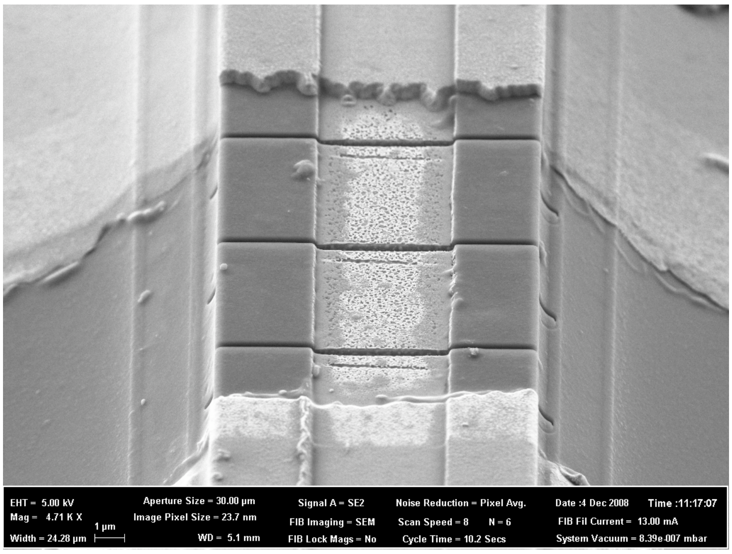

Figure 3.11: Multiple sections electrically isolated by FIB-cutting
Scanning electron micrograph of a multi-section cavity sample where sections have been electrically isolated by three 120-150 nm wide trenches that have been cut into the top cladding layer by focused ion beam.

versatile tool and it proofed very suitable to cut narrow trenches into the top cladding layer. In our test sample that is shown in Fig. 3.11 three, 120-150 nm wide trenches were cut into the top cladding layer down to the active region. The resulting measurements that are further discussed in section 5.5.3 of chapter 5 have shown that both, dry etched and focused-ion-beam cut samples showed similar results.

Effect of unbiased segments and coupling losses

In the previous sections we assumed that segments separating the sections are neutral and have no effect on the measurements. Unfortunately this is not always the case. In our samples sections $\mathcal{A}$ and $\mathcal{B}$ are separated by a $20\,\mu$m long segment that is mechanically treated either by focused ion beam or dry-etching in order to obtain acceptable inter-section resistances. This can reduce the optical coupling between sections. For $360\,\mu$m long sections for example a coupling loss of $13\,\%$ results in a positive offset of $4\,\mathrm{cm}^{-1}$ in the absorption measurement. Coupling losses are assumed to be constant in the narrow spectral range of the measurement and independent of temperature. The bias of this segment is close to zero and therefore another artifact may arise from it when the structure is highly absorbing. An example is discussed in section 5.5.3 of chapter 5. This additional absorption is supposed to be dependent on temperature: directly through the temperature dependent losses in the structure and indirectly through the temperature induced change of its differential resistance. The active region has a higher resistance at low temperature and current leaking from the two sections is able to pull the bias of the intermediate segment to a higher value, resulting in smaller absorption.

Differential gain measurements are only affected indirectly by these artifacts through a lower signal to noise ratio and therefore gain coefficients are also not affected. In order to reduce or eliminate this offset, the sections need to be separated in a way that the aforementioned effects are minimized while maintaining a high inter-section resistance. This could be achieved with a more careful isolating procedure, for example cutting only one trench with focused ion beam instead of three. But no tests have been performed so far to verify that sufficiently high inter-section resistances are obtained.

3.6.4 Measurement setup

Multi-section cavity gain measurements are performed on the electroluminescence measurement setup that is described in section 3.3.2. Because two sections need to be driven independently a second HP8114A pulse generator is necessary and they must be equipped with the baseline option in order to be able to apply a baseline voltage on the sections. During the development of this technique we had a lot of issues with clock jitter and insufficient voltage levels in the triggering line. Therefore a global clock signal is provided by an Agilent 33210A function generator with $50\,\Omega$ output impedance and the triggering line is terminated with a $50\,\Omega$ resistor. A frequency f_0 is chosen such that its value multiplied by four is still below the maximal bandwidth of the lock-in amplifier (250 kHz) and possible signal pre-amplifiers. Typically a frequency $f_0 = 51020\,\mathrm{Hz}$ is chosen (period 19.6 us) because when a phase-sensitive detection scheme (section 3.6.5) is used it still allows to adjust the required pulse delays with a precision of 10 ns. Multi-section cavity gain measurements need a detector that is fast, sensitive and that has a response that is linear with the photon flux on a large dynamic range. Therefore we use a photovoltaic HgCdTe detector. Its specifications are listed in appendix A.3. The signal from the detector is pre-amplified with a Sonoma Instrument 310 low noise amplifier and fed to the lock-in amplifier. Data acquisition is performed with the lock-in amplifier itself and triggered by the Fourier-transform spectrometer. In-phase and quadrature channel data is downloaded to the measurement computer after each step-scan and treated as described in section 3.6.6.

Another point that needs discussion is the current measurement. Although additional processing is performed to isolate the sections electrically, the inter-section resistance is typically only between 100 and 400 Ω and leaking currents cannot be neglected. The driving current provided by the pulse generator not only drives the section but also contains leaking currents to the absorber and/or the other section. Therefore the principle measurement parameters are the voltage biases applied to the sections. The current is determined later either by using a reference current-voltage curve of another device from the same process at same temperature or it can be measured in a separate experiment. To that end the baseline voltage of both pulse generators is set to zero and the same bias is applied on both sections. In that case there is no leaking current between the sections because they are on the same potential and the current flowing into section $\mathcal{B}$ can be measured with a current probe.

Measurement procedures for baseline absorption and gain measurements can be found in appendix B.

3.6.5 Phase-sensitive detection

As we have seen in Equ. (3.18) in section 3.6.2 the absorption is calculated from the electroluminescence spectra of sections $\mathcal{A}$ and $\mathcal{B}$. If these two spectra are measured consecutively and the measurement signal decreases by 10 % in between (which is not uncommon) due to a drift in the optical alignment, this results in an offset of 3 cm^{-1} for a sample with 360 μm long sections. One of the big advantages of Fourier transform spectroscopy is that the signal on the detector, for a given optical path difference between the branches of the interferometer, contains the information for all the wavelengths within the optical bandwidth of the instrument. Therefore a drift in the optical alignment only affects the intensity and the the SNR, but does not change considerably the shape of the spectrum. Taking advantage of the orthogonality of the in-phase and quadrature channel in the lock-in amplifier the two spectra can be acquired in parallel. In case of a drift of the optical alignment, both spectra are equally affected and no offset will result in the calculated absorption spectrum. This is true only for small drifts and does not hold for important spikes and steps in the interferograms. Moreover, the acquisition time in case of absorption measurements is reduced by a factor of two and in case of gain measurements maximum a factor of three.

The principle behind the phase-sensitive detection is shown in Fig. 3.12. By carefully aligning the electrical pumping pulses with the reference of the lock-in amplifier, baseline absorption (a) and differential gain (b) measurements are acquired in only one step-scan. Fig. 3.12(a) shows a timing diagram over one period of the driving signals for a baseline absorption measurement. Using the procedures described in the appendix B the lock-in amplifier reference is synchronized with the probe current pulse that drives section $\mathcal{B}$. A quarter period later a pulse with the same probe current density is sent to section $\mathcal{A}$ while section $\mathcal{B}$ is biased with a constant baseline current. The resulting detector signal is acquired on the quadrature channel of the lock-in amplifier while its effect is canceled-out on the in-phase channel due to orthogonality. The acquisition of a differential gain measurement works in a similar way with the exception that an additional spectrum subtraction

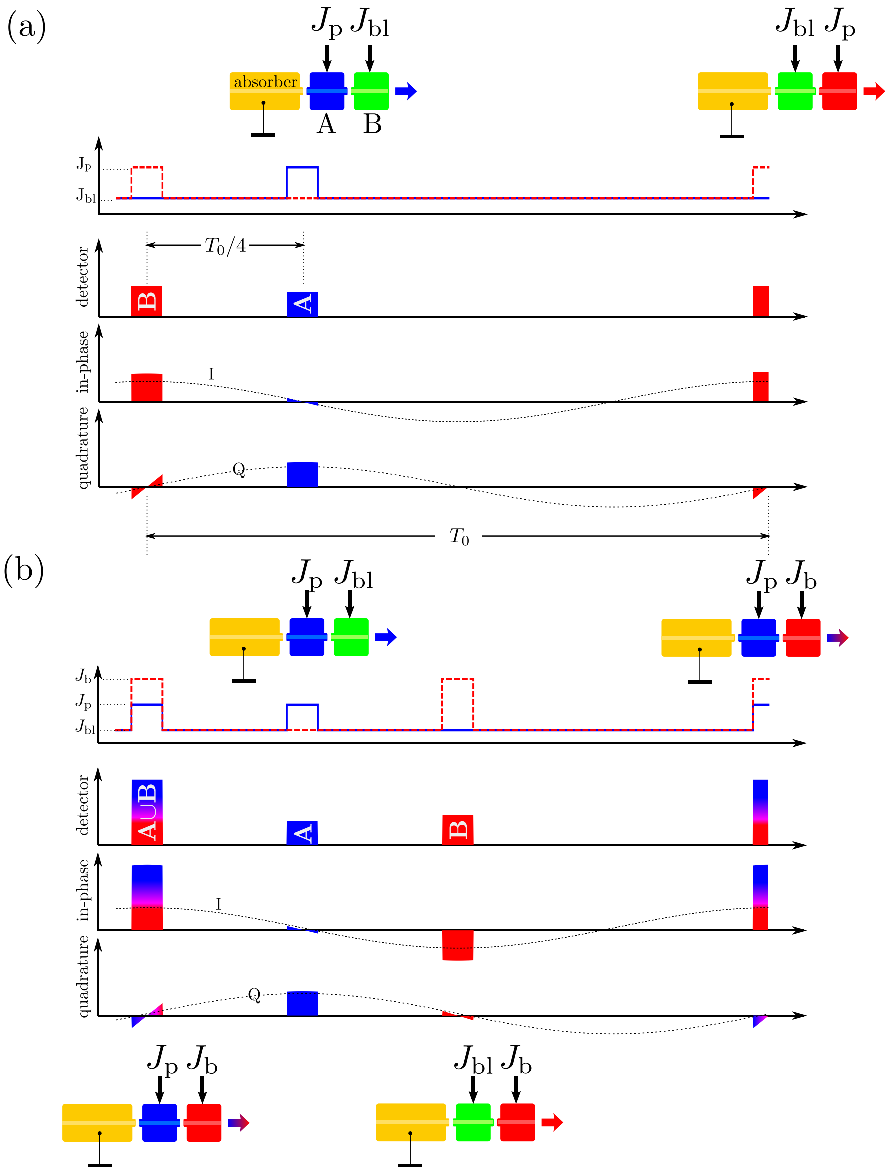

Figure 3.12: Phase-sensitive detection technique

(a) Schematic illustration of the phase-sensitive detection technique for absorption measurements. The timing diagram show how the pulses are placed within one period of the lock-in reference. Sections are pumped with the probe current J_p *and when idle they are biased with the baseline current* J_p*. Electroluminescence spectra of both sections are measured independently on the in-phase and quadrature channel of the lock-in amplifier. (b) For gain measurements the scheme is similar. The electroluminescence spectrum when* sections $\mathcal{A}$ and $\mathcal{B}$ *are biased is measured in-phase and the spontaneous emission of* section $\mathcal{B}$ *is subtracted half a period* $(T_0/2)$ *later. On the quadrature channel the spectrum of* section $\mathcal{A}$ *is measured independently.*

is performed on the in-phase channel. In phase with the reference signal a probe current pulse J_{p} is sent to section $\mathcal{A}$ and section $\mathcal{B}$ is driven with the current density J_{b} at which the differential gain has to be measured. The resulting signal on the detector is acquired on the in-phase channel of the lock-in amplifier and the spontaneous emission is subtracted by sending a pulse with the same intensity J_{b} half a period later. Due to the properties of Fourier transform spectroscopy and strong averaging in the lock-in amplifier with an integration time constant much larger (typically 10'000) than the period of the driving signals, this is equivalent to acquiring the interferograms sequentially and subtracting the spectra after Fourier transformation. Fig. 3.13 shows a comparison between a baseline absorption measurement where the electroluminescence spectra from sections $\mathcal{A}$ and $\mathcal{B}$ have been acquired in sequential step-scans and in parallel using phase-sensitive detection. The absorption was measured on sample N258Re1a at 274 K heat sink temperature, a 8.0 V bias at probe current, 4.0 V baseline voltage and 800 ns long pulses. Graphs (c) and (d) in Fig. 3.13 show the spectrum of section $\mathcal{B}$ (full lines) and section $\mathcal{A}$ (dashed lines) at a bias of 8.0 V while the other section is at baseline voltage. The resulting baseline absorption is shown in Fig. 3.13(e). A very good agreement is found between the measurements from approximately 130 to 180 meV. Between 180 and 200 meV the "shoulder" of the first absorption measurement is slightly offset by $2\,\mathrm{cm}^{-1}$ and for higher energies the noise increases dramatically due to the limited spectral width of the probe pulse. One can also observe a faster cut-off for the phase-sensitive detection measurements at 125 and 200 meV. This cut-off is due to electrical cross talk and parasitic light emitted from the substrate. While some parasitic light is also present in the sequential measurement, the electrical cross talk is much reduced and therefore the later cut-off.

3.6.6 Data processing

Spectra are typically acquired with $16\,\mathrm{cm}^{-1}$ resolution, resulting in double-sided interferograms with 3554 data points. Double-sided interferograms are acquired in order not to have to apply phase correction that could introduce artifacts in the measurement and to keep the data processing simple. After the data points of the two interferograms are read from the lock-in amplifier, the offset is subtracted from the interferograms and symmetrically zero-filled to 4096 points. Then apodization with a Blackman-Harris window is performed and magnitude spectra are calculated by performing a Fourier transform. Absorption is then calculated according to Equ. (3.18) and differential gain according to Equ. (3.22).

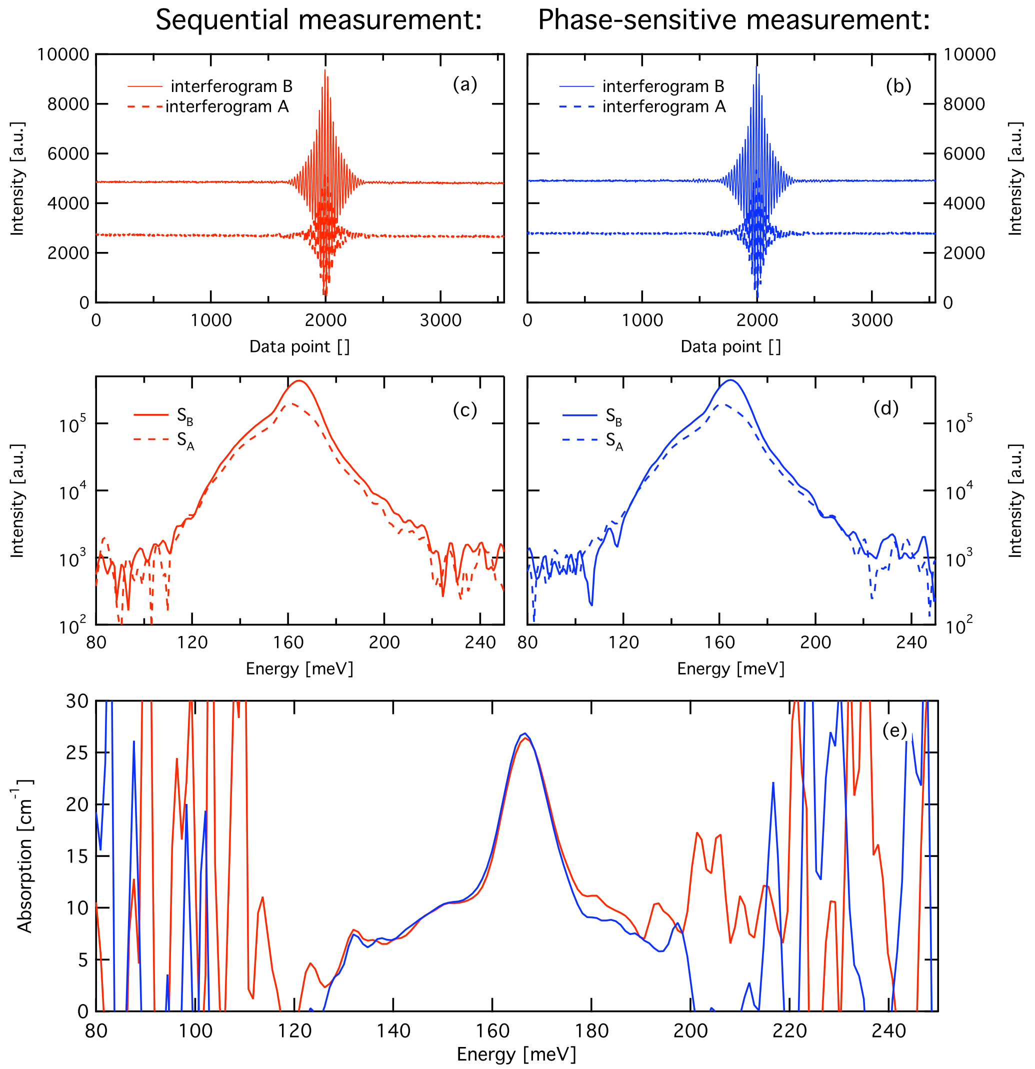

Figure 3.13: Comparison sequential and phase-sensitive measurement

Comparison between a baseline absorption measurement where the interferograms have been acquired sequentially (a) and by phase-sensitive detection (b). The interferograms were acquired during three sequential step-scans. Graphs (c) and (d) show the emission spectra of section $\mathcal{B}$ *(full lines) and* section $\mathcal{A}$ *(dashed lines) and graph (e) shows the calculated absorption. The measurement parameters are: Sample N258Re1a (dry etched), temperature: 274 K, pulse width: 800 ns, frequency: 51'020 Hz, bias at probe current: 8.0 V, baseline voltage: 4.0 V, lock-in integration time constant: 200 ms.*

Chapter 4

Waveguides

4.1 Introduction

The development of quantum cascade lasers in the tree main research directions, namely performance improvement, extension of the accessible wavelength range and new material systems goes in hand with the development and optimization of the waveguides the gain medium is placed in. This probably was true for the first demonstration of a quantum cascade laser by Faist *et al.*[53] and the subsequent extension to longer mid-infrared wavelengths.[57, 58] It certainly was true for the demonstration of GaAs/AlGaAs-based quantum cascade lasers,[64] the demonstration of quantum cascade lasers emitting in the far-infrared region,[73] or the the demonstration of quantum cascade lasers based on the unconventional InAs/AlSb material system that emit at wavelengths below 3 μm.[107] It was the double-metal waveguide that allowed THz quantum cascade lasers to operate at record heat sink temperatures and sophisticated multi-stack waveguides allow to obtain extremely high peak powers and slope and wall plug efficiencies.[4, 5] In the development of high power quantum cascade lasers the minimization of the waveguide losses, and thus the threshold current densities, is crucial to obtain continuous-wave operation at high temperature and large average powers.[186]

In this chapter we will shortly discuss the basic principles behind the waveguides used in mid-infrared quantum cascade lasers and the tools that are used to design them. Then in section 4.3 we will discuss the properties of quantum cascade lasers with large waveguide cores containing multiple gain stacks and discuss the results.

4.2 Mid-infrared quantum cascade laser waveguides

4.2.1 Dielectric slab waveguide

In Fig. 4.1 a comparison between waveguides that were used in the early development of quantum cascade lasers is shown. The waveguide used in the first quantum cascade laser is shown in Fig. 4.1(a) where the blue line represents the refractive index profile that was calculated taking into account the change of the complex refractive index due to free carriers in the doped semiconductor material using the Drude-Lorenz model. Intensity profiles of the fundamental and excited TM modes[1] are represented by red lines. Modes were calculated using a transfer matrix method where the Helmholtz equation

---

[1] Quantum cascade lasers emit TM polarized light due to the selection rule for intersubband transitions.

is solved in the waveguide structure with appropriate boundary conditions that are determined by the layer parameters.[187] As Fig. 4.1(a) shows the structure was grown on a doped ($n = 4\times10^{17}\mathrm{cm}^{-3}$) InP substrate. The active region is embedded between two 300 nm thick $\mathrm{Ga}_{0.47}\mathrm{In}_{0.53}\mathrm{As}$ ($n = 1\times10^{17}\mathrm{cm}^{-3}$) waveguiding layers that help to increase the refractive index contrast with respect to the cladding layers and therefore better confine the mode. The cladding layers themselves are based on $\mathrm{Al}_{0.48}\mathrm{In}_{0.52}\mathrm{As}$ and, because the overlap factor of the optical mode with cladding layers is still 27 %, the material was relatively low doped ($n = 1.5\times10^{17}\mathrm{cm}^{-3}$) in order to limit free-carrier absorption. The top cladding layer is split in two parts with different doping levels ($n = 1.5\times10^{17}\mathrm{cm}^{-3}$, respectively $n = 5\times10^{17}\mathrm{cm}^{-3}$) in order to find a trade-off between series resistance of the device and waveguide losses. An important factor is the overlap factor that is defined as

$$\Gamma = \frac{\int\limits_{\text{active}} |E|^2 dV}{\int\limits_{\text{volume}} |E|^2 dV} \overset{\text{1D}}{=} \frac{\int\limits_{\text{active}} |E_\mathrm{z}|^2 dz}{\int\limits_{\text{depth}} |E_\mathrm{z}|^2 dz} \tag{4.1}$$

and that takes into account that the mode is not entirely confined in the active region. It has a value of 0.5 for this particular structure. Higher order TM modes, as shown in Fig. 4.1(a) as the dashed and dotted line, have a small overlap with the active region and high losses due to their large overlap with lossy regions. As these modes exhibit little gain and have high losses only the fundamental mode will lase above threshold.

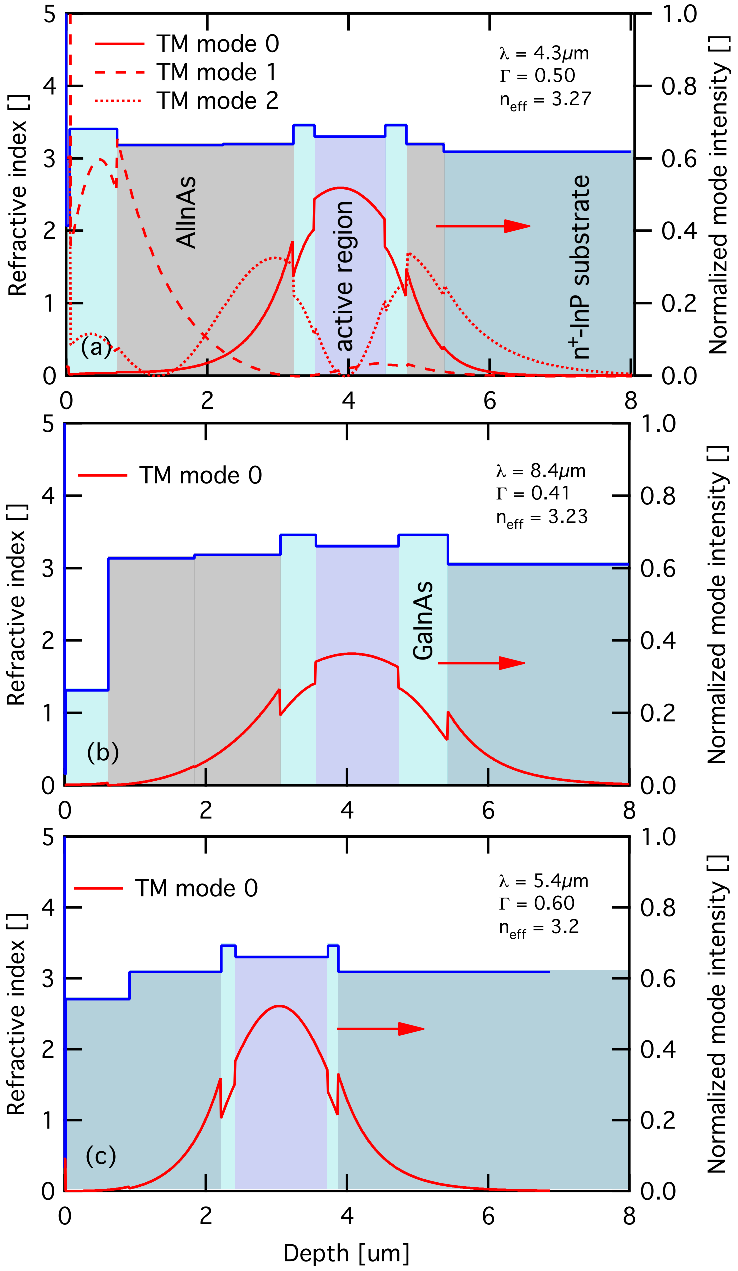

Figure 4.1: Historical and plasmon-enhanced waveguides

(a) Refractive index profile (blue) and calculated intensity (E_z^2) of the fundamental (red, continuous line) and higher order TM modes (dashed, dotted) calculated for the waveguide used in the first quantum cascade laser. (b) Plasmon-enhanced waveguide for quantum cascade lasers emitting at longer wavelengths. (c) Plasmon-enhanced waveguide with InP top cladding layer. (Same color coding is used for all figures.)

4.2.2 Plasmon enhanced waveguide

For longer wavelength the optical mode penetrates much more into the cladding and thicker cladding layers would be required to reduce the waveguide losses to an acceptable value and prevent the mode from coupling to interface plasmon modes. But thick cladding layers are not desirable. On one hand because it complicates and prolongs the growth and on the other hand for reasons of thermal management. A solution to this problem was proposed by Sirtori *et al.*[57] where a highly doped GaInAs layer ($n\!=\!7\!\times\!10^{18}\text{cm}^{-3}$) is grown above the cladding layer as shown in Fig. 4.1(b). The doping of this layer is carefully chosen in a way that the plasma frequency approaches the one of the waveguide mode. There the material shows an anomalous dielectric dispersion that makes the real part of the refractive index drop strongly. As a result the coupling between the fundamental mode and the high-loss plasmon mode propagating along the metal-contact/semiconductor interface is suppressed. Fig. 4.2(a) shows the plasma frequency and corresponding wavelengths (b) as a function of carrier density and for various materials. The plasma frequency is defined as:[188]

$$\omega_{\mathrm{p}} \;=\; \sqrt{\frac{nq^2}{\varepsilon_0\varepsilon_\infty\, m^*}}$$

Where n is the carrier density, q is the electron charge, ε_0 and ε_∞ are the vacuum and material dielectric constants and m^* is the electron effective mass. In the picture of a Lorentz oscillator model, the dielectric function for

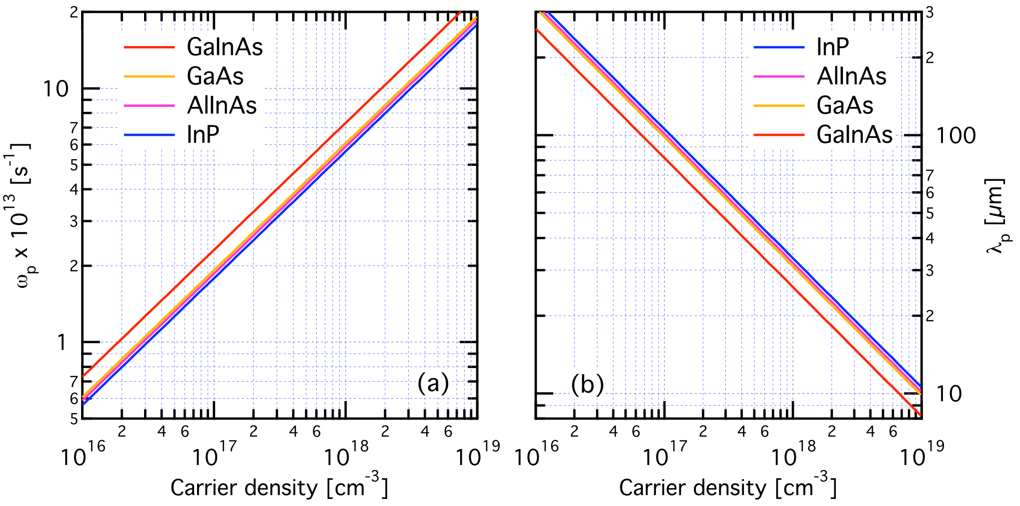

Figure 4.2: Plasma frequency as a function of carrier concentration
Plasma frequency (a) and corresponding wavelength (b) as a function of carrier density for different materials.

a semiconductor can thus be written as:[188]

$$\varepsilon(\omega) \;=\; \varepsilon' + i\,\varepsilon'' \;=\; \varepsilon_{\mathrm{el}}\left(1 - \frac{\omega_{\mathrm{p}}^2}{\omega\left(\omega + i\frac{1}{\tau}\right)}\right)$$

With τ the relaxation time.[2] Refractive index n_{r} and absorption constant α can be calculated from the dielectric function using equations (for non-magnetic media):

$$(n_{\mathrm{r}} + i\kappa)^2 = \varepsilon \qquad \text{and} \qquad \alpha \;=\; 2\kappa\frac{\omega}{c}$$

An illustration for the change of the refractive index close to the plasma resonance is shown in Fig. 4.3 where the refractive index (a) and the absorption constant (b) are plotted as a function of wavelength for GaInAs with

---

[2] A value of $\tau = 150\,\mathrm{fs}$ was used for the numerical calculations.

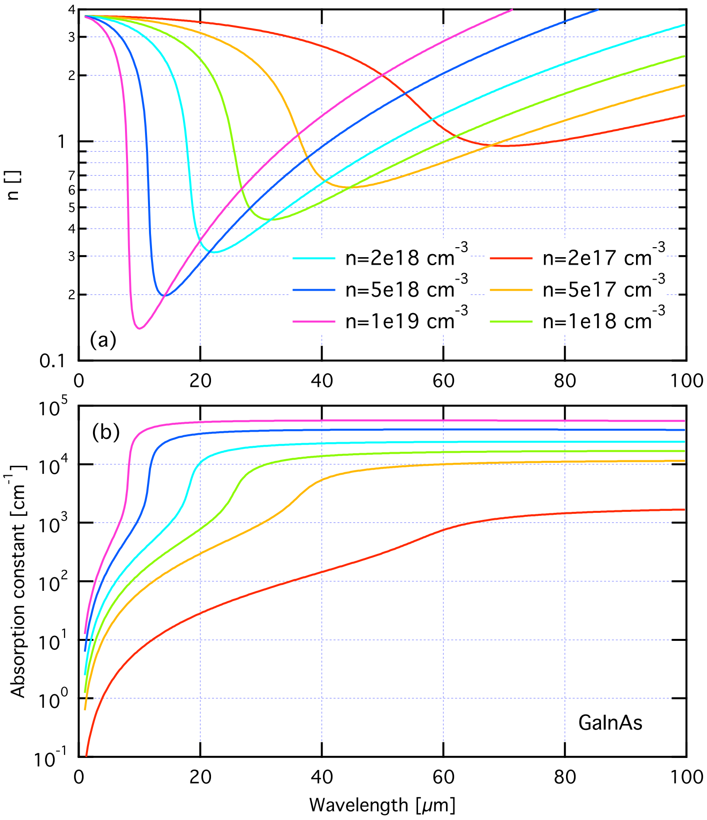

Figure 4.3: Anomalous dielectric dispersion for GaInAs

Refractive index (a) and absorption constant (b) of GaInAs as a function of wavelength and for various doping densities.

various carrier densities. Fig. 4.1(b) also shows how the optical mode can be symmetrised by carefully choosing the relative thicknesses of the GaInAs confinement layers, despite the different materials used for bottom and top cladding.

4.2.3 Free-carrier absorption

Our structures are pumped electrically and therefore they must be conductive. The free electrons in the material can interact with the optical field resulting in an absorption. A very simplistic model of this free-carrier absorption is provided by the Drude model. We consider a free electron gas of density n where the electrons have an effective mass m^* and collision time τ in the order of 100 fs. The absorption of this electron gas is given by:[146]

$$\alpha_{\mathrm{fc}} = \frac{Z_0}{4\pi c^2\, n_{\mathrm{r}}} \frac{n q^2 \lambda_0^2}{m^*\, \tau} \tag{4.2}$$

where $Z_0 = \sqrt{\mu_0/\varepsilon_0}$ is the impedance of free space. We note that α_{fc} is inversely proportional to the effective mass and scales with the square of the wavelength. However, the Drude model completely neglects the quantum mechanical origin of the processes that lead to free-carrier absorption and therefore only represents a crude approximation. Experiments show that the quadratic dependence with λ_0 does not hold but scales with $\lambda_0^p, 1.5 \leq p < 3.0$ where p depends on the material. More complete models and calculations of free-carrier absorption in III-V semiconductors have been published, for example Ref. [189], and also the influence of free-carrier absorption on the threshold current density of quantum cascade lasers has been studied.[190] But the calculations are complex and therefore the use of a phenomenological formula is more convenient. Such a formula is given by:[146]

$$\alpha_{\mathrm{fc}} = \mathcal{K} \left(\frac{n\ [\mathrm{cm}^{-3}]}{10^{17}} \right) \left(\frac{\lambda_0\ [\mu\mathrm{m}]}{9} \right)^p \tag{4.3}$$

where the phenomenological parameters for a couple of materials are given in Tab. (4.1).

Table 4.1: Phenomenological parameters for free-carrier absorption

Material	n [$\times 10^{17}\,\mathrm{cm}^{-3}$]	$\mathcal{K}$	p
GaAs	1-5	3	3
InAs	0.3 - 8	4.7	3
InP	0.4 - 4	4	2.5

4.2.4 Waveguides in different material systems

GaInAs/AlInAs material system

The standard waveguide for quantum cascade lasers based on the GaInAs / AlInAs material system was introduced by Faist *et al.*[54] and is illustrated in Fig. 4.1(c) as an example. In this waveguide the AlInAs top cladding that was used in the first quantum cascade laser is replaced by an InP cladding. This symmetrises the refractive index profile, enhances the confinement due to higher refractive index contrast and the thermal conductivity of InP is also much better ($0.68\,\mathrm{W\,cm^{-1}\,K^{-1}}$) than for AlInAs and GaInAs ($0.05\,\mathrm{W\,cm^{-1}\,K^{-1}}$). With growth equipment that can grow the the active region materials (GaInAs/AlInAs) as well as the material for the cladding layers (InP), people typically use a highly doped InP substrate and start the growth with a low-doped InP bottom cladding layer.[191] This method has the advantage that highly doped InP substrates are of superior quality and the series resistance across the $\approx 100\,\mu$m thick substrate is smaller. Otherwise a slightly doped substrate ($n = 1 - 2 \times 10^{17}\mathrm{cm}^{-3}$) serves as the bottom cladding layer and after the growth of the active region the wafer needs to be transferred to another epitaxy equipment to grow the InP cladding layers, typically by metal-organic vapor phase epitaxy.

GaAs/AlGaAs material system

The first material system people worked on and that was not the conventional GaInAs/AlInAs material system grown on InP substrates was GaAs/ $Al_xGa_{1-x}As$ that was grown on heavily doped ($n = 2-4 \times 10^{18}\text{cm}^{-3}$) GaAs substrates. Unlike GaInAs/AlInAs where a comfortably high refractive index contrast exists between the active region and the substrate and where the confinement can easily be enhanced by adding GaInAs wave guiding layers, GaAs ($n \approx 3.23$)[3] has a higher refractive index than the active region ($n \approx 3.21$). For this situation Sirtori et al. suggest to use a "double plasmon-enhanced" confinement.[58]

InAs/AlSb material system

The InAs/AlSb material system is very interesting for quantum cascade lasers because it exhibits a conduction band discontinuity ΔE_c of approximately 2.1 eV and therefore is a promising material system to realize short-wavelength quantum cascade lasers. The structures are usually grown on InAs substrates that are available in high quality. In initial InAs/AlSb-based quantum cascade lasers a plasmon enhanced waveguide was used. As an example, Teissier *et al.*[106] embedded their 25-period active region emitting at $\lambda = 4.5\,\mu$m between two 1.33 μm thick, low doped InAs ($n = 5 \times 10^{16}\text{cm}^{-3}$) spacers that separated the active region from InAs cladding layers that were highly doped ($n = 1 \times 10^{19}\text{cm}^{-3}$) in order to improve the refractive index contrast. However, this approach is not possible at much shorter wavelength

---

[3] Value taken from Ref. [58].

because InAs has its interband absorption edge at approximately 360 meV. Although this edge can be shifted by more than 300 meV with very high doping ($n = 3 \times 10^{19}\mathrm{cm}^{-3}$) and the induced conduction band filling, this is not applicable to the spacer layers because losses due to free-carrier absorption would get prohibitively high. A InAs/AlSb-based quantum cascade laser emitting at short wavelength (λ =4.5 μm) could only be demonstrated once a suitable waveguide has been developed. The solution of Devenson *et al.*[108] consisted in replacing the bulk InAs spacer layers by InAs/AlSb superlattice spacers that have been designed in a way to shift the interband absorption to 700 meV and the resonant absorption in the superlattice to 560 meV. This waveguide design proved also successful in the demonstration of quantum cascade lasers emitting below 3 μm wavelength.[107]

4.3 Large optical cavity waveguides

Potential and actual applications for quantum cascade lasers have been discussed in section 1.5 of chapter 1. For a number of those, especially long-path remote sensing and countermeasures, large peak and average powers are essential. In a quantum cascade laser electrons are injected from period to period, emitting photons at each step. For this reason the power is expected to grow linearly with the number of periods in the active region. Scaling of the optical power was demonstrated already by Gmachl *et al.* in a series of experiments.[192] However, for a fixed waveguide width, as the number of periods increases, the overlap factor of each individual period with the optical mode will decrease as they are inserted in a region with lower optical field. As a result the threshold current density will saturate as the overlap factor of the gain medium reaches unity.[192] Moreover, as we will show in the next section, the slope efficiency also decreases below the ideal value due to vertical spatial hole burning.

4.3.1 Vertical spatial hole burning

We look at the rate equations for a three level system, as they were introduced in chapter 2, section 2.4. However, we now treat each individual period separately. Let us consider a waveguide core consisting in N_p active region periods and let n_3^i be the upper state population, n_2^i the lower state population and Γ_i the overlap factor of the i^th stage. Then the rate equations (neglecting spontaneous emission) write:

$$\frac{dn_3^i}{dt} = \frac{J}{q} - \frac{n_3^i}{\tau_3} - g_\mathrm{c}\Gamma_i S\left(n_3^i - n_2^i\right) \tag{4.4a}$$

$$\frac{dn_2^i}{dt} = \frac{n_3^i}{\tau_{32}} - \frac{n_2^i}{\tau_2} + g_\mathrm{c}\Gamma_i S\left(n_3^i - n_2^i\right) \tag{4.4b}$$

$$\frac{dS}{dt} = \frac{c}{n}\left[\sum_{i=1}^{N_\mathrm{p}} g_\mathrm{c}\Gamma_i\left(n_3^i - n_2^i\right) - \alpha_\mathrm{tot}^\mathrm{opt}\right]\cdot S \tag{4.4c}$$

where S is the linear photon density of the laser mode, g_c is the differential gain cross section, $\alpha_\mathrm{tot}^\mathrm{opt}$ are the total optical losses in the cavity, J is the current density and q is the electron charge. Setting the time derivatives to zero to find the steady state solution and neglecting the electron population of the first excited state ($n_2^i = 0$), Equ. (4.4c) yields:

$$\alpha_\mathrm{tot}^\mathrm{opt} = \sum_{i=1}^{N_\mathrm{p}} g_\mathrm{c}\Gamma_i n_3^i \tag{4.5}$$

Solving Equ. (4.4a) for n_3^i and inserting it into Equ. (4.5) we can calculate J as a function of the linear photon density:

$$J \;=\; \frac{q\,\alpha_{\mathrm{tot}}^{\mathrm{opt}}}{g_{\mathrm{c}}}\,\frac{1}{\sum_{i=1}^{N_{\mathrm{p}}} \frac{\Gamma_i}{1/\tau_3+g_{\mathrm{c}}\Gamma_i S}} \tag{4.6}$$

Equ. (4.6) shows that unless all Γ_i are equal we do not have a linear relationship between S and J. We can now calculate the slope efficiency to the first order in S and close to threshold where the linear photon density S is small. Assuming ($\tau_3\, g_{\mathrm{c}}\, \Gamma_i\, S \ll 1$), Equ. (4.6) becomes:

$$J \;\simeq\; \frac{q\,\alpha_{\mathrm{tot}}^{\mathrm{opt}}}{g_{\mathrm{c}}}\,\frac{1}{\sum_{i=1}^{N_{\mathrm{p}}} \tau_3\,\Gamma_i\,(1-\tau_3\,g_{\mathrm{c}}\,\Gamma_i\,S)} \tag{4.7}$$

Or, solving Equ. (4.7) for the linear photon density S yields:

$$S \;=\; \frac{g_{\mathrm{c}}\,J\,\tau_3 \sum_{i=1}^{N_{\mathrm{p}}}\Gamma_i \;-\; q\,\alpha_{\mathrm{tot}}^{\mathrm{opt}}}{g_{\mathrm{c}}^2\,J\,\tau_3^2 \sum_{i=1}^{N_{\mathrm{p}}}\Gamma_i^2}$$

Calculating the derivative with respect to current and replacing J by Equ. (4.7) we find:

$$\frac{dS}{dJ} \;=\; \frac{1}{q\,\alpha_{\mathrm{tot}}^{\mathrm{opt}}}\,\frac{\left(\sum_{i=1}^{N_{\mathrm{p}}}\Gamma_i - g_{\mathrm{c}}\,\tau_3\,S\,\sum_{i=1}^{N_{\mathrm{p}}}\Gamma_i^2\right)^2}{\sum_{i=1}^{N_{\mathrm{p}}}\Gamma_i^2}$$

Thus, the initial slope efficiency at threshold is

$$\left.\frac{dS}{dJ}\right|_{S=0} \;=\; \frac{1}{q\,\alpha_{\mathrm{tot}}^{\mathrm{opt}}}\,\underbrace{\frac{\left(\sum_{i=1}^{N_{\mathrm{p}}}\Gamma_i\right)^2}{\sum_{i=1}^{N_{\mathrm{p}}}\Gamma_i^2}}_{\eta_{\mathrm{v}}} \tag{4.8}$$

where η_v is the relative slope efficiency representing the reduction of the slope efficiency due to vertical spatial hole burning. One can easily see that for identical Γ_i the usual result $dS/dJ = N_\mathrm{p}/q\,\alpha_\mathrm{tot}^\mathrm{opt}$ is recovered.[4]

Effect of finite lower state population

The same calculations can be performed in case of finite lower state population ($n_2^i > 0$). Setting time derivatives to zero to find the solution of the steady state and solving Equ. (4.4b) for n_2^i and Equ. (4.4a) for n_3^i and inserting into Equ. (4.4c) yields:

$$\alpha_\mathrm{tot}^\mathrm{opt} \;=\; \frac{J}{q}\,g_\mathrm{c}\,\tau_3 \sum_{i=1}^{N_\mathrm{p}} \frac{\Gamma_i\left(1-\frac{1/\tau_{32}+g_\mathrm{c}\Gamma_i S}{1/\tau_2+g_\mathrm{c}\Gamma_i S}\right)}{1+g_\mathrm{c}\,\tau_3\,\Gamma_i\,S\left(1-\frac{1/\tau_{32}+g_\mathrm{c}\Gamma_i S}{1/\tau_2+g_\mathrm{c}\Gamma_i S}\right)} \tag{4.9}$$

Again, assuming conditions close to threshold where S is very small ($\tau_j\,g_\mathrm{c}\,\Gamma_i S \ll 1,\ j \in \{32,3,2\}$) and thus neglecting higher order terms in ($\tau_j\,g_\mathrm{c}\,\Gamma_i S,\ j \in \{32,3,2\}$), Equ. (4.9) becomes:

$$J \;=\; \frac{q\,\alpha_\mathrm{tot}^\mathrm{opt}}{g_\mathrm{c}\,\tau_\mathrm{eff}}\,\frac{1}{\sum_{i=1}^{N_\mathrm{p}}\Gamma_i - g_\mathrm{c}\left(\tau_\mathrm{eff}+\tau_2\right)\sum_{i=1}^{N_\mathrm{p}}\Gamma_i^2\;\cdot\;S} \tag{4.10}$$

where $\tau_\mathrm{eff} = \tau_3\,(1-\tau_2/\tau_{32})$ has been introduced as in section 2.4 in chapter 2. Deriving J with respect to the photon density S yields:

$$\frac{dJ}{dS} \;=\; q\,\alpha_\mathrm{tot}^\mathrm{opt}\left[1+\frac{\tau_2}{\tau_\mathrm{eff}}\right]\;\frac{\sum_{i=1}^{N_\mathrm{p}}\Gamma_i^2}{\left[\sum_{i=1}^{N}\Gamma_i - g_\mathrm{c}\left(\tau_\mathrm{eff}+\tau_2\right)\sum_{i=1}^{N_\mathrm{p}}\Gamma_i^2\;\cdot\;S\right]^2} \tag{4.11}$$

---

[4] Valid under the assumption of negligible lower state population.

And, again looking at the initial slope efficiency at threshold:

$$\left.\frac{dS}{dJ}\right|_{S=0} = \frac{1}{q\,\alpha_{\mathrm{tot}}^{\mathrm{opt}}}\frac{1}{(1+\tau_2/\tau_{\mathrm{eff}})}\underbrace{\frac{\left[\sum_{i=1}^{N_{\mathrm{p}}}\Gamma_i\right]^2}{\sum_{i=1}^{N_{\mathrm{p}}}\Gamma_i^2}}_{\eta_{\mathrm{v}}} \tag{4.12}$$

The slope efficiency is again proportional to η_{v}, but this time there is another multiplicative factor taking into account the finite lower state population as it was also the case in section 2.4.2.

Fig. 4.4 shows a comparison between three different types of waveguides where the relative slope efficiency has been calculated. Evaluating η_{v} for a hypothetical symmetric slab waveguide as shown in Fig. 4.4(a) with a 3.3 μm thick active region ($n_{\mathrm{eff}} = 3.3$, $n = 6\times10^{16}\mathrm{cm}^{-3}$) and InP cladding layers ($n=1\times10^{17}\mathrm{cm}^{-3}$) and emitting at a wavelength of 4.3 μm yields $\eta_{\mathrm{v}} = 85\,\%$. Burying the active region between 300 nm thick GaInAs ($n=6\times10^{16}\mathrm{cm}^{-3}$) buffer layers for stronger guiding improves this value to 95 %. With the tri-stack waveguide design we present in the next section, a relative slope efficiency of 99.4 % is obtained. A maximum relative slope efficiency ($\eta_{\mathrm{v}} = 1$) is obtained when all Γ_i are the same, meaning that the optical mode should have a rectangular profile.

Large optical cavity waveguides with quasi rectangular mode profile not only can reach maximal slope efficiency but also have other advantages. One advantage is to delay the onset of gain compression. Saturation of the gain medium will naturally occur in the periods of the active region at the peak of the optical mode. In a quasi-rectangular waveguide the peak intensity of the optical mode is considerably decreased and therefore the onset of gain

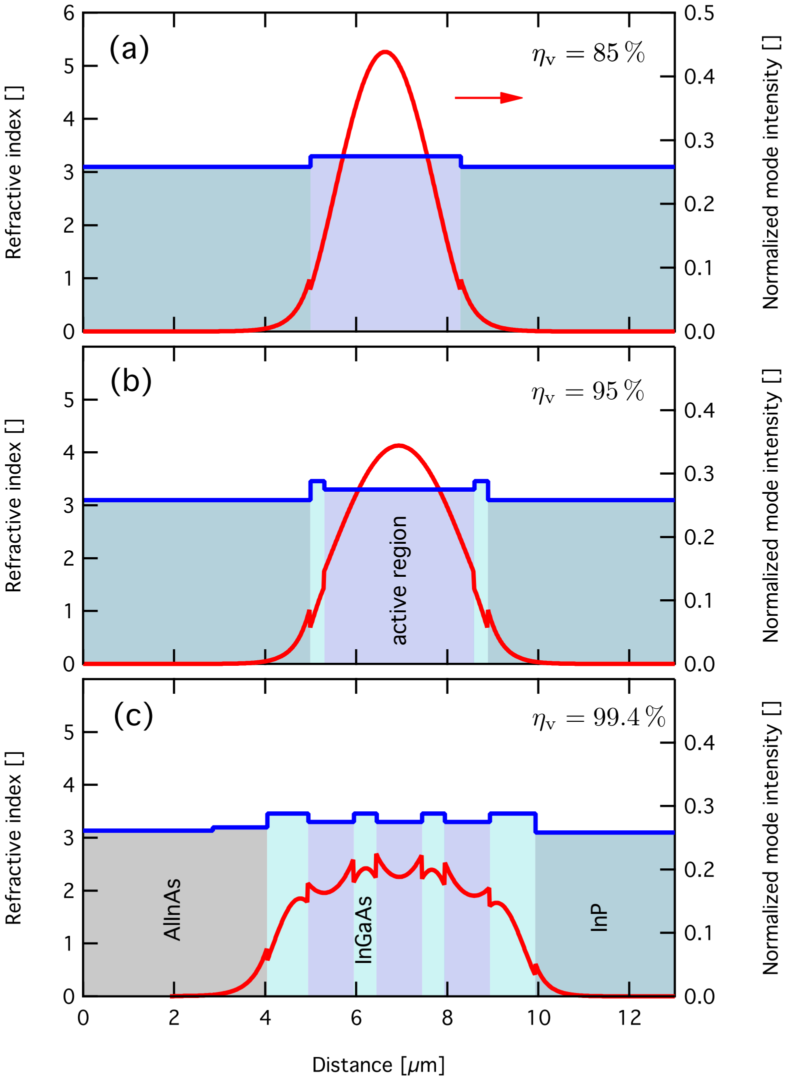

Figure 4.4: Vertical spatial hole burning in different waveguides

Comparison of the relative slope efficiency (vertical spatial hole burning) between different types of waveguides. The blue curve represents the refractive index profile whereas the red curve represents the relative mode intensity in the growth direction of the structure. Graph (a) shows a slab waveguide where a 3.3 µm thick active region is sandwiched between InP cladding layers. In graph (b) additional GaInAs wave guiding layers were introduced and graph (c) shows the situation where the active region has been split in three stacks with intermediate GaInAs buffer layers (tri-stack waveguide).

saturation will occur at much higher optical power. Looking at the calculated waveguide modes in Fig. 4.4, the normalized intensity in graph (a) has a peak value of 0.44 whereas, in case of the quasi-rectangular mode profile of graph (c), it only reaches 0.22. Therefore, for a slab waveguide as shown in graph (a), the onset of gain saturation will occur for an optical power smaller by a factor of two compared to the waveguide with quasi-rectangular optical mode profile. Other advantages include a narrower farfield, thus requiring less sophisticated optics, and reduced beam steering effects.[5, 193]

4.3.2 Tri-stack waveguides

A quasi-rectangular optical mode profile with optimal slope efficiency and low peak intensity of the optical mode can be obtained by splitting a gain medium in three groups of active region periods that are separated with two GaInAs buffer layers. The waveguide core is then further separated from the cladding layers by thick $Ga_{0.47}In_{0.53}As$ waveguiding layers. This separation also helps to maintain the electrical stability of the structure. The refractive index profile of such a waveguide and the calculated fundamental optical mode are shown in Fig. 4.4(c). The optical mode profile has a large spatial extension and a relatively flat intensity distribution. In a first experiment three structures with tri-stack waveguide were grown: N505, N513 and N515. The structures were grown by molecular beam epitaxy in one run and AlInAs cladding layers were used. A detailed listing of the waveguide designs can be found in appendix D. Structures N505 and N513 are based on the same strain-compensated active region designed to emit

Table 4.2: Summary of key-differences between N505, N513 and N505

	N505	N513	N515
n [cm^{-3}]	3.8E+16	2.9E+16	1.6E+16
n_{s} [cm^{-2}]	2.2E+11	1.7E+11	8.2E+10
design	b2c_strp5s_46	b2c_strp5s_46	b2c_strp5_52
λ @78 K [μm]	4.06	4.31	5.00
λ @RT [μm]	4.24	4.47	5.20

around 4.6 μm. In structure N513 the average doping was reduced from $n = 3.8 \times 10^{16}\mathrm{cm}^{-3}$ to $n = 2.9 \times 10^{16}\mathrm{cm}^{-3}$ and, due to different growth conditions, they emit at slightly different wavelengths. Structure N515 is based on a strain-compensated active region emitting around 5.2 μm and the average doping was further reduced to $n = 1.9 \times 10^{16}\mathrm{cm}^{-3}$. A detailed listing of the active region for structures N505 and N513 can be found in appendix C.4 and for structure N515 in appendix C.5. A summary of some key-differences between the structures is shown in Tab. (4.2).

The growth of these structures is challenging because at typical MBE growth-rates ($\approx 1\,\mu$m/h) it takes a long time to grow 8 μm of material. Additionally, the growth conditions need to be changed between the growth of the active region stacks with strained material and the $\mathrm{Ga_{0.47}In_{0.53}As}$ buffer layers that have to be lattice-matched to the InP substrate. The molecular fluxes need to be well calibrated and the active region design well balanced in order to prevent the epilayers from relaxing. Slightly doped ($n = 1-2 \times 10^{17}\mathrm{cm}^{-3}$) InP:S wafers were used as substrates. In the case of N505 growth started with the usual InP-to-GaInAs grading layers and was then followed by a 1 μm thick buffer layer of lattice-matched $\mathrm{Ga_{0.47}In_{0.53}As}$

($n=4\times10^{16}\text{cm}^{-3}$). Growth was then interrupted and conditions were changed to grow strained $\text{Al}_{0.546}\text{In}_{0.454}\text{As}$ as barrier and $\text{Ga}_{0.391}\text{In}_{0.609}\text{As}$ as well material with approximately 0.5% strain. The first gain stack consisting in 17 active/injection region pairs and totalling to a thickness of 0.99 μm and an average doping of $n = 3.8\times10^{16}\text{cm}^{-3}$ was then grown. Then growth conditions for growing lattice-matched $\text{Al}_{0.48}\text{In}_{0.52}\text{As}$ and $\text{Ga}_{0.47}\text{In}_{0.53}\text{As}$ had to be restored and a 0.5 μm thick GaInAs ($n=4\times10^{16}\text{cm}^{-3}$) spacing layer was grown. Two additional gain stacks were then grown in the same manner and growth of the waveguide core was terminated by a 0.9 μm thick $\text{Ga}_{0.47}\text{In}_{0.53}\text{As}$ ($n = 4\times10^{16}\text{cm}^{-3}$) waveguiding layer. The top cladding consists in a first, 1.2 μm thick $\text{Al}_{0.48}\text{In}_{0.52}\text{As}$ $n = 1\times10^{17}\text{cm}^{-3}$ and a second, 0.85 μm thick $\text{Al}_{0.48}\text{In}_{0.52}\text{As}$ ($n=2\times10^{18}\text{cm}^{-3}$) layer and the growth was terminated with a 10 nm thick $\text{Ga}_{0.47}\text{In}_{0.53}\text{As}$ ($n=2\times10^{19}\text{cm}^{-3}$) contact layer. Visual inspection of structure N505 after it was removed from the growth chamber revealed dislocation lines over the whole surface, structures N513 and N515 only showed the usual point defects.

Grown structures were processed into 14 to 24 μm wide ridge waveguides as described in section 3.4.1 in chapter 3. Waveguide ridges were fabricated by wet etching using $\text{HBr:HNO}_3\text{:H}_2\text{O}$ (1:1:10), resulting in waveguides with a trapezoidal cross section. Therefore, the width of the gain stacks varies with the topmost gain stack being the narrowest one. Measurements with an optical microscope show that the second and third active region stacks are typically 3, respectively 6 μm wider than the first one. The indicated waveguide widths refer to the mean width of the central active region stack. Calculations show that, for a laser with 17, 20 and 23 μm wide active region stacks, the threshold current density would be underestimated by 1.5 % in respect to a laser with uniform, 20 μm wide active regions. However, this calculation does not take into account the higher waveguide losses expected in case of a trapezoidal waveguide cross section. For the ridge insulation a 300 nm thick layer of $Si0_2$ was deposited by plasma enhanced chemical vapor deposition. A 6-8 μm thick layer of gold was deposited on the top contact by electro-plating for improved heat sinking. After finalization of the process, laser devices with lengths up to 5.3 mm were cleaved along crystallographic planes and soldered with indium on copper mounts. In order to decrease mirror losses, devices were coated on the back facet using a highly-reflective Al_2O_3:Au:Al_2O_3 (300/100/100) coating.

Fig. 4.5 shows Fabry-Pérot emission spectra of the three structures in pulsed operation at 78 K and at room temperature. As can be seen in the graph structure N505 emits around 4.06 μm (2467 cm^{-1}) at 78 K and 4.24 μm (2360 cm^{-1}) at 302 K heat sink temperature. Structure N513, having the same active region but due to different growth conditions, emits at 4.31 μm (2322 cm^{-1}), respectively 4.47 μm (2237 cm^{-1}), whereas structure N515 emits at 5.00 μm (1998 cm^{-1}), respectively 5.20 μm (1925 cm^{-1}).

Quantum cascade lasers with standard waveguides have a strongly diverging beam in the axis perpendicular to the epilayers. Therefore expensive optics with high numerical aperture are required in order to efficiently collect the emitted beam. As mentioned above, in a quantum cascade laser with a tri-stack waveguide the optical mode has a large spatial extension, leading to a narrow farfield. A measured farfield emission pattern of a 15 μm wide and 3.8 mm long laser device of structure N505 is shown in Fig. 4.6. Crosses

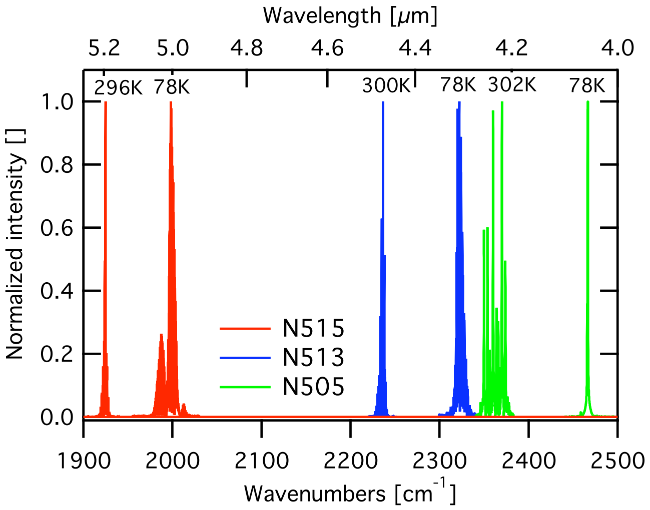

Figure 4.5: Emission spectra at 78 K and room temperature

Fabry-Pérot emission spectra of structures N505, N513 and N515 in pulsed operation at 78 K and room temperature. Structure N505 emits at 4.06 μm at 78 K, respectively 4.24 μm at 302 K heat sink temperature. Structure N513 at 4.31 μm, respectively 4.47 μm and structure N515 at 5.00 μm and 5.20 μm. The spectra were acquired slightly above threshold current at 1 % duty-cycle.

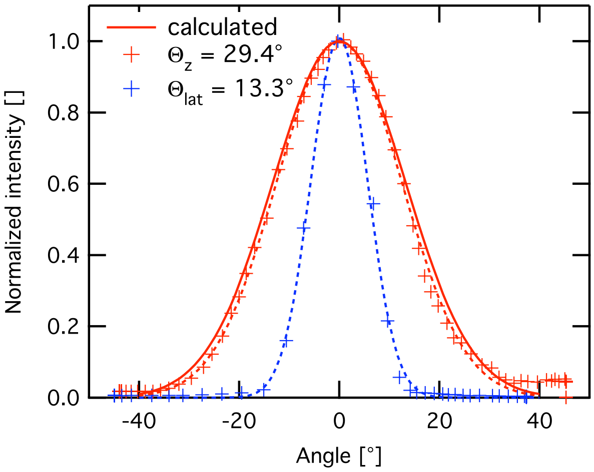

Figure 4.6: Farfield of a laser with tri-stack waveguide

Farfield emission pattern of device N505A6a in the growth (red) and lateral (blue) direction. Dashed lines represent Gaussian fits with a full-width at half-maximum of 29.4° in the growth and 13.4° in the lateral direction. The full line represents the calculated far field in the growth direction with a full-width at half maximum of 31.1° that fits well with the experimental curve.

represent the measured optical intensity as a function of the angle in the growth (red) and lateral direction. Dashed lines represent fitted Gaussian curves with a full-width at half-maximum of 29.4 ° in the growth and 13.4 ° in the lateral direction. Calculation of the far field in the growth direction (solid red line) yields a full-width at half-maximum of 31.1 ° which is in good agreement with the measured value. We did not measure the far field patterns of devices of structures N513 and N515. Calculations yield slightly larger values of 32.7 ° and 35.6 ° due to the shift to longer wavelength. The farfield shows that the device indeed lases on the fundamental transverse mode as it is shown in Fig. 4.4(c). The reported divergence angles in the growth direction are much narrower than the values we measure for lasers with similar active region design but with conventional waveguide (68 °) or the value of 49 ° reported by Yu *et al.* at similar wavelength.[77]

The combination of a high number of active region periods, the delay of the onset of gain compression and a relative slope efficiency parameter (η_{v}) close to unity leads to very high peak power in pulsed operation. Fig. 4.7 shows light-current-voltage characteristics in pulsed operation at 1 % duty-cycle (100 kHz, 100 ns pulse width) of three laser devices with a highly-reflective coating on the back facet. Due to the high current requirement of devices from structures N505 and N513 they could only be measured in the setup with LLH100 housing as described in section 3.4.2 of chapter 3 with the uncertainties associated with the voltage and current measurements as discussed therein. A 5.02 mm long and 24 μm wide device was measured for structure N505 and the results are shown in Fig. 4.7(a). At 30 ℃ a threshold current density of 3.0 kA cm^{-2} and a maximal peak power of 2.2 W were measured with an initial slope efficiency of 0.8 W/A. At -30 ℃ these values improved to 1.7 kA cm^{-2} for the threshold current density and 5.0 W, respectively 1.6 W/A for maximal peak power and initial slope efficiency. Measurements of a device of structure N513 with a 5.3 mm long and 21 μm wide cavity are shown in Fig. 4.7(b). At 30 ℃ a maximal peak power of 2.1 W, an initial slope efficiency of 1.1 W/A and a threshold current density of 1.9 kA cm^{-2} are measured. These values improve to 4.0 W, respectively 1.8 W/A and 1.4 kA cm^{-2} at -15 ℃.

The true potential of the concept of diluted waveguides can be seen in the measurements of a device of structure N515. In this structure the nominal active region doping was reduced by a factor of two in respect to structure N505 which reduced considerably the threshold current density. As it will be shown later in this chapter the performance of these devices is strongly limited by the low thermal conductance of the waveguide core and the entire device. Therefore reducing the threshold current results in a strong increase of the emitted power as self-heating effects are reduced. Due to reduced current requirements devices of structure N515 could be measured in the cryostat setup as described in section 3.4.2 of chapter 3. This has the advantage that the device performance can be measured over a large temperature range from 4 to 320 K and that the voltage and current measurements are more accurate. Measurements of a device with a 3.44 mm long and 20 μm wide cavity are shown in Fig. 4.7(c). At 15 K a maximal peak power above 14 W and an initial slope efficiency of 11 W/A at a threshold current density of 0.3 kA cm^{-2} was measured. The threshold current density increases to 0.9 kA cm^{-2} and 1.1 kA cm^{-2} at -33 ℃, respectively 7 ℃. At 7 ℃ a maximal

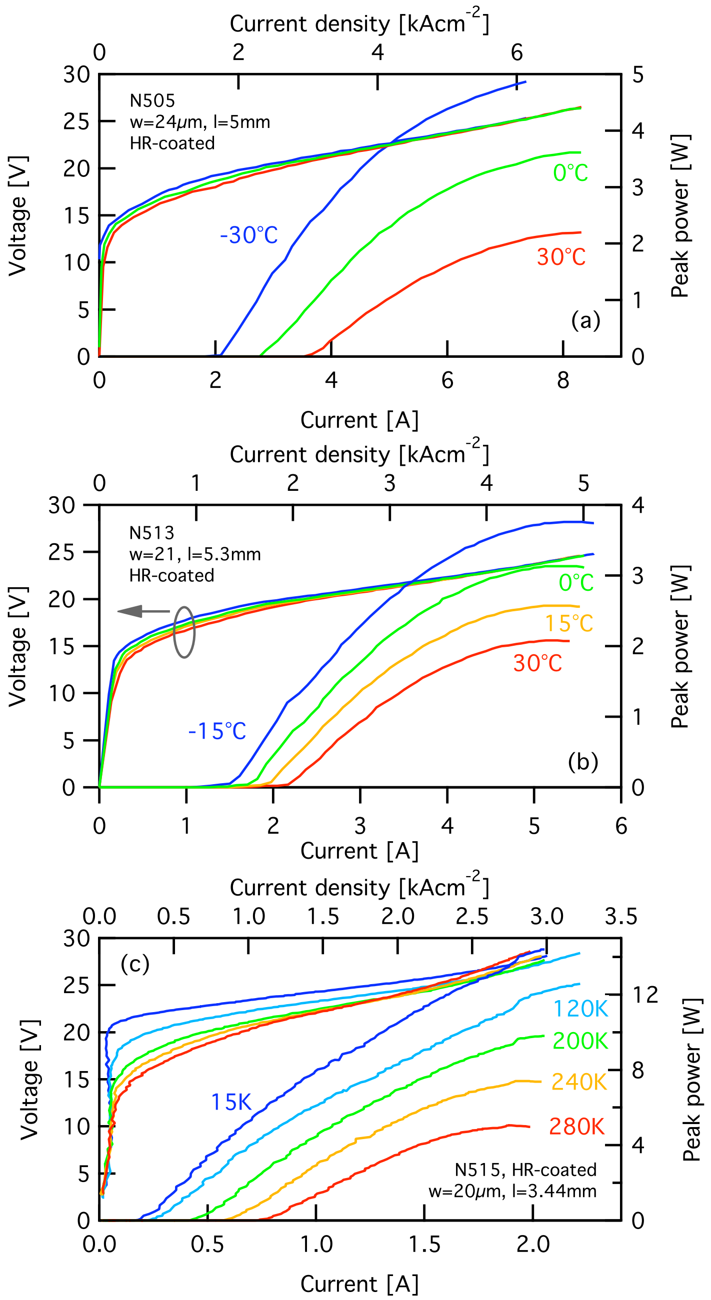

Figure 4.7: Power-current-voltage characteristics in pulsed operation
Power-current-voltage curves of three devices of structures N505 (a), N513 (b) and N515 (c) at various temperatures. Measurements were performed in pulsed operation at 1 % duty-cycle with 100 kHz repetition rate and 100 ns pulse width.

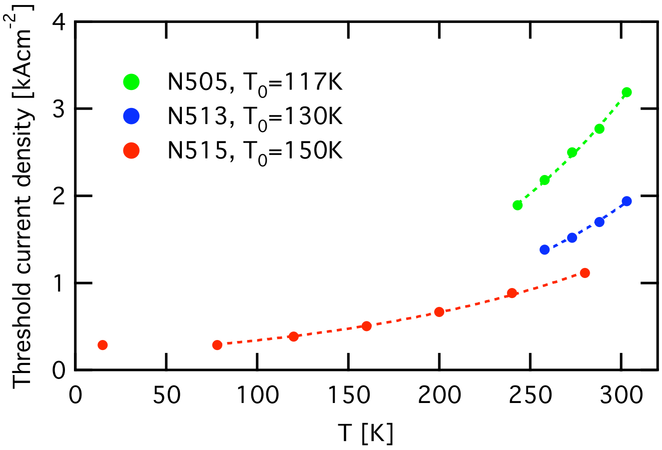

Figure 4.8: Temperature dependence of the threshold current
Threshold current density as a function of temperature of the same devices as in Fig. 4.7. The data points fit an exponential dependence [$J_{\mathrm{th}} = J_0 \exp(T/T_0)$] with characteristic temperatures $T_0 = 117\,K$ for device N505 and $T_0 = 130\,K$ and $T_0 = 150\,K$ for device N513, respectively device N515.

peak power of 7.4 W and an initial slope efficiency of 6.0 W/A was measured. Fig. 4.8 shows the threshold current density of the three devices as a function of temperature. The data points follow an exponential dependence [$J_{\mathrm{th}} = J_0 \exp(T/T_0)$] with characteristic temperatures $T_0 = 117\,\mathrm{K}$ for device N505 and $T_0 = 130\,\mathrm{K}$ and $T_0 = 150\,\mathrm{K}$ for device N513, respectively device N515. Qualitatively, smaller T_0 are expected for structures N505 and N513 as the higher threshold currents lead to more pronounced self-heating effects. A summary of these performance related values is shown in Table (4.3).

For the device Fig. 4.7(c) it is interesting to have a look at the wall plug efficiency as it is shown in Fig. 4.9. At 15 K the wall plug efficiency in pulsed operation peaks at a value of 34 % and at 280 K still 11 % are measured. The number at 15 K is close to the fundamental limit for the wall plug efficiency for a quantum cascade laser emitting at 5 μm if one considers the model by

Table 4.3: Summary of power characteristics

	N505	N513	N515
Max. peak power [W]	2.2 (30 ℃) 5.0 (-30 ℃)	2.1 (30 ℃) 4.0 (-15 ℃)	5.0 (7 ℃) 7.4 (-33 ℃)
J_{th} [kA cm^{-2}]	3.0 (30 ℃) 1.7 (-30 ℃)	1.9 (30 ℃) 1.4 (-15 ℃)	1.12 (7 ℃) 0.90 (-33 ℃)
dP/dI [W/A]	0.8 (30 ℃) 1.6 (-30 ℃)	1.1 (30 ℃) 1.8 (-15 ℃)	6.0 (7 ℃) 7.5 (-33 ℃)
T_0 [K]	117 ± 4	130 ± 6	150 ± 3
J_0 [kA cm^{-2}]	0.241 ± 0.018	0.189 ± 0.020	0.175 ± 0.005

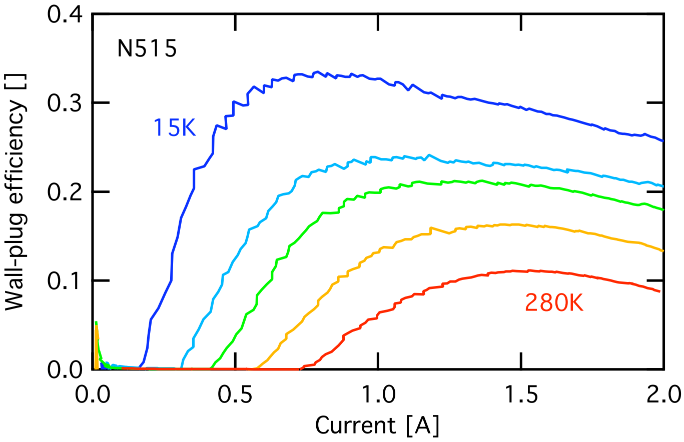

Figure 4.9: Wall plug efficiency of device N515 in pulsed operation

Wall plug efficiency of device N515 whose power-current-voltage characteristics are shown in Fig. 4.7(c). At 15 °C a maximal wall plug efficiency of 34 % is achieved. The maximal wall plug efficiencies at 240, respectively 280 K are 16 % and 11 %.

Table 4.4: Modal gain coefficient and waveguide losses

	N505	N513	N515
$g\,\Gamma$ [$\mathrm{cm\,kA^{-1}}$]	2.2 ± 0.8 (0 ℃)	3.2 ± 0.9 (0 ℃)	5.1 ± 1.5 (0 ℃) 8.8 ± 1.9 (15 K)
α_{w} [$\mathrm{cm^{-1}}$]	4.3 ± 2.4 (0 ℃)	3.6 ± 1.7 (0 ℃)	3.8 ± 2.1 (0 ℃) 1.1 ± 1.0 (15 K)

Faist that is also briefly mentioned in section 2.4.3 in chapter 2 and if an in-plane dephasing time of 140 fs is assumed.[158] According to the model in this letter, shorter emission wavelength and/or longer in-plane dephasing time is necessary, in order to obtain higher wall plug efficiencies.

Another important feature of these waveguides is their low waveguide losses. Waveguide losses were estimated studying the dependence of the threshold current with cavity length as described in chapter 3, section 3.4.3. The threshold current densities as a function of reciprocal cavity length for devices of structures N505 (green), N513 (blue) and N515 (red) are shown in Fig. 4.10. Linear fitting using the least-squares method (dashed lines) yields the coefficients of which the modal gain coefficient $g\Gamma$ and waveguide losses α_{w} are calculated. The calculated facet power reflectivity for this waveguide is $R = 0.28$. Table (4.4) shows a summary of the obtained values for the modal gain coefficient and waveguide losses of the three different structures. These values are consistent with the assumption that the waveguide losses are strongly determined by free carrier absorption. In fact, although structure N505 lases at the shortest wavelength it shows the highest waveguide losses because it was also the structure with the highest doping level ($n = 3.8 \times 10^{16}\mathrm{cm}^{-3}$). Structure N515 has the lowest doping level ($n = 1.6 \times 10^{16}\mathrm{cm}^{-3}$)

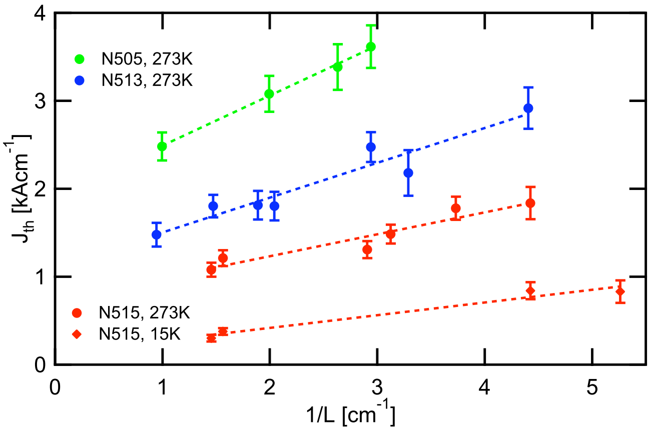

Figure 4.10: Threshold current vs. reciprocal cavity length

Threshold current density as a function of reciprocal cavity length of lasers of structure N505 (green), N513 (blue) and N515 (red dots) at 0°C. The red diamond shaped dots represent data points of structure N515 at 15 K. Dashed lines show the linear fits obtained by least-square fitting.

but emits at larger wavelength (5.2 μm) and thus suffers stronger free-carrier absorption due its nearly λ^2-dependency. Much smaller waveguide losses of $1.1 \pm 1.0\,\text{cm}^{-1}$ was measured at 15 K. We mainly attribute this to the lack of thermal back-filling at cryogenic temperatures.

Although these structures with large optical cavity lead to record peak power, the maximal obtainable average powers are moderate due to the poor thermal conductance of the waveguide core as well as the the entire device and the resulting heat-extraction bottle neck. Fig. 4.11 shows a measurement of the average power of three devices as a function of duty-cycle at -30 and 30 ℃ heat sink temperature. A maximal average power of 290 mW at -30 ℃ was obtained with device N515 at a duty-cycle of 8 %. Another example illustrating the importance of the self-heating effects in case of structure N505 is shown in Fig. 4.12 where the power-voltage-current characteristics

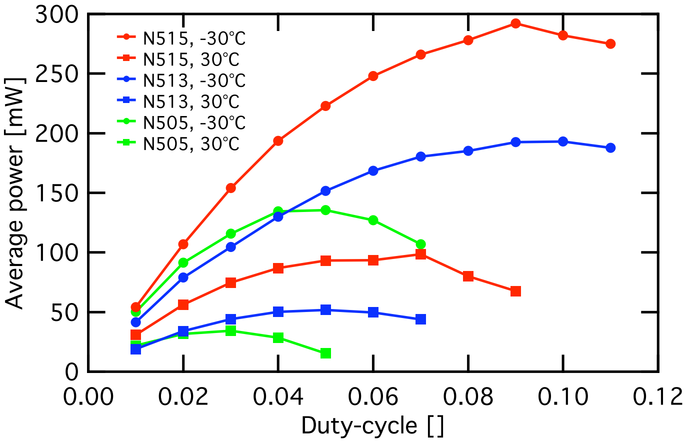

Figure 4.11: Average power vs. duty-cycle

Measurement of the average power as a function of duty-cycle at -30 (dots) and 30°C (squares) heat sink temperature. Three devices were measured: N505A9a (green, l=5 mm, w=24 µm), N513A1a (blue, l=5.3 mm, w=21 µm) and N515A1a (red, l=3.4 mm, w=20 µm). All of the devices were HR-coated on the back-facet. The continuous lines are guides to the eye.

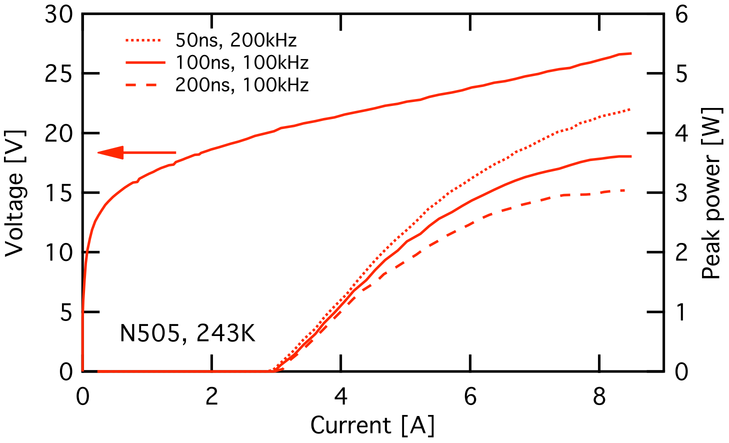

Figure 4.12: LI-measurement as a function of pulse parameters

Measured power-current-voltage characteristics of device N505 for various pulse settings at 243 K heat sink temperature. Reducing the pulse width from 100 ns (continuous line) to 50 ns (dotted line) while maintaining the same duty-cycle (1 %) increases the maximal peak power by 20 %. Leaving a pulse width of 100 ns and increasing the duty cycle to 2 % (dashed line) decreases the maximal peak power by 16 %.

were measured with different pulse parameters at 243 K. As the graph shows, reducing the pulse width from 100 ns to 50 ns, while maintaining the same duty-cycle (1 %) increases the maximal peak power by 20 %. Keeping the pulse width constant (100 ns) and increasing the duty cycle to 2 % decreases the maximal peak power by 16 %. This sensitivity to the pulse width is attributed to the bad thermal conductance of the waveguide core as the time constant is too short for the heat pulse to propagate further.

In case of structure N515 a structure was grown with identical active region but a standard waveguide with 25 active/injection region periods. However, no direct comparison is possible as the data published by Blaser *et al.*[163] is on distributed-feedback quantum cascade lasers. For a structure with similar doping they report a threshold current density of 1.38 kA cm^{-2} at -30 ℃ in continuous-wave operation and a T_0 of 155 K. For a structure with 2.5 times higher doping they measured a threshold current density of 1.7 kA cm^{-2} at -30 ℃ in pulsed operation which is similar to the threshold current density measured on devices of structure N505 that has similar doping.

4.3.3 Bi-stack waveguides

As the previous structures were severely limited by self-heating effects that prevented the devices from lasing in continuous-wave operation, a new structure with a bi-stack waveguide and InP top cladding layer was grown. Each gain stack contained 21 periods of the active/injection region. The idea was on one hand to improve the thermal conductance of the waveguide by re-

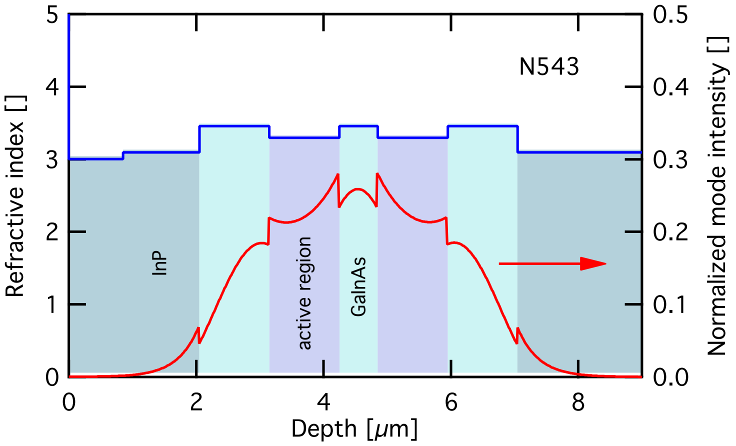

Figure 4.13: Refractive index and optical mode profile of structure N543
Refractive index profile of structure N543 with bi-stack waveguide (blue) and the profile of the calculated fundamental optical mode for emission at $\lambda = 5.2\,\mu$*m.*

placing the AlInAs top cladding by an InP cladding with 14 times higher thermal conductivity. On the other hand we wanted to reduce the total electrical power dissipated in the device under the penalty of lower peak powers. The same active region design was used as for structure N515 but the average doping was slightly increased ($n = 2 \times 10^{16}\text{cm}^{-3}$). Details of the waveguide design are listed in appendix D.3 and Fig. 4.13 shows the refractive index profile (blue) and the normalized intensity (red) of the calculated fundamental optical mode. Because these devices were targeted for continuous-wave operation, no throughout characterization was performed in pulsed operation at room temperature. Power-current-voltage characteristics of a device of structure N543 with a 3.44 mm long and 23 μm wide waveguide in pulsed operation at 1 % duty-cycle are shown in Fig. 4.14(a). A summary of the measured performances is shown in Tab. (4.5). Threshold current density and slope efficiency for pulsed and continuous-wave operation at 78 K are almost identical with values of 0.31 kA cm^{-2} and 3.1 W/A, respectively for threshold

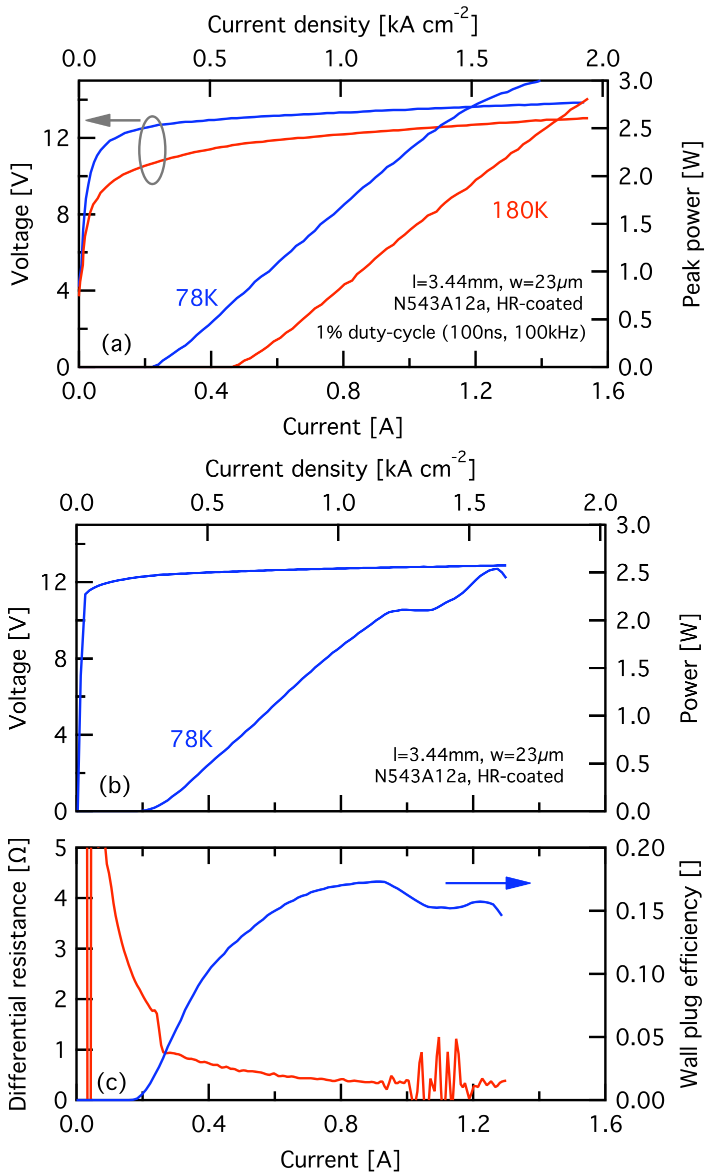

Figure 4.14: Power-current-voltage characteristics of device N543A12a

(a) Power-current-voltage characteristics of a 3.44 mm long and 23 μm wide device with HR-coating on the back-facet, measured at 1 % duty-cycle and 78 K (blue), respectively 180 K (red) heat sink temperature. (b) Continuous-wave power-current-voltage characteristics of the same device at 78 K heat sink temperature. (c) Plot of the differential resistance (red) and the wall plug efficiency (blue) determined from the data points shown in graph (b). Power was corrected assuming a 75 % collection efficiency.

Table 4.5: Power characteristics of device N543A12a-c

	pulsed (1 %) 78 K	pulsed (1 %) 180 K	cw 78 K
Max. (peak) power [W]	3.0	2.7	2.5
J_{th} [kA cm^{-2}]	0.31	0.63	0.31
dP/dI [W/A]	3.0	2.8	3.1

current density and slope efficiency. The value of the slope efficiency in pulsed operation is slightly lower (3.0 W/A) that we attribute to optical misalignment. This threshold current density is 10 % higher than what we measured with structure N515 and as expected peak power and slope efficiency are smaller. The threshold current doubles for pulsed operation at 180 K and the slope efficiency decreases to 2.8 W/A. Power-current-voltage characteristics in continuous-wave operation at 78 K heat sink temperature are shown in Fig. 4.14(b). At a current of 1.3 A a power of 2.5 W was emitted and, as the plot of the differential resistance (red) in Fig. 4.14(c) shows, the emission gets unstable when the power reaches 2 W. This instability is attributed to beam-steering, however no spectrum or far field measurements were performed in this condition. As shown with the blue curve in Fig. 4.14(c) a maximal wall plug efficiency in continuous wave operation of 16 % was measured. The same device was measured in continuous-wave operation on a wider temperature range before the highly-reflective coating was applied. At 78 K a threshold current density of 0.67 kA cm^{-2} and a peak power of 0.9 W was measured. These values increased to 1.17 kA cm^{-2} and 0.37 W at 140 K and at 180 K with a threshold current density of 2.1 kA cm^{-2} the emission with approximately 1 mW of power was barely visible.

4.3.4 Quad-stack waveguides

As we have shown in the previous section the structures with multi-stack waveguides were strongly limited by self-heating effects at room temperature. Even structure N515 with the smallest operating current reached only 100 mW average power at room temperature at a maximum duty-cycle of 4 %. In order to get devices that operate at higher duty-cycles with higher average powers (or even operate in continuous wave) these self-heating effects need to be reduced. This can be achieved on one hand by increasing the thermal conductance of the device that results in a lower active region temperature for the same amount of dissipated electrical power. Thermal conductance of the waveguide core can be increased by replacing the $Ga_{0.47}In_{0.53}As$ in the buffer layers by InP. Lateral and top heat extraction can be improved by more sophisticated processing and mounting (*e.g.* buried-heterostructure process and junction-down mounting). On the other hand several possibilities exist to reduce the overall operation and the threshold current of the device resulting in less dissipated electrical power that scales with the square of the current. The beneficial effects of reducing the operating and threshold current in the device are clearly visible by comparing the performances of structures N515 and N505 discussed above. Reducing the structures maximal current is achieved by reducing the doping of the active region.[162] This also results in a lower threshold current due to reduced free-carrier absorption. A small threshold current of the device is important because the power dissipated at threshold results in an offset of the active region temperature.[5]

---

[5] The active regions of two lasers with equal $J_{\max}$ but different threshold currents will reach different temperatures.

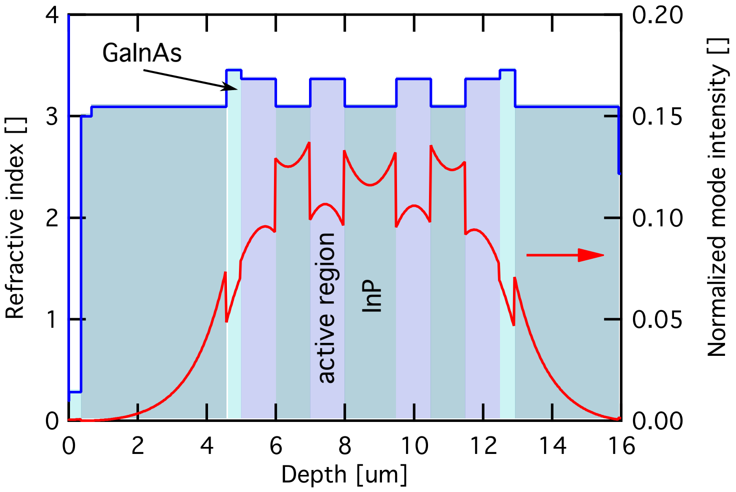

Figure 4.15: Refractive index and optical mode profile of structure D121
Refractive index profile of structure D121 (blue) and the profile of the calculated fundamental optical mode for emission at $\lambda = 10.5\,\mu m$.

The latter can be decreased further by reducing the waveguide losses, for example by reducing scattering losses at the ridge sidewalls and the absorption of the insulating layer. A standard practise to decrease the threshold current density is to decrease the mirror loss by depositing a highly reflective coating on one facet. Another important factor is, of course, the choice of a design with high injection efficiency and low thermal backfilling as it is discussed in chapter 2, section 2.4.

A new waveguide was designed in order to address several of these issues. The GaInAs inter-layers were replaced by InP inter-layers as its thermal conductivity is about 14 times better than for GaInAs[6] and the number of active region stacks was increased to four. The structure was grown by metal-organic vapor-phase epitaxy at AL Technologies GmbH in Darmstadt, Germany. The waveguide design of structure D121 is shown in appendix D.7

---

[6] `http://www.ioffe.rssi.ru/SVA/NSM/Semicond/`

and profiles of the refractive index and the calculated fundamental optical mode are shown in Fig. 4.15. Because we estimated the growth of the 16 μm thick structure to be already difficult, a design was chosen that could be grown with lattice-matched $Ga_{0.47}In_{0.53}As$ and $Al_{0.48}In_{0.52}As$ material and that was already grown by AL Technologies. The design is a bound-to-continuum design emitting at λ =10.5 μm and for the details we refer to appendix C.2. To reduce the free carrier absorption in the waveguide core a low average doping was used inside the active region ($n = 1.3 \times 10^{16} \mathrm{cm}^{-3}$) as well as the InP inter-layers ($n = 2 \times 10^{16} \mathrm{cm}^{-3}$). A non-negligible factor contributing to the waveguide losses of lasers emitting around λ =10.5 μm is the absorption in the dielectric layer that insulates the waveguide ride from the top contact because the materials that are typically used ($\mathrm{Si_x\,N_y}$, $\mathrm{Si\,O_x}$) are strongly absorbing in this wavelength region. Another contribution comes from sidewall roughness, although it is less critical at long wavelength.[159] Both of these issues were addressed by selectively wet etching an air gap laterally into the active region. Reducing the effective refractive index of the material at the sidewalls the optical mode is pushed inside the waveguide core and reduces its overlap with the lossy insulating layer. A cross section image of such a waveguide, acquired by a scanning-electron microscope, is shown in Fig. 4.16. Optical simulations with a commercial finite-difference time-domain software package[7] show that for $20-50\,\mu$m wide waveguides optical losses drop sensibly for air gaps up to $2.5-3\,\mu$m deep and reaching successively a plateau. Therefore, further lateral etching would not reduce considerably optical losses while compromising the mechanical stability of

---

[7] FullWAVE by RSoft, Inc.: `http://www.rsoftinc.com/`

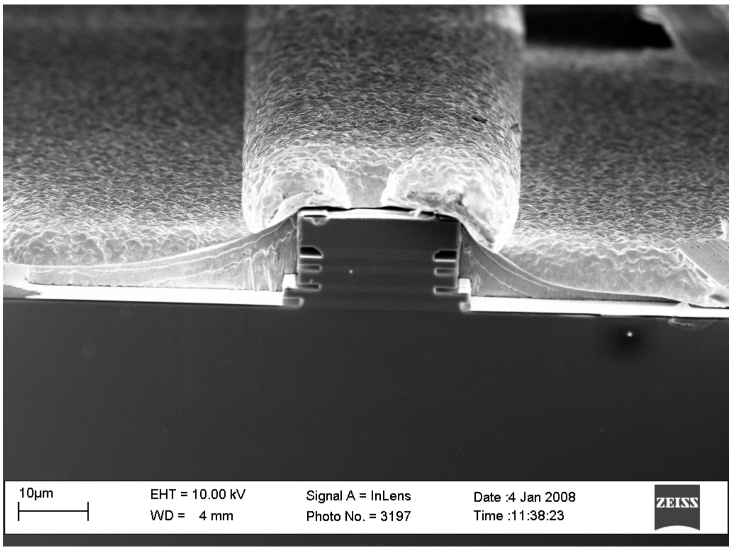

Figure 4.16: Scanning electron micrograph of the waveguide cross section
Scanning electron micrograph of the cleaved facet of a ridge waveguide of structure D121. The four separated active region stacks can be distinguished form the InP material as the lighter layers. (Image by courtesy of Alfredo Bismuto)

the structure. Waveguide losses are expected to be approximately $2.7\,\mathrm{cm}^{-1}$ for an air gap of $2.5\,\mu$m. Without air gap additional losses up to $1\,\mathrm{cm}^{-1}$ have been estimated. The effect is more pronounced in case of narrower waveguide ridges ($12\,\mu$m) where the optical mode has more intensity at the sidewall and therefore additional losses up to $4\,\mathrm{cm}^{-1}$ are expected. This calculation does not take into account the additional losses coming from sidewall roughness, also supposed to be reduced by the lateral etching process step. For an air gap up to $5\,\mu$m, a maximal $0.5\,\%$ reduction is expected for the overlap of the optical mode with the active region.

The structure was processed into $34-54\,\mu$m wide ridges as described in section 3.4.1 of chapter 3. Due to the considerable thickness of the epilayer, a combined dry/wet etching technique has been used to preserve etching uniformity and minimize sidewall roughness and undercut. Ridges have been etched first by inductively-coupled plasma reactive-ion etching using a $CH_4/Cl_2/Ar/H_2$ chemistry. Active regions were then laterally etched using a wet etchant that is selective to InP ($H_2SO_2/H_2O_2/H_2O$) in order to form a 2.5 μm deep air gap. A 400 nm thick $Si_x N_y$ layer was deposited by plasma enhanced chemical vapor deposition to isolate the waveguide ridge from the top contact. Due to the intrinsic non-directionality of this technique it is not possible to completely prevent the $Si_x N_y$ from entering into the air gap. Inspection with a scanning electron microscope shows that the deposited layer at the sidewall inside the air gap has a thickness of approximately 100 nm. In computing the waveguide losses, the presence of this thin, lossy layer has been taken into account. After the selective etching step only O_2 plasma ashing was used as an additional precaution in order to avoid contamination inside the air gap region. Inspection with a scanning electron microscope showed that these regions were clean from residuals. Thermal simulations predict that an important increase in the thermal conductance of the structure is obtained for gold layer thicknesses up to 7 μm and a subsequent saturation. Therefore a 8 μm thick layer of gold was deposited on the top contact by electro-plating. Samples have been cleaved along crystallographic planes and mounted junction-up on copper blocks using indium solder. Finally, devices were coated on the back facet with a highly reflective (Al_2O_3/Ti/Au) coating and measured in a setup as described in section 3.4.2 of chapter 3.

Fig. 4.17 shows the power-current-voltage characteristics of a device of structure D121 measured at 1 % duty-cycle (100 kHz, 100 ns pulse width) and heat sink temperatures between -30 and 27 ℃. The device has a 5.4 mm long cavity and 49 μm wide active regions and the back facet was coated with a highly reflective Al_2O_3:Au:Al_2O_3 (300/100/100) coating. Peak powers of 7.8 and 4.7 W and slope efficiencies of 1.7 and 1.3 W/A were measured at -30 and 27 ℃, respectively. The threshold current density is 1.2 kA cm^{-2} at 243 K and increases to 1.6 kA cm^{-2} at 300 K. Its dependence on temperature follows an exponential function $J_{\mathrm{th}} = J_0 \exp(T/T_0)$ with T_0=180 K and J_0=0.3 kA cm^{-2}. Slope efficiencies up to 1.6 W/A, threshold current densities between 1.6 and 1.7 kA cm^{-2} and peak powers ranging between 1.5 and 4 W were measured at 300 K with 3 mm long and narrower devices ($w = 30 - 40\,\mu$m). Total waveguide losses of our structures were determined from the threshold current density of a first uncoated and then coated device. Assuming a facet power reflectivity of $R = 0.27$ our devices show waveguide losses α_{w} ranging from 6 to 7.5 cm^{-1} whereas simulations yield a value of 2.7 cm^{-1}. The difference between measured and simulated waveguide losses is attributed to a strong parasitic absorption that was identified in the injection region and that was not taken into account in the simulations. Maximal wall plug efficiency in pulsed mode operation at 300 K ranges between 4 and 4.3 %.

In Fig. 4.18 the average power emitted from the same device as in Fig. 4.17 is shown as a function of duty-cycle at various temperatures. At 258 K a maximal average power of 580 mW is measured at a duty-cycle of 17 %. At 273 K heat sink temperature this value decreases to 470 mW and at 300 K still 310 mW are measured at a duty-cycle of 12 %. As a comparison, with structure N515 a maximal average power of 100 mW at 303 K heat sink temperature was measured at a duty-cycle of 4 %. Thus, the duty-cycle at average power roll-over as well as the average power was increased by a factor or three

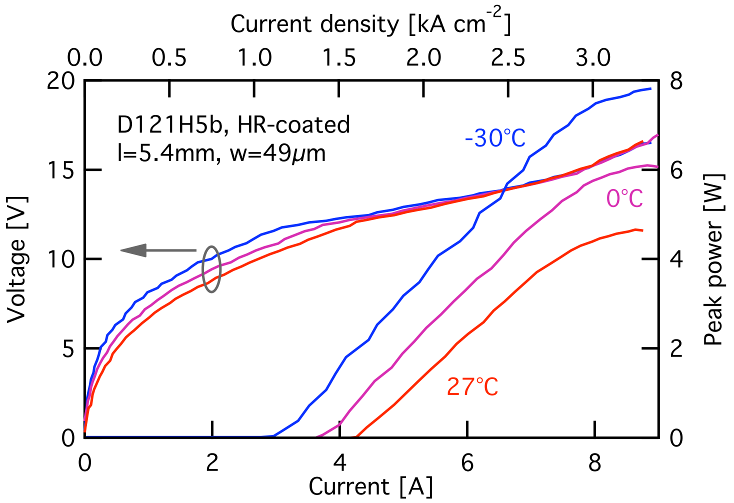

Figure 4.17: Power-current-voltage characteristics

Power-current-voltage characteristics of a device of structure D121 measured at 1 % duty-cycle (100 kHz, 100 ns pulse width) and heat sink temperatures between -30 and 27°C. The device has a 5.4 mm long cavity and 49 μm wide active regions and a HR-coating on the back facet. (Image by courtesy of Alfred Bismuto)

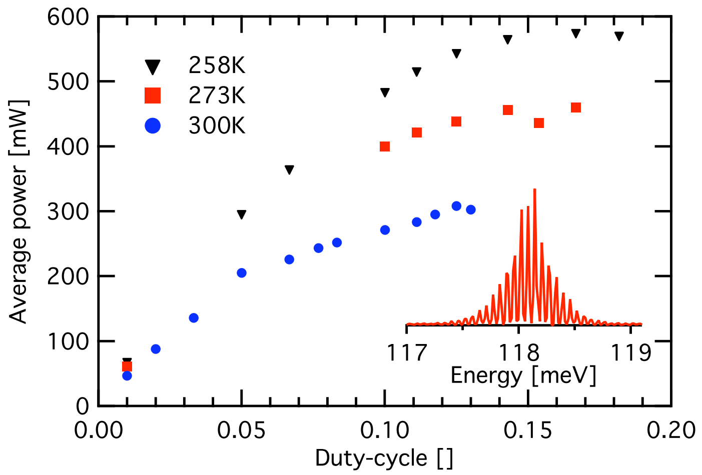

Figure 4.18: Average power as a function of duty-cycle

Average power of the device shown in Fig. 4.17 as a function of duty-cycle. The inset shows a Fabry-Pérot emission spectrum acquired slightly above threshold at 300 K heat sink temperature. The emission is centered at 118 meV ($\lambda \approx 10.5\,\mu m$)*. (Image by courtesy of Alfred Bismuto)*

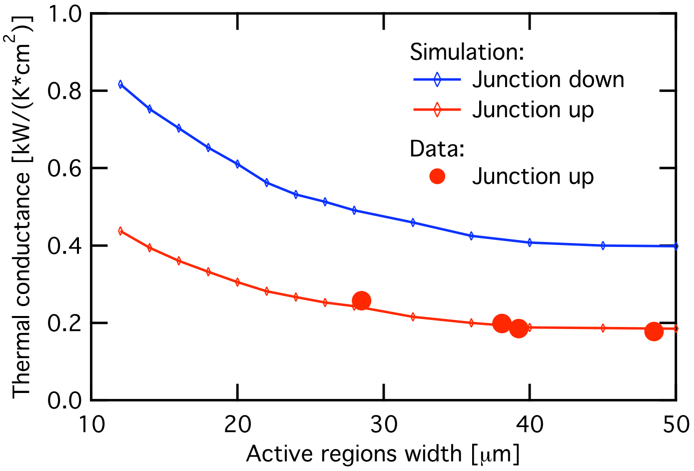

Figure 4.19: Simulated and measured thermal conductances

Simulated (continuous lines) and measured (dots) thermal conductances of structure D121 as a function of active region width. Simulation was performed on junction-down (blue) as well as junction-up (red) mounted devices. (Image by courtesy of Alfred Bismuto)

despite the larger waveguide ridges and the higher-than-expected waveguide losses caused by resonant absorption inside the active region. This increase of performance is attributed mainly to the improved thermal conductance of the structure as well as the improved waveguide design. Fig. 4.19 shows a comparison between measured (red dots) and simulated (red line) thermal conductance of the structure as a function of active region width. The thermal conductance of our devices was determined measuring the threshold current as a function of temperature and then using this dependence to determine the active region temperature as a function of duty-cycle. Specific thermal conductances of $200 - 260\,\mathrm{W\,K^{-1}\,cm^{-2}}$ were estimated for devices with active region widths between 29 and 49 μm and as the graph shows this agrees well with the simulated values. As a comparison the thermal conductances were also calculated for the case where the sample is mounted junction-down on a diamond heat spreader. The values are shown in Fig. 4.19 as the blue line. In this case simulations predict thermal conductances of approximately $850\,\mathrm{W\,K^{-1}\,cm^{-2}}$ for a device with a narrow ($\approx 12\,\mu$m) active region and $400-600\,\mathrm{W\,K^{-1}\,cm^{-2}}$ for $20-50\,\mu$m wide active regions. Therefore, we would expect considerably higher average powers with devices that are mounted junction-down. However, due to the relatively high ridges the devices are not suitable for this procedure.

In Fig. 4.20(a) the measured two-dimensional farfield pattern of a 3 mm long device of structure D121 with a $40\,\mu$m wide cavity is shown. Fitting Gaussian curves to the horizontal and vertical cuts through the center of the farfield yields full-widths at half-maximum of 18.7 and 39.8 ° in the lateral and growth direction, respectively. The cuts are represented in Fig. 4.20(b) as the dotted lines. Comparison with the results of a two-dimensional optical simulation (dashed lines) that yields values of 17.8 and 39 °, respectively shows a good agreement. A good agreement with simulations is obtained also in the case of $30\,\mu$m wide active regions where measured full-widths at half-maximum are 24 and 39.8 ° and simulated ones are 22.4 and 39 °. These values are much smaller than the values reported for traditional waveguides at similar wavelength where a beam divergence with a full-width at half-maximum of 43 ° was measured in the lateral and 67 ° in the growth direction.[82] Measurement of the farfield emission pattern as a function of increasing current revealed no change and thus, no beam-steering effect was observed.[193]

A structure with the same active region and identical doping and standard waveguide consisting in 35 active/injection region periods was also grown at

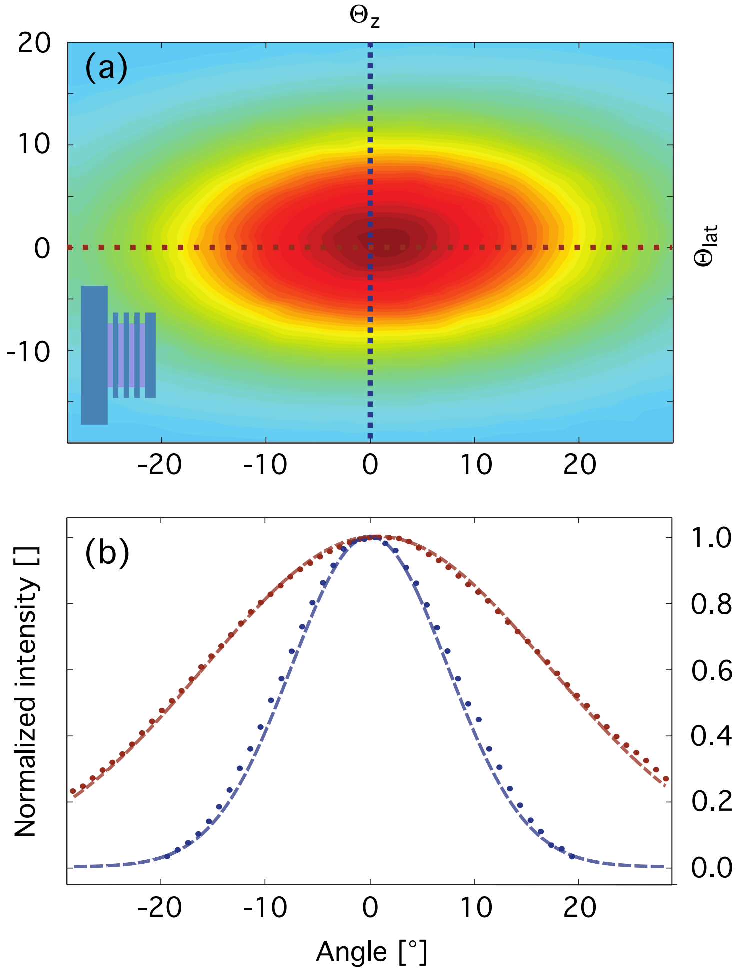

Figure 4.20: 2D farfield measurement

(a) Measured farfield pattern of a 3 mm long device of structure D121 with 40 µm wide active regions. Gaussian fits in the lateral and growth direction yield full-widths at half-maximum of 18.7°, respectively 39.8°. (b) Comparison between measured (dots) and simulated farfield pattern (dashed lines) in the growth (red) and lateral (blue) directions. (Image by courtesy of Alfredo Bismuto)

AL Technologies GmbH in Darmstadt and processed by Andreas Wittmann to Fabry-Pérot lasers with buried-heterostructure waveguide. Devices with active region widths between 5 and 14 μm and mounted junction-down operated in continuous wave up to 295 K. Despite the advanced device processing threshold current densities measured at 2 % duty-cycle were relatively high with 3.2 kA cm^{-2} at 243 K and 4.3 kA cm^{-2} at 300 K. We attribute this to the high resonant losses of the active region design. Consequently the measured slope efficiency of 360 mW/A and peak power of 300 mW at 243 K, respectively 320 mW/A and 150 mW at 300 K are smaller than values reported by other groups for lasers with similar process and wavelength. Slivken *et al.*[82] reported on a device with 50 active/injection region periods, emitting at $\lambda =$10.6 μm and that achieved continuous-wave operation up to 85 ℃. With a 3 mm long laser with a highly-reflective coating on the back facet they measured a threshold current density of only 0.73 kA cm^{-2} at room temperature that they attributed to the low waveguide losses they measured (1.2 cm^{-1}). Thus, comparing the performances of structure D121 with the ones obtained with a standard waveguide, threshold current density, slope efficiency and peak powers could be considerably improved with the quad-stack waveguide. Furthermore, looking at the performances reported by Slivken *et al.*[82], we also believe that a careful optimization of our active region design in order to reduce the resonant absorption, would lead to even better performances.

Chapter 5

Strain-compensated active regions

5.1 Introduction

With the advancement of the epitaxial growth techniques in the seventies people realized that thin epitaxial layers did not have to be of the same lattice periodicity as the substrates. Therefore, a much larger range of optical and electronic materials was suddenly available for epitaxial growth. It was also found out that by adding strain to these layers through a lattice mismatch, the resulting band structure of the material could be changed considerably. This valence-band engineering led to the development of strained quantum well lasers where the threshold current and overall properties of quantum well lasers could be considerably improved by adding bi-axial compressive strain to the material, thus reducing intersubband mixing of the valence bands and improving band parabolicity.[194] Adding strain to the layers not only changes the properties of the valence band but also the ones of the conduction band and that proved to be very useful for the development of short wavelength quantum cascade lasers while staying in the AlInAs/GaInAs/InP material system. Although other material systems are envisageable to develop such lasers the material growth and technology is very demanding and therefore the best performances in the mid-infrared region between 3.5 and 12 μm are still obtained with quantum cascade lasers based on GaInAs/AlInAs grown on InP substrates.

A fundamental limit to obtain the shortest wavelength with a quantum cascade laser in a given material system is the width of the conduction band discontinuity ΔE_{c} that arises at the interface between the barrier and well materials grown next to each other. This conduction band discontinuity for $\mathrm{Ga_{0.47}In_{0.53}As/Al_{0.48}In_{0.52}As}$ lattice-matched on the InP substrate is approximately 0.52 eV and experience has shown that with this ΔE_{c} quantum cascade lasers with acceptable performances can be realized down to a wavelength of $\lambda \approx 5.5\,\mu$m (227 meV). If shorter wavelengths need to be obtained with the same material system the conduction band discontinuity can be artificially increased by adding strain to the layers. The change of the band alignment due to added bi-axial strain in the plane is well described with the model solid theory that will be treated shortly in section 5.2 below. Because in quantum cascade lasers the total thickness of grown epilayers is very thick, the strain needs to be carefully balanced in order not to surpass the critical thickness of the pseudomorph growth or otherwise the structure will relax. The first strain compensated quantum cascade laser was developed at AT&T Bell Labs and published by Faist *et al.* in 1998.[65] These devices held the short-wavelength record for quantum cascade lasers for eight years until operating devices in more suitable material systems for short wavelength could be demonstrated.[108]

5.2 GaInAs/AlInAs grown on InP

The most used and advanced material system for mid-infrared quantum cascade lasers is clearly $\mathrm{Ga}_x\mathrm{In}_{1-x}\mathrm{As}$ wells and $\mathrm{Al}_y\mathrm{In}_{1-y}\mathrm{As}$ barriers grown on InP substrates. Fig. 5.1 shows the band diagram of $\mathrm{Ga}_{0.47}\mathrm{In}_{0.53}\mathrm{As}$ for illustrative purposes. In the rest of this chapter we will limit ourselves to the energy maximum of the valence bands at the Γ-point and the energy minima of the conduction band at Γ, X and L-points and they will be represented in illustrations as straight lines.

As we have seen before a fundamental parameter for the design of quantum cascade lasers is the conduction band discontinuity between the chosen barrier and well material. However, this parameter is difficult to measure and experimental values exist only for a limited number of material systems. The model-solid theory developed by Van de Walle *et al.*[195] provides a useful tool to determine band offsets at the interface of heterojunctions and predicts accurately the effect on the band structures when introducing strain.

For a detailed description of this theory we refer to the publication by Van de Walle *et al.*[195] and to the references therein. In model-solid theory *ab initio* pseudo potentials are used to describe individual bulk semiconductors. Density-function calculations are then performed in order to calculate an accurate band structure of the semiconductor. These calculations predict

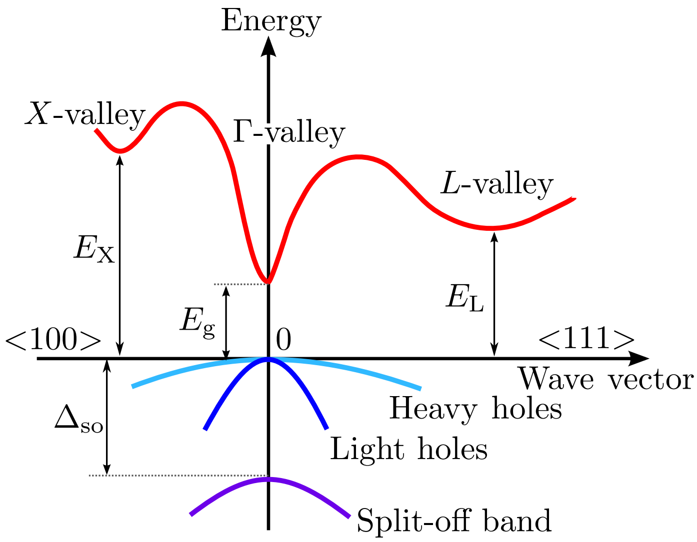

Figure 5.1: $Ga_{0.47}In_{0.53}As$ band structure

Important minima of the conduction band and maxima of the valence band of $Ga_{0.47}In_{0.53}As$*. Reproduced from an image of Ref. [196]*

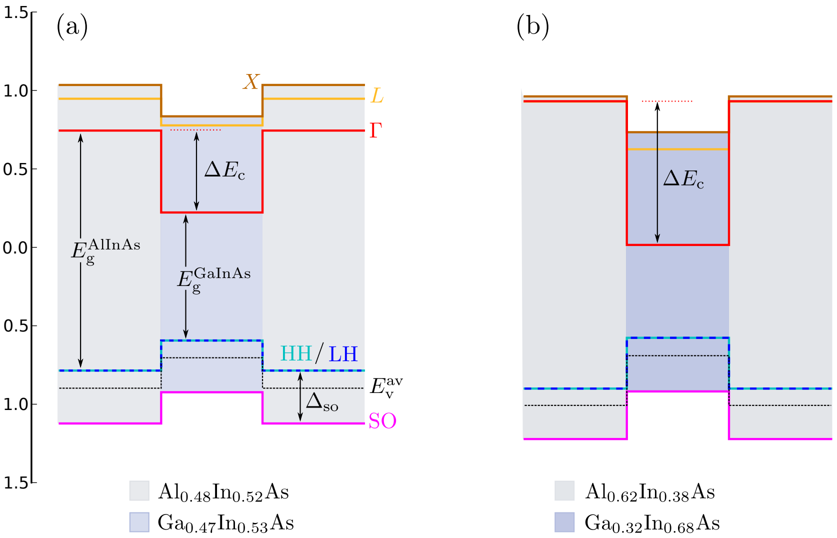

Figure 5.2: GaInAs/AlInAs heterostructures

(a) Type I heterostructure between $Al_{0.48}In_{0.52}As$ *and* $Ga_{0.47}In_{0.53}As$*. (b) Heterostructure between* $Ga_{0.32}In_{0.68}As/Al_{0.62}In_{0.38}As$*. Band gap energies and other parameters are calculated from parameters listed in Ref. [100] assuming* $T = 0\,K$ *and no strain-induced shifts are taken into account.*

accurately the changes in the band structure induced by hydrostatic or shear strain but also have some deficiencies like being unable to predict the correct band gap. Another feature of this theory is that it allows to align the calculated band structures of the individual semiconductors on an absolute energy scale and thus allows to determine band offsets between two semiconductors simply by subtracting the individual lineups. The type I heterojunction between $Ga_{0.47}In_{0.53}As$ and $Al_{0.48}In_{0.52}As$ that can be grown lattice-matched on InP is shown in Fig. 5.2(a). Practically, an average valence band is introduced because it is a suitable reference to describe the splitting of the valence bands due to spin-orbit interaction and optionally shear strain. The energy levels are defined with respect to the valence band edge of InSb as tabulated by Vurgaftman.[100] The spin-orbit split-off band lies Δ_{so} below the degenerate heavy and light holes bands and the average valence band is $\Delta_{\mathrm{so}}/3$ below the valence band edge. The position of the Γ, L and X-valley minima is obtained by adding the corresponding band gap energies to the valence band edge. For the conduction band offset at Γ-point a value of ΔE_{c}=0.52 meV is obtained and the minimum of the indirect L-valley lies slightly above the minimum at the Γ-point of $Al_{0.48}In_{0.52}As$. Changing the composition of these alloy semiconductors first of all changes the properties of the band structure. We use the parameters by Vurgaftman *et al.*[100] to determine these parameters and bowing parameters are used where available. Fig. 5.2(b) shows the heterostructures when the compositions are changed to $Ga_{0.32}In_{0.68}As/Al_{0.62}In_{0.38}As$ neglecting band shifting induced by strain. As can be seen in the figure the conduction band at Γ-point considerably shifts upwards and the conduction band discontinuity increases to ΔE_{c}=0.91 meV.

However, because changing the alloy composition also changes the lattice constant of the material and the latter is grown on an InP substrate with a lattice constant of a_{lc}=5.86 Å at T=0 K, strain is induced in the material resulting in further shifts of the energy levels. These shifts are accurately described by the model-solid theory in the form of deformation potentials. For simplicity we only treat here the case where the interface is oriented in the <001> direction. A more generic description can be found in the article by Van de Walle.[195] If two semiconductor materials with their respective thicknesses h_1 and h_2 are grown on a surface with <001> orientation the respective lattice constants and strain parallel and perpendicular to this surface are given by:

$$\begin{aligned} a_{||} &= \frac{a_1 G_1 h_1 + a_2 G_2 h_2}{G_1 h_1 + G_2 h_2} && (5.1) \\ \epsilon_{i,||} &= \frac{a_{||}}{a_i} - 1 && (5.2) \\ a_{i,\perp} &= a_i \left[1 - D_i^{001} \epsilon_{i,||}\right] && (5.3) \\ \epsilon_{i,\perp} &= \frac{a_{i,\perp}}{a_i} - 1 && (5.4) \end{aligned}$$

where i denotes the respective material with lattice constant a_i and G_i its shear modulus that is given by:

$$G_i = 2(c_{1,ii} + 2c_{i,12}) \left(1 - \frac{D_i^{001}}{2}\right) \qquad (5.5)$$

where $c_{i,11}$ and $c_{i,12}$ are elastic constants for the individual semiconductors and D_i^{001} is the reciprocal value of the Poisson ratio and is given for <001>

interface orientation by:

$$D_i^{001} \quad = \quad 2\,\frac{c_{i,12}}{c_{i,11}} \tag{5.6}$$

It has to be noted that the lattice constant of a ternary alloy $\mathrm{A}_{(1-x)}\mathrm{B}_x\mathrm{C}$ is obtained by linear interpolation between the two constituting binary semiconductors. However, shear modulus G and reciprocal value D of the Poisson-ratio cannot be interpolated directly. Instead, elastic stiffness constants $c_{\{11,12,44\}}$ need to be interpolated taking into account weighting by the lattice constant:[197]

$$c_{\{11,12,44\}}^{\mathrm{A}_{(1-x)}\mathrm{B}_x\mathrm{C}} \quad = \quad \frac{(1-x)\cdot a_{\mathrm{lc}}^{\mathrm{AC}}\cdot c_{\{11,12,44\}}^{\mathrm{AC}} \;+\; x\cdot a_{\mathrm{lc}}^{\mathrm{BC}}\cdot c_{\{11,12,44\}}^{\mathrm{BC}}}{a_{\mathrm{lc}}^{\mathrm{A}_{(1-x)}\mathrm{B}_x\mathrm{C}}} \tag{5.7}$$

Shear modulus and reciprocal value of the Poisson ratio are then calculated according to Equations (5.5) and (5.6). Pseudomorph layers can be grown up to a characteristic thickness where plastic relaxation will occur due to excessive strain in the layer.[198] The mechanics in strained semiconductor layers have been studied extensively and we refer to the publications by Matthews and Freund for a detailed treatment of the subject.[198, 199, 200, 201] In quantum cascade lasers based on strained materials the material compositions are chosen in a way such that the overall strain of the active region with respect to the substrate is close to zero.[65] For a two-material active region this is achieved by choosing material compositions that yield a lattice constant a_{p} as given by Equ. (5.1) equal to the one of the substrate material.[1]

The effect of the strain on the alignment of the valence bands is twofold.

---

[1] For thin films the shear modulus is set to 1.

The hydrostatic strain component results in a common shift of the valence bands that is described by a hydrostatic deformation potential a_{v} and is given for the average valence band by:[195]

$$\Delta E_{\mathrm{v}}^{\mathrm{av}} \quad = \quad a_{\mathrm{v}} \times \frac{\Delta\Omega}{\Omega} \tag{5.8}$$

Where $\Delta\Omega/\Omega$ is the fractional volume change due to hydrostatic strain and is given by the trace of the strain tensor:

$$\frac{\Delta\Omega}{\Omega} \;=\; \mathrm{Tr}(\overleftrightarrow{\epsilon}) \;=\; (\epsilon_{\mathrm{xx}} + \epsilon_{\mathrm{yy}} + \epsilon_{\mathrm{zz}}) \;=\; (2\epsilon_{||} - \epsilon_{\perp}) \tag{5.9}$$

For the hydrostatic potential a_{v} of the average valence band different sign conventions are used in literature. Generally, the band gap (that is the parameter that is measured experimentally) increases for compressive strain with the conduction band edge moving upward in energy and the valence band downward, as it is shown schematically in Fig. 5.3. Under positive hydrostatic pressure, i.e. negative strain, the change in the band gap energy E_{g} must be positive, and thus the hydrostatic potential a negative. We use the same sign convention here as Van de Walle *et al.*[195] where a_{v} typically has a positive value and the hydrostatic potential of the band gap energy is calculated as $a = a_{\mathrm{c}} - a_{\mathrm{v}}$. Shear components of the strain lead to a further splitting of the valence bands and also the otherwise degenerate bands of heavy-hole and light-hole states are split. Formulas yielding the valence band positions in respect to the average valence band position are given in Ref. [195]. Positions of the conduction band are calculated by

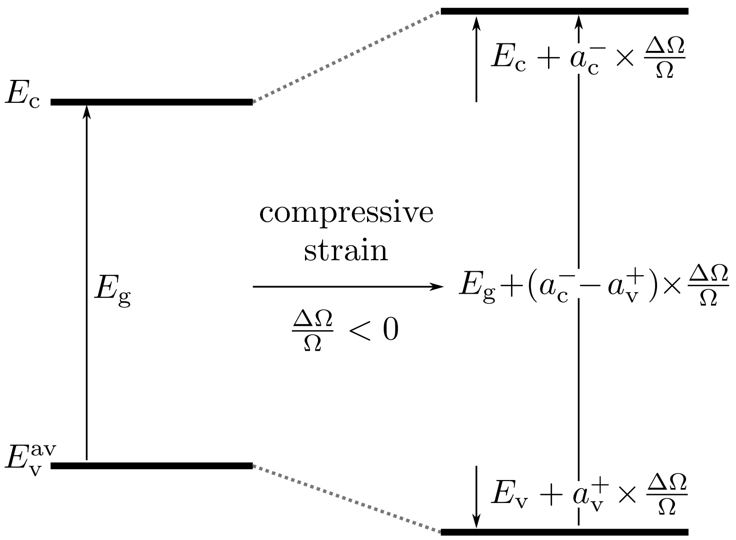

Figure 5.3: Shift of the band edges due to hydrostatic strain

Illustration of the energy shift of the band edges due to compressive strain. The shifts are defined by hydrostatic deformation potentials a_c *and* a_v*. We use the sign conventions where* a_c *typically has a negative* (a_c^-) *and* a_v *a positive* (a_v^+) *value.*

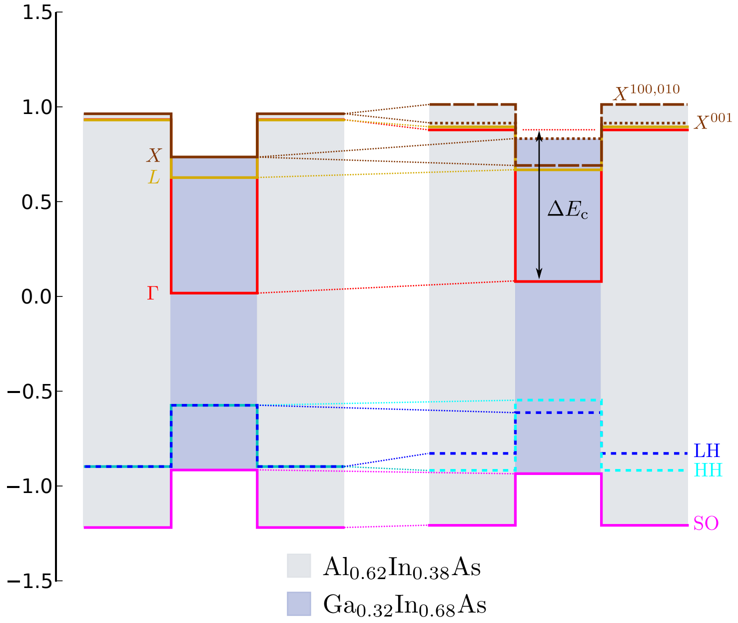

Figure 5.4: Band energies in strained $Ga_{0.32}In_{0.68}As/Al_{0.62}In_{0.38}As$

Heterojunction of $Ga_{0.32}In_{0.68}As/Al_{0.62}In_{0.38}As$ *showing the band energies when strain effects are neglected (left). On the right hand side shifting and splitting of the energy levels induced by strain is shown.*

adding the experimental values of the band gap energies to the valence band edge because the model-solid theory is unable to predict accurate values. An additional shift proportional to the band gap energy, the hydrostatic deformation potential for the respective valley and the fractional volume change is then added. For uni-axial strain along the (001) direction at the X-point the conduction bands along [100] and [010] are split off from the one along [001] and for values the shear deformation potentials we refer to Ref. [195] and [202]. An illustration showing how the strain changes the alignment of the bands in the case of $\mathrm{Ga_{0.32}In_{0.68}As/Al_{0.62}In_{0.38}As}$ is shown in Fig. 5.4 where on the left hand side a heterostructure is shown with band energies where effects of strain were neglected and on the right hand side taking into account strain. As can be seen in the figure the conduction band discontinuity at Γ-point is approximately 0.8 eV that is much larger than the 0.52 eV in the unstrained material but it also shows that in the well material the X and L-point energies lie inside the quantum well with the difference between the lowest indirect valley and the Γ-point conduction band energy being 0.59 eV. The conduction band discontinuity for AlInAs/GaInAs heterostructures for In concentrations between 0 and 1 and pseudomorphically grown on InP substrates is shown in Fig. 5.5(a) as contour plot. As it can be seen in the graph the conduction band discontinuity is much more sensitive to a variation of the In concentration in AlInAs than in GaInAs. The design of a quantum cascade laser structure should therefore be compensated by fixating the composition of $\mathrm{Al}_x\mathrm{In}_{1-x}\mathrm{As}$ and choosing a composition of $\mathrm{Ga}_x\mathrm{In}_{1-x}\mathrm{As}$ that compensates the strain and not vice versa. The compositions that yield materials lattice-matched to the InP substrate are indicated as black dashed lines and the resulting conduction band discontinuity is $\Delta E_\mathrm{c} \approx 0.52\,\mathrm{eV}$. The compositions used in Ref. [65] are indicated as dashed red lines and the resulting ΔE_c is $0.78\,\mathrm{eV}$. Faist *et al.* calculated a slightly smaller value of $\Delta E_\mathrm{c} \approx 0.74\,\mathrm{eV}$.[65] We attribute this to the usage of different data sets.

Fig. 5.5(b) shows the bulk material effective masses as a function of In concentration. Although people suggest that the electron effective mass becomes highly anisotropic in strained material and depends strongly on the latter,[197] we use the values for the bulk material as the precision of our measurements does not allow to rule-out either model.

5.3 Surface segregation

Surface segregation is a very important mechanism controlling the composition profiles in quantum cascade lasers based on indium-containing materials as volatile species tend to accumulate on the growth surface and influence considerably the heterointerfaces. Many attempts have been made, both experimentally[203, 204, 205, 206, 207] and theoretically[208, 209], to understand the mechanisms and general trends in surface segregation. Other studies investigated the influence of surface segregation on the electrical and optical properties of quantum wells.[210, 211, 212] However, a high sensitivity of surface segregation to the growth conditions like growth temperature, V/III-ratio, strain and many other factors make it difficult to determine surface segregation quantitatively.

A kinetic model for indium segregation was developed by Dehaese *et al.*[209] and it describes well the observed decreasing of indium segrega-

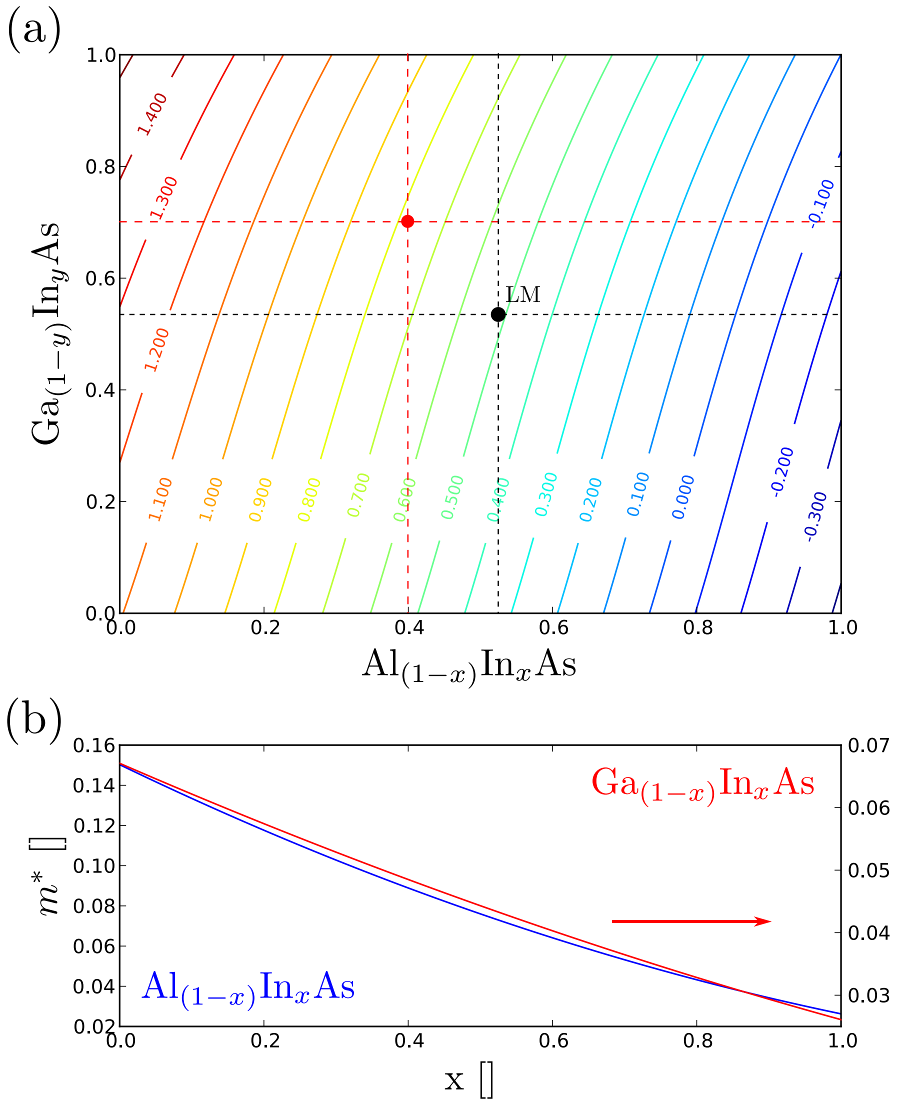

Figure 5.5: Conduction band discontinuity

(a) Contour plot of the conduction band discontinuity of the GaInAs/AlInAs material system for In concentrations between 0 and 1. Effects of strain are taken into account assuming that thin layers of material are grown on a InP substrate. The black dot represents the lattice-matched composition resulting in $\Delta E_\mathrm{c} \approx 0.52\,eV$ *and the red dot represents the materials used in the first strain-compensated quantum cascade laser. (b) Bulk-material effective mass at* Γ*-point.*

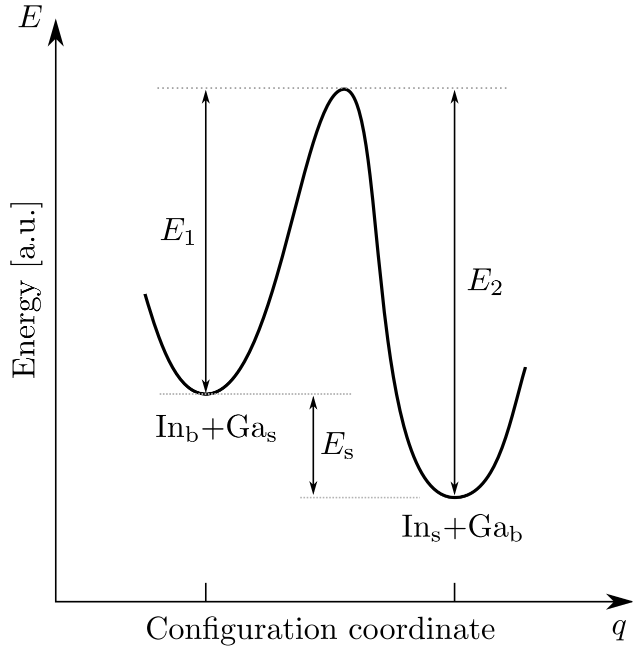

Figure 5.6: Configuration diagram for In/Ga exchange process
Configuration diagram for the kinetic segregation model showing the all free energy of the system as a function of configuration coordinate.

tion with growth temperature.[213] Segregation during epitaxy is regarded as near-surface processes between the surface and bulk phase. The surface phase is defined as the last (incomplete) mono-layer grown and the bulk phase as the previous one. In case of GaInAs exchange occurs between Ga and In atoms in these two monolayers and we denote $X_{\mathrm{s}}^{\{\mathrm{In,Ga}\}}$ and $X_{\mathrm{b}}^{\{\mathrm{In,Ga}\}}$ the concentration of In (Ga) in the surface and bulk phase, respectively. A configuration diagram for the exchange process between In and Ga is shown in Fig. 5.6 where the free energy E of the system as a function of the configuration coordinate q is plotted. The first energy minimum corresponds to the configuration where an In atom is in the bulk phase and a Ga atom in the surface phase. In order to exchange the two atoms an energy barrier E_1

needs to be passed and the exchange rate for this process is:

$$P_1 = \nu \ \exp\left(-\frac{E_1}{k_\mathrm{B}\,T}\right) \tag{5.10}$$

where ν is a vibration frequency, k_B is the Boltzmann constant and T is the substrate temperature. For the reverse process an energy barrier of height $E_2 = E_1 + E_\mathrm{s}$ needs to be passed and the rate is:

$$P_2 = \nu \ \exp\left(-\frac{E_2}{k_\mathrm{B}\,T}\right) \tag{5.11}$$

The energy difference between the two configurations corresponds to the phenomenological segregation energy E_s used in the McLean segregation law. Supposing that the exchange process is the only process involved in surface segregation the evolution of the number of In, respective Ga surface atoms can be written as:

$$\frac{dX_\mathrm{s}^\mathrm{In}(t)}{dt} = \Phi^\mathrm{In} + P_1 X_\mathrm{b}^\mathrm{In}(t) X_\mathrm{s}^\mathrm{Ga}(t) - P_2 X_\mathrm{s}^\mathrm{In}(t) X_\mathrm{b}^\mathrm{Ga}(t) \tag{5.12}$$

$$\frac{dX_\mathrm{s}^\mathrm{Ga}(t)}{dt} = \Phi^\mathrm{Ga} - P_1 X_\mathrm{b}^\mathrm{In}(t) X_\mathrm{s}^\mathrm{Ga}(t) + P_2 X_\mathrm{s}^\mathrm{In}(t) X_\mathrm{b}^\mathrm{Ga}(t) \tag{5.13}$$

where Φ^In and Φ^Ga are the fluxes of impinging In and Ga atoms. Adding the constraints that the number of surface atoms and the number of total atoms need to be conserved one can derive differential equations that can be solved numerically. In case of AlInAs/GaInAs hetero structures exchange processes between Ga and Al and In and Al are added. Tab. (5.2) shows the activation energies of the different processes that we use in our surface

Table 5.1: Activation energies for the different exchange processes between bulk and surface phase.

bulk	surface	E	bulk	surface	E
In	Ga	1.8[a] eV	Ga	In	2.0[a] eV
Ga	Al	1.7[b] eV	Al	Ga	1.8[b] eV
In	Al	1.7[c] eV	Al	In	1.8[c] eV

[a] Ref. [209]

[b] Ref. [214]

[c] Chosen to be equal to the values for the Al↔Ga exchange process

segregation calculation. A simulation of a composition profile taking into account surface segregation is shown in Fig. 5.7. The thicknesses of the layers are (50/**50**/50/**20**/10/**50**) where $\mathrm{Ga_{0.47}In_{0.53}As}$ layers are in roman and $\mathrm{Al_{0.48}In_{0.52}As}$ layers are bold and thicknesses are given in [Å]. For the activation energies of the different exchange processes between bulk and surface phase we used the values published by Dehaese *et al.*[209] and Spencer *et al.*[214] and a vibration frequency of $\nu = 10^{11}\,\mathrm{s}^{-1}$ was used and it was assumed to be equal for all exchange processes. The simulation predicts small positive and negative spikes for the In concentration at the hetero interface and a Ga-rich region at the beginning of the growth and an In-rich region at the surface. Because the material-constituting atoms have a finite size the interfaces between the two materials are not perfectly flat and surface segregation further smoothness it. This becomes even more evident in Fig. 5.7(b) where the corresponding conduction band profile is shown. The simulations predict that the quantum wells become asymmetric with barriers that have

Table 5.2: Electron eigenstate energies calculated with and without surface segregation effects in double quantum well structures.

	Design [meV]	Segregation [meV]	Δ [%]	Design [meV]	Segregation [meV]	Δ [%]
1	69.25	68.92	0.47	157.26	156.11	0.74
2	163.15	163.41	-0.16	229.88	228.8	0.47
3	242.97	242.14	0.34	479.61	472.59	1.46
4	431.15	425.14	1.39			
5	499.65	495.09	0.91			
	Large QWs			Narrow QWs		

a slightly sawtooth-shaped profile and that the quantum wells become narrower at the bottom. An example how surface segregation influences the electron eigenstate energies in a double quantum well sample is shown in Fig. 5.8. First a sample was chosen with layer thicknesses (**50**/80/**20**/40/**50**) where Ga$_{0.47}$In$_{0.53}$As layers are in roman and Al$_{0.48}$In$_{0.52}$As layers are bold and thicknesses are given in [Å]. Electron eigen states and wave functions have been calculated in the structure with and without surface segregation effects and the results are shown in Fig. 5.8(a) and (b), respectively. Results of another calculation with narrower quantum wells (**50**/40/**20**/30/**50**) are shown in Fig. 5.8(c) and (d). The values of the elecron eigenstate energies and the corresponding relative differences compared to a square potential are shown in Tab. (5.2). As can be seen in Fig. 5.8 effects of surface segregation on the electron eigenstates are the most important close to the bottom and the edge of the quantum wells. On can also notice the step-like profile of the segregated potential. This is due to the "discretization" that is inherent to this kinetic model as a certain thickness of the monolayer needs

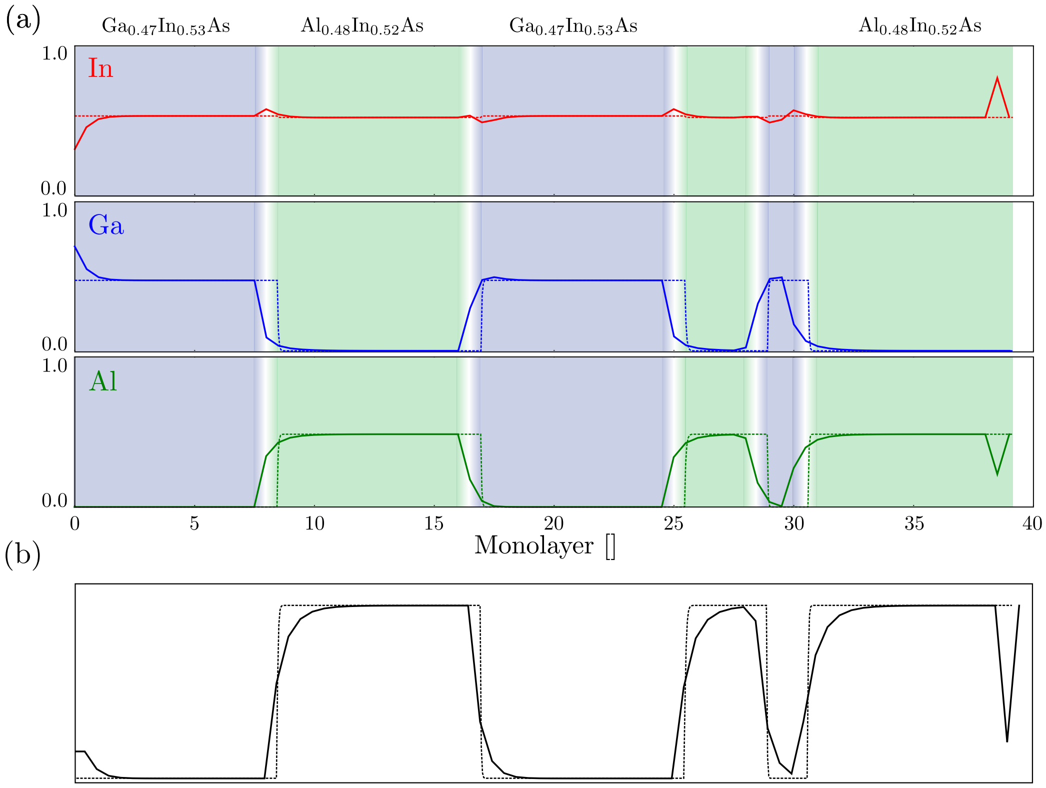

Figure 5.7: Surface segregation simulation

*(a) Concentration of In, Ga and Al as a function of structure thickness (in mono-layers). Dashed lines represent the designed composition profile (50/***50***/50/***20***/10/***50***) where* $Ga_{0.47}In_{0.53}As$ *layers are in roman and* $Al_{0.48}In_{0.52}As$ *layers are bold and thicknesses are given in [Å]. Continuous lines show the simulated composition profiles taking into account surface segregation. (b) Calculated corresponding profiles of the conduction band at* Γ*-point. The simulation was performed with a resolution of half a mono-layer and the resulting conduction band discontinuity is approximately 0.52 eV as expected.*

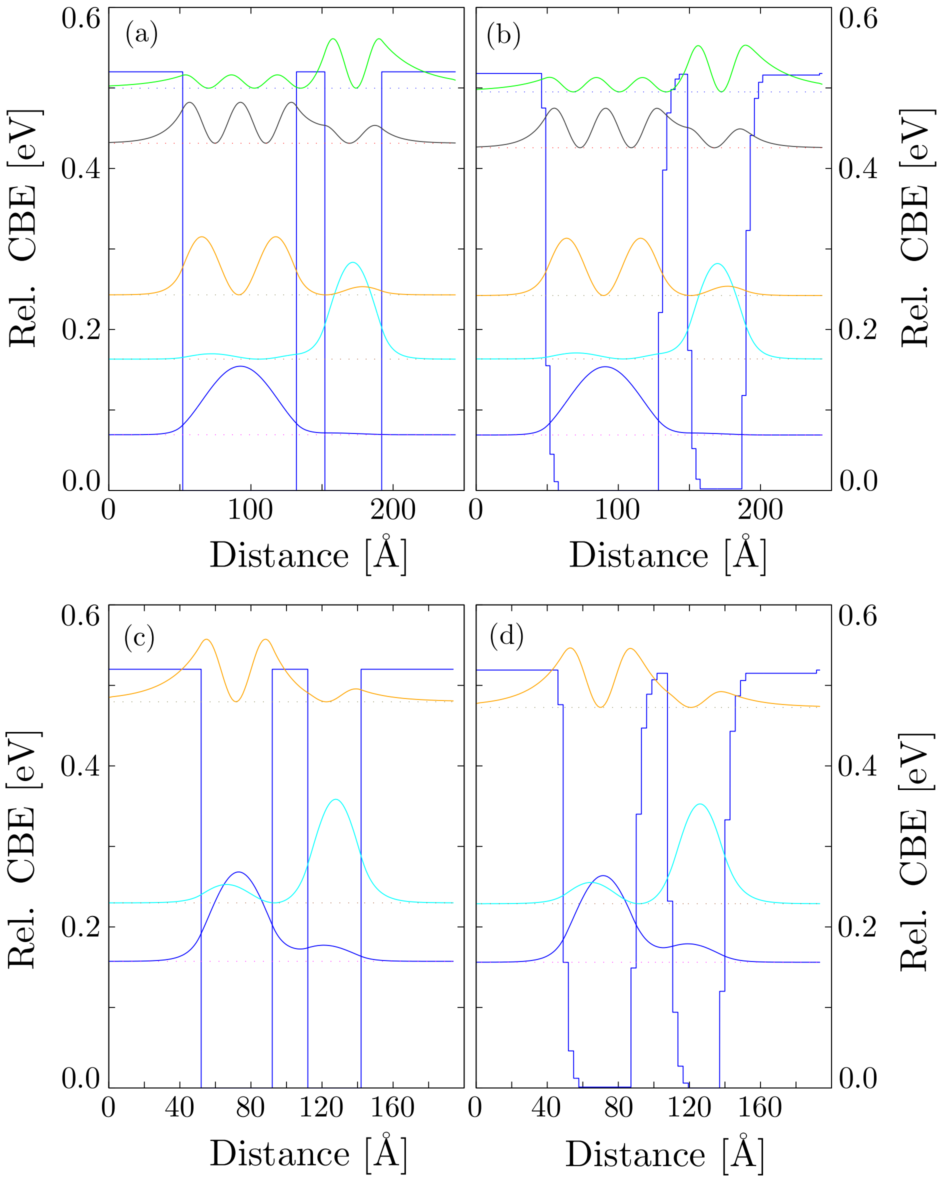

Figure 5.8: Surface segregation in double quantum well

Influence of surface segregation on the electron eigenstate energies in a double quantum well sample. A structure with large quantum wells (**50**/*80*/**20**/*40*/**50**) *with and without surface segregation is shown in graphs (b) and (a), respectively. A structure with narrower quantum wells is shown in graphs (c) and (d). Moduli squared of the electron wave functions are shown as continuous lines and the corresponding eigenstate energies as dotted lines.*

to be assumed. In this case we chose a monolayer thickness of 2.9 Å. Keeping the same simulation parameters and test structure but changing to strained $Al_{0.595}In_{0.405}As/Ga_{0.294}In_{0.706}As$ material as it is shown in Fig. 5.9 does not drastically change surface segregation effects if one neglects direct effects of the strain on the exchange processes. However, smoothing effects at the interfaces get more pronounced in short wavelength quantum cascade lasers as barriers and wells are narrower.

There are several ways how the effect of surface segregation can be limited. As it was mentioned before segregation decreases with decreasing substrate temperature. However, decreasing substrate temperature also reduces atom rearrangements at the surface and thus material quality. Experiments as for example by Kadoiwa *et al.* show that replacing the solid As source in molecular beam epitaxy equipment by a gas source (AsH_3) significantly reduces In segregation and entirely stops it at growth temperatures below 450 ℃.[215] It also has been shown that super-flat GaInAs/AlInAs interfaces can be realized by growing onto (411)A substrates.[216] For example, Aoki *et al.* observed much intenser and narrower photo luminescence peaks in the (411)A material compared to the (100) material. However, changing the substrate orientation also changes the electronic properties of the material and band parameters are more difficult to establish. Another way to reduce effects of surface segregation without changing the growth facility or the established material system consists in correcting layer thicknesses and material sequences in a way that the potential of the grown structure resembles the designed one as much as possible. However, this requires a model for surface segregation that is quantitatively accurate.

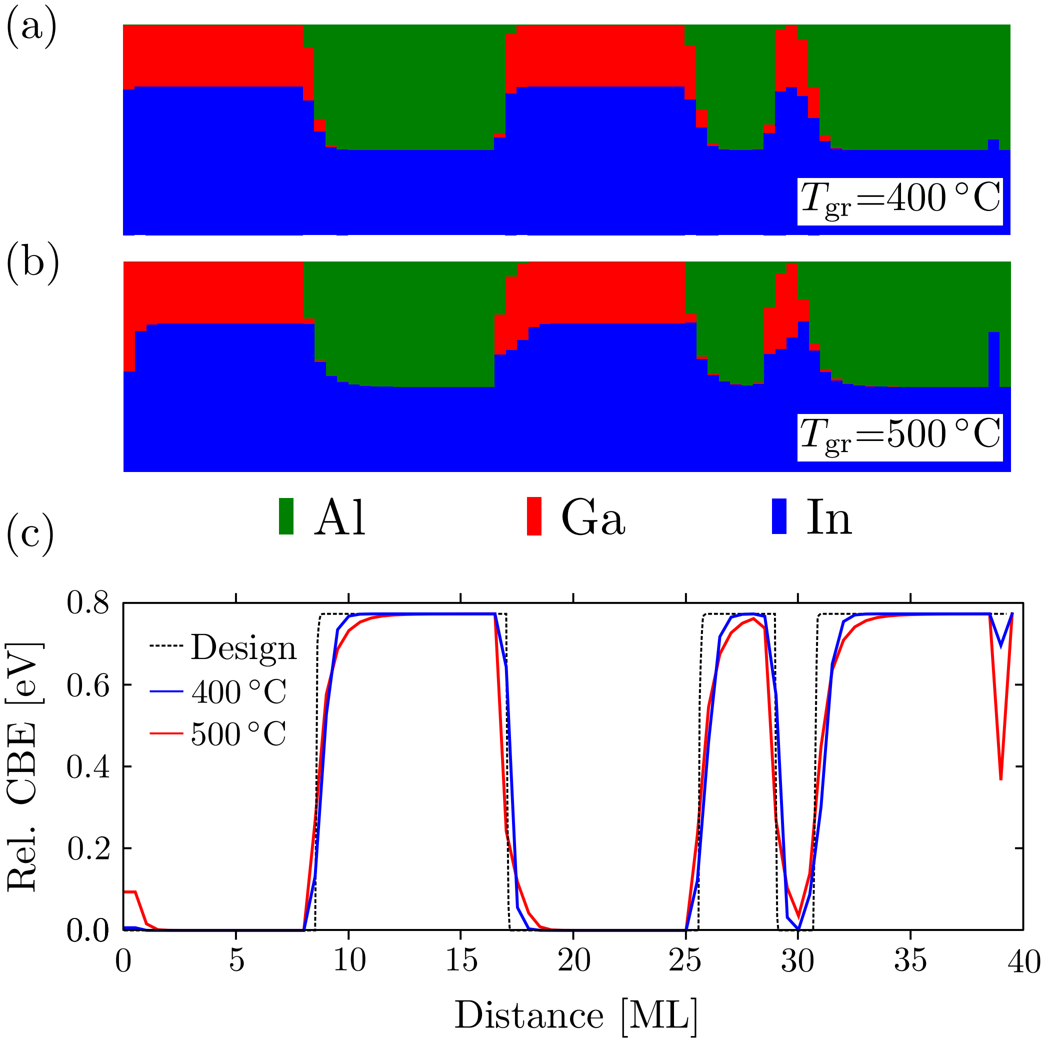

Figure 5.9: Surface segregation in strained material

Simulation of surface segregation in strained $Al_{0.595}In_{0.405}As/Ga_{0.294}In_{0.706}As$ *grown on InP at 400°C (a) and 500°C (b) substrate temperature. The layer thicknesses are identical to the ones of the test structure with lattice-matched material. (c) Calculated profile of the conduction band energy at* Γ*-point. Simulations were performed with a resolution of half a mono-layer.*

Surface segregation not only changes the energy positions of the quantum well states but also increases alloy and interface roughness scattering. It has been shown by Vasanelli *et al.*[154] that these scattering processes present a strong contribution to the relaxation rate of the upper lasing state. Therefore it is advisable to try to reduce surface segregation as much as possible by optimizing the growth technique. Once this has been achieved a model as we present it here can be used to predict the effect of the remaining surface segregation on the electron wavefunctions and to take into account surface segregation in the design process.

5.4 Simulations

Recently, in our group a code has been developed that calculates the transport through quantum cascade laser structures with a model of sequential resonant tunneling and that allows to simulate the performances of our structures in a quantitative manner.[217] In order to simulate a design, a structure description is first generated using the design with layer thicknesses and their material compositions as input. Composition-depending material parameters are calculated as described in section 5.2 using data extracted from the publication by Vurgaftman *et al.*[100]. Surface segregation is treated using the kinetic model as described in section 5.3. Although simulations cannot take into account the quality of the grown material, in many cases we were able to find a very good agreement between predicted and measured characteristics of our devices.

As an example we show structure N547 that was a copy of the first quantum cascade lasers with strain compensated design,[65] but grown in the growth facility of our research group that was in Neuchâtel at that time. In a first step we tried to determine the right value for the monolayer thickness in the surface segregation model. To that end, electroluminescence spectra measured at 78 K heat sink temperature were compared with simulated ones. Other structures with GaInAs/AlInAs/InP material system have shown that this value is situated around 3 Å. In this particular case we found a very good agreement for a monolayer resolution setting of 2.5 Å. Different spectra are shown in Fig. 5.10(a). We then compared measured and simulated spectra at 302 K as it is shown in Fig. 5.10(b). Whereas the center wavelength of the electroluminescence peak shows a good agreement, the simulated spectrum is much larger (52 meV FWHM). We attributed this to an overestimation of the electronic temperature calculated by the simulation code and that yields a valuest of $T_\mathrm{e} = 680\,\mathrm{K}$ at an injected current density of $5.3\,\mathrm{kA\,cm^{-2}}$. Setting this value to a lower value of $T_\mathrm{e} = 400\,\mathrm{K}$ indeed resulted in a electroluminescence spectrum with comparable width (38 meV FWHM). An electronic temperature of $T_\mathrm{e} = 400\,\mathrm{K}$ also agrees better with the measured current-voltage characteristics at 302 K then for temperatures calculated by the simulation code. This is shown in Fig. 5.10(c). However, for lower temperatures the curves differ considerably that we attribute to a contact problem on our samples and a less accurate model at low temperatures. A 4.52 mm long and 12 μm wide laser device was measured at 78 K heat sink temperature. Emission wavelength was $\lambda \approx 3.5\,\mu\mathrm{m}$ and thus a bit shorter than the value obtained by Faist *et al.*[65] (3.5 μm at 10 K). A threshold current density of

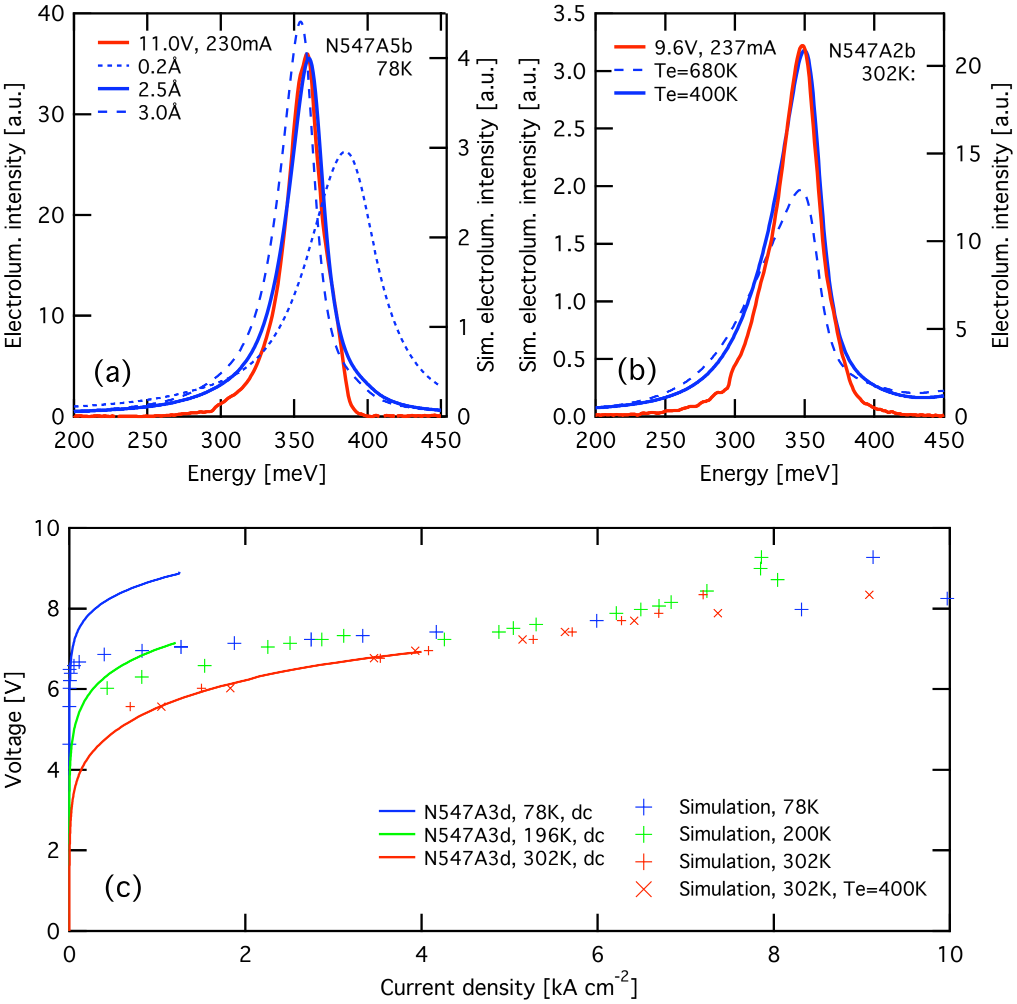

Figure 5.10: Simulated characteristics of structure N547

(a) Comparison between measured and simulated electroluminescence spectra at 78 K. Simulations were performed for monolayer thicknesses of 0.2, 2.5 and 3.0 Å and for an applied bias of 9.0 V; chosen to be lower than the measurement voltage due to electrical contact. High-frequency cut-off of the HgCdTe photoconductive detector is approximately at 390 meV. (b) Comparison at 302 K heat sink temperature. Simulations were performed assuming a monolayer width of 2.5 Å, an electric field of 104 kV cm^{-1} *(10 V) and assuming electronic temperatures of 400 and 680 K. (c) Simulated and measured current-voltage characteristics of structure N547 at heat sink temperatures of 78, 200 and 302 K. Measurements were performed in continuous-wave operation and the voltage offset at low temperatures is attributed to a bad sample contact. Last simulation (red cross) was performed by fixing the electronic temperature to 400 K instead of letting the simulation code to calculate it.*

$4.4\,\mathrm{kA\,cm^{-2}}$ and slope-efficiency of $470\,\mathrm{mW/A}$ was measured.[2] Depositing a highly reflective coating on the sample back facet improved these values to $3.7\,\mathrm{kA\,cm^{-2}}$ and $590\,\mathrm{mW/A}$, respectively. Using the $1/L$-method with these two data points yields values of $1.9\,\mathrm{cm\,kA^{-1}}$ and $5.7\,\mathrm{cm^{-1}}$ for the modal gain coefficient and extrapolated losses, respectively. Simulations yield a higher but still very low modal gain coefficient of $\approx 2.7\,\mathrm{cm\,kA^{-1}}$ at 78 K and Faist *et al.* determined a value of $\approx 3.6\,\mathrm{cm\,kA^{-1}}$ with Hakki-Paoli measurements at 20 K heat sink temperature and that also yield waveguide losses of $7.1\,\mathrm{cm^{-1}}$ at the same conditions. The threshold current density they measured was approximately $3\,\mathrm{kA\,cm^{-2}}$ at 100 K for a 3 mm long laser. Due to lack of sufficient data we are not able to say if the higher threshold currents we measure on our devices are due to a lower gain coefficient, device processing related issues or if self-heating effects already appear at this low temperature. Comparison between simulated and measured current-voltage characteristics shown in Fig. 5.10(b) suggests that the devices have a bad contact what would increase the dissipated electrical power. At 302 K the simulation still predicts a similar gain coefficient if an electronic temperature of $T_\mathrm{e} = 400\,\mathrm{K}$ is assumed. However, the current needed to align the structure and start to exhibit gain becomes very high with a value above $4.3\,\mathrm{kA\,cm^{-2}}$. With the resulting large threshold current densities self-heating effects become important even at pulsed operation with 1 % duty-cycle and could explain why no lasing was observed at higher temperatures. Faist *et al.* used a much lower duty-cycle of 2.25×10^{-4} (50 ns pulse width, 4.5 kHz) and measured their devices up to 280 K, with a maximal threshold current density of $\approx 20\,\mathrm{kA\,cm^{-2}}$,

---

[2] A collection efficiency of 70 % was assumed for the power measurement.

whereas we stopped measurements at 200 K heat sink temperature.

As this example shows our simulation code allows us to relatively well reproduce fundamental characteristics of our structures like emission wavelength for different temperatures and transport. However, we cannot take into account material quality and device processing adds important uncertainties to the device characteristics. Moreover, it lacks a thermal model for the moment that would allow to take into account self-heating effects. Due to the young nature of this code we only use it in this work to reproduce and discuss the measured results. In a future step the goal will (of course) be to use it to design quantum cascade laser structures with optimal performances. However, this is beyond the scope of this work.

5.5 Spiked designs

5.5.1 N664

Derived from structure N513 that was discussed in chapter 4 a new structure with the name N664 and designed to emit near 4.6 μm was grown. The design is based on $\mathrm{Ga_{0.391}In_{0.609}As}$ for the wells and $\mathrm{Al_{0.546}In_{0.454}As}$ for the barriers with 0.51 % compressive strain parallel to the growth direction in the well and 0.48 % tensile strain in the barriers when grown on an InP substrate. The resulting conduction band discontinuity is approximately 0.65 eV. In order to reduce electron escape into the continuum of states situated above the structure AlAs spikes with sub-mono layer thickness (2 Å) were inserted in the barriers downfield the active region and InAs spikes with identical thickness were introduced inside the wells to compensate for the additional local strain.[218, 219] The active region design is specified in appendix C.4. Measurements using X-ray diffraction showed that the structure was grown 2.44 % narrower than designed and the center of the gain of this structure is at $\lambda \approx 4.5\,\mu$m. For an illustration of the conduction band diagram of structure N664 we refer to the discussion of structure N808 with identical design in section 5.5.3.

Some of the simulation results are shown in Fig. 5.11. In Fig. 5.11(a) the electron transport through the structure was calculated as a function of the applied electric field at temperatures between 123 and 333 K and the device voltage and electric field, respectively, are shown as a function of current density. The resulting curves (dots) are compared to experimental data. An excellent agreement between simulation and measured data is found at 303 K. The lower the sample temperature the bigger the difference between simulated and experimental values whereas experimental curves show higher values for the voltage at similar current. Not shown on the graph are results of simulations neglecting surface segregation. In general, simulations using the same design but perfectly flat interfaces result in a overestimation of the voltage by approximately 1 V, respectively a slightly smaller current at similar applied electric field. An excellent agreement is also found between measured and calculated electroluminescence spectra. Fig. 5.11(b) shows the center position of simulated electroluminescence spectra as a function of device voltage and applied electric field (dashes) respectively. Experimental data at 303 K and measured on a sample that has been fabricated by a “fast” process as described in section 3.3.1 of chapter 3 are represented as dots.

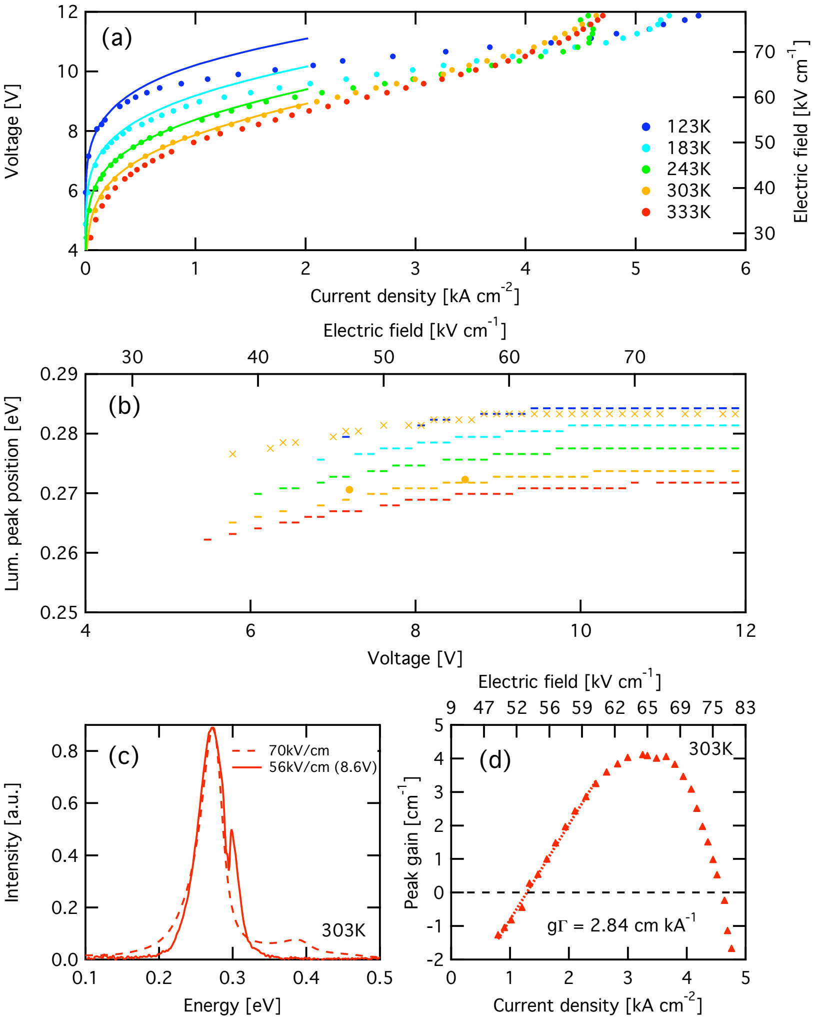

Figure 5.11: Simulated structure N664

(a) Simulated (dots) and experimental voltage-current characteristics of structure N664 between 123 and 333 K. The experimental curves were measured on device N664A23a (w=13 μm, l=380 μm) in continuous-wave operation. (b) Peak position of the electroluminescence as a function of device voltage. Simulated values are represented as dashes and for 303 K results of the simulation neglecting surface segregation is shown (crosses). Measurements obtained on a "fast" electroluminescence sample are represented as dots. (c) Comparison between simulated (dashed) and measured (continuous lines) electroluminescence spectra. The strong dip in the measured curve at 290 meV is due to CO_2 *absorption. (d) Simulated peak gain as a function of current. The dashed line represents a linear fit yielding a gain coefficient of* $\Gamma g \approx 2.8\,cm\,kA^{-1}$.

Neglecting surface segregation yields peak energies that are approximately 10 meV higher as it is shown by the orange crosses for results at 303 K. A comparison between a simulated electroluminescence spectrum at 70 kV cm^{-1} and a measured one at 56 kV cm^{-1} at 303 K is shown in Fig. 5.11(c) and in Fig. 5.11(d) the simulated peak gain of the structure is shown as a function of injected current. An overlap factor of $\Gamma = 0.7$ for a standard waveguide was assumed and fitting a line in the linear part of the curve yields a modal gain coefficient of $g\Gamma = 2.8\,\mathrm{cm\,kA^{-1}}$. According to the simulation a current of $\approx 0.8\,\mathrm{kA\,cm^{-2}}$ has to be injected into the device in order to align the structure.

The design of the waveguide is listed in appendix D.5. Fabry-Pérot lasers have been fabricated using the technology described in section 3.4.1 of chapter 3. Wet-etching of the waveguide ridges using HBr:HNO$_3$:H$_2$O (1:1:10) resulted in active region widths between 8 and 13 μm. Si O$_\mathrm{x}$ was used as dielectric layer and the top contacts were covered with 5 μm thick electro-plated gold for improved heat sinking.

Laser performances of a 3 mm long and 10 μm wide device in pulsed operation at 1 % duty-cycle are shown in Fig. 5.12(a). Power-current-voltage curves are shown for heat sink temperatures between 240 and 322 K. The threshold current density at 240 K is 2.5 kA cm^{-2} and increases to 3.1, respectively 3.6 kA cm^{-2} at 296 and 322 K. After depositing a highly reflective coating on the back facet this value reduces to 2.45 kA cm^{-2} at 296 K. The threshold current shows an exponential dependence with temperature with $T_0 = 218$ K as shown in the figure inset. The measured slope efficiency was 720 mW/A and the peak power reached 510 mW. A maximal average power

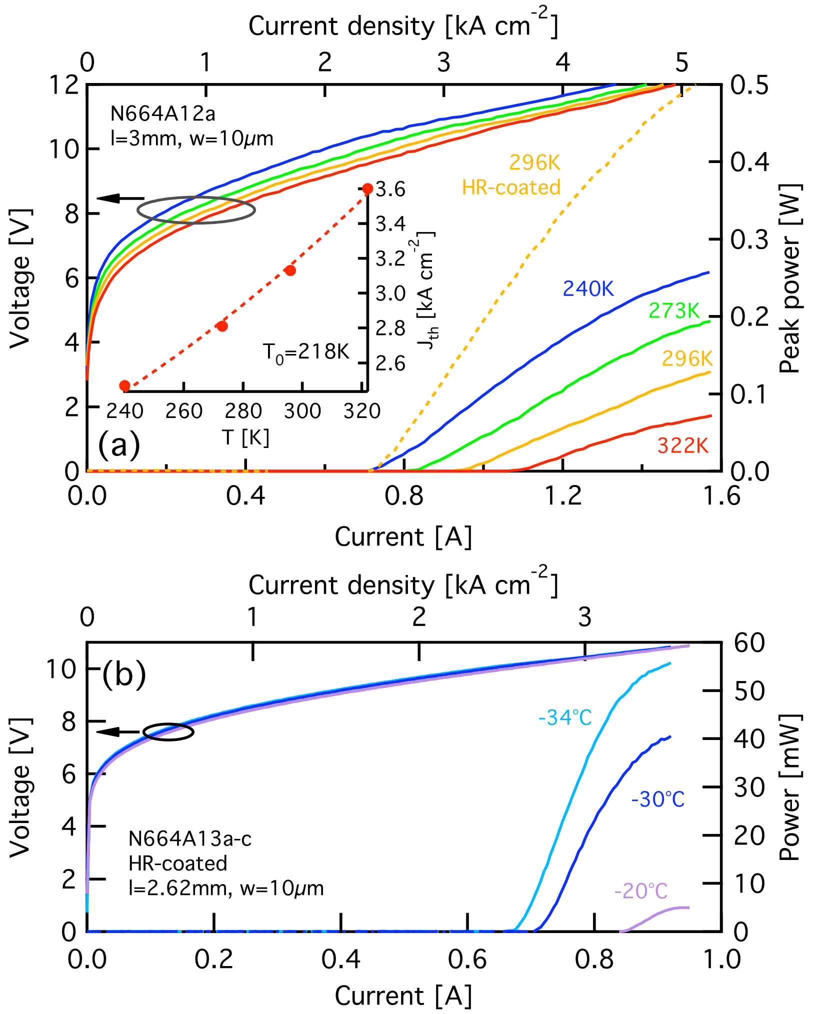

Figure 5.12: LIV in pulsed and continuous-wave operation (N664A)

(a) Voltage and emitted peak power (per facet) of a 3 mm long and 10 µm wide Fabry-Pérot laser of process N664A at various heat sink temperatures between 240 and 322 K. The dashed line shows the power characteristics of the same sample at 296 K, after a highly reflective coating was deposited on its back facet. In the figure inset the exponential increase of the threshold current with temperature is shown. No correction for non-unity collection efficiency was applied. The uncoated device was measured with a collection efficiency of ≈70 % whereas the coated device was measured with collection efficiency close to unity. (b) Power-current-voltage characteristics of a 2.6 mm long, 10 µm wide and back facet coated device in continuous-wave operation.

of 110 mW at 36 % duty-cycle was measured at -20 ℃ heat sink temperature. Fabry-Pérot devices emit at $\lambda \approx 4.5\,\mu$m at room temperature which is at a little shorter wavelength than the lasers were designed for. This can be attributed to the mismatch of 2.44 % between the length of the designed quantum cascade laser period and the grown one.

Devices also worked in continuous-wave operation up to a heat sink temperature of -20 ℃. Power-current-voltage curves measured with a 2.6 mm long, 10 μm wide device with a highly reflective coating on the back facet are shown in Fig. 5.12(b). At -34 ℃ a maximal power of 55 mW is measured and increasing the heat sink temperature to -20 ℃ increases the threshold current density from 2.5 to 3.1 kA cm^{-2} and the maximal average power drops to 5 mW. Fig. 5.13 shows the dependence of the threshold current density at 298 K as a function of mirror losses. Data from waveguide ridges with different widths are plotted as different data sets and the modal gain coefficient and waveguide losses were determined as described in section 3.4.3 of chapter 3. Within the error of the data threshold current density seems to be independent of cavity width but 9 μm wide devices show a larger spread due to larger relative uncertainty of the measured ridge width. A modal gain coefficient of 2.5 ± 0.4 cm kA^{-1} and waveguide losses of 3.6 ± 0.9 cm^{-1} were determined. The measured value of the gain coefficient agrees well with the simulated one of 2.8 cm kA^{-1}. Waveguide losses are more difficult to compare as our simulations do not take into account the exact device geometry and scattering losses and absorption in the cladding and dielectric layers are neglected. Extrapolation of the peak-gain curve shown in Fig. 5.11(d) yields a value of $\alpha_0 = 3.65$ cm^{-1}. To this value the missing loss contributions need

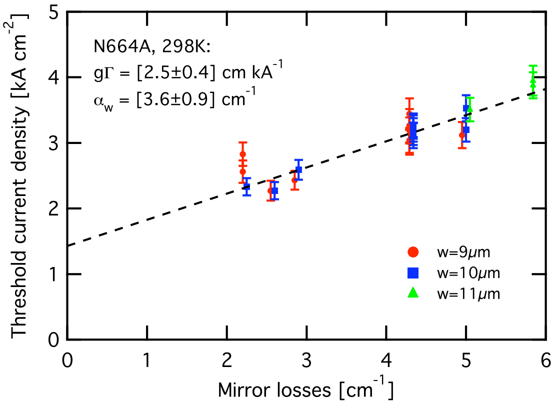

Figure 5.13: $1/L$-measurement at 298 K (N664A)
Threshold current density as a function of mirror losses, measured at 298 K heat sink temperature. Devices fabricated in the process N664A with various widths and length and before and after depositing a highly reflective coating were used. The dashed line represents the best linear fit for the data.

to be added in order to obtain the total waveguide losses.

Comparing the experimental values of α_w discussed above with values obtained on structure N808 described below and with the simulated (incomplete) value $\alpha_0 = 3.65\,\mathrm{cm}^{-1}$ we believe that the actual value of α_w is close to the upper limit of the indicated uncertainty interval ($\alpha_\mathrm{w} \approx 4.4\,\mathrm{cm}^{-1}$).

The same epilayer was also used to fabricate distributed feedback lasers[59] emitting around 4.5 µm. The distributed feedback grating was patterned holographically by Lubos Hvozdara at AlpesLasers SA and devices with 4 to 8 µm wide active regions were fabricated. Power-current-voltage characteristics of a 3.2 mm long and 4 µm wide device in continuous-wave operation are shown in Fig. 5.14(a). Due to narrower waveguide ridges the current and therefore the dissipated power were reduced considerably. Therefore, self heating effects were reduced and the device worked in continuous-wave operation up to 303 K. Fig. 5.14(b) shows the differential resistance of the

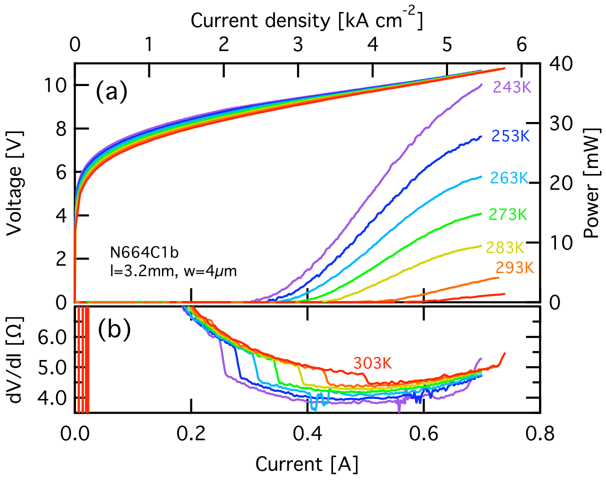

Figure 5.14: Continuous-wave LIV of a DFB device (N664C1b)

(a) Power-current-voltage (LIV) characteristics of a distributed feedback device of structure N664 at various heat sink temperatures in continuous-wave operation. The waveguide ridge is 3.2 mm long and 4 μm wide. The curves were acquired in "adiabatic" mode and therefore the measurement of the power output is delayed. A better measurement of the threshold current is obtained by calculating the differential resistance, as shown in figure (b).

device where the discontinuities at threshold and at laser turn-off are clearly visible. The measured threshold current density at 243 K is 2.0 kA cm^{-2} and it increases to 3.9 kA cm^{-2} at 303 K and the emitted power decreases from 36 mW to 1.4 mW.

Single-mode spectra of the same device and measured slightly above threshold current are shown in Fig. 5.15 for 243, 273 and 298 K heat sink temperature. Emission wavelength is 2254 cm^{-1} at 243 K and shifts to 2237 cm^{-1} at 298 K heat sink temperature.

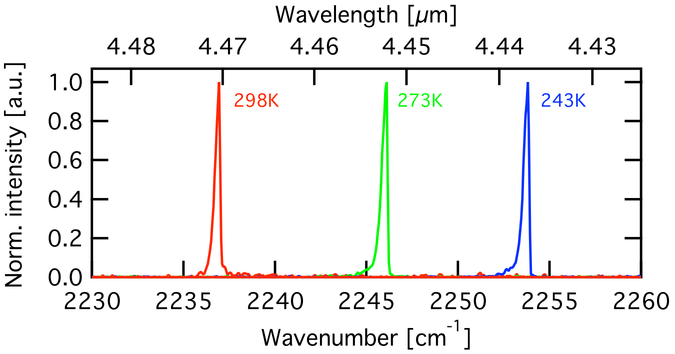

Figure 5.15: Emission spectra of a DFB device (N664C1b)
Emission spectra of a distributed feedback quantum cascade laser in continuous-wave operation slightly above threshold and at various heat sink temperatures.

5.5.2 N665

A structure with exactly the same active region but 65 instead of 25 active region periods was grown in the subsequent run. The waveguide design is listed in appendix D.6. Fabry-Pérot lasers have been fabricated using the technology described in section 3.4.1 of chapter 3. Wet-etching of the waveguide ridges using HBr:HNO_3:H_2O (1:1:10) resulted in waveguides with 14 to 20 μm wide active regions, $Si\,O_x$ was used as dielectric layer and the top contacts were covered with 5 μm thick electro-plated gold for improved heat sinking.

Fig. 5.16 shows the power-current-voltage characteristics of a 1.52 mm long and 18 μm wide device operated in pulsed mode at 1 % duty-cycle at heat sink temperatures between 243 and 322 K. The device was coated with a highly reflective Al_2O_3:Au:Al_2O_3 (300/100/100) on the back facet and a threshold current density of 2.2 kA cm^{-2}, a slope efficiency of 2.2 W/A and a maximal peak power of 850 mW was measured at a heat sink temperature of 297 K. These values improved to 1.6 kA cm^{-2}, 3.0 W/A and 1.6 W, at 243 K. The threshold current increased exponentially with characteristic temperature $T_0 = 178$ K as shown in the inset of Fig. 5.16. Due to the thick waveguide core and the resulting poor thermal conductivity of the structure the average power obtained form these devices was small. Fig. 5.17 shows measurements of the average power of device N665B13b-c as a function of duty-cycle at heat sink temperatures of 243 K and 297 K. A maximal average power of 100 mW was measured at 243 K at a duty-cycle of 14 % (29.2 V, 900 mA) and this value decreased to 40 mW at 297 K with a duty-cycle of 7 % (31V, 1A).

Fig. 5.18 shows the dependence of the threshold current density as a function of mirror losses of a selection of devices where power-current-voltage characteristics were measured under same conditions before and after depositing a highly reflective Al_2O_3:Au:Al_2O_3 (300/100/100) coating on the back facet. The modal gain coefficient as well as waveguide losses were then determined as described in section 3.4.3 in chapter 3. Fig. 5.18(a) shows the situation where the different measurements have been considered independent and the best line was fitted to all data points using the Levenberg-Marquardt algorithm. The resulting line coefficients were then used to determine the modal gain coefficient and waveguide losses and the standard deviations determined the respective errors. The major contribution to the high uncertainty associated with the threshold current densities was the error on the ridge width due to measurement uncertainty and width fluctuations of the very thick active region. A modal gain coefficient of 4.0±1.2 cm kA^{-1} and waveguide losses of 4.6±1.7 cm^{-1} were determined. However, assuming

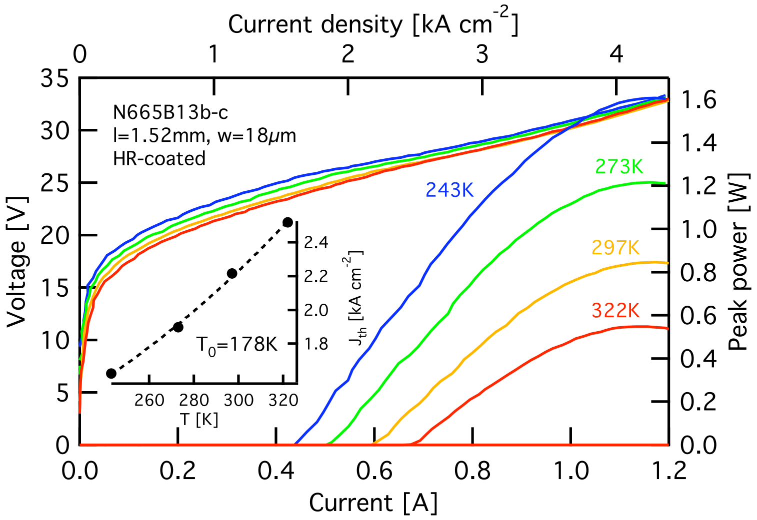

Figure 5.16: Pulsed LIV (N665B13b-c)

Power-current-voltage characteristics of the 1.5 mm long and 18 μm wide and back facet coated device N665B13b-c. Measurements were obtained in pulsed operation (100 kHz, 100 ns pulse width) at heat sink temperatures between 243 and 322 K and have been corrected for 80 % collection-efficiency (measured). The exponential dependence (dashed line) of the threshold current with temperature is shown in the figure inset.

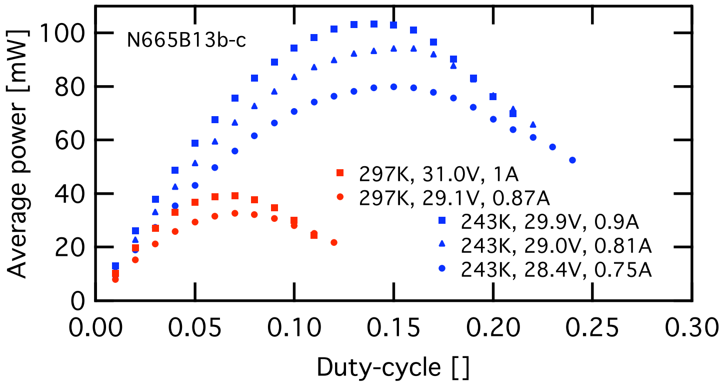

Figure 5.17: Average power as a function of duty-cycle (N665B13b-c)

Measurement of the average power of device N665B13b-c as a function of duty-cycle at heat sink temperatures of 243 K (blue) and 297 K (red). Curves were measured with a pulse width of 100 ns and corrected for 80 % collection efficiency (measured).

that the coatings are identical and present no current leaks and using the fact that the active region width before and after depositing a coating are identical, the uncertainty on these values can be considerably reduced. Data points before and after coating are therefore fitted for each device separately and mean values of the fitted slope and line offset coefficients are then used to determine the modal gain coefficient and waveguide losses. Uncertainties are obtained from the standard deviations determined from fitted line coefficients using error propagation. This is shown in Fig. 5.18(b) and values of $3.91\pm0.29\,\mathrm{cm\,kA^{-1}}$, respectively $4.47\pm0.40\,\mathrm{cm^{-1}}$ were determined. Waveguide losses agree very well with the value we determined for structure N664 whereas for the gain coefficient, taking into account calculated overlap factors and number of periods, has a 16 % smaller value. This is attributed to vertical spacial hole burning effects as described in section 4.3.1 of chapter 4.

5.5.3 N808

Later in the growth campaign structure N664 was re-grown with slightly lower doping ($n_\mathrm{s}=8.8\times10^{10}\,\mathrm{cm^{-2}}$) and resulting lasers were emitting around $\lambda\approx4.8\,\mu$m. X-ray diffraction measurements show that the structure period was grown 2.55 % larger than designed. However, simply scaling the structure thickness in the simulation did not explain the shift of the wavelength to $\lambda\approx4.8\,\mu$m. Also with the doping we find a discrepancy between the specified value and experimental observations. With the doping specified one would expect the negative differential resistance region to onset at a current density of approximately $3\,\mathrm{kA\,cm^{-2}}$. But experiments show that this region is closer

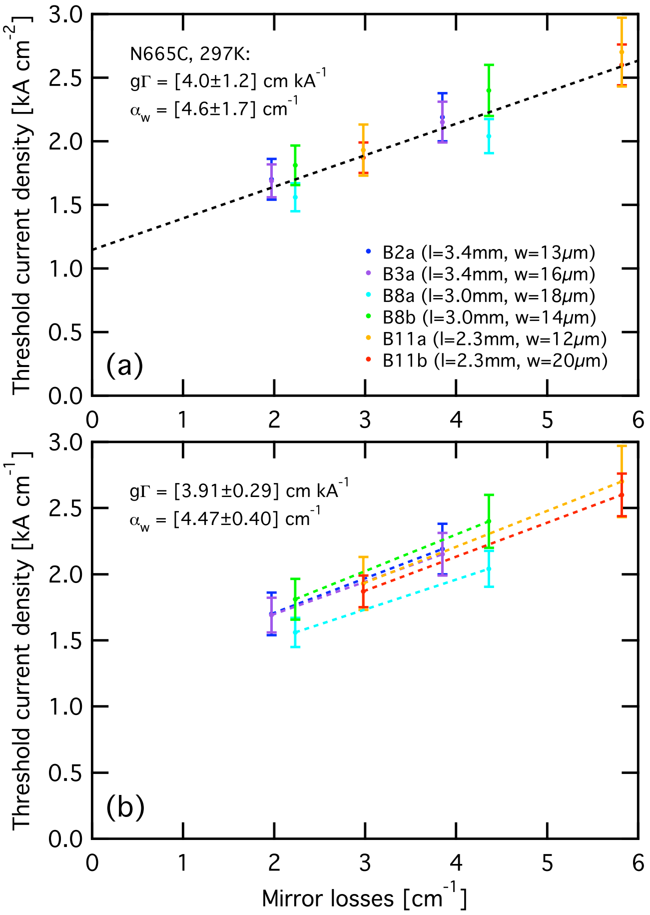

Figure 5.18: $1/L$-measurement 297 K (N665B)

Threshold current density as a function of mirror losses at 297 K heat sink temperature. The devices of process N665B were measured in pulsed operation (100 kHz, 100 ns pulse width) before and after depositing a highly reflective coating on the back facet. In figure (a) all devices were treated together to determine the modal gain coefficient as well as the waveguide losses. In figure (b) devices were treated separately.

to 5 kA cm^{-2}. This, together with indications that will be discussed below, suggests that the growth conditions were probably quite different from what we thought they would be. In order to reproduce the onset of the negative differential resistance at 5 kA cm^{-2} that is observed in experiments we need to increase the doping by 50 %. in our transport simulation. Reproducing the optical characteristics of the structure with the simulation code was only possible by assuming that the growth rate of GaInAs was 5 % higher than expected and including surface segregation with a resolution of 3.5Å. Results of electroluminescence and current simulations are shown in Fig. 5.19. As Fig. 5.19(a) shows the optical characteristics of the structure could be reproduced relatively well over a temperature range from 80 to 303 K. Less agreement between simulations and experiment was found for the current-voltage characteristics as shown in Fig. 5.19(b). We were not able to find a set of simulation parameters that would reproduce the optical as well as the electrical properties of the structure accurate at the same time. Whereas the simulated current-voltage characteristics at 303 K reproduce the measured one relatively well, simulations at lower temperature yield voltages that are approximately 1 V smaller than measured ones.

Electroluminescence spectra whose peak energies are plotted in Fig. 5.19(a) are shown in Fig. 5.20 at 80, 200 and 274 K. The spectra show three principal optical peaks. The peak at approximately 245 meV is due to diagonal transitions from the two lower states of the injection region to lower lasing state $|\ell 1\rangle$ in the active region. Fig. 5.21 shows the calculated band diagram of structure N808 at an applied electric field of 50 kV cm^{-1} and the moduli squared of the simulated electron wavefunctions as well as their eigenstate

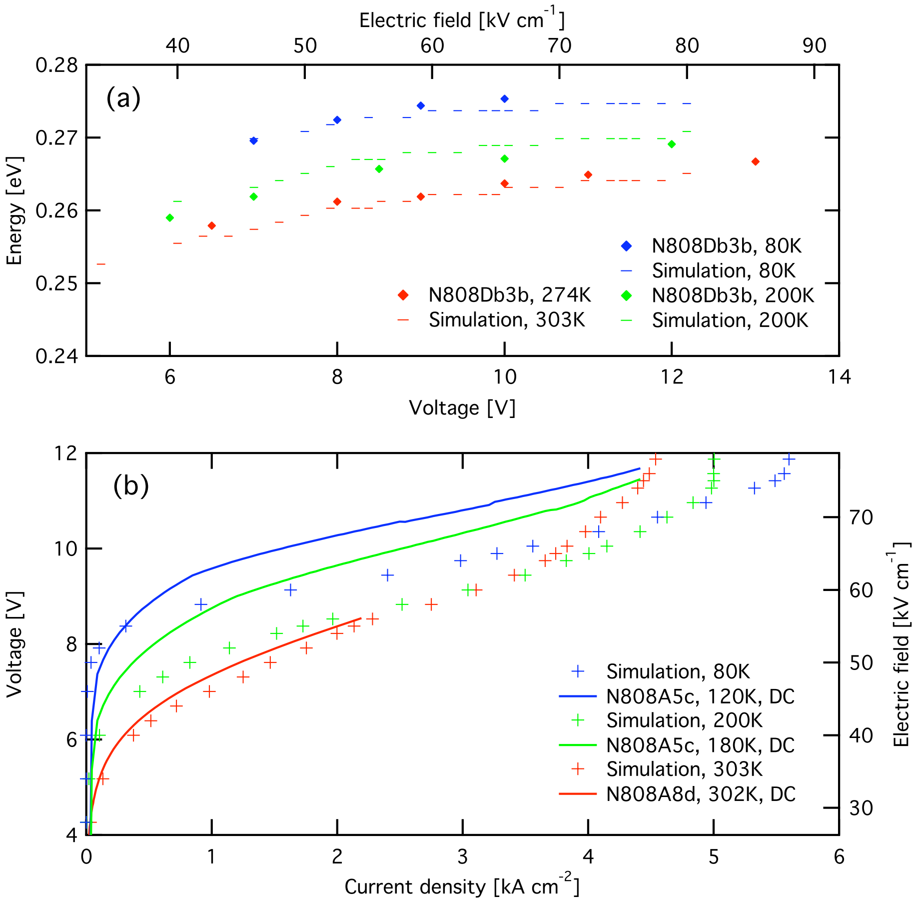

Figure 5.19: Simulations N808

(a) Comparison between the center of the simulated (dashes) and measured (dots) electroluminescence spectra as a function of applied voltage and at various temperatures. (b) Simulated (pluses) and measured current-voltage characteristics at temperatures between 80 and 303 K.

energies. According to the simulation the populations densities of these two states at an applied electric field of 50 kV cm^{-1} and a lattice temperature of 303 K are 3.8 and 2.9×10^{10} cm^{-2}, respectively. The simulation shows that there is a difference of 23 meV between the lowest state of the injection region and the upper lasing state at an applied electric field of 50 kV cm^{-1} where the injector starts to be aligned. This means that structure N808 has a misaligned injector as these two states should be aligned for a maximal injection efficiency. At lower temperatures these transitions should become weaker according to the simulations but measurements show that they remain. The central peak is the principal, vertical transition from the upper lasing state $|u\rangle$ to state $|\ell 1\rangle$. Finally, the third transition at approximately 290 meV is not visible on the simulation results because for calculation of the transport using sequential tunneling the structure has been cut at the fourth barrier and thus the transition originating from the upper lasing state $|u\rangle$ and ending in the fourth well is omitted.

The wafer was processed into conventional Fabry-Pérot lasers with ridge waveguides that were fabricated by wet-etching and resulting in trapezoidal active region cross sections with a mean width between 9 and 13 μm. A 300 nm thick SiO$_x$ layer for insulation and 5 μm thick electro-plated gold was deposited on the top contacts for improved heat sinking. Fig. 5.22 shows performances of a 3 mm long and 9 μm wide device with a highly reflective coating on the back facet. In pulsed operation at 2 % duty-cycle and 30 ℃ heat sink temperature the threshold current density is 1.7 kA cm^{-2}. For the slope efficiency we measure 1 W/A and the maximum peak power is 680 mW. The temperature dependence of the threshold is shown in the figure inset and

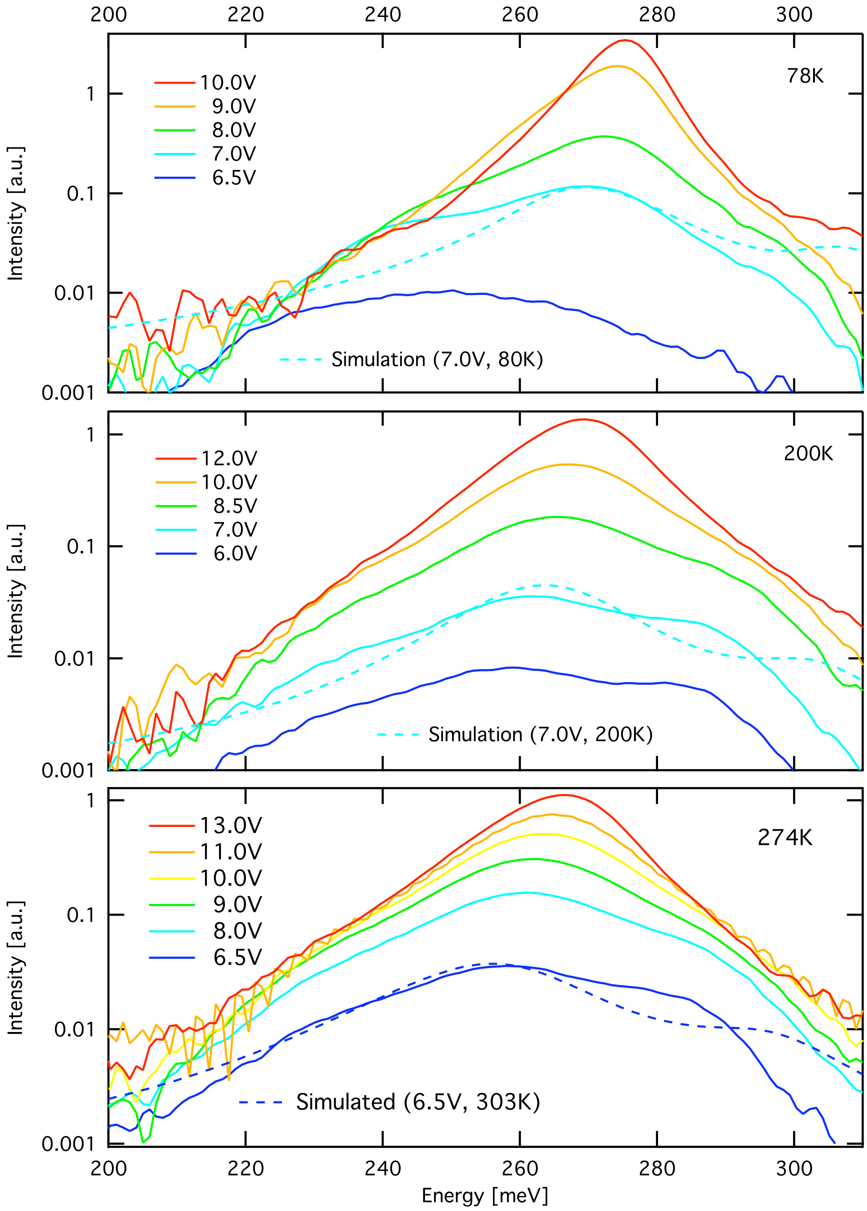

Figure 5.20: Electroluminescence measurements N808

Electroluminescence spectra of device N808Db3b at various voltages and temperatures. For comparison simulated spectra at 7 V (6.5 V for 274 K) are shown as dashed lines.

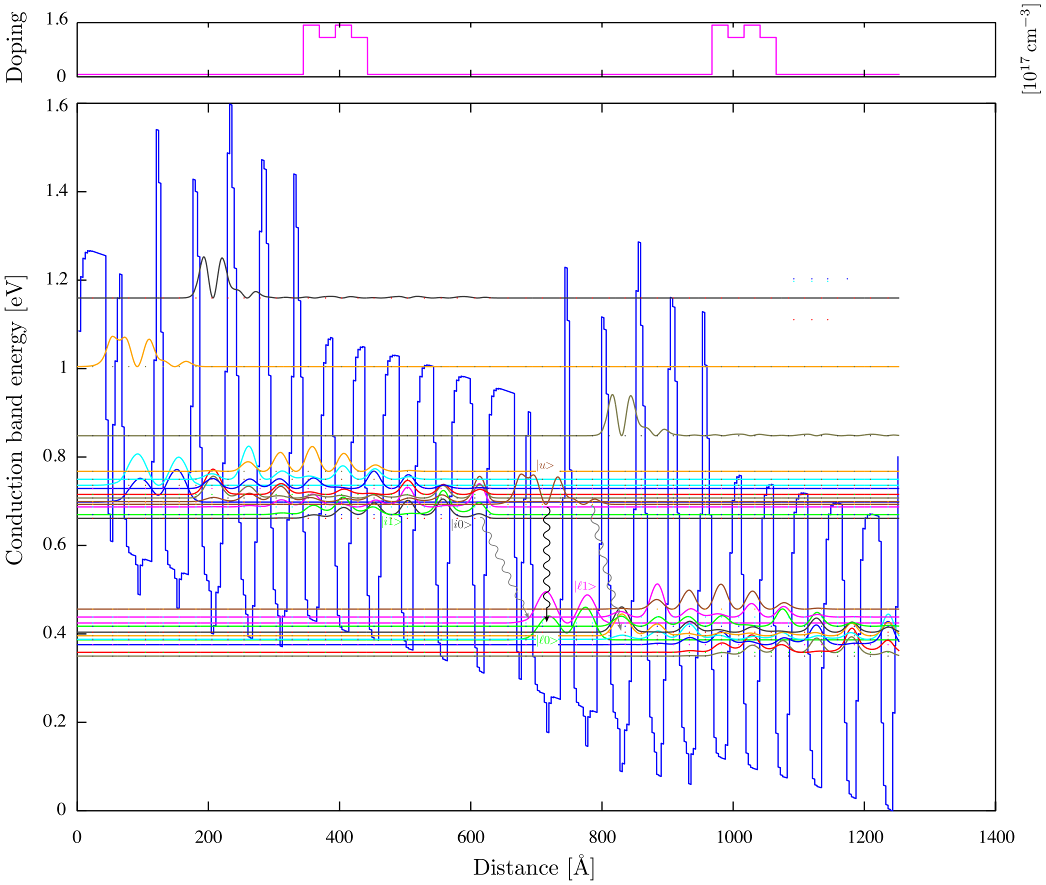

Figure 5.21: Conduction band diagram N808

Simulated conduction band diagram of structure N808 at an applied electric field of 50 $kV\,cm^{-1}$. Squared moduli of the electron wave functions are shown as coloured lines and their eigen energies are indicated as dotted lines.

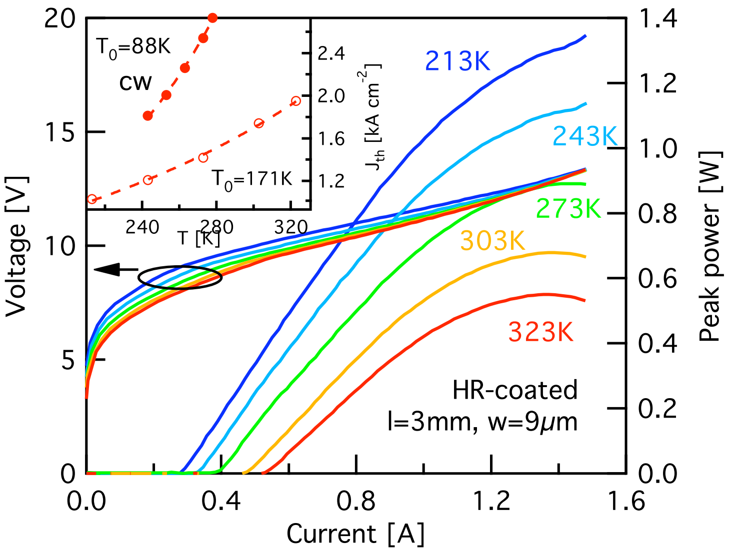

Figure 5.22: Pulsed LIV N808A5a-coated

Peak power and voltage as a function of current of a 3 mm long and 9 μm wide device with a HR-coating on the back facet in pulsed operation (100 kHz, 200 ns pulse width). The inset shows the exponential dependence of the threshold current with temperature in pulsed (circles) and cw-operation (full dots) with characteristic temperatures $T_0 = 171$ K and $T_0 = 88$ K, respectively.

characteristic temperature is $T_0 = 171$ K. The device worked in continuous-wave operation up to 5 ℃ with a threshold current density of 2.73 kA cm^{-2} and a maximal emitted power of 7 mW. These improved to 1.81 kA cm^{-2} and 140 mW at 243 K heat sink temperature for the threshold current density and emitted power, respectively. With a 4.14 mm long and 13 μm wide, HR-coated device a maximal average power of 480 mW at -30 ℃ and 210 mW at 30 ℃ was measured at a duty-cycle of 50 %. Devices worked in cw operation up to 15 ℃ heat sink temperature. Higher threshold currents and smaller slope efficiencies than observed in other groups[186, 83] are attributed to the reduced injection due to the misalignment of the injector and also to a less sophisticated processing technology and heat-sinking.

Fig. 5.23 shows the threshold current density of various measured devices as a function of mirror losses for heat sink temperatures of 77, 243, 300 and 320 K. High uncertainties are associated with the measured threshold current densities due to the many different measurement setups used and the uncertainty of the measurement of the active region width. Comparison of the values obtained at 300 K with the ones obtained for structures N664 and N665 show that structure N808 exhibits slightly more gain. Waveguide losses of $5.0 \pm 2.3\,\mathrm{cm}^{-1}$ seem to be too high but due the large uncertainty it is not clear if the fabrication process was less optimal and resulted in lossier waveguides or not.

For further investigation of the gain and waveguide losses of these lasers samples were fabricated that allowed to do multi-section cavity gain measurements as described in section 3.6 of chapter 3. Resulting gain and absorption spectra are shown in Fig. 5.24 where measurements between 80 and 322 K are shown. The absorption at the individually chosen baseline voltage are shown as grey, dashed lines. The error bars indicate the uncertainty of the gain measurement at a given energy and current. They take into account errors on section lengths and the measurement noise but do not consider the uncertainty on the injected current. Error bars are minimal at the energy where the probe signal has the highest intensity and become very large at the queues of the electroluminescence spectrum. Gain measurements at 80 K yield a symmetric line shape with a full-width at half-maximum of 16 meV and centered at 274 meV. The peak gain increases linearly with the injected current up to the negative differential resistance region where a maximum gain of $46\,\mathrm{cm}^{-1}$ is reached (orange curve). At higher currents the peak gain

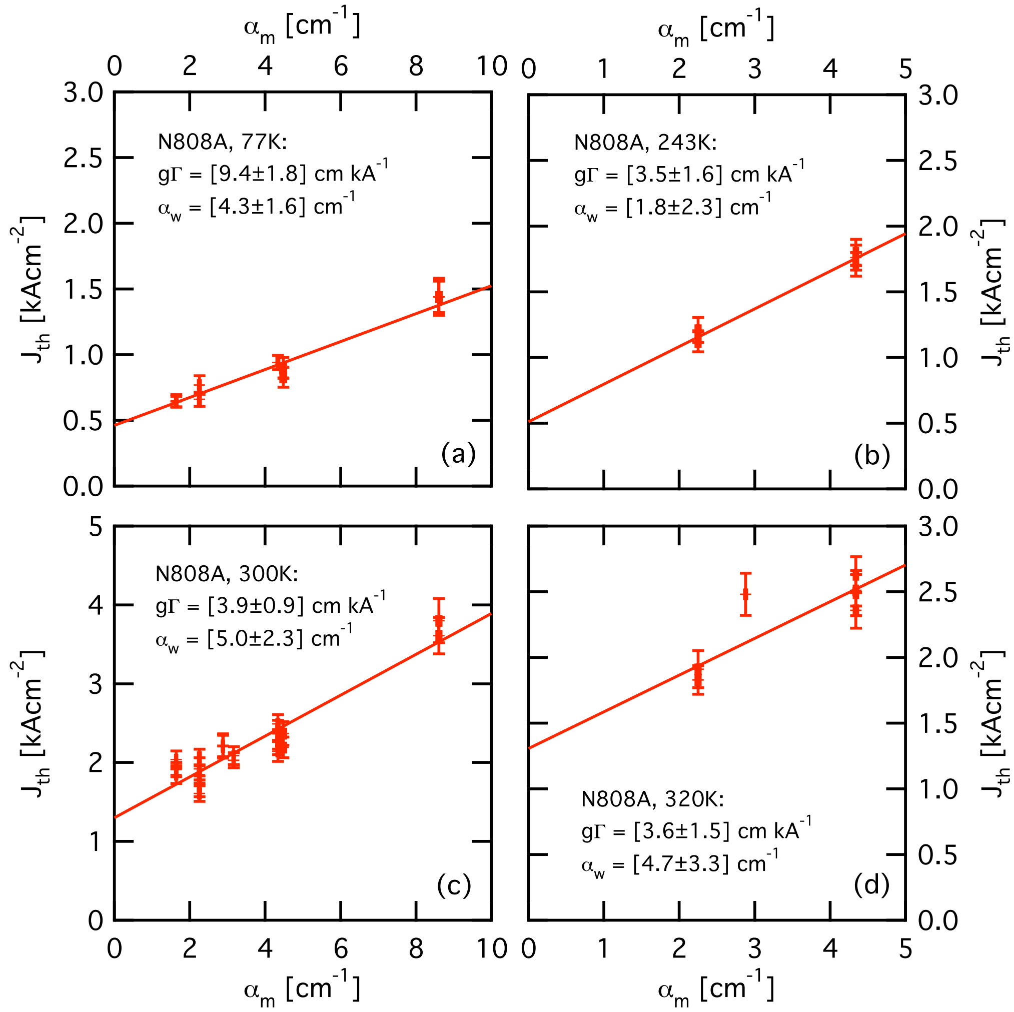

Figure 5.23: Threshold current vs. mirror losses (N808A)

Threshold current of various devices of process N808A as a function of mirror losses and temperature. Graph (a) shows data at 77 K, graph (b) at 243 K, graph (c) at 300 K and graph (d) at 320 K. The continuous lines show the linear fits that yield the coefficients needed to determine the modal gain coefficient and waveguide losses as described in section 3.4.3 of chapter 3.

drops rapidly due to the detuning of the ground state of the injector with the upper lasing state. When the heat sink temperature is increased the peak value of the gain decreases and the gain curves shift to lower energy and broaden. At 274 K the peak gain is reduced by a factor of four compared to the measurement at 80 K and the gain broadens by 25 % and is centered at 267 meV. The absence of a dispersive line shape shows that the device operates with a large population inversion.[7] A quantitative analysis is shown in Fig. 5.25(a) where the evolution of the peak gain as a function of current is plotted for the measured temperatures. We observe linear behavior up to the NDR region. Carrier leakage due to lattice or electron heating would be expected to lead to a sub-linear behavior of the gain. This suggests that the electrons are well confined in the conduction band structure. However, for the last point in Fig. 5.25(a), at 322 K, it is not clear if the sub-linear behaviour is due to self-heating of the active region or due to carrier heating effects. Circles represent measurements obtained with a sample where sections have been isolated by etching the contact and plasmon layers by dry etching. The black triangles show a measurement at 298 K and that was performed on a sample where sections were isolated by cutting trenches into the top cladding layer using focused ion beam. As can be seen on Fig. 5.25(a) the two samples yield practically the same results. The slope of these lines yields the gain coefficient whose values are depicted in Fig. 5.25(b) as a function of temperature (dots). The dashed line on the same graph shows a fitted exponential function [$g = g_0 \times \exp(-T/T_0)$] with $T_0 = 221\,\mathrm{K}$ and $g_0 = 14.2\,\mathrm{cm\,kA^{-1}}$. The dotted line shows the expected temperature dependence assuming that the only important non-radiative channel is optical phonon scattering with a rate

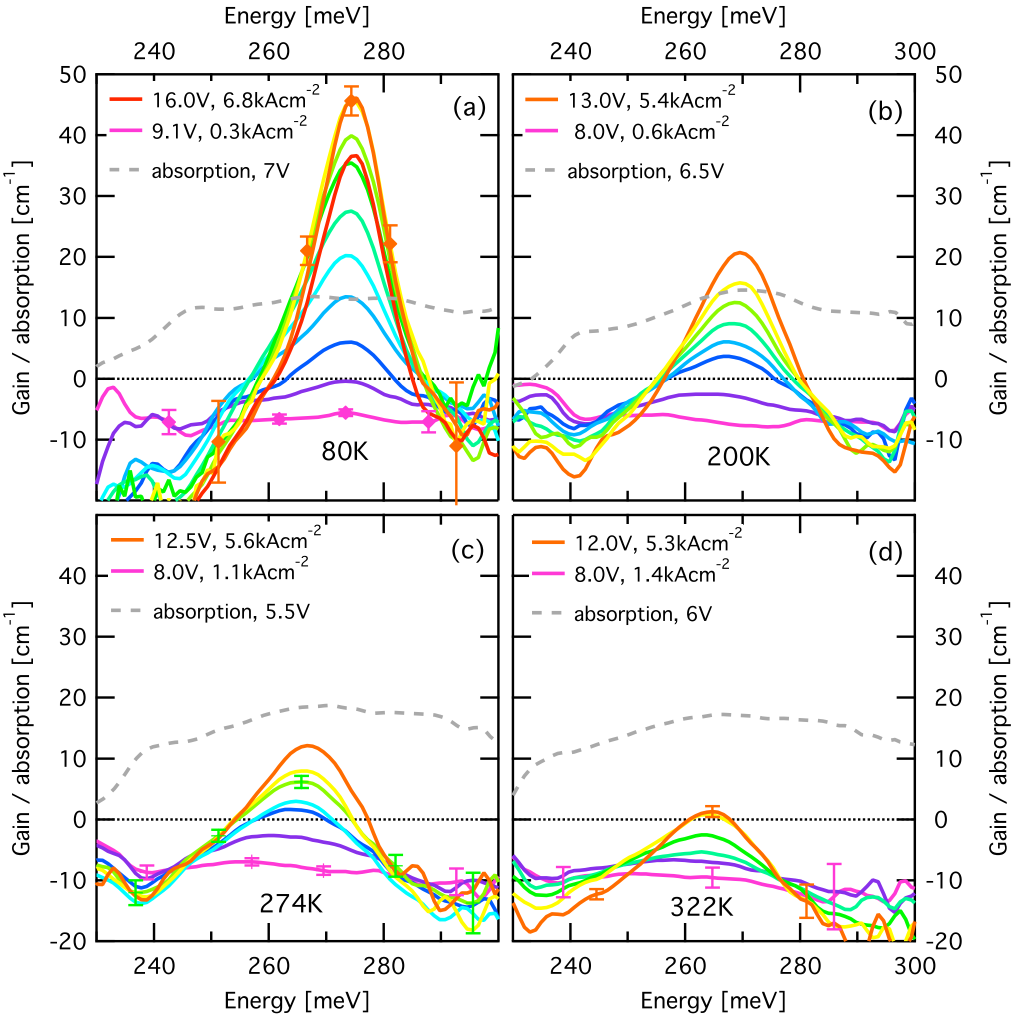

Figure 5.24: Modal gain as a function of temperature (N808)

Spectrally resolved modal gain as a function of injected current. Figure (a) shows measurements between 0.3 and 6.8 kA cm^{-2} at 80 K, figure (b) between 0.6 and 5.4 kA cm^{-2} at 200 K, figure (c) between 1.1 and 5.6 kA cm^{-2} at 274 K and figure (d) between 1.4 and 5.3 kA cm^{-2} at 322 K. Baseline absorption measurements are shown as dashed lines. What appears to be an absorption at energies below 255 meV is an artifact due to electrical and optical crosstalk between sections.

proportional to $[2n(T) + 1]$, where n is the Bose-Einstein factor associated with optical phonons and $\hbar\omega_{\mathrm{lo}} = 34\mathrm{meV}$ is the energy of the phonon in the material. A good agreement is obtained if one takes into account that the gain at 274 K broadens by 25 %. This suggests that no other relevant non-radiative channels exist. These gain coefficients are compared to the values obtained from laser data as determined above and shown in Fig. 5.23. The corresponding values are shown as squares in Fig. 5.25(b) and, considering the error of the measurements, there is a good agreement. We also simulated the gain in structure N808 and the results are shown in Tab. (5.3) using the same nomenclature as introduced in the discussion of structure N664 in section 5.5.1. For the modal gain coefficient we simulate a value at 303 K that is between the measured values and thus shows a good agreement. At 80 K however, simulation yields a slightly smaller modal gain coefficient of 8.1 $\mathrm{cm\,kA^{-1}}$ whereas measured values are close to 10 $\mathrm{cm\,kA^{-1}}$.

Table 5.3: N808 gain simulation results

T [K]	$g\Gamma$ [$\mathrm{cm\,kA^{-1}}$]	α_0 [$\mathrm{cm^{-1}}$]
303	3.8	5.5
200	6.5	3.4
80	8.1	0.3

In Fig. 5.25(c) waveguide losses obtained with $1/L$- and gain measurements are compared. Values obtained by $1/L$-measurements shown above are represented as blue squares and show an almost constant value of approximately 4.5 $\mathrm{cm^{-1}}$ between 80 and 322 K.[3] This value is comparable to

---

[3] With exception of the measurement at 243 K that is off.

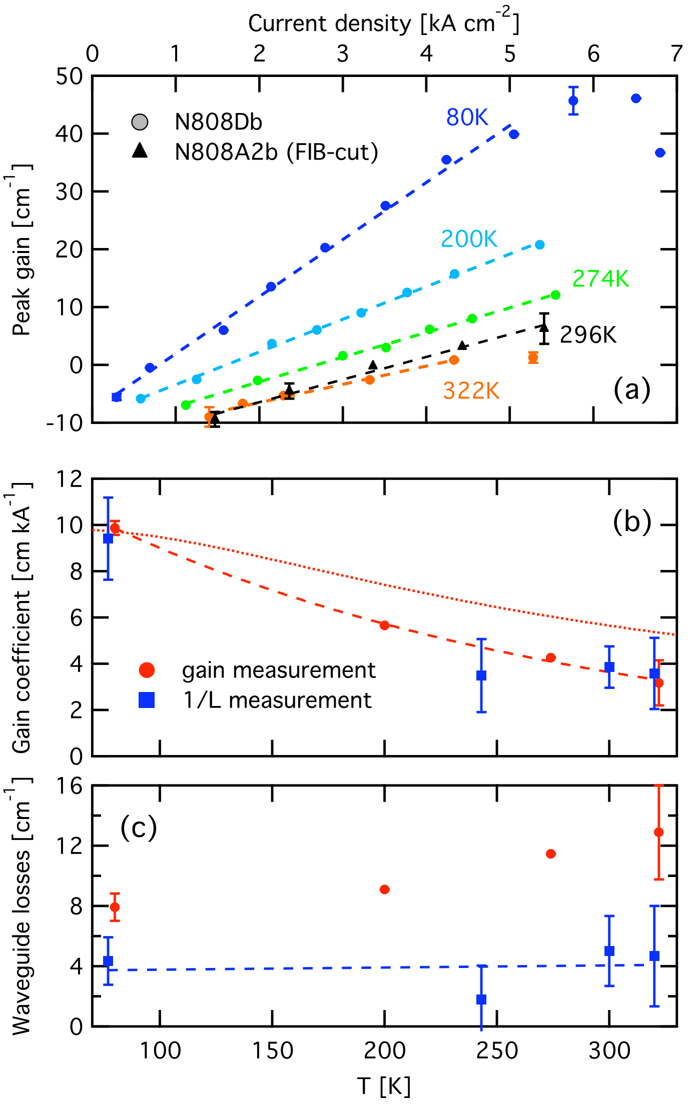

Figure 5.25: Gain and waveguide loss analysis (N808)

(a) Peak values of the modal gain as a function of injected current and for temperatures between 80 and 322 K. Dashed lines represent linear fits that yield the gain coefficient and waveguide losses. Black triangles represent measurements made with a sample whose sections were isolated using a focused ion beam. (b) Comparison between gain coefficients obtained by 1/L-measurements (squares) and multi-section cavity gain measurements (dots) at temperatures between 80 and 322 K. The dashed line in shows an exponential fit of the gain coefficients ($g = 14.2 \times \exp(-T/221\,K)$) *and the dotted line the expected temperature dependence, assuming that optical phonon scattering is the only non-radiative channel and neglecting gain broadening. (c) Waveguide losses as a function of temperature and determined by the two methods.*

the values obtained for structures N664 and N665 and is slightly higher than the value ($3.3\,\mathrm{cm}^{-1}$ at $300\,\mathrm{K}$) reported by Lyakh *et al.* for a buried-heterostructure laser at similar wavelength.[186] Simulation of the peak gain at different temperatures yields α_0 parameters with a very strong temperature dependence that we do not observe on the devices. Values of α_0 are shown in Tab. (5.3) but comparison with other devices and $1/L$-measurements indicates that the simulated values are off. For example the value of $5.5\,\mathrm{cm}^{-1}$ at $303\,\mathrm{K}$ is much higher than the one obtained with the simulation of structure N664.

Multi-section cavity gain measurements yield higher waveguide losses that range from $8\,\mathrm{cm}^{-1}$ at $80\,\mathrm{K}$ to $13\,\mathrm{cm}^{-1}$ at $322\,\mathrm{K}$. This discrepancy is attributed to absorption and coupling loss in the $20\,\mu\mathrm{m}$ long, partially etched and unbiased segment between sections (see section 3.6.3 in chapter 3). At $322\,\mathrm{K}$ we measure an absorption with a peak value of $46\,\mathrm{cm}^{-1}$ for the unbiased structure. For the $20\,\mu\mathrm{m}$ long separation this translates into an offset of maximally $3\,\mathrm{cm}^{-1}$ at the center of the absorption. An additional constant offset of $4\,\mathrm{cm}^{-1}$ can be explained by coupling losses of $13\,\%$.

Fig. 5.26 shows a comparison between gain spectra measured using the multi-section cavity technique at $274\,\mathrm{K}$ and corresponding electroluminescence spectra obtained at same bias and temperature. The two line shapes are virtually identical, justifying the practise of using electroluminescence measurements to estimate the shape of the gain for devices with large population inversion. The gain spectrum at $8\,\mathrm{V}$ bias shows a slight red shift with respect to the peak of the luminescence spectrum. This could be caused by a non-negligible population of the ground state but the difference between the

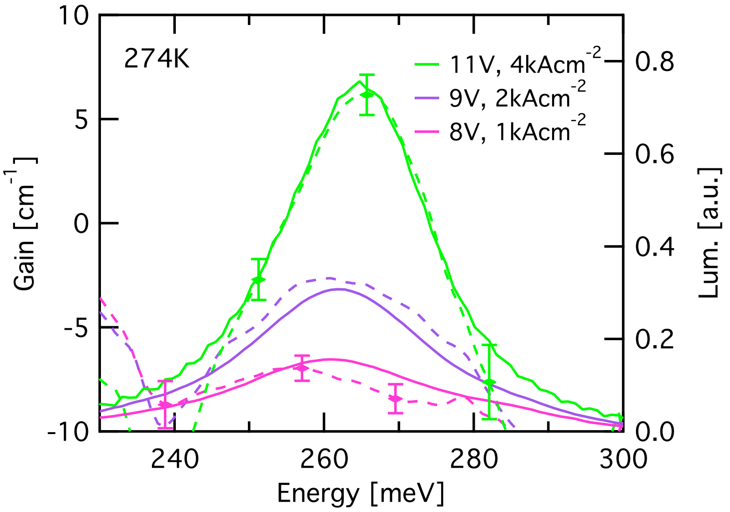

Figure 5.26: Gain vs. electroluminescence (N808)

Comparison between gain (continuous line) and electroluminescence (dashed) spectra at same bias at 274 K.

two curves is close to the accuracy of the measurements. Scattering assisted second order gain will be treated in chapter 6. The slight offset between the curves at 9 V bias can be attributed to the uncertainty associated with the measurement of the current during multi-section cavity gain measurements.

5.5.4 N810

Using the same active region design and doping as for structure N808 a structure with tri-stack waveguide as described in section 4.3.2 of chapter 4 was grown. Each of the tree stacks consisted in 20 active/injection region pairs pairs and for the exact description of the waveguide we refer to appendix D.4. According to X-ray diffraction measurements the structure was grown 3 % larger than designed but emission wavelength did not shift compared to devices from structure N808.

Table 5.4: Laser performances N810A3b-c (1 % duty-cycle)

	243 K	303 K
J_{th}	$1.32\,\mathrm{kA\,cm^{-2}}$	$1.96\,\mathrm{kA\,cm^{-2}}$
dP/dI	5.8 W/A	4 W/A
Peak power	3.8 W	1.8 W
η_{wp}	11 %	6 %

Power-current-voltage characteristics in pulsed operation (100 kHz, 100 ns pulse width) of a 3.02 mm long and 14 μm wide laser with a highly reflective coating on the back facet are shown in Fig. 5.27(a). The laser was measured up to a current of 1.3 A and at 243 K heat sink temperature the threshold current density was $1.3\,\mathrm{kA\,cm^{-2}}$. A high slope efficiency of 5.8 W/A and the emitted peak power at an injected current of 1.3 A was 3.8 W. A maximal wall plug efficiency of 11 % was obtained. At 303 K the threshold current density increased to $2.0\,\mathrm{kA\,cm^{-2}}$ and the slope efficiency decreased to 4 W/A. At an injected current of 1.3 A the measured peak power was 1.8 W, resulting in a wall plug efficiency of 6 %. These values are summarized in Tab. (5.4). Although these lasers show very good performances in pulsed operation at 1 % duty-cycle the latter decrease rapidly at higher duty-cycles. The inset in Fig. 5.27(a) shows a comparison of the average power emitted by lasers N808A10b-c (triangles) and N810A3b-c (dots) as a function of duty-cycle at 243 K. The curve of the tri-stack device is much steeper due to the higher slope efficiency of the device but rolls over at 10 % already with an average power of 320 mW. However, the device with standard waveguide and narrower ridges rolls over much later (55 %) and a higher average power of 480 mW is obtained. This clearly shows how the tri-stack devices are thermally limited

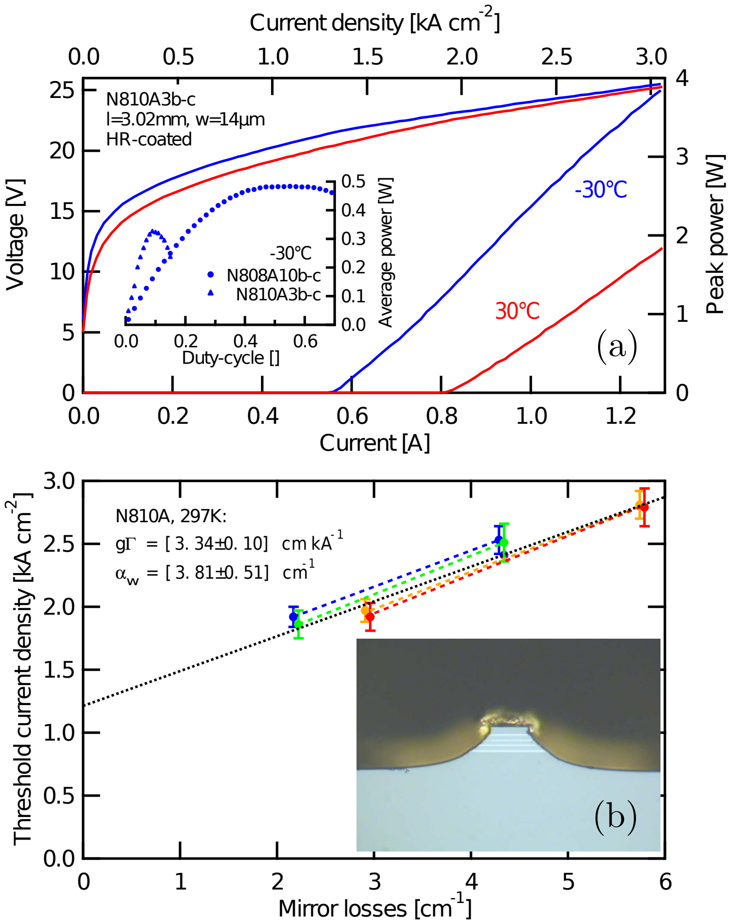

Figure 5.27: Laser characteristics in pulsed mode (N810A3b)

(a) Power-current-voltage characteristics of a 3 mm long and 14 µm wide laser of structure N810 with a highly reflective coating on the back facet. The figure inset shows a comparison of the maximal average power obtained with lasers N810A3b-c and N808A10b-c, respectively, as a function of duty-cycle. L-I curve at 243 K was corrected for optical collection efficiency (72 %, measured). (b) Threshold current density as a function of mirror losses for various devices of process N810A before and after depositing a highly reflective coating on the back facet. Dashed lines represent the linear fits yielding the coefficients needed to determine waveguide losses and the modal gain coefficient. The dotted line shows a linear fit considering all the data points. In the figure inset an image of the cross section of a laser of process N810A with a mean width of 20 µm is shown.

by the poor thermal conductivity of the device as we have shown already in chapter 4.

In Fig. 5.27(b) a study of the threshold current density of various devices of process N810A as a function of mirror loss is shown. Devices were measured before and after depositing a highly reflective coating on the back facet at 297 K heat sink temperature and lines were fitted to each pair of data points. Waveguide losses of $3.81 \pm 0.51\,\mathrm{cm}^{-1}$ and a modal gain coefficient of $3.34 \pm 0.10\,\mathrm{cm\,kA}^{-1}$ are determined. The inset in Fig. 5.27(b) shows an image of the cross section of a laser of process N810A where the waveguide ridge has a mean width of $20\,\mu$m. The $\mathrm{Ga_{0.47}In_{0.53}As}$ buffer layers can clearly be distinguised (bright color) from the rest of the material.

5.6 Comparison

A summary of the characteristics of the lasers discussed in this chapter is shown in Tab. (5.5) and Fig. 5.28 compares the current-power-voltage characteristics (per period) of similar devices from structures N664, N665, N808 and N810. As can be seen in Fig. 5.28 devices have similar current-voltage characteristics although earlier grown samples (N664 and N665) can clearly be distinguished from later grown samples (N808 and N810) due to the lower voltage-shoulder of the latter. This is attributed to the slightly lower doping as well as the longer emission wavelength due to the thicker periods (see Tab. (5.5) for details) whereas structures N664 and N665 were grown shorter. The reduced doping in structures N808 and N810 also leads to an earlier onset of the negative differential resistance region. Comparison with the other

Table 5.5: Summary

	N664	N665	N808	N810	
δL_p	-2.44	-0.67	+2.5	+3.1	[%]
N_p	25	65	25	3×20	[]
n_s	1.1E+11	1.1E+11	8.8E+10	8.8E+10	[cm^{-2}]
λ (@RT)	4.5	4.39 (100 K)	4.79	4.79	[μm]
η_v	0.98	0.99	0.98	1.0	[]
Γ	0.71	0.83	0.69	0.63	[]
$g\Gamma$ (@RT)	2.5 ± 0.4^a	3.91 ± 0.29^a	3.9 ± 0.9^a 3.58 ± 0.47^b	3.34 ± 0.10^a	[$\mathrm{cm\,kA}^{-1}$]
α_w (@RT)	3.6 ± 0.9^a	4.47 ± 0.40^a	5.0 ± 2.3^a	3.81 ± 0.51^a	[cm^{-1}]
J_th	2.45^c	2.2^d 1.8^g	1.7^e	1.96^f	[$\mathrm{kA\,cm}^{-2}$]
dP/dI	0.72^c	2.2^d 1.9^g	1.0^e	4.0^f	[W/A]
peak power	0.56^c	0.85^d	0.68^e	1.8^f	[W]

[a] $1/L$-measurement

[b] Multi-section cavity measurement

[c] T=296 K, l=3.02 mm, w=10 μm, HR-coated

[d] T=297 K, l=1.52 mm, w=18 μm, HR-coated

[e] T=303 K, l=3.02 mm, w=9 μm, HR-coated

[f] T=303 K, l=3.02 mm, w=14 μm, HR-coated

[g] T=297 K, l=3.02 mm, w=14 μm, HR-coated

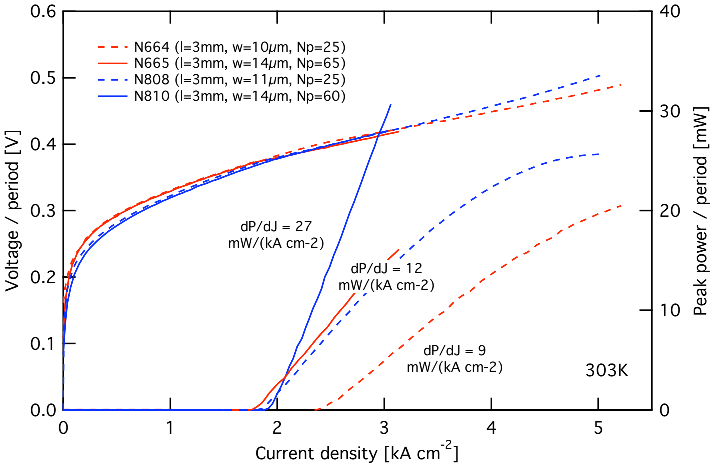

Figure 5.28: Comparison L-I-V characteristics N664, N665, N808 and N810
Voltage (per period) and peak power (per period) as a function of current density for similar devices from structures N664, N665, N808 and N810 measured at room temperature in pulsed operation (100 kHz, 100 ns pulse width).

devices shown in Tab. (5.5) suggests that the values of the total waveguide losses and modal gain coefficient of device N664 are higher than measurements indicate. Higher threshold current is partly explained by the higher active region doping and additional losses due to bad material quality and/or a problem with the device processing. Devices N665 and N808 show similar threshold current and slope efficiency (per period) suggesting that devices have similar waveguide losses and modal gain. Also device N810 has a similar threshold current despite the smaller overlap factor. This is attributed to the smaller waveguide losses that compensate for the reduced overlap factor and modal gain. The device shows a slope efficiency [$27\,\mathrm{mW/(kA\,cm^{-2})}$] that is more than two times larger than the one of devices N665 and N808 [$12\,\mathrm{mW/(kA\,cm^{-2})}$]. As all four devices show values close to unity for the relative slope efficiency η_{v} we attribute this improvement to the reduced waveguide losses as well as a delayed onset of gain saturation in the center of the optical mode and an improved thermal conductivity of the device due to the introduction of passive regions in the waveguide core.

Although in device N810 with a tri-stack waveguide we see a large improvement of the slope efficiency compared to the other devices we know from the discussion in section 4.3.2 in chapter 4 or for example from the figure inset in Fig. 5.27(a) that these devices are not well-suited for operation at high duty-cycle. In order to obtain better performace at high duty-cycles the threshold current of the devices would have to be considerably reduced by optimization of the active region gain and improved device processing. As we have shown in section 4.3.4 of chapter 4 replacing the $\mathrm{Ga_{0.47}In_{0.53}As}$ of the inter-stacks by InP further improves the thermal conductivity of the device. Fabricating narrow waveguide ridges ($\approx 5\,\mu$m) with vertical sidewalls and buried in insulating InP for reduced waveguide losses and improved heat extraction would allow to reduce the dissipated electrical power and the associated heat-extraction bottle neck.

Chapter 6

Scattering-assisted gain

6.1 Introduction

In solids electrons have a fixed relation between momentum and energy: they are moving along energy bands as known from condensed matter theory. When an electric field is applied they are accelerated but the lattice forces a periodic motion at a defined Bloch frequency. This phenomenon is known as Bloch oscillations,[220] and the idea was successfully used by Zener to explain the dielectric breakdown.[221] However, in usual solids the strong scattering due to impurities and carrier-carrier interaction prevents the observation of such oscillations because the lattice constant is too short to allow the electrons to complete even one oscillation cycle. In superlattices, the lattice constant is designed and a subtle engineering may allow electrons to achieve a few oscillations before scattering. As this phenomenon is fascinating from a condensed matter point of view, it also opens new perspectives for optics since charge oscillations naturally couple to radiation and offer a way to emit coherent radiation.

First Ktitorov [21] and then Ignatov and Romanov [22] addressed the problem theoretically with Boltzmann equations and succeeded to provide a definitive signature for Bloch oscillations in superlattices in terms of a particular spectral response: the Bloch oscillations are found to amplify electromagnetic field (optical gain) on the low energy side of the oscillation frequency, while they absorb photons on the high energy side. This particular shaped gain – Bloch gain – is the main feature (in terms of photonics) of the Bloch oscillator. A series of experiments [222, 223, 224] using pulsed ultrafast techniques have successfully shown the existence of Bloch oscillations as electrons are pumped in a higher energy band and collectively oscillate over their dephasing time. However, the Bloch gain extends to zero frequencies and the structure becomes unstable in steady-state, so far preventing the observation of net gain in superlattices, although some evidence in photo current [225] and more recently in absorption [226] were demonstrated by driving superlattices with a strong terahertz field.

Recently, Bloch gain was investigated in a pure quantum mechanical perspective in a density matrix formalism, as reported by Willenberg *et al.*[7], and in also in a Green function formalism, as reported by Wacker.[227, 228] These theoretical work demonstrated that Bloch gain can arise between any pair of subbands in a semiconductor heterostructure and that the latter does not need to be a superlattice. As these theories do not require any specific shape for the heterostructure potential, Bloch gain should also be observed in a sample where an injection region has been inserted between active wells to stabilise electrically the structure, as it is routinely done in quantum cascade lasers. Moreover, the model of scattering-assisted gain allows to treat subbands with arbitrary populations, from perfect inversion (no lower state population), equal population (in which case it was shown numerically to yield the same results as Boltzmann models), to absorption (no upper state population) and therefore generalizes the concept of gain in semiconductor heterostructures.

The motivation of this work was to see if we were able to observe the spectral signatures predicted by this model in samples based on a single quantum well active region. The structures were designed to work in a regime of very low population inversion where theory of scattering-assisted gain predicts a dispersive shape of the gain, in contrast to the standard model where Lorentzian broadening is introduced in an *ad-hoc* manner. The use of more sophisticated models allows to create more accurate tools, for example to simulate transport in quantum cascade lasers,[217] and that then can be used to design new quantum cascade laser structures. Moreover, because scattering-assisted gain predicts gain in quantum cascade laser structures with small or negative population inversion, the understanding of structures working in this regime might help to develop THz quantum cascade lasers that work at room temperature, and to optimize high-temperature operation of QCLs in general. Additionally, the characteristic shape of the gain of these structures is expected to induce a strong dispersion which could be interesting for quantum cascade laser devices for applications where a broad tuning range is required.

6.2 Model

The model of scattering-assisted gain is developed in an analogous way to the pioneering work by Kazarinov and Suris (see section 2.3 in chapter 2) and is described in detail in the publication by Willenberg *et al.*[7]. The current is expressed in a density matrix formalism and an expression for the coherence between two (at first spatially separated) subband states that are coupled by tunneling and broadened by intrasubband scattering is developed. This coherence determines current density as well as optical transitions. In the work by Kazarinov and Suris second-order mechanisms were averaged-out and the resonance curve was found Lorentzian with a homogeneous broadening given by the average value of elastic scattering matrix elements. In this new model these second-order terms are kept and a new expression is found for the current density J between two spatially separated states and that is given by:[7]

$$J \;=\; \frac{q\,d\,|\hbar\Omega_{21}|^2}{\hbar} \sum_k \frac{\gamma_k^1\left(f_k^{22}-f_{q+}^{11}\right)+\gamma_k^2\left(f_{q-}^{22}-f_k^{11}\right)}{\epsilon^2+\left(\gamma_k^1+\gamma_k^2\right)^2} \tag{6.1}$$

where q is the electron charge, $d = z_{22} - z_{11}$ is the difference between the two centroids of the wave functions, $\hbar$ is Planck's constant divided by 2π, $\hbar\Omega_{21}$ is the coupling energy through the barrier, $\epsilon = \epsilon_{2k} - \epsilon_{1k}$ is the subband separation, f_k^{ii} is the carrier distribution in subband i at wave vector k and γ_k^i is the scattering-induced broadening of the transition. The in-plane momentum of the final states $q_\pm$ is given by:

$$q_\pm \;=\; \hbar^{-1}\sqrt{2m^*\left(\epsilon_k \pm \epsilon\right)} \tag{6.2}$$

For a detailed discussion of scattering-induced current in heterostructures we refer to the publication by Terazzi *et al.*[217]. We note that the current results from differences in population and that the result by Kazarinov and Suris can be obtained by allowing only transitions with identical initial and final states ($q_\pm = k$) and using a constant broadening γ:

$$J \;\approx\; \frac{q\,d\,|\hbar\Omega_{21}|^2}{\hbar}\,\frac{\gamma}{\epsilon^2+\gamma^2}\,\Delta n \tag{6.3}$$

where $\Delta n = \sum_k \left(f_k^{22} - f_k^{11}\right)$ is the density of excess electrons in either state and that drives the current. Although this approximation does predict the resonant current peaks in a superlattice that occur whenever ground and excited states align, it fails to account for the current between equivalent states in the Wannier-Stark ladder.

An expression is then developed for the photon-induced current and absorption. Transforming to the basis of eigen states of the biased heterostructure (the Wannier-Stark basis for the superlattice) the model is finally extended to describe optical transitions between any pair of subbands and yields for the absorption/gain:[7]

$$\alpha(\omega) \;=\; -\frac{q^2|z_{21}|^2\epsilon^2}{\varepsilon_0 n_\mathrm{r} c\hbar^2\omega}\sum_k \frac{\gamma_k^1\left(f_k^{22}-f_{k+}^{11}\right)+\gamma_k^2\left(f_{k-}^{22}-f_k^{11}\right)}{\left(\epsilon-\hbar\omega\right)^2+\left(\gamma_k^1+\gamma_k^2\right)^2} \tag{6.4}$$

where z_{21} is the dipole matrix element, $\epsilon = \epsilon_2 - \epsilon_1$ is the intersubband transition energy, f_k^{ii} is the distribution function and γ_k^i the homogeneous broadening of state i at wavevector k; q is the electron charge, ε_0 the vacuum permittivity, n_r the refractive index, c the speed of light and $\hbar$ is Plank's constant divided by 2π. The in-plane momenta of the final states are denoted by $k_{\pm} = \hbar^{-1}\sqrt{2m^{*}\left[\epsilon_k \pm (\epsilon - \hbar\omega)\right]}$.

The differences in population in Equ. (6.4) can be rewritten as

$$\gamma_k^1\left(f_k^{22} - f_{k+}^{11}\right) = \gamma_k^1\left[\underbrace{f_k^{22}\left(1 - f_{k+}^{11}\right)}_{\text{emission}|2>\rightarrow|1>} - \underbrace{f_{k+}^{11}\left(1 - f_k^{22}\right)}_{\text{absorption}|1>\rightarrow|2>}\right] \tag{6.5a}$$

$$\gamma_{\mathrm{k}}^2\left(f_{\mathrm{k}-}^{22} - f_{\mathrm{k}}^{11}\right) = \gamma_{\mathrm{k}}^2\left[\underbrace{f_{\mathrm{k}-}^{22}\left(1 - f_{\mathrm{k}}^{11}\right)}_{\text{emission}|2>\rightarrow|1>} - \underbrace{f_{\mathrm{k}}^{11}\left(1 - f_{\mathrm{k}-}^{22}\right)}_{\text{absorption}|1>\rightarrow|2>}\right] \tag{6.5b}$$

where the states $|2k\rangle$ and $|1k+\rangle$, respectively $|1\rangle$ and $|2k-\rangle$ are related by the emission/absorption of a non-resonant photon ($\hbar\omega < \epsilon$, $k \neq k+$, respectively $\hbar\omega > \epsilon$, $k \neq k-$), assisted by relaxation within the lower (upper) state via γ_{k}^1 (γ_{k}^2) that ensures momentum transfer. These different quantum-mechanical paths are illustrated in Fig. 6.1. As a consequence, as compared to direct transitions, the population inversion requirement for these second-order processes are relaxed, since population inversion is only necessary between states with different wavevector and not globally between subbands. For example, in the particular case were both subbands have the same populations, gain is achieved for photon energies smaller than the transition energy.

Willenberg *et al.* also calculated the generalized gain profile for a terahertz quantum cascade laser emitting at an energy of 18.7 meV. Calculations were performed assuming a constant relaxation time $\tau = 0.5\,\mathrm{ps}$ and a fixed upper state population of $n_2 = 3\times10^9\,\mathrm{cm}^2$. The population of the lower state was then varied between negligible lower state population and a population equal to the upper state and the generalized gain profile was calculated as a function of $\Delta n/n$. Resulting gain curves are shown in Fig. 6.2. It can be

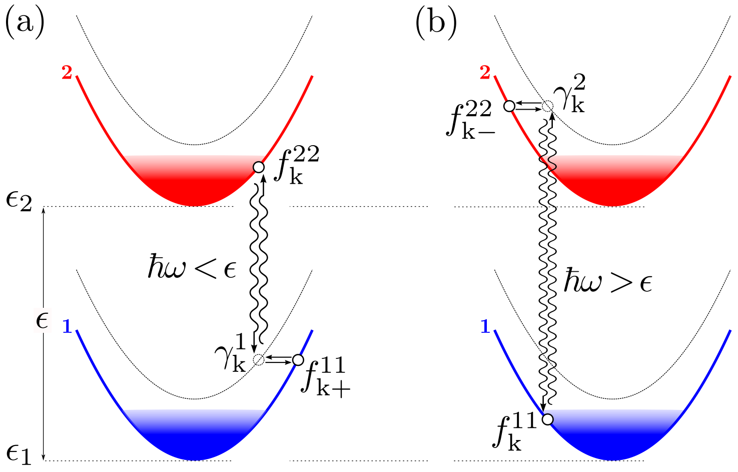

Figure 6.1: Quantum-mechanical paths in scattering-assisted gain

Possible quantum-mechanical paths for scattering-assisted transitions with non-resonant photons and connecting states with different wavevectors. (a) A “shorter” photon ($\hbar\omega < \epsilon$) *is absorbed/emitted due to transition into an intermediate state and subsequent relaxation into the final state. (b) Transitions with “larger” photons are also possible. Energy and momentum are conserved in these second-order processes.*

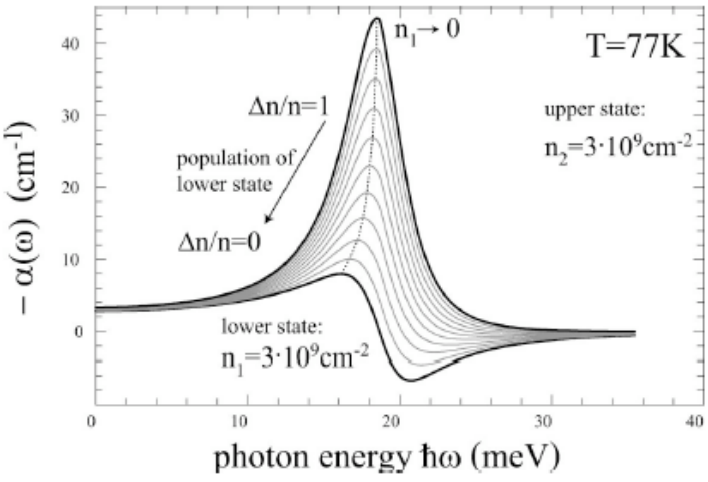

Figure 6.2: Generalized gain profile for quantum cascade laser

Generalized gain profile in a quantum cascade laser as calculated by Willenberg et al.[7] for a fixed upper state population $n_2 = 3\times10^9$ *cm*^{2} *and lower state population* n_1 *varying between* $n_1 = 0$ *and* $n_1 = n_2$*. Figure reprinted from Ref. [7].*

seen that for a small lower state population ($\Delta n \approx 1$) the gain is dominated by resonant photon emission due to the population inversion between equivalent k states. The gain profile is nearly Lorentzian-shaped and its height depends linearly with population inversion Δn. However, for the limiting case of equal populations the profile changes drastically into a dispersive shape, resembling the predicted gain of the semi-classical Bloch-oscillator. Gain is predicted for photons with energies below the transition energy whereas photons with higher energies are absorbed.

6.3 Single quantum well active regions

The shape of scattering-assisted gain is supposed to differ considerably from the one predicted by the Lorentzian model when the population inversion between the upper and lower level of the optical transition is small or negligible. Therefore, a set of structures with single quantum well active region has been grown. The conduction band structure of sample N258 at an applied bias of $48\,\mathrm{kV\,cm^{-1}}$ is shown in Fig. 6.3. The active period consists of an injection region coupled to an active quantum well by an injection and extraction tunnel barrier. Under the designed bias of $48\,\mathrm{kV\,cm^{-1}}$, the band structure is aligned so that electrons tunnel resonantly from the injector ground state $|g\rangle$ of the previous period to the upper lasing state $|2\rangle$. As shown in Ref. [156], the thickness of the injection barrier must be optimized: in the low coupling regime (thick injection barrier), the maximum current that can be injected in the upper state is proportional to the coupling strength; in the opposite (thin injection barrier) the maximum current is only limited by the upper state

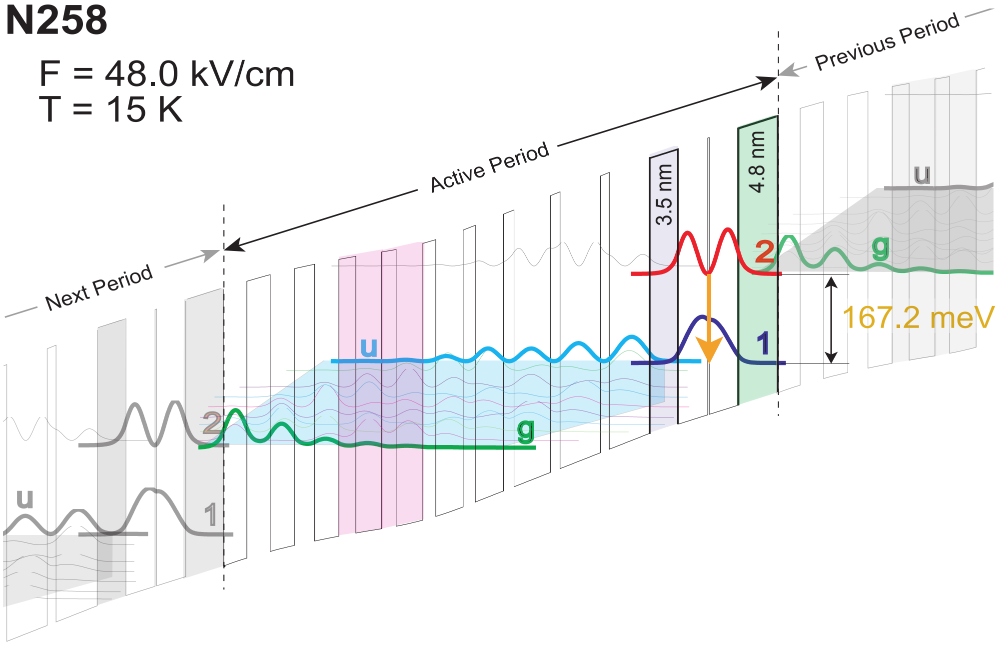

Figure 6.3: Band structure N258

Conduction band structure of sample N258 at an applied electric field of $48\,\mathrm{kV\,cm^{-1}}$ *and 15 K lattice temperature.*

Table 6.1: Thickness of the injection and extraction barriers, typical threshold current density and approximate value of the thickness dependent factor proportional to the tunneling rate. H_i is the barrier height for electrons occupying the eigen state with energy E_i, m_b is the electron effective mass in the barrier and $\hbar$ is Planck's constant divided by 2π.

Sample	w_inj [Å]	w_ext [Å]	J_th [kA cm^{-1}]	$e^{-2w_\mathrm{ext}\sqrt{2m_\mathrm{b}H_i}/\hbar}$ [s^{-1}]
N113	42	30	6.5[a]	5.1E-3
N127	42	35	5.6[b]	2.1E-3
N257	48	30	4.0[c]	5.1E-3
N258	48	35	4.8[d]	2.1E-3
N487	48	40	not lasing	8.7E-4

[a] R2b, 1720x20μm^2, 300 K
[b] B4b, 1510x47μm^2, 150 K
[c] R12b, 1910x22μm^2, 304 K
[d] R5b, 1920x26μm^2, 274 K

lifetime but leakage currents are then proportional to the coupling. Downfield of the active well, an extraction barrier allows to control population of the lower lasing state $|1\rangle$: since $|1\rangle$ is the ground state of the active well, coupling to the upper state $|u\rangle$ of the injector region is achieved by tunneling of electrons through the barrier; by varying the width thereof, the extraction time and therefore the population of the lower state can be tuned.

An overview of the samples is shown in Tab. (6.1) where the thickness of the injection and extraction barriers, typical threshold current densities and an approximate value of the factor $e^{-2\,w_\mathrm{ext}\sqrt{2m_\mathrm{b}H_i}/\hbar}$ that is proportional to the extraction tunneling rate[9] is indicated. As the table shows, due to the lower tunneling rate, we expect the population of the lower laser state of sample N487 to be approximately 2.4 times higher than for sample N258. For the layer thicknesses of the different samples that were designed to emit around $\lambda \approx 7.5\,\mu$m we refer to appendix C. Samples N113 and N127 with the thinner injection barrier showed very weak performances and sample N487 did not lase at cryogenic temperatures. Therefore in this chapter we will concentrate on samples N257 and N258.

Samples were grown using the InGaAs/AlInAs material system lattice matched on InP substrate and consisted in 35 periods of the injector/active region pair placed in the center of a standard optical waveguide with InP cladding layer. A few layers in the center of the injectors were Si-doped in order to yield a sheet density of $n_\mathrm{s} = 3\times10^{11}\,\mathrm{cm}^{-2}$ per period. The five designs are detailed in appendix C.5.

Despite the expected low population inversion and the relatively high doping in the active region and in the cladding layers devices lased up to room temperature; although with small peak powers and high threshold current densities. Typical power-current-voltage characteristics of 2.2 mm long samples of structure N257 and N258 are shown in Fig. 6.4. For sample N257 we measure a threshold current density that is $2.5\,\mathrm{kA\,cm}^{-2}$ at 183 K heat sink temperature and that increases to $4.4\,\mathrm{kA\,cm}^{-2}$ at 323 K. The characteristic temperature is $T_0 = 260\,\mathrm{K}$. Slope efficiency and peak power at 1 % duty-cycle are 0.68 W/A and 1.2 W at 183 K and 0.34 W/A and 0.25 W at 323 K. The population inversion is expected to be smaller in sample N258 and as it can be seen in Fig. 6.4 the threshold current density is higher than in sample N257 with $3.7\,\mathrm{kA\,cm}^{-2}$ at 183 K and $4.9\,\mathrm{kA\,cm}^{-2}$ at 276 K that also was the

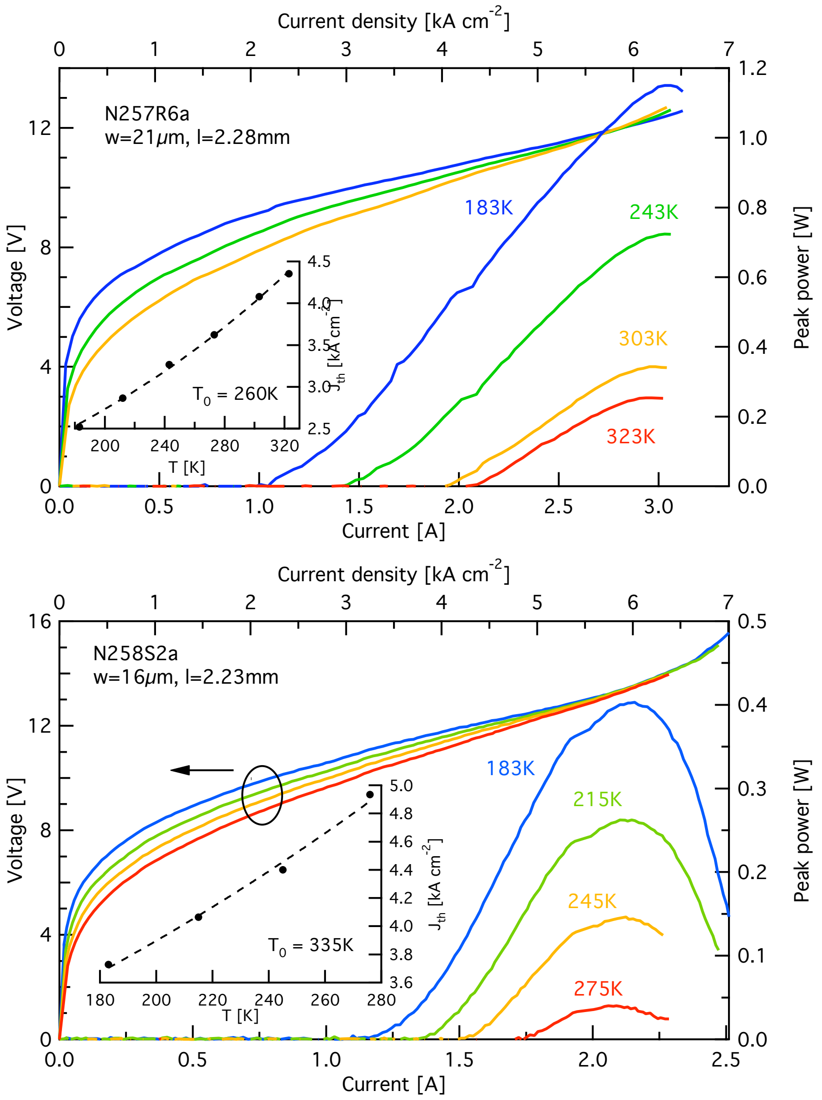

Figure 6.4: Current-voltage-power characteristics (N257/N258)

Current-voltage-power characteristics of samples N257 and N258 at heat sink temperatures between 183 and 323 K (N257) and measured in pulsed operation at 1 % duty-cycle (100 kHz, 100 ns pulse width). The figure insets show the threshold current density as a function of heat sink temperature and the dashed lines represent the least-squares fit with an exponential function $J_{\mathrm{th}} = J_0 \exp(T/T_0)$ *yielding the characteristic temperature* T_0*. Values of the threshold current density were obtained by fitting the linear part of the current-power curves and extrapolating to zero power (not shown).*

maximal operation temperature for this sample. The characteristic temperature is very high with a value of $T_0 = 335\,\mathrm{K}$ and slope efficiency and peak powers are 0.62 W/A and 0.4 W at 183 K and 0.18 W/A and 40 mW at 276 K.

6.3.1 Low temperature gain measurements

Low temperature gain measurements were performed using a variant of the multi-section cavity technique described in section 3.6 of chapter 3. At cryogenic temperatures the dynamical resistance of the structure at low bias is extremely high what makes the sample very sensitive to currents leaking through the etched region. Therefore, a 360 μm long intermediate section has been introduced that is continuously biased at baseline voltage (see section 3.6) and further reduces the crosstalk between light source and amplifier sections. Due to limitation of the number of input ports on the cryostat this intermediate section was connected through a low-pass LC filter directly to the amplifying section. Characteristics of this filter are detailed in appendix A.6. A relatively wide measurement window from 140 to 190 μm was obtained by driving the light source section above the onset of negative differential resistance (NDR). In this manner, the injection process is non-resonant and does not only populate the upper state but also the quasi-continuum of states lying above, providing a broad emission spectrum.

In a first step the baseline voltage was determined. As Fig. 6.5(a) shows with a baseline setting of -5.3 VDC on the HP8114 pulse generator a flat absorption spectrum could be obtained where resonant absorption and emission processes cancel each other out and only waveguide and free-carrier absorp-

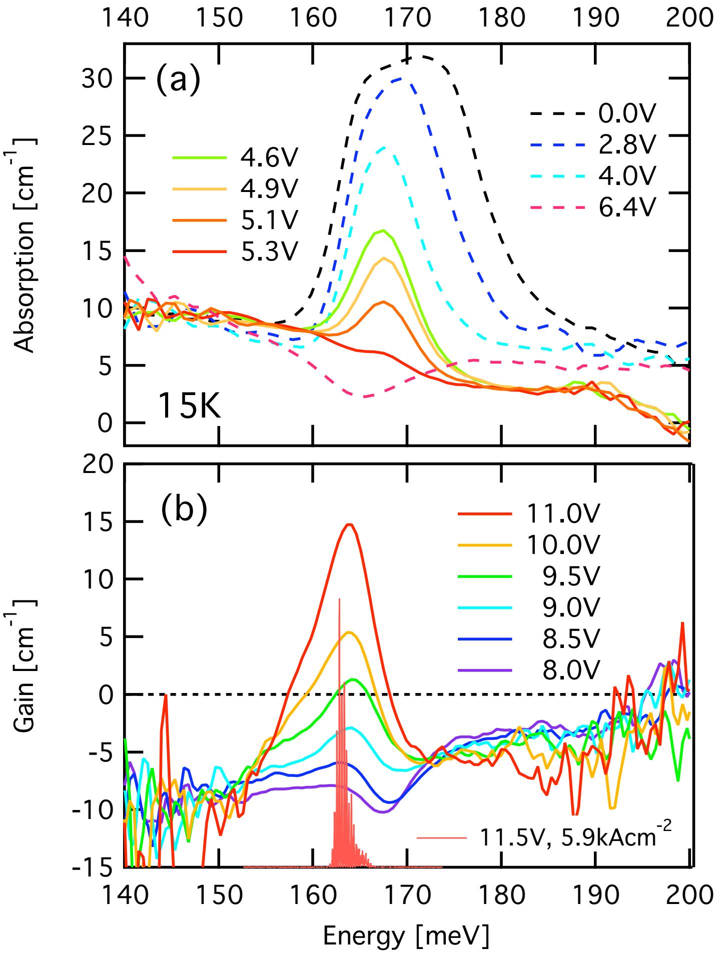

Figure 6.5: Low temperature gain measurements (N258, 15K)

(a) Absorption measurements as a function of baseline voltage. At -5.3 VDC a relatively flat condition is reached where resonant absorption and emission processes cancel each other out and only waveguide and free-carrier absorption persist. Dashed lines represent measurements that have been performed a day earlier and show an offset of 5 cm^{-1} *at higher energies due to stability issues with the setup. Voltages indicated reflect the setting on the pulse generator and do not represent the voltage applied to the structure. (b) Modal gain as a function of the bias voltage applied to the amplifier section. Voltages range between 8 and 11 V and the resulting current densities between 0.16 and 5.0 kA cm*$^{-2}$*. On the same graph the emission spectrum of a laser with 16 µm wide and 1.24 mm long cavity at a bias of 11.5 V is shown.*

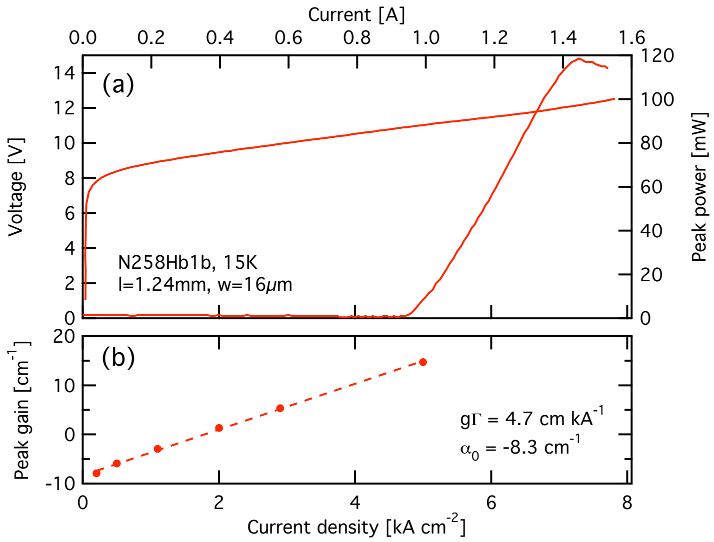

Figure 6.6: Current-voltage-power characteristics and peak gain (N258)
(a) Current-voltage-power characteristics of a 1.24 mm long and 16 μm wide laser device at 15 K heat sink temperature. (b) Peak value of the measured modal gain as a function of injected current. The dashed line represents the linear fit yielding a gain coefficient of 4.7 cm kA^{-1} and an offset of -8.3 cm^{-1}.

tion persists. Lower biases result in a strong resonant absorption between the lower and upper laser level in the single quantum well active region and that peaks at 0 V where the measurement probably saturates.

Once the optimal baseline voltage had been determined the differential gain with respect to this baseline was measured with biases on the amplifying section ranging between 8 and 11 V resulting in current densities between 0.16 and 5.0 kA cm^{-2}. Measured gain spectra obtained by subtracting the baseline absorption spectrum from the differential gain spectra are shown in Fig. 6.5(b). At the lower current densities the gain shows a clear dispersive shape, with gain for photon energies below the expected transition energy and loss at higher energies. As the current is increased, a more symmetric shape is recovered, indicating an improvement in the population inversion as the injection is made more resonant. An emission spectrum of a 1.24 mm long and 16 μm wide laser device[1] at same heat sink temperature and an applied bias of 11.5 V is shown in the same figure. The position of the laser emission agrees well with the position of the measured gain peak. Current-voltage-power characteristics of this laser are shown in Fig. 6.6(a) and the peak value of the measured gain is plotted in Fig. 6.6(b) as a function of injected current. We observe a linear dependence between the peak value of the modal gain and injected current with a gain coefficient of 4.7 cm kA^{-1} and an offset of -8.3 cm^{-1}. The predicted value for the threshold current density of a 1.24 mm long laser with 10 cm^{-1} of mirror losses would therefore be 4.0 kA cm^{-2}. A higher value of 4.8 kA cm^{-2} was measured which can be attributed to higher waveguide losses in the laser that was fabricated from the same material as the samples for gain measurements with etched notches between sections.

As a reference, we also studied a sample emitting at similar wavelength and based on a coupled well with vertical optical transition where a strong population inversion is expected due to its efficient lower state LO-phonon depopulation.[229] Gain measurements of the control sample yield gain curves whose shape was almost symmetric for the whole range of injected current.[1]

6.3.2 High temperature gain measurements

The gain of samples N257 and N258 was also measured at higher temperatures. However, no baseline setting could be found at which the resonant ab-

---

[1] Actually it was recycled from the gain measurement device after the latter partially burned.

sorption is suppressed without excessively heating the waveguide core. With structure N258 at 274 K heat sink temperature and a baseline of 6 VDC the remaining resonant absorption still had a peak value of 25 cm^{-1} and therefore samples without intermediate section had to be used to shorten the path for the probe light. Results are shown in Fig. 6.7(a) for structure N257 and Fig. 6.7(b) for structure N258 where the dashed line represents the measured absorption at 6 VDC baseline. Gain measurements as a function of the current injected into the amplifier section are shown as continuous, colored curves. Both samples show a strong absorption feature at 165 meV as a consequence of the large electron population in the lower lasing state. The absorption measured in sample N258 is significantly stronger. We attribute this to the thicker extraction barrier, resulting in a longer lower state lifetime and therefore a larger lower-state population. The gain peak is red-shifted with respect to the electroluminescence spectrum (not shown) that peaks at approximately the same energy as the measured baseline absorption and that is very different to samples with large population inversion as discussed in chapter 5. This suggests that even at high current densities the population inversion is very small.

Although the heat sink temperature was held constant at 274 K we noticed that the temperature of the active region was considerably higher due to self-heating caused by the high baseline setting of 6 VDC that resulted in a continuous current of approximately 0.6 $\mathrm{kA\,cm}^{-2}$. In a separate experiment the peak position of the electroluminescence at applied biases of 10 and 11 V was measured as a function of the heat sink temperature. The data is shown in Fig. 6.8(a) where the position of the electroluminescence

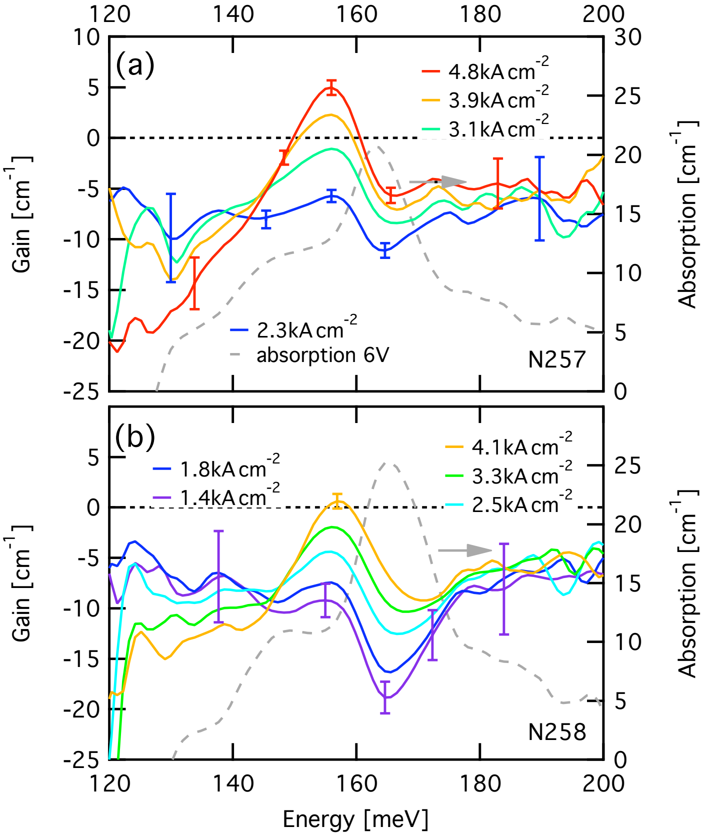

Figure 6.7: High temperature gain measurements (N257/N258)
Spectrally resolved modal gain of structures N257 (a) and N258 (b) measured at 274 K heat sink and 330 K (estimated) active region temperature. Dashed lines represent the absorption during measurement conditions (6V baseline) and full lines the spectral gain for given current injected into the amplifying section. The increasing absorption with increasing current that appears below 150 meV is an artifact due to electrical crosstalk between sections.

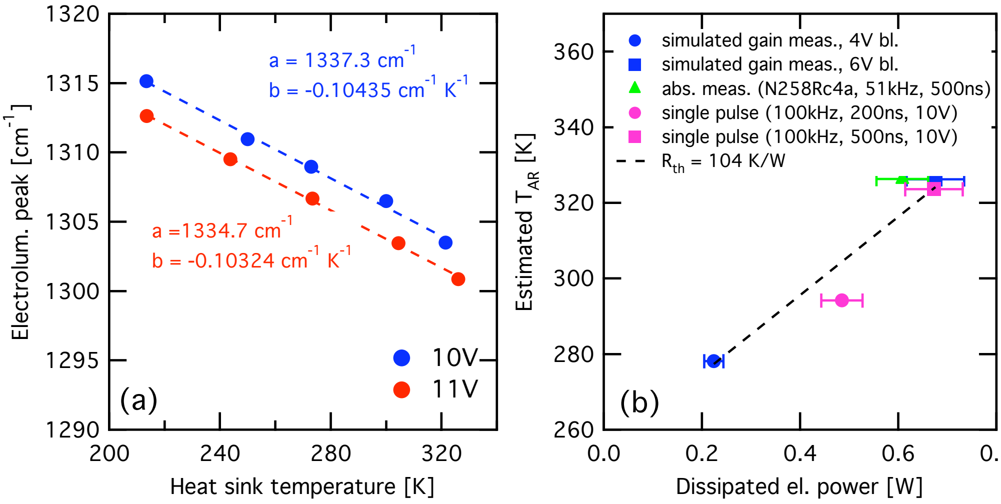

Figure 6.8: Estimation of active region temperature (N258)

(a) Position of the electroluminescence peak as a function of heat sink temperature for applied biases of 10 and 11 V and yielding tuning coefficients of -0.104 and -0.103 $\mathrm{cm}^{-1}\,\mathrm{K}^{-1}$*, respectively (dashed lines). (b) Estimated active region temperature as a function of dissipated electrical power. The dashed line represents a least-squares fit yielding a thermal resistance of 104 K/W for the 360* μ*m long section.*

peak is plotted as a function of heat sink temperature for applied biases of 10, respectively 11 V. For an applied bias of 10 V a tuning coefficient of -0.104 $\mathrm{cm}^{-1}\,\mathrm{K}^{-1}$ was determined. Electroluminescence was then measured at 274 K heat sink temperature simulating gain measurements with 4 and 6 VDC baseline, respectively and the center of the electroluminescence peak together with calibration data was used to determine the active region temperature. We determined an active region temperature of 330 K for the measurements with 6 VDC baseline setting and that did not vary considerably with the intensity of the current pulses, as the total power dissipated in the device was dominated by the high baseline voltage. In order to cross-check our estimated active region temperatures we plotted the latter as a function of the calculated dissipated electrical power. As it is shown in Fig. 6.8(b) the data points together with some control points lie approximately on a line, yielding a thermal resistance of 104 K/W for the 360 μm long section.

Evolution of the peak gain with increasing current is shown in Fig. 6.9(a) where sample N257 is represented by squares and sample N258 by circles. Within the measured current range from 2.3 to5 kA cm^{-2} for sample N257 and 1.4 to 4.1 kA cm^{-2} for sample N258 we find a linear relationship between peak gain and current. A linear fit yields gain coefficients $g = [4.3 \pm 0.5]$ cm kA^{-1} and $g = [3.7 \pm 0.9]$ cm kA^{-1} and offset values of $[15.1 \pm 1.8]$ cm^{-1} and $[14.0 \pm 2.9]$ cm^{-1} for samples N257 and N258, respectively. Fig. 6.9(b) shows gain coefficients for samples N257 (diamonds) and N258 (squares) as a function of temperature and compares them, in case of sample N258, to the values obtained from the analysis of the dependence of the threshold current of lasers with cavity length (circles). We find a good agreement for gain coefficients of sample N258 where both methods yield an almost constant gain coefficient with temperature. The systematic offset of approximately 0.8 cm kA^{-1} is attributed to the uncertainty of the current measurements. This situation is clearly different to the one of lasers working with a strong population inversion where the temperature dependence of the gain coefficient is mainly governed by the decrease of the upper-state lifetime of the lasing transition due to optical-phonon scattering as shown in chapter 5. In case of sample N257 working with a larger population inversion higher gain but also a stronger dependence of the gain coefficient with temperature is expected.

In Fig. 6.9(c) the values of the total waveguide losses obtained by extrapolation of the peak gain to zero current are shown for samples N257 (diamonds) and N258 (squares). In the measured temperature range values vary between 12.7 and 15.0 cm^{-1} for sample N257 and between 8.6 and 14.0 cm^{-1} for sample N258. Values obtained from $1/L$-measurements with lasing devices of structure N258 are represented as circles in the same graph, and they vary between 13.5 cm^{-1} at 183 K and 19.3 cm^{-1} at 273 K. Both techniques measure the same property of the laser and are therefore expected to yield the same results, however big uncertainties associated with the measurements make it difficult to give a value for the waveguide losses and to determine the temperature dependence. We expect it to be somewhere between 10 and 13 cm^{-1}. Calculation of the losses of the empty waveguide treating the active region as a bulk semiconductor with the same average doping and considering free-carrier absorption yields waveguide losses of 4.1 cm^{-1}. The difference is attributed to resonant absorption from the highly populated lower state of the lasing transiton to the upper state on one hand and to coupling losses and absorption in the unbiased segment (as discussed in section 3.6.3 of chapter 3) on the other hand.

6.3.3 Simulations

Although the design of these single quantum well structures looks simple at a first glance, their gain turned out to be very tedious to simulate. Because they operate in a regime of small population inversion they are very sensitive to the latter. Fig. 6.10(a) shows the simulation of the current-voltage characteristics and (b) of the electron population density in the upper and lower

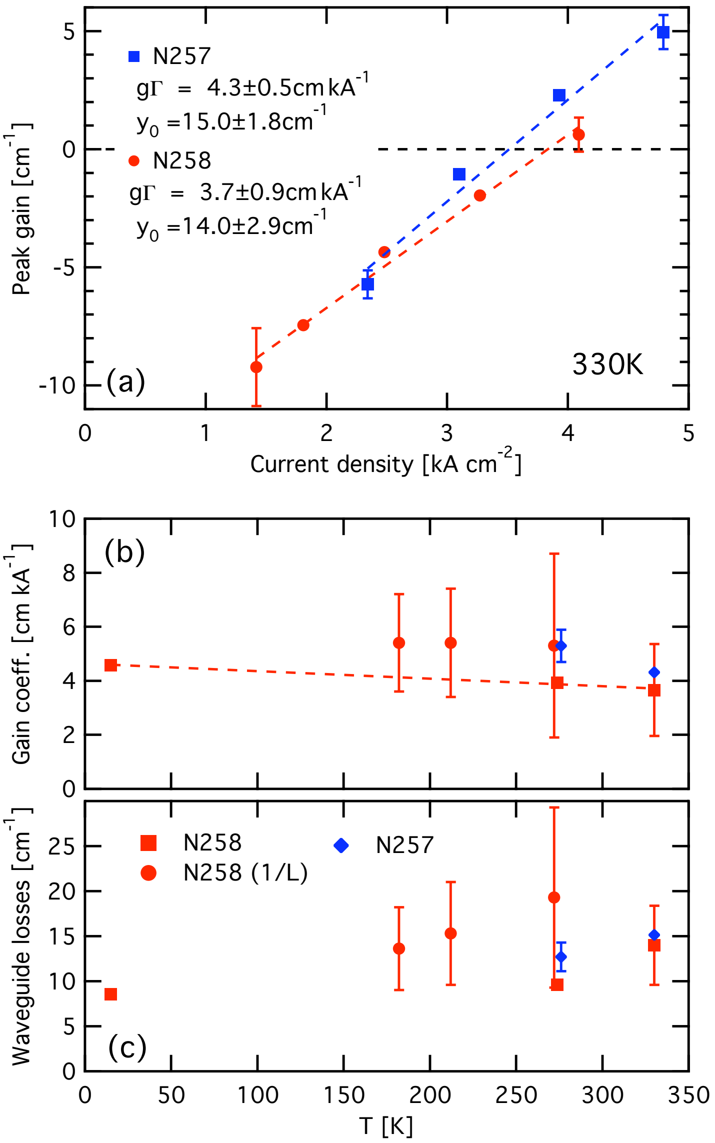

Figure 6.9: Quantitative gain analysis (N257/N258)

(a) Peak gain of devices N257 (blue) and N258 (red) as a function of injected current at 274 K heat sink and estimated 330 K active region temperature. Dashed lines show the linear fits yielding modal gain coefficient and zero-bias absorption. (b) Modal gain coefficients of devices N257 (blue) and N258 (red) as a function of temperature. Gain coefficients determined for device N258 using 1/L-measurements are shown as red circles. (c) Total waveguide losses as a function of temperature for the same devices as in (b).

states of the laser transition. The simulation code was developed by Terazzi *et al.*[217] and calculates the carrier transport of heterostructures through resonant tunneling and takes into account explicitly elastic scattering. As can be seen in Fig. 6.10(a) an excellent agreement between the simulated current-voltage characteristics and the measured ones is obtained if we assume a global electron temperature $T_\mathrm{e} = 50\,\mathrm{K}$ and a series resistance in the measurement setup of $1\,\Omega$ that is very reasonable for a pulsed measurement. The carrier population n_2 of the upper state shows a steady increase with current that corresponds to an upper state lifetime of $\tau = 0.66\,\mathrm{ps}$. However, the lower state population, as shown in Fig. 6.10(b), is unstable and a population inversion is never attained – in contradiction to the gain measurements that indicate a positive population inversion at higher currents.

The gain profile predicted by the model of scattering-assisted transitions was therefore calculated assuming a global electron temperature $T_\mathrm{e} = 50\,\mathrm{K}$ and an upper state lifetime $\tau = 0.66\,\mathrm{ps}$, as determined by the transport simulation, but fixating the lower state population to a constant value. Results are shown in Fig. 6.11 for lower state populations $n_1 = 8.5\times10^{9}\,\mathrm{cm}^{-2}$ (dashed lines) and $n_1 = 1.3\times10^{10}\,\mathrm{cm}^{-2}$ (continuous lines), respectively. We find a relatively good agreement between the measured gain in Fig. 6.5(b) and the simulated profile. Although far from perfect, it reproduces the transition from a dispersively-shaped gain profile at low current to a nearly Lorentzian-shaped profile at high current densities as observed in the measured gain spectra, and suggests that the lower state population is situated around a value of approximately $n_1 = 9\times10^{9}\,\mathrm{cm}^{-2}$. Looking at the difference between the maximum and minimum values of the gain over the probed current range

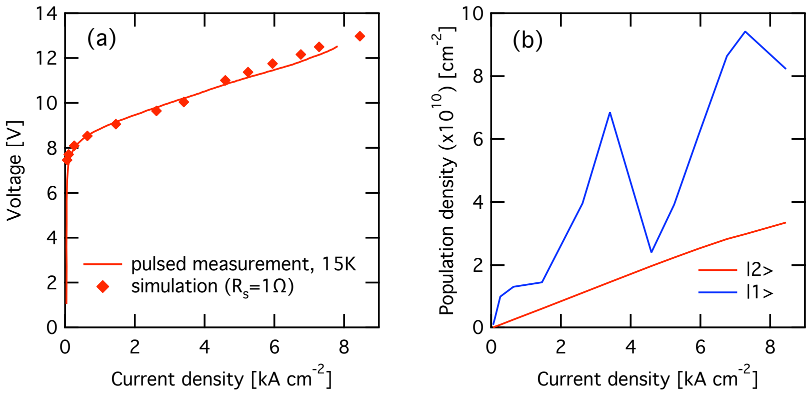

Figure 6.10: Transport simulation (N258, 15K)

(a) Simulation of the current-voltage characteristics of sample N258 at 15 K (dots). The continuous line represents data measured on sample N258Hb1b in pulsed operation. Simulation was performed assuming a global electron temperature of $T_\mathrm{e} = 50$ *K and a series resistance of 1* Ω *was assumed that is very reasonable for a pulsed measurement. (b) Simulated population density of the upper (red) and lower (blue) states of the laser transition. The population of the upper state increases linearly with injected current, corresponding to upper state lifetime of* $\tau = 0.66$ *ps.*

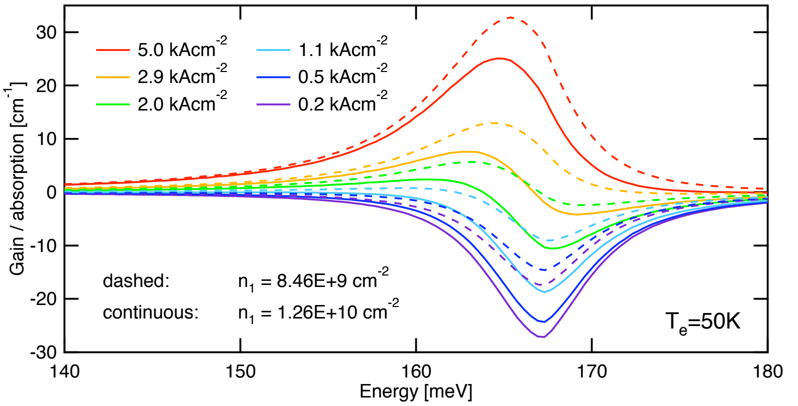

Figure 6.11: Model gain (N258, 15K)

Gain calculated according to the model of scattering-assisted transitions, and including non-parabolicity of the subbands. For the upper state a lifetime of $\tau = 0.66\,ps$ *was assumed and the population of the lower state was held constant at* $n_1 = 8.5 \times 10^9\ cm^{-2}$ *(dashed lines), respectively* $n_1 = 1.3 \times 10^{10}\ cm^{-2}$ *(continuous lines).*

we find that the simulation yields a value of approximately $35\,\mathrm{cm}^{-1}$ that is about 40 % higher than measured ($\approx 25\,\mathrm{cm}^{-1}$). We attribute this to a slight underestimation of the gain on the experimental side due to un-accounted absorption and coupling losses in the $20\,\mu$m long, unbiased waveguide segments separating the different sections on the sample. On the theoretical side the crude assumption of constant lower state population and uncertainties on the input parameters for the simulation lead to a big uncertainty associated with the amplitude of the gain profile.

In order to include the non-parabolicity of the bands, all energies, including the wavevectors k_+ and k_- at which the distribution functions are evaluated were computed assuming an energy-dependent effective mass with the form $m^*(E) = m^*(0)(1 + E/E_G)$ where E_G is the effective gap.[149] Although inclusion of the non-parabolicity was important to achieve a good agreement between the shape of the experimental data and the theory, the key ingredient needed to predict both dispersive shape and right magnitude of the gain curve is the Bloch component of the second-order gain and not the non-parabolicity.

Chapter 7

Conclusion

In this work we presented different approaches in the domain of active region and waveguide engineering of mid-infrared quantum cascade lasers.

We fabricated quantum cascade lasers with large optical cavity waveguides that exhibit very high peak powers and we show that using this approach we obtain a slope efficiency that is close to the optimum value that is reached with a hypotetical rectangular mode profile. Furthermore the relatively flat mode intensity profile delays the onset of gain saturation in the active region periods that are in the center of the waveguide core where the mode ususally has the highest intensity. Moreover, the spatially extended mode profile leads to a narrow farfield and the sharp decline of the mode intensity at outside the waveguide core reduces the overlap with lossy layers and thus reduces the waveguide losses. The introduction of passive regions in the waveguide core helps to stabilize the electric field inside the waveguide core which can be important for structures with many active region periods and they also improve the thermal conductance of the device. We have also shown that the thermal conductance of the device is increased comparing to a single-stack active region core and can be further increased by using InP inter-stacks. Due to the use of non-optimized active regions with high threshold current densities and limitations in the fabrication process that lead to wide waveguide ridges with very trapezoidal cross section the energy dissipated in the device was very high ($30 - 40\,\mathrm{W}$). This resulted in a heat-extraction bottle neck and limited the operation of these devices to low duty-cycles. Performance of these devices could be considerably improved by optimizing the active region and its doping as well as the doping of the inter-stacks and cladding layers for low threshold current as well as advanced processing techniques.

Quantum cascade lasers are seen as ideal sources of coherent radiation in many spectroscopic applications in the mid-infrared region. The material system based on the $\mathrm{Ga_{0.47}In_{0.53}As}$ and $\mathrm{Al_{0.48}In_{0.52}As}$ materials that are lattice-matched to the InP substrate they are grown on is very well mastered makes it easy to fabricate waveguides. However, the conduction band discontinuity of this material system limits the emission wavelength of devices with acceptable performance to above $\lambda \approx 5\,\mu\mathrm{m}$. A way that has been proven to be very successful is to use the same materials but change their composition in order to add strain to the layers and thus increase the conduction band discontinuity. After introducing the framework that allows us to calculate the band structure of these strain-compensated designs and predicts the correct emission wavelengths at different temperatures we present active region designs with spikes. These structures are grown with relatively low strain in the layers ($\pm\,0.5\,\%$) and locally add spikes of AlAs and InAs with sub-monolayer thickness in the barriers and wells, respectively, that are close to the lasing transition. Using this concept several devices emitting at $\lambda \approx 4.5\,\mu$m and $\lambda \approx 4.8\,\mu$m were fabricated. Devices worked in continuous-wave operation up to room temperature and a maximal average power of 200 mW was observed at 303 K.

Last but not least we presented an improved technique that allows to measure the gain of a quantum cascade laser structure by dividing the waveguide in multiple, independently driven sections that are biased with a suitable sequence of pulses. This technique is self-aligned, allows to measure gain at high current densities and high temperatures and the spectral width of the measurement is limited by the width of the structure's electroluminescence spectrum at a given probe current. Furthermore the measurement yields a direct, quantitative measurement of the gain. Although the method used to electrically isolate the regions needs to be developed further and adapted to the low-loss buried-heterostructure processes that are routinely done in our group today, this method provides a convenient way to measure the gain and absorption in future structures and use the results to refine the models in our simulations.

We also used this technique to measure the gain and absorption in structures that are based on single-quantum-well active regions and that work in a regime of very weak or vanishing population inversion between the upper and lower electronic states of the lasing transition. At low population inversion these samples show a dispersive spectral gain curve that resembles the one of a superlattice whereas with increasing upper-state population a more Lorentzian-shaped gain curve is recovered. We showed that the evolution of this gain is predicted by a model that also includes scattering-assisted transitions between the two subband states. Although the usefulness of devices based on single-quantum-well active regions and working in a regime of low inversion may appear questionable, samples with a dispersively shaped gain might be interesting for niche applications. Due to the dispersive gain shape we expect a change of the active region's refractive index that is much larger than for a conventional active region. This could be an interesting feature to achieve a wider tuning range in distributed feedback quantum cascade lasers.

Appendix A

Equipment

A.1 IST Wideband Current Probe

Manufacturer:	Integrated Sensor Technologies http://www.isensortech.com/
Model:	711 S
Rise time:	<1.3 ns
Pulse width:	5-2000 ns
Sensitivity:	1 V/A (@50 Ω)
Accuracy:	±2 %

For current measurements with high duty-cycle the measurement needs to be corrected by

$$I_{\text{real}} = \frac{I_{\text{meas}}}{1 - dc}$$

where I_{real} is the real current, I_{meas} is the measured current and dc is the duty-cycle.

A.2 Sonoma Instr. 310 Low Noise Amplifier

Manufacturer:	Sonoma Instrument http://www.sonoma-instrument.com/
Model: 310 Low Noise Amplifier	
Bandwidth:	9 kHz - 1 GHz
Gain:	32 dB (@100 MHz, 50 Ω load)
Equivalent input noise voltage:	$0.55\,\mathrm{nV}/\sqrt{\mathrm{Hz}}$ (5-500 MHz)
Impedance:	50 Ω

A.3 Kolmar Tech. PV-HgCdTe Detector

Manufacturer:	Kolmar Technologies, Inc. `http://www.kolmartech.com`
Model:	KMPV11-0.1-J1/DC
Serial No.:	3802-1 C
Active area:	7.85E-05 cm^2
Detector responsivity:	6.97 A/W
Quantum efficiency:	0.87 (peak) @0.06V bias
Peak wavelength:	10 μm
Cut-off wavelength:	12.37 μm
Rise time:	11 ns
Bandwidth:	20 MHz (-3dB)
D^*:	2.23E+10 Jones (@ 10 μm, 50 kHz)
Responsivity:	6.97E+04 V/W

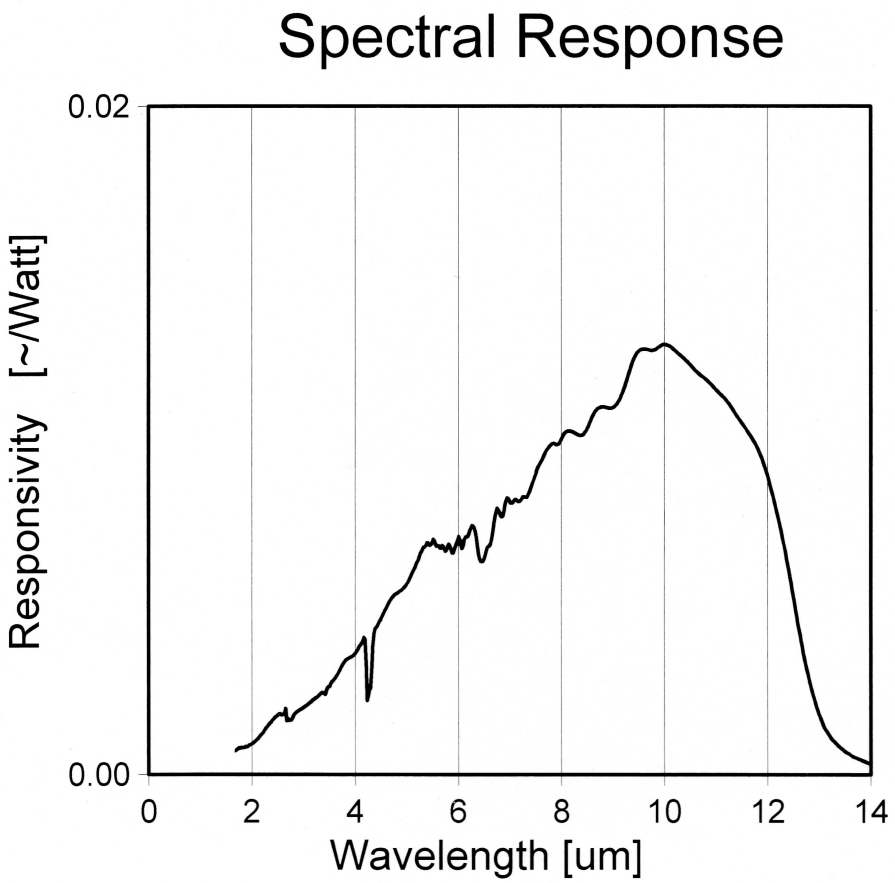

A.4 Graseby Infrared PC-HgCdTe Detector

Manufacturer:	Graseby Infrared, Ltd.
Model:	FTIR-M16-0.25
Serial No.:	GIL-2085-W
Active area:	6.25E-04 cm^2
Detector responsivity:	18382 V/W (16 mA biasing current)
Peak wavelength:	13.8 μm
Cut-off wavelength:	16.8 μm
D^*:	5.1E+10 Jones (@ peak, 10 kHz)

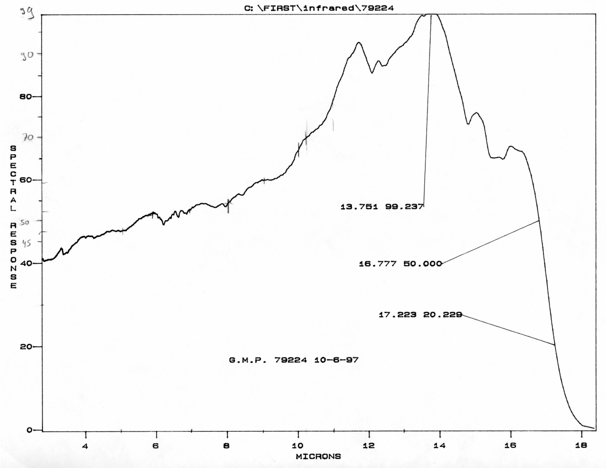

A.5 RT-HgCdTe Detector

Manufacturer:	Vigo System Ltd.
Model:	PEM-L-3
Serial No.:	554
Active area:	1 mm^2
Spectral range:	2-12 μm
Response time:	<0.5 ns
Voltage responsivity:	0.045 V/W
Peak wavelength:	8 μm
D^*:	>4E+6 Jones (@ 10.6 μm)
D^*:	>8E+6 Jones (@ peak)
Operation frequency range:	DC to 800 MHz

A.6 Low-pass LC-filter for intermed. section

The figure below shows the equivalent circuit of the low-pass LC-filter that was used to bias the middle section of sample N258H1b for low-temperature gain measurements (see section 6.3.1, chapter 6). Simulations were performed with the "Quite Universal Circuit Simulator" (QUCS)[1] and the sections were represented by equation defined devices (EDD) described by

$$I = 7.6\times 10^{-2} \cdot \exp(V - 10.5) \qquad [\mathrm{A}]$$

that was obtained by fitting the low-temperature current-voltage characteristics of structure N258.

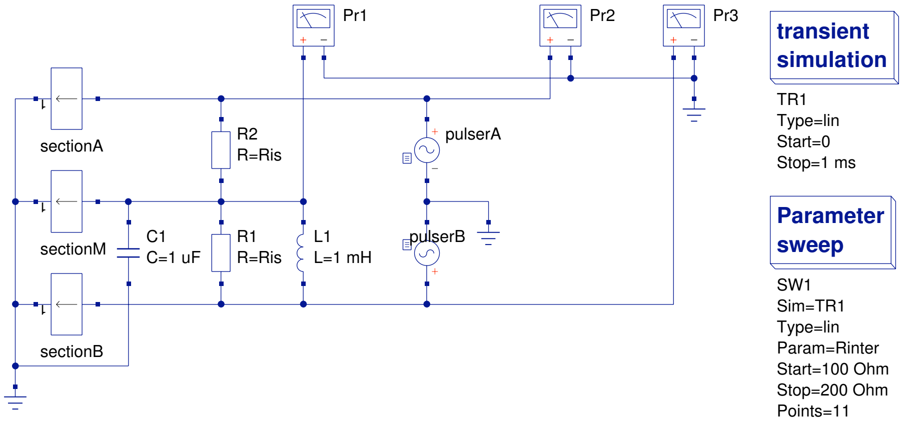

A transitent simulation using the same pulse sequence and parameters (frequency 51020 Hz, 300 ns pulse width, 5 V baseline) and sweeping the intersection resistance between 100 and 200 Ω is shown below. Bias voltages for the probe and amplifying pulses were 10 V.

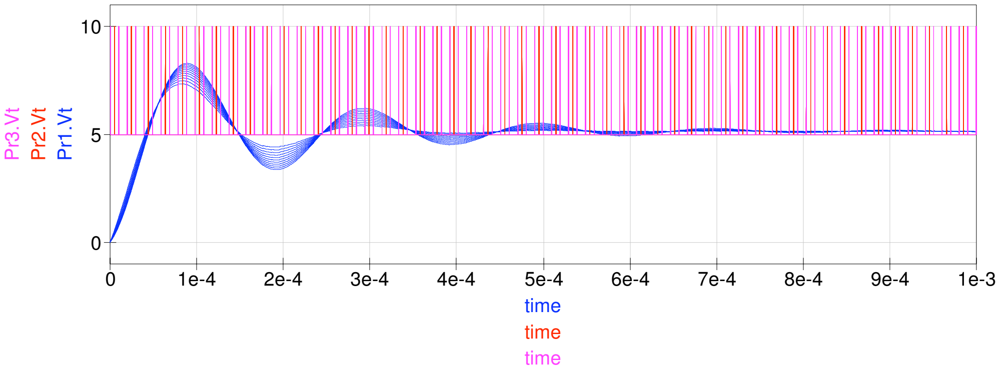

---

[1] `qucs.sourceforge.net`

As the simulations show after some ring-in time of approximately 1 ms a stable voltage of 5.15 V is obtained to bias the intermediate section. The remaining voltage ripples have an amplitude of maximal 0.02 V and their influence is therefore negligible.

However, the bias voltage of the intermediate section slightly depends on the voltage that is applied to the amplifier section and that is varied. This is shown in the next figure where the pulse voltage on section $\mathcal{B}$ has been varied between 8 and 11 V.

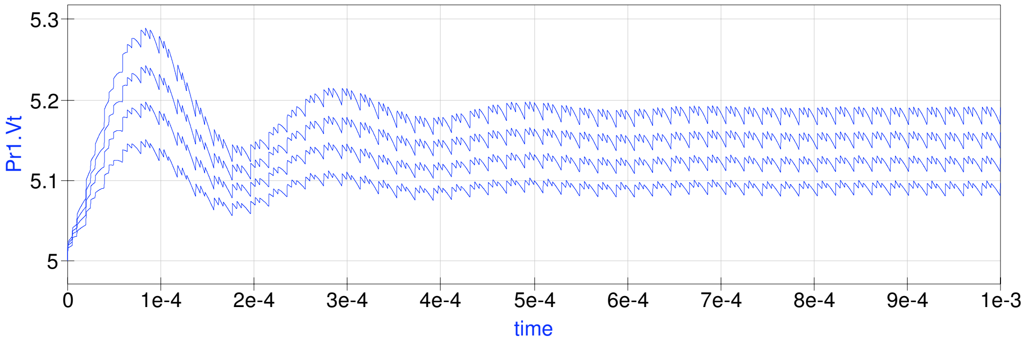

Simulations show that the voltage varies by 0.1 V when the pulse voltage on section $\mathcal{B}$ is changed between 8 and 11 V. Looking at the absorption measurements in section 6.3.1 of chapter 6 we see that the peak of the absorption changes by approximately 5 cm^{-1} when the bias voltage is changed by 0.2 V. In our situation (0.1 V variation, 380 μm long section) this translates into a maximal uncertainty of 0.1 cm^{-1} at the center of the absorption peak due to variation of the bias voltage of the intermediate section.

Appendix B

Measurement procedures

B.1 Electroluminescence measurements

B.1.1 Phase adjustment

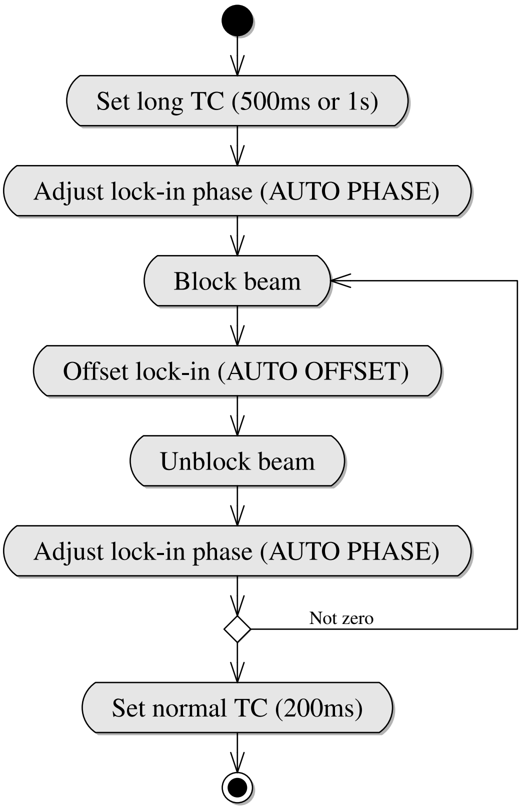

B.1.2 Spectrum measurement

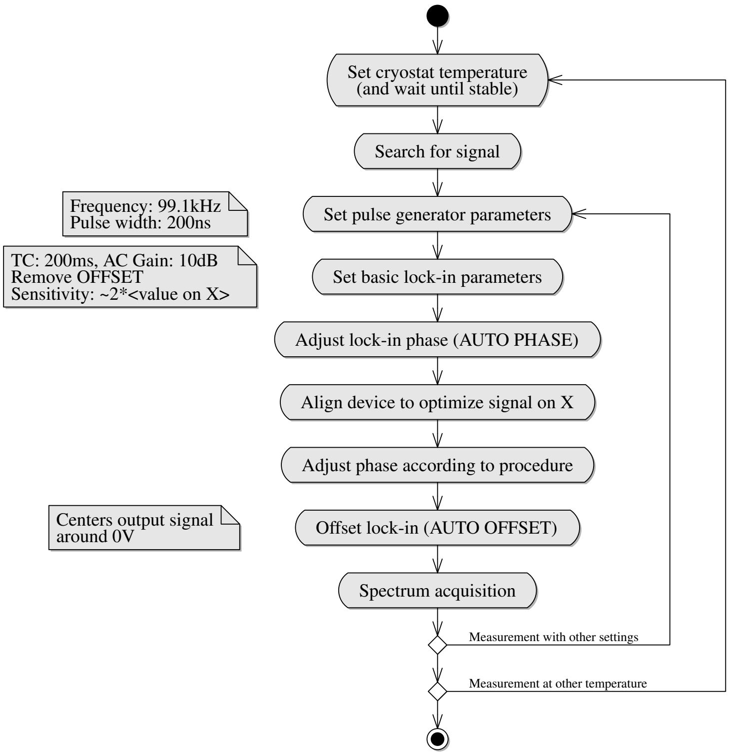

B.1.3 Current measurement

This procedure allows to measure correctly the current flowing into section $\mathcal{B}$ despite finite inter-section resistance.

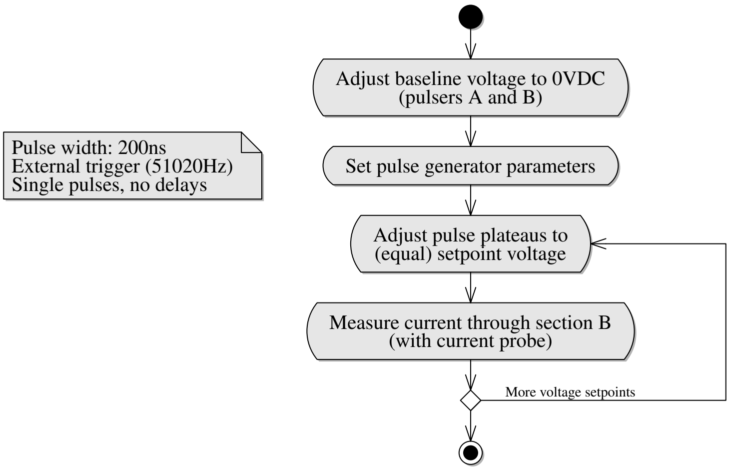

B.2 Multi-section cavity measurements

B.2.1 Absorption measurement

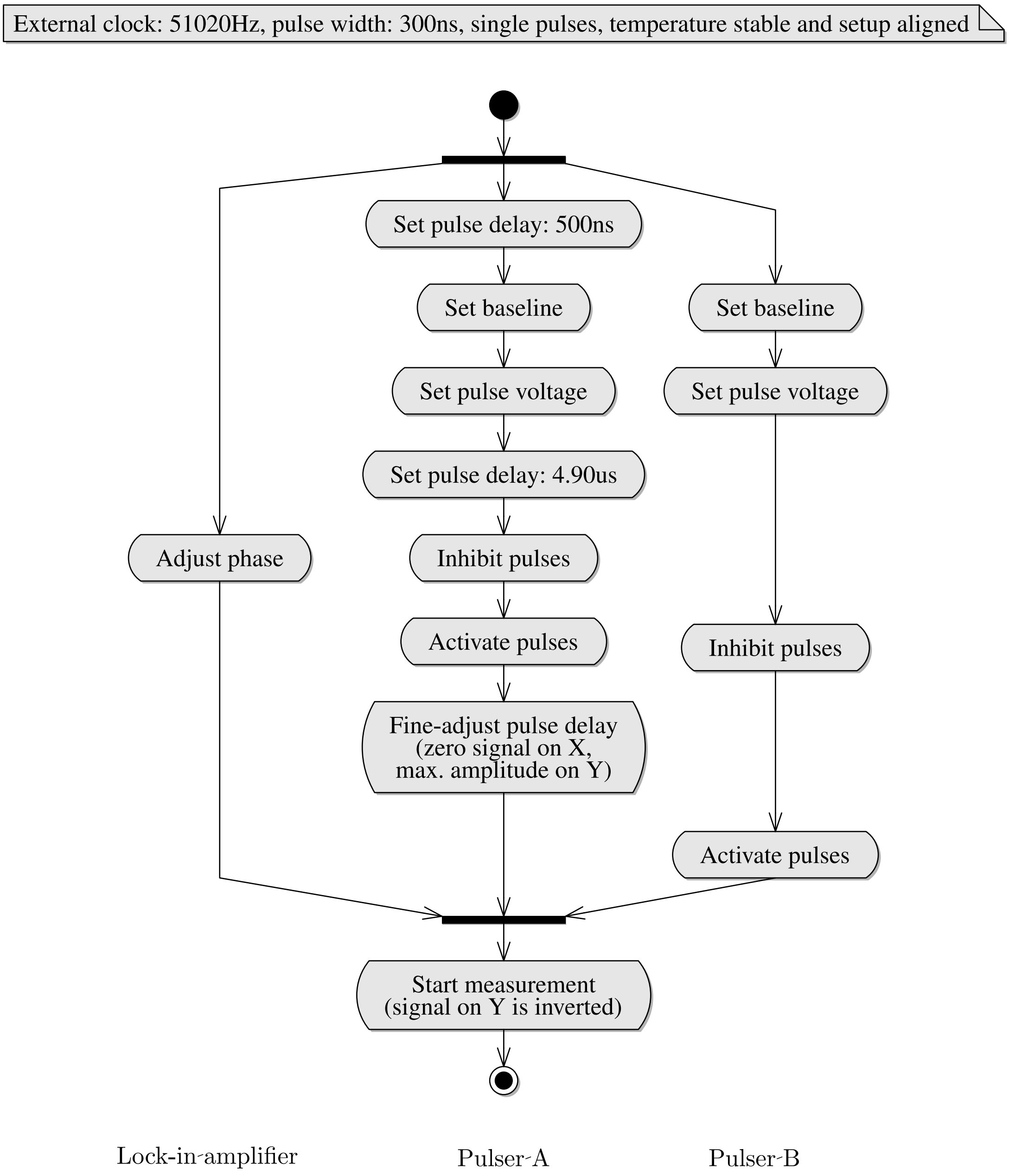

External clock: 51020Hz, pulse width: 300ns, single pulses, temperature stable and setup aligned

B.2.2 Gain measurement

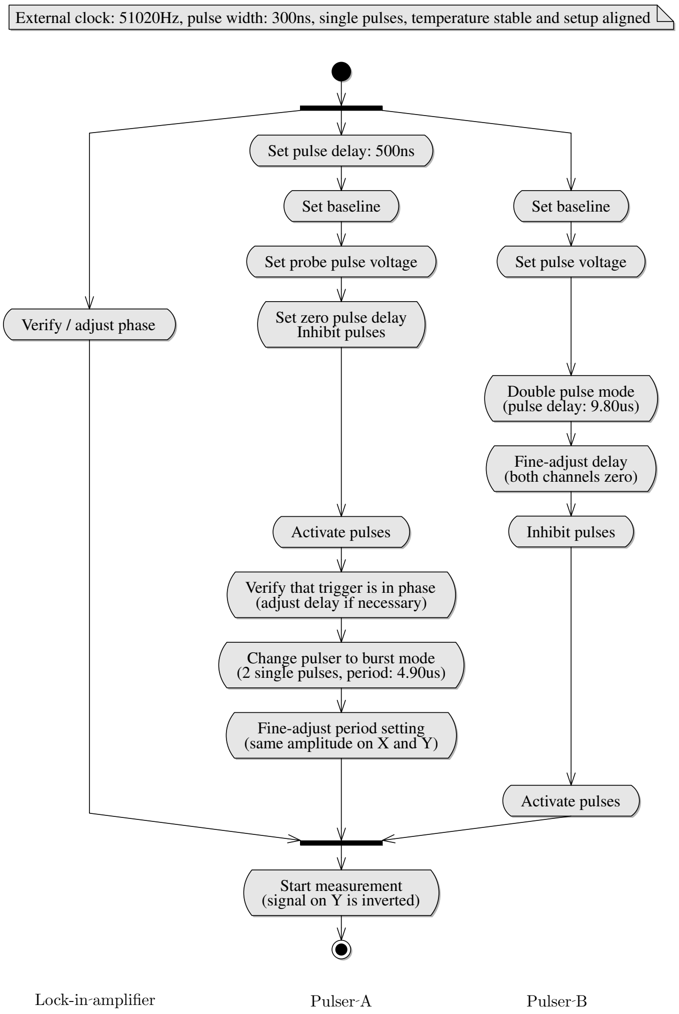

B.2.3 Notes

The generation of the two pulses with a HP8114A pulse generator: There are two ways to generate two pulses that are trigged externally. The first way is to generate a “pulse stream” of “double pulses”. In this mode the period between the two pulses is set by the “double delay” setting and it is used for the pulse generator of section $\mathcal{B}$ because only this mode allows to specify a period equal or longer than half the period of the trigger signal. The second possibility is to generate a “burst” of “2-single pulses”. The period between the pulses is set by the “period” setting and the “delay” setting can therefore be used to delay the pulses with respect to the trigger signal. This additional freedom can be used to synchronize the pulses between sections $\mathcal{A}$ and $\mathcal{B}$.

Appendix C

Active region designs

C.1 N113 (lattice-matched)

Material	Thickness [Å]	Doping [cm^{-3}]	
AlInAs	42	*i*	Act. region
InGaAs	36	*i*	
AlInAs	2	*i*	
InGaAs	36	*i*	
AlInAs	30	*i*	Injector region
InGaAs	51	*i*	
AlInAs	11	*i*	
InGaAs	50	*i*	
AlInAs	12	*i*	
InGaAs	45	*i*	
AlInAs	13	*i*	
InGaAs	35	*i*	
AlInAs	15	*i*	
InGaAs	34	3.0E+17	
AlInAs	16	3.0E+17	
InGaAs	33	3.0E+17	
AlInAs	18	3.0E+17	
InGaAs	32	*i*	
AlInAs	21	*i*	
InGaAs	30	*i*	
AlInAs	25	*i*	
InGaAs	30	*i*	
AlInAs	29	*i*	
InGaAs	29	*i*	

Several structures have been grown with varying injection and extraction barrier thicknesses. The table below lists the respective thicknesses:

Sample	w_{inj} [Å]	w_{ext} [Å]
N113	42	30
N127	42	35
N257	48	30
N258	48	35
N487	48	40

C.2 D121 (lattice-matched, MOVPE-grown)

Material	Thickness [Å]	Doping [cm^{-3}]	
AlInAs	37	*i*	Active region
InGaAs	23	*i*	
AlInAs	7	*i*	
InGaAs	65	*i*	
AlInAs	9	*i*	
InGaAs	62	*i*	
AlInAs	11	*i*	
InGaAs	58	*i*	
AlInAs	13	*i*	
InGaAs	44	*i*	
AlInAs	14	*i*	
InGaAs	40	*i*	
AlInAs	15	*i*	Injector region
InGaAs	37	*i*	
AlInAs	18	9.0E+16	
InGaAs	35	9.0E+16	
AlInAs	20	9.0E+16	
InGaAs	34	9.0E+16	
AlInAs	21	*i*	
InGaAs	33	*i*	
AlInAs	22	*i*	
InGaAs	33	*i*	

C.3 N515 / N543 (strain-compensated)

Material	Thickness [Å]	Doping [cm^{-3}]	
AlInAs	42	*i*	Active region
InGaAs	13	*i*	
AlInAs	14	*i*	
InGaAs	50	*i*	
AlInAs	15	*i*	
InGaAs	44	*i*	
AlInAs	16	*i*	
InGaAs	39	*i*	
AlInAs	18	*i*	
InGaAs	29	*i*	
AlInAs	19	*i*	Injector region
InGaAs	26	*i*	
AlInAs	20	8.2E+16[1]	
InGaAs	23	1.1E+17[2]	
AlInAs	21	8.2E+16[1]	
InGaAs	22	1.1E+17[2]	
AlInAs	23	*i*	
InGaAs	21	*i*	
AlInAs	30	*i*	
InGaAs	21	*i*	

Materials are $Ga_{0.406}In_{0.594}As$ (0.41 % compressive strain) in the wells and $Al_{0.561}In_{0.439}As$ (0.58 % tensile strain) in the barriers.

---

[1] N543: 9.8E+16

[2] N543: 1.3E+17

C.4 N505 / N513 (strain-compensated)

Material	Thickness [Å]	Doping [cm^{-3}]	
AlInAs	46	*i*	Active region
InGaAs	9	*i*	
AlInAs	14	*i*	
InGaAs	20	*i*	
InAs	2	*i*	
InGaAs	19	*i*	
AlInAs	7	*i*	
AlAs	2	*i*	
AlInAs	7	*i*	
InGaAs	18	*i*	
InAs	2	*i*	
InGaAs	17	*i*	
AlInAs	8	*i*	
AlAs	2	*i*	
AlInAs	7	*i*	
InGaAs	16	*i*	
InAs	2	*i*	
InGaAs	15	*i*	
AlInAs	11	*i*	Injector region
AlAs	2	*i*	
AlInAs	10	*i*	
InGaAs	12	*i*	
InAs	2	*i*	
InGaAs	12	*i*	
AlInAs	10	*i*	
AlAs	2	*i*	
AlInAs	9	*i*	
InGaAs	23	*i*	
AlInAs	22	*i*	
InGaAs	20	*i*	
AlInAs	23	*i*	
InGaAs	19	*i*	
AlInAs	25	*i*	
InGaAs	18	2.7E+17[1]	
AlInAs	30	2.0E+17[2]	
InGaAs	17	2.7E+17[1]	
AlInAs	34	2.0E+17[2]	
InGaAs	16	*i*	
AlInAs	36	*i*	
InGaAs	16	*i*	

Materials are $Ga_{0.391}In_{0.609}As$ (0.51 % compressive strain) in the wells and $Al_{0.546}In_{0.454}As$ (0.48 % tensile strain) in the barriers.

---

[1] N513: 2.0E+17

[2] N513: 1.5E+17

C.5 N664 / N665 / N808 / N810 (strain-compensated)

Material	Thickness [Å]	Doping [cm^{-3}]	
AlInAs	46	*i*	Active region
InGaAs	10	*i*	
AlInAs	14	*i*	
InGaAs	20	*i*	
InAs	2	*i*	
InGaAs	21	*i*	
AlInAs	7	*i*	
AlAs	2	*i*	
AlInAs	7	*i*	
InGaAs	19	*i*	
InAs	2	*i*	
InGaAs	18	*i*	
AlInAs	8	*i*	
AlAs	2	*i*	
AlInAs	7	*i*	
InGaAs	13	*i*	
InAs	2	*i*	
InGaAs	2	*i*	
InAs	2	*i*	
InGaAs	13	*i*	
AlInAs	9	*i*	Injector region
AlAs	2	*i*	
AlInAs	2	*i*	
AlAs	2	*i*	
AlInAs	9	*i*	
InGaAs	11	*i*	
InAs	2	*i*	
InGaAs	2	*i*	
InAs	2	*i*	
InGaAs	10	*i*	
AlInAs	7	*i*	
AlAs	2	*i*	
AlInAs	2	*i*	
AlAs	2	*i*	
AlInAs	8	*i*	
InGaAs	12	*i*	
InAs	2	*i*	
InGaAs	12	*i*	
AlInAs	10	*i*	
AlAs	2	*i*	
AlInAs	10	*i*	
InGaAs	24	1.4E+17[1]	
AlInAs	23	1.0E+17[2]	
InGaAs	22	1.4E+17[1]	
AlInAs	25	1.0E+17[2]	
InGaAs	21	*i*	
AlInAs	30	*i*	
InGaAs	20	*i*	
AlInAs	33	*i*	
InGaAs	19	*i*	
AlInAs	37	*i*	
InGaAs	18	*i*	

Materials are $Ga_{0.391}In_{0.609}As$ (0.51 % compressive strain) in the wells and $Al_{0.546}In_{0.454}As$ (0.48 % tensile strain) in the barriers.

---

[1] N808/N810: 1.1E+17

[2] N808/N810: 8.1E+16

Appendix D

Waveguide designs

D.1 N505 / N513

MBE	0.85 μm	AlInAs (LM)[1]	Si: $n = 2\,\mathrm{E}{+}18\,\mathrm{cm}^{-3}$
	1.2 μm	AlInAs (LM)	Si: $n = 1\,\mathrm{E}{+}17\,\mathrm{cm}^{-3}$
	0.9 μm	GaInAs (LM)	Si: $n = 4\,\mathrm{E}{+}16\,\mathrm{cm}^{-3}$
	0.99 μm	17× active region (SC)[2]	[1]Si: $n = 3.8\,\mathrm{E}{+}16\,\mathrm{cm}^{-3}$
	0.5 μm	GaInAs (LM)	Si: $n = 4\,\mathrm{E}{+}16\,\mathrm{cm}^{-3}$
	0.99 μm	17× active region (SC)	[3]Si: $n = 3.8\,\mathrm{E}{+}16\,\mathrm{cm}^{-3}$
	0.5 μm	GaInAs (LM)	Si: $n = 4\,\mathrm{E}{+}16\,\mathrm{cm}^{-3}$
	0.99 μm	17× active region (SC)	[3]Si: $n = 3.8\,\mathrm{E}{+}16\,\mathrm{cm}^{-3}$
	1 μm	GaInAs (LM)	Si: $n = 4\,\mathrm{E}{+}16\,\mathrm{cm}^{-3}$
		InP substrate	S: $n = 1-2\,\mathrm{E}{+}17\,\mathrm{cm}^{-3}$

---

[1] Lattice-matched to InP

[2] Strain-compensated layer

[3] Average active region doping for structure N513 is Si: $n = 2.9\,\mathrm{E}{+}16\,\mathrm{cm}^{-3}$

D.2 N515

MBE	0.85 μm	AlInAs (LM)	Si: $n = 2$ E+18 cm^{-3}
	1.4 μm	AlInAs (LM)	Si: $n = 1$ E+17 cm^{-3}
	1.1 μm	GaInAs (LM)	Si: $n = 4$ E+16 cm^{-3}
	1.01 μm	20× active region (SC)	Si: $n = 1.6$ E+16 cm^{-3}
	0.5 μm	GaInAs (LM)	Si: $n = 4$ E+16 cm^{-3}
	1.01 μm	20× active region (SC)	Si: $n = 1.6$ E+16 cm^{-3}
	0.5 μm	GaInAs (LM)	Si: $n = 4$ E+16 cm^{-3}
	1.01 μm	20× active region (SC)	Si: $n = 1.6$ E+16 cm^{-3}
	1.25 μm	GaInAs (LM)	Si: $n = 4$ E+16 cm^{-3}
		InP substrate	S: $n = 1-2$ E+17 cm^{-3}

D.3 N543

MOVPE	0.85 μm	InP	Si: $n = 2$ E+18 cm^{-3}
	1.2 μm	InP	Si: $n = 1$ E+17 cm^{-3}
MBE	1.1 μm	GaInAs (LM)	Si: $n = 4$ E+16 cm^{-3}
	1.06 μm	21× active region (SC)	Si: $n = 2.0$ E+16 cm^{-3}
	0.6 μm	GaInAs (LM)	Si: $n = 4$ E+16 cm^{-3}
	1.06 μm	21× active region (SC)	Si: $n = 2.0$ E+16 cm^{-3}
	1.1 μm	GaInAs (LM)	Si: $n = 4$ E+16 cm^{-3}
		InP substrate	S: $n = 1-2$ E+17 cm^{-3}

D.4 N810

MOVPE	0.4 μm	GaInAs (LM)	Si: $n = 2$ E+18 cm^{-3}
	2.0 μm	InP	Si: $n = 1$ E+17 cm^{-3}
MBE	1.0 μm	GaInAs (LM)	Si: $n = 4$ E+16 cm^{-3}
	1.22 μm	20× active region (SC)	Si: $n = 1.44$ E+16 cm^{-3}
	0.5 μm	GaInAs (LM)	Si: $n = 4$ E+16 cm^{-3}
	1.22 μm	20× active region (SC)	Si: $n = 1.44$ E+16 cm^{-3}
	0.5 μm	GaInAs (LM)	Si: $n = 4$ E+16 cm^{-3}
	1.22 μm	20× active region (SC)	Si: $n = 1.44$ E+16 cm^{-3}
	1.0 μm	GaInAs (LM)	Si: $n = 4$ E+16 cm^{-3}
		InP substrate	S: $n = 1-2$ E+17 cm^{-3}

D.5 N664 / N808

MOVPE	0.4 μm	InP	Si: $n = 2\,\mathrm{E}{+}18\,\mathrm{cm}^{-3}$
	2.0 μm	InP	Si: $n = 1\,\mathrm{E}{+}17\,\mathrm{cm}^{-3}$
MBE	0.3 μm	GaInAs (LM)	Si: $n = 4\,\mathrm{E}{+}16\,\mathrm{cm}^{-3}$
	1.52 μm	25× active region (SC)	[1]Si: $n = 1.8\,\mathrm{E}{+}16\,\mathrm{cm}^{-3}$
	0.2 μm	GaInAs (LM)	Si: $n = 4\,\mathrm{E}{+}16\,\mathrm{cm}^{-3}$
		InP substrate	S: $n = 1 - 2\,\mathrm{E}{+}17\,\mathrm{cm}^{-3}$

D.6 N665

MOVPE	0.4 μm	InP	Si: $n = 2\,\mathrm{E}{+}18\,\mathrm{cm}^{-3}$
	2.0 μm	InP	Si: $n = 1\,\mathrm{E}{+}17\,\mathrm{cm}^{-3}$
MBE	0.65 μm	GaInAs (LM)	Si: $n = 4\,\mathrm{E}{+}16\,\mathrm{cm}^{-3}$
	3.96 μm	65× active region (SC)	Si: $n = 1.8\,\mathrm{E}{+}16\,\mathrm{cm}^{-3}$
	0.65 μm	GaInAs (LM)	Si: $n = 4\,\mathrm{E}{+}16\,\mathrm{cm}^{-3}$
		InP substrate	S: $n = 1 - 2\,\mathrm{E}{+}17\,\mathrm{cm}^{-3}$

D.7 D121

MOVPE	0.3 μm	InP	Si: $n = 5\,\mathrm{E}{+}17\,\mathrm{cm}^{-3}$
	3.9 μm	InP	Si: $n = 4\,\mathrm{E}{+}16\,\mathrm{cm}^{-3}$
	0.43 μm	GaInAs (LM)	Si: $n = 2\,\mathrm{E}{+}16\,\mathrm{cm}^{-3}$
	1.0 μm	15× active region (LM)	Si: $n = 1.3\,\mathrm{E}{+}16\,\mathrm{cm}^{-3}$
	1.0 μm	InP	Si: $n = 2\,\mathrm{E}{+}16\,\mathrm{cm}^{-3}$
	1.0 μm	15× active region (LM)	Si: $n = 1.3\,\mathrm{E}{+}16\,\mathrm{cm}^{-3}$
	1.5 μm	InP	Si: $n = 2\,\mathrm{E}{+}16\,\mathrm{cm}^{-3}$
	1.0 μm	15× active region (LM)	Si: $n = 1.3\,\mathrm{E}{+}16\,\mathrm{cm}^{-3}$
	1.0 μm	InP	Si: $n = 2\,\mathrm{E}{+}16\,\mathrm{cm}^{-3}$
	1.0 μm	15× active region (LM)	Si: $n = 1.3\,\mathrm{E}{+}16\,\mathrm{cm}^{-3}$
	0.44 μm	GaInAs (LM)	Si: $n = 2\,\mathrm{E}{+}16\,\mathrm{cm}^{-3}$
	3.0 μm	InP	Si: $n = 4\,\mathrm{E}{+}16\,\mathrm{cm}^{-3}$
		InP (100) substrate	S: $n = 3\,\mathrm{E}{+}18\,\mathrm{cm}^{-3}$

---

[1] Average active region doping for structure N808 is Si: $n = 1.4\,\mathrm{E}{+}16\,\mathrm{cm}^{-3}$

Bibliography

[1] Romain Terazzi, Tobias Gresch, Marcella Giovannini, Nicolas Hoyler, Norihiko Sekine, and Jerome Faist. Bloch gain in quantum cascade lasers. *Nat Phys*, 3(5):329–333, 2007.

[2] Tobias Gresch, Romain Terazzi, Jérôme Faist, and Marcella Giovannini. Bloch gain in quantum cascade lasers at high temperature. *Applied Physics Letters*, 94(3):031102, 2009.

[3] Tobias Gresch, Jérôme Faist, and Marcella Giovannini. Gain measurements in strain-compensated quantum cascade laser. *Applied Physics Letters*, 94(16):161114, 2009.

[4] T. Gresch, M. Giovannini, N. Hoyer, and J. Faist. Quantum cascade lasers with large optical waveguides. *Photonics Technology Letters, IEEE*, 18(3):544–546, 1, 2006.

[5] A. Bismuto, T. Gresch, A. Bächle, and J. Faist. Large cavity quantum cascade lasers with inp interstacks. *Applied Physics Letters*, 93(23):231104, 2008.

[6] Miriam S. Vitiello, Tobias Gresch, Antonia Lops, Vincenzo Spagnolo, Gaetano Scamarcio, Nicolas Hoyler, Marcella Giovannini, and Jérôme Faist. Influence of inas, alas delta layers on the optical, electronic, and thermal characteristics of strain-compensated gainas/alinas quantum-cascade lasers. *Applied Physics Letters*, 91(16):161111, 2007.

[7] H. Willenberg, G. H. Döhler, and J. Faist. Intersubband gain in a bloch oscillator and quantum cascade laser. *Phys. Rev. B*, 67(8):085315, Feb 2003.

[8] A. L. Schawlow and C. H. Townes. Infrared and optical masers. *Phys. Rev.*, 112(6):1940–1949, Dec 1958.

[9] C. Cohen-Tannoudji, B. Diu, and F. Laloe. *Quantenmechanik, Tl.1.* de Gruyter, 1999.

[10] Theodore H. Maiman. Stimulated optical radiation in ruby. *Nature*, 187:493–494, August 1960.

[11] A. Javan, W. R. Bennett, and D. R. Herriott. Population inversion and continuous optical maser oscillation in a gas discharge containing a he-ne mixture. *Phys. Rev. Lett.*, 6(3):106–110, Feb 1961.

[12] H. Krömer. Proposed negative-mass microwave amplifier. *Phys. Rev.*, 109(5):1856, Mar 1958.

[13] Benjamin Lax. Cyclotron resonance and impurity levels in semiconductors. In C. H. Townes, editor, *Proceedings of the International Symposium on Quantum Electronics*, New York, 1960. Columbia University Press.

[14] T. M. Quist, R. H. Rediker, R. J. Keyes, W. E. Krag, B. Lax, A. L. McWhorter, and H. J. Zeigler. Semiconductor maser of gaas. *Applied Physics Letters*, 1(4):91–92, 1962.

[15] R. N. Hall, G. E. Fenner, J. D. Kingsley, T. J. Soltys, and R. O. Carlson. Coherent light emission from gaas junctions. *Phys. Rev. Lett.*, 9(9):366–368, Nov 1962.

[16] Marshall I. Nathan, William P. Dumke, Gerald Burns, Jr. Frederick H. Dill, and Gordon Lasher. Stimulated emission of radiation from gaas p-n junctions. *Applied Physics Letters*, 1(3):62–64, 1962.

[17] H. Kressel and H. Nelson. Close-confinement gaas p-n junction lasers with reduced optical loss at room temperature. *RCA Rev.*, 30:106–113, March 1969.

[18] I. Hayashi, M. Panish, and P. Foy. A low-threshold room-temperature injection laser. *Quantum Electronics, IEEE Journal of*, 5(4):211–212, Apr 1969.

[19] R. F. Kazarinov and R. A. Suris. Possibility of the amplification of electromagnetic waves in a semiconductor with a superlattice. *Sov. Phys.-Semicond.*, 5(4):707–709, Oct 1971.

[20] R. F. Kazarinov and R. A. Suris. Electric and electromagnetic properties of semiconductors with a superlattice. *Sov. Phys.-Semicond.*, 6(1):120–131, Jul 1972.

[21] S. Ktitorow, G. Simin, and V. Sindalovskii. n/a. *Fiz. Tverd. Tela*, 13:2230, 1971.

[22] Anatoly A. Ignatov and Yu. A. Romanov. Nonlinear electromagnetic properties of semiconductors with a superlattice. *Phys. Stat. Sol. (b)*, 73(1):327–333, 1976.

[23] R. Tsu and L. Esaki. Tunneling in a finite superlattice. *Applied Physics Letters*, 22(11):562–564, 1973.

[24] L. L. Chang, L. Esaki, and R. Tsu. Resonant tunneling in semiconductor double barriers. *Applied Physics Letters*, 24(12):593–595, 1974.

[25] L. Esaki and L. L. Chang. New transport phenomenon in a semiconductor "superlattice". *Phys. Rev. Lett.*, 33(8):495–498, Aug 1974.

[26] R. Tsu and G. Döhler. Hopping conduction in a "superlattice". *Phys. Rev. B*, 12(2):680–686, Jul 1975.

[27] R. Dingle, W. Wiegmann, and C. H. Henry. Quantum states of confined carriers in very thin algaas-gaas-algaas heterostructures. *Phys. Rev. Lett.*, 33(14):827–830, Sep 1974.

[28] T. C. L. G. Sollner, W. D. Goodhue, P. E. Tannenwald, C. D. Parker, and D. D. Peck. Resonant tunneling through quantum wells at frequencies up to 2.5 thz. *Applied Physics Letters*, 43(6):588–590, 1983.

[29] A. R. Bonnefoi, R. T. Collins, T. C. McGill, R. D. Burnham, and F. A. Ponce. Resonant tunneling in gaas/alas heterostructures grown by metalorganic chemical vapor deposition. *Applied Physics Letters*, 46(3):285–287, 1985.

[30] E. E. Mendez, W. I. Wang, B. Ricco, and L. Esaki. Resonant tunneling of holes in alas-gaas-alas heterostructures. *Applied Physics Letters*, 47(4):415–417, 1985.

[31] T. J. Shewchuk, P. C. Chapin, P. D. Coleman, W. Kopp, R. Fischer, and H. Morkoç. Resonant tunneling oscillations in a gaas-al[sub x]ga[sub 1 - x]as heterostructure at room temperature. *Applied Physics Letters*, 46(5):508–510, 1985.

[32] T. C. L. G. Sollner, P. E. Tannenwald, D. D. Peck, and W. D. Goodhue. Quantum well oscillators. *Applied Physics Letters*, 45(12):1319–1321, 1984.

[33] B. Ricco and M. Ya. Azbel. Physics of resonant tunneling. the one-dimensional double-barrier case. *Phys. Rev. B*, 29(4):1970–1981, Feb 1984.

[34] B. Jogai and K. L. Wang. Dependence of tunneling current on structural variations of superlattice devices. *Applied Physics Letters*, 46(2):167–168, 1985.

[35] Serge Luryi. Frequency limit of double-barrier resonant-tunneling oscillators. *Applied Physics Letters*, 47(5):490–492, 1985.

[36] M. B. Panish. Molecular beam epitaxy. *Science*, 208(4446):916–922, 1980.

[37] A. Y. Cho and J. R. Arthur. Molecular beam epitaxy. *Progress in Solid State Chemistry*, 10(Part 3):157–191, 1975.

[38] A. Y. Cho, C. N. Dunn, R. L. Kuvas, and W. E. Schroeder. Gaas impatt diodes prepared by molecular beam epitaxy. *Applied Physics Letters*, 25(4):224–226, 1974.

[39] A. Kamgar, P. Kneschaurek, G. Dorda, and J. F. Koch. Resonance spectroscopy of electronic levels in a surface accumulation layer. *Phys. Rev. Lett.*, 32(22):1251–1254, Jun 1974.

[40] E. Gornik and D. C. Tsui. Voltage-tunable far-infrared emission from si inversion layers. *Phys. Rev. Lett.*, 37(21):1425–1428, Nov 1976.

[41] A. Pinczuk, H. L. Strmer, R. Dingle, J. M. Worlock, W. Wiegmann, and A. C. Gossard. Observation of intersubband excitations in a multilayer two dimensional electron gas. *Solid State Communications*, 32(11):1001–1003, 1979.

[42] A. Harwit and Jr. J. S. Harris. Observation of stark shifts in quantum well intersubband transitions. *Applied Physics Letters*, 50(11):685–687, 1987.

[43] A. Harwit, Jr. J. S. Harris, and A. Kapitulnik. Calculated quasi-eigenstates and quasi-eigenenergies of quantum well superlattices in an applied electric field. *Journal of Applied Physics*, 60(9):3211–3213, 1986.

[44] M. Helm, P. England, E. Colas, F. DeRosa, and S. J. Allen. Intersubband emission from semiconductor superlattices excited by sequential resonant tunneling. *Phys. Rev. Lett.*, 63(1):74–77, Jul 1989.

[45] F. Capasso, R. Paiella, R. Martini, R. Colombelli, C. Gmachl, T.L. Myers, M.S. Taubman, R.M. Williams, C.G. Bethea, K. Unterrainer, H.Y. Hwang, D.L. Sivco, A.Y. Cho, A.M. Sergent, H.C. Liu, and E.A. Whittaker. Quantum cascade lasers: ultrahigh-speed operation, optical wireless communication, narrow linewidth, and far-infrared emission. *Quantum Electronics, IEEE Journal of*, 38(6):511–532, Jun 2002.

[46] Federico Capasso, Khalid Mohammed, and Alfred Y. Cho. Sequential resonant tunneling through a multiquantum well superlattice. *Applied Physics Letters*, 48(7):478–480, 1986.

[47] B. F. Levine, K. K. Choi, C. G. Bethea, J. Walker, and R. J. Malik. New 10 mu m infrared detector using intersubband absorption in resonant tunneling gaalas superlattices. *Applied Physics Letters*, 50(16):1092–1094, 1987.

[48] D. D. Coon, R. P. G. Karunasiri, and H. C. Liu. Fast response quantum well photodetectors. *Journal of Applied Physics*, 60(7):2636–2638, 1986.

[49] F. Capasso, K. Mohammed, and A. Cho. Resonant tunneling through double barriers, perpendicular quantum transport phenomena in superlattices, and their device applications. *Quantum Electronics, IEEE Journal of*, 22(9):1853–1869, Sep 1986.

[50] H. C. Liu. A novel superlattice infrared source. *Journal of Applied Physics*, 63(8):2856–2858, 1988.

[51] Jerome Faist, Federico Capasso, Carlo Sirtori, Debbie Sivco, Albert L. Hutchinson, Sung-Nee G. Chu, and Alfred Y. Cho. Mid-infrared field-tunable intersubband electroluminescence at room temperature by photon-assisted tunneling in coupled-quantum wells. *Applied Physics Letters*, 64(9):1144–1146, 1994.

[52] Jérôme Faist, Federico Capasso, Carlo Sirtori, Deborah L. Sivco, Albert L. Hutchinson, Sung Nee G. Chu, and Alfred Y. Cho. Narrowing of the intersubband electroluminescent spectrum in coupled-quantum-well heterostructures. *Applied Physics Letters*, 65(1):94–96, 1994.

[53] Jérôme Faist, Federico Capasso, Deborah L. Sivco, Carlo Sirtori, Albert L. Hutchinson, and Alfred Y. Cho. Quantum cascade laser. *Science*, 264(5158):553–556, 1994.

[54] Jérôme Faist, Federico Capasso, Carlo Sirtori, Deborah L. Sivco, James N. Baillargeon, Albert L. Hutchinson, Sung-Nee G. Chu, and Alfred Y. Cho. High power mid-infrared (lambda 5 mu m) quantum cascade lasers operating above room temperature. *Applied Physics Letters*, 68(26):3680–3682, 1996.

[55] Carlo Sirtori, Jérôme Faist, Federico Capasso, Deborah L. Sivco, Albert L. Hutchinson, S. N. George Chu, and Alfred Y. Cho. Continuous wave operation of midinfrared (7.4–8.6 mu m) quantum cascade lasers up to 110 k temperature. *Applied Physics Letters*, 68(13):1745–1747, 1996.

[56] C. Sirtori, J. Faist, F. Capasso, D. L. Sivco, A. L. Hutchinson, and A. Y. Cho. Long wavelength infrared (lambda [approximately-equal-to] 11 mu m) quantum cascade lasers. *Applied Physics Letters*, 69(19):2810–2812, 1996.

[57] Carlo Sirtori, Jerome Faist, Federico Capasso, Deborah L. Sivco, Albert L. Hutchinson, and Alfred Y. Cho. Quantum cascade laser with plasmon-enhanced waveguide operating at 8.4 mu m wavelength. *Applied Physics Letters*, 66(24):3242–3244, 1995.

[58] Carlo Sirtori, Claire Gmachl, Federico Capasso, Jérôme Faist, Deborah L. Sivco, Albert L. Hutchinson, and Alfred Y. Cho. Long-wavelength ($\lambda \approx 8 - 11.5 \mu$m) semiconductor lasers with waveguides based on surface plasmons. *Opt. Lett.*, 23(17):1366–1368, 1998.

[59] Jérome Faist, Claire Gmachl, Federico Capasso, Carlo Sirtori, Deborah L. Sivco, James N. Baillargeon, and Alfred Y. Cho. Distributed feedback quantum cascade lasers. *Applied Physics Letters*, 70(20):2670–2672, 1997.

[60] Claire Gmachl, Federico Capasso, Jerome Faist, Albert L. Hutchinson, Alessandro Tredicucci, Deborah L. Sivco, James N. Baillargeon, S. N. George Chu, and Alfred Y. Cho. Continuous-wave and high-power pulsed operation of index-coupled distributed feedback quantum cascade laser at lambda [approximate] 8.5 mu m. *Applied Physics Letters*, 72(12):1430–1432, 1998.

[61] Gaetano Scamarcio, Federico Capasso, Carlo Sirtori, Jerome Faist, Albert L. Hutchinson, Deborah L. Sivco, and Alfred Y. Cho. High-Power Infrared (8-Micrometer Wavelength) Superlattice Lasers. *Science*, 276(5313):773–776, 1997.

[62] Alessandro Tredicucci, Federico Capasso, Claire Gmachl, Deborah L. Sivco, Albert L. Hutchinson, and Alfred Y. Cho. High performance interminiband quantum cascade lasers with graded superlattices. *Applied Physics Letters*, 73(15):2101–2103, 1998.

[63] Alessandro Tredicucci, Federico Capasso, Claire Gmachl, Deborah L. Sivco, Albert L. Hutchinson, Alfred Y. Cho, Jérôme Faist, and Gaetano Scamarcio. High-power inter-miniband lasing in intrinsic superlattices. *Applied Physics Letters*, 72(19):2388–2390, 1998.

[64] Carlo Sirtori, Peter Kruck, Stefano Barbieri, Philippe Collot, Julien Nagle, Mattias Beck, Jérôme Faist, and Ursula Oesterle. GaAs/AlGaAs quantum cascade lasers. *Applied Physics Letters*, 73(24):3486–3488, 1998.

[65] Jérôme Faist, Federico Capasso, Deborah L. Sivco, Albert L. Hutchinson, Sung-Nee G. Chu, and Alfred Y. Cho. Short wavelength (lambda 3.4 mu m) quantum cascade laser based on strained compensated ingaas/alinas. *Applied Physics Letters*, 72(6):680–682, 1998.

[66] Shun Lien Chuang. Introduction to the feature issue on mid-infrared quantum-cascade lasers. *Quantum Electronics, IEEE Journal of*, 38(6):510–510, Jun 2002.

[67] J. Faist, D. Hofstetter, M. Beck, T. Aellen, M. Rochat, and S. Blaser. Bound-to-continuum and two-phonon resonance, quantum-cascade lasers for high duty cycle, high-temperature operation. *Quantum Electronics, IEEE Journal of*, 38(6):533–546, Jun 2002.

[68] C. Sirtori, H. Page, C. Becker, and V. Ortiz. Gaas-algaas quantum cascade lasers: physics, technology, and prospects. *Quantum Electronics, IEEE Journal of*, 38(6):547–558, Jun 2002.

[69] C. Gmachl, A. Straub, R. Colombelli, F. Capasso, D.L. Sivco, A.M. Sergent, and A.Y. Cho. Single-mode, tunable distributed-feedback and multiple-wavelength quantum cascade lasers. *Quantum Electronics, IEEE Journal of*, 38(6):569–581, Jun 2002.

[70] I. Vurgaftman and J.R. Meyer. Photonic-crystal distributed-feedback quantum cascade lasers. *Quantum Electronics, IEEE Journal of*, 38(6):592–602, Jun 2002.

[71] A.A. Kosterev and F.K. Tittel. Chemical sensors based on quantum cascade lasers. *Quantum Electronics, IEEE Journal of*, 38(6):582–591, Jun 2002.

[72] Mattias Beck, Daniel Hofstetter, Thierry Aellen, Jerome Faist, Ursula Oesterle, Marc Ilegems, Emilio Gini, and Hans Melchior. Continuous wave operation of a mid-infrared semiconductor laser at room temperature. *Science*, 295(5553):301–305, 2002.

[73] Rudeger Kohler, Alessandro Tredicucci, Fabio Beltram, Harvey E. Beere, Edmund H. Linfield, A. Giles Davies, David A. Ritchie, Rita C. Iotti, and Fausto Rossi. Terahertz semiconductor-heterostructure laser. *Nature*, 417(6885):156–159, 2002.

[74] Michel Rochat, Jérôme Faist, Mattias Beck, Ursula Oesterle, and Marc Ilegems. Far-infrared (lambda = 88 mu m) electroluminescence in a quantum cascade structure. *Applied Physics Letters*, 73(25):3724–3726, 1998.

[75] Raffaele Colombelli, Kartik Srinivasan, Mariano Troccoli, Oskar Painter, Claire F. Gmachl, Donald M. Tennant, A. Michael Sergent, Deborah L. Sivco, Alfred Y. Cho, and Federico Capasso. Quantum Cascade Surface-Emitting Photonic Crystal Laser. *Science*, 302(5649):1374–1377, 2003.

[76] A. Evans, J. S. Yu, S. Slivken, and M. Razeghi. Continuous-wave operation of lambda 4.8 mu m quantum-cascade lasers at room temperature. *Applied Physics Letters*, 85(12):2166–2168, 2004.

[77] J.S. Yu, A. Evans, S. Slivken, S.R. Darvish, and M. Razeghi. Short wavelength (4.3 m) high-performance continuous-wave quantum-cascade lasers. *Photonics Technology Letters, IEEE*, 17(6):1154–1156, June 2005.

[78] J. S. Yu, A. Evans, S. Slivken, S. R. Darvish, and M. Razeghi. Temperature dependent characteristics of lambda 3.8 mu m room-temperature continuous-wave quantum-cascade lasers. *Applied Physics Letters*, 88(25):251118, 2006.

[79] A. Evans, J. Nguyen, S. Slivken, J. S. Yu, S. R. Darvish, and M. Razeghi. Quantum-cascade lasers operating in continuous-wave mode above 90 [degree]c at lambda 5.25 mu m. *Applied Physics Letters*, 88(5):051105, 2006.

[80] J. S. Yu, S. Slivken, A. Evans, S. R. Darvish, J. Nguyen, and M. Razeghi. High-power lambda 9.5 mu m quantum-cascade lasers operating above room temperature in continuous-wave mode. *Applied Physics Letters*, 88(9):091113, 2006.

[81] A. Evans, S. R. Darvish, S. Slivken, J. Nguyen, Y. Bai, and M. Razeghi. Buried heterostructure quantum cascade lasers with high continuous-wave wall plug efficiency. *Applied Physics Letters*, 91(7):071101, 2007.

[82] S. Slivken, A. Evans, W. Zhang, and M. Razeghi. High-power, continuous-operation intersubband laser for wavelengths greater than 10 mu m. *Applied Physics Letters*, 90(15):151115, 2007.

[83] Y. Bai, S. R. Darvish, S. Slivken, W. Zhang, A. Evans, J. Nguyen, and M. Razeghi. Room temperature continuous wave operation of quantum cascade lasers with watt-level optical power. *Applied Physics Letters*, 92(10):101105, 2008.

[84] Y. Bai, S. Slivken andS. R. Darvish, and M. Razeghi. Room temperature continuous wave operation of quantum cascade lasers with 12.5 *Applied Physics Letters*, 93:021103, July 2008.

[85] L. Diehl, D. Bour, S. Corzine, J. Zhu, G. Höfler, M. Lončar, M. Troccoli, and Federico Capasso. High-temperature continuous wave operation of strain-balanced quantum cascade lasers grown by metal organic vapor-phase epitaxy. *Applied Physics Letters*, 89(8):081101, 2006.

[86] L. Diehl, D. Bour, S. Corzine, J. Zhu, G. Höfler, M. Lončar, M. Troccoli, and Federico Capasso. High-power quantum cascade lasers grown by low-pressure metal organic vapor-phase epitaxy operating in continuous wave above 400 k. *Applied Physics Letters*, 88(20):201115, 2006.

[87] S. Németh, B. Grietens, and G. Borghs. Compositional dependence of alas[sub y]sb[sub 1 - y] ternaries on the ratio of sb/as fluxes and on the substrate temperature. *Journal of Applied Physics*, 77(7):3552–3553, 1995.

[88] C. Renard, X. Marcadet, J. Massies, and O. Parillaud. Molecular beam epitaxy of (ga,al)assb alloys on inp(001) substrates. *Journal of Crystal Growth*, 278(1-4):193 – 197, 2005. 13th International Conference on Molecular Beam Epitaxy.

[89] D. G. Revin, L. R. Wilson, E. A. Zibik, R. P. Green, J. W. Cockburn, M. J. Steer, R. J. Airey, and M. Hopkinson. Ingaas/alassb quantum cascade lasers. *Applied Physics Letters*, 85(18):3992–3994, 2004.

[90] Q. Yang, C. Manz, W. Bronner, Ch. Mann, L. Kirste, K. Köhler, and J. Wagner. Gainas/alassb quantum-cascade lasers operating up to 400 k. *Applied Physics Letters*, 86(13):131107, 2005.

[91] Quankui Yang, Christian Manz, Wolfgang Bronner, Klaus Köhler, and Joachim Wagner. Room-temperature short-wavelength (lambda 3.7–3.9 mu m) gainas/alassb quantum-cascade lasers. *Applied Physics Letters*, 88(12):121127, 2006.

[92] C. V.-B. Grimm, M. Priegnitz, S. Winnerl, H. Schneider, M. Helm, K. Biermann, and H. Künzel. Intersubband relaxation dynamics in single and double quantum wells based on strained ingaas/alas/alassb. *Applied Physics Letters*, 91(19):191121, 2007.

[93] C. V.-B. Tribuzy, S. Ohser, S. Winnerl, J. Grenzer, H. Schneider, M. Helm, J. Neuhaus, T. Dekorsy, K. Biermann, and H. Künzel. Femtosecond pump-probe spectroscopy of intersubband relaxation dynamics in narrow ingaas/alassb quantum well structures. *Applied Physics Letters*, 89(17):171104, 2006.

[94] C. V.-B. Tribuzy, S. Ohser, M. Priegnitz, S. Winnerl, H. Schneider, M. Helm, J. Neuhaus, T. Dekorsy, K. Biermann, and H. Knzel. Inefficiency of intervalley transfer in narrow ingaas/alassb quantum wells. *physica status solidi (c)*, 5(1):229–231, 2008.

[95] D. G. Revin, J. W. Cockburn, M. J. Steer, R. J. Airey, M. Hopkinson, A. B. Krysa, L. R. Wilson, and S. Menzel. Ingaas/alassb/inp quantum cascade lasers operating at wavelengths close to 3 mu m. *Applied Physics Letters*, 90(2):021108, 2007.

[96] D. G. Revin, J. W. Cockburn, M. J. Steer, R. J. Airey, M. Hopkinson, A. B. Krysa, L. R. Wilson, and S. Menzel. Ingaas/alassb/inp strain compensated quantum cascade lasers. *Applied Physics Letters*, 90(15):151105, 2007.

[97] S. Y. Zhang, D. G. Revin, J. W. Cockburn, K. Kennedy, A. B. Krysa, and M. Hopkinson. lambda 3.1 mu m room temperature ingaas/alassb/inp quantum cascade lasers. *Applied Physics Letters*, 94(3):031106, 2009.

[98] Q. Yang, C. Manz, W. Bronner, L. Kirste, K. Kohler, and J. Wagner. Gainas/algaassb quantum-cascade lasers. *Applied Physics Letters*, 86(13):131109, 2005.

[99] Quankui Yang, Christian Manz, Wolfgang Bronner, Nico Lehmann, Frank Fuchs, Klaus Köhler, and Joachim Wagner. High peak-power (10.5 w) gainas/algaassb quantum-cascade lasers emitting at lambda 3.6–3.8 mu m. *Applied Physics Letters*, 90(12):121134, 2007.

[100] I. Vurgaftman, J. R. Meyer, and L. R. Ram-Mohan. Band parameters for iii–v compound semiconductors and their alloys. *Journal of Applied Physics*, 89(11):5815–5875, 2001.

[101] J. Spitzer, A. Höpner, M. Kuball, M. Cardona, B. Jenichen, H. Neuroth, B. Brar, and H. Kroemer. Influence of the interface composition of inas/alsb superlattices on their optical and structural properties. *Journal of Applied Physics*, 77(2):811–820, 1995.

[102] Gary Tuttle, Herbert Kroemer, and John H. English. Effects of interface layer sequencing on the transport properties of inas/alsb quantum wells: Evidence for antisite donors at the inas/alsb interface. *Journal of Applied Physics*, 67(6):3032–3037, 1990.

[103] C. Renard, X. Marcadet, J. Massies, I. Prvot, R. Bisaro, and P. Galtier. Indium surface segregation in alsb and gasb. *Journal of Crystal Growth*, 259(1-2):69 – 78, 2003.

[104] K. Ohtani and H. Ohno. Inas/alsb quantum cascade lasers operating at 10 mu m. *Applied Physics Letters*, 82(7):1003–1005, 2003.

[105] R. Teissier, D. Barate, A. Vicet, D.A. Yarekha, C. Alibert, A.N. Baranov, X. Marcadet, M. Garcia, and C. Sirtori. Inas/alsb quantum cascade lasers operating at 6.7[emsp4 1/4-em space][micro sign]m. *Electronics Letters*, 39(17):1252–1254, 2003.

[106] R. Teissier, D. Barate, A. Vicet, C. Alibert, A. N. Baranov, X. Marcadet, C. Renard, M. Garcia, C. Sirtori, D. Revin, and J. Cockburn. Room temperature operation of inas/alsb quantum cascade lasers. *Applied Physics Letters*, 85(2):167–169, 2004.

[107] J. Devenson, R. Teissier, O. Cathabard, and A. N. Baranov. Inas/alsb quantum cascade lasers emitting below 3 μm. *Applied Physics Letters*, 90(11):111118, 2007.

[108] J. Devenson, D. Barate, O. Cathabard, R. Teissier, and A. N. Baranov. Very short wavelength (lambda = 3.1–3.3 mu m) quantum cascade lasers. *Applied Physics Letters*, 89(19):191115, 2006.

[109] X. Marcadet, C. Renard, M. Carras, M. Garcia, and J. Massies. Inas/alassb based quantum cascade lasers. *Applied Physics Letters*, 91(16):161104, 2007.

[110] G. Dehlinger, L. Diehl, U. Gennser, H. Sigg, J. Faist, K. Ensslin, D. Grutzmacher, and E. Muller. Intersubband Electroluminescence from Silicon-Based Quantum Cascade Structures. *Science*, 290(5500):2277–2280, 2000.

[111] R. Akimoto, K. Akita, F. Sasaki, and S. Kobayashi. Short-wavelength (lambda [less-than] 2 mu m) intersubband absorption dynamics in znse/bete quantum wells. *Applied Physics Letters*, 80(14):2433–2435, 2002.

[112] Thierry Aellen, Stéphane Blaser, Mattias Beck, Daniel Hofstetter, Jérôme Faist, and Emilio Gini. Continuous-wave distributed-feedback quantum-cascade lasers on a peltier cooler. *Applied Physics Letters*, 83(10):1929–1931, 2003.

[113] J. S. Yu, S. Slivken, S. R. Darvish, A. Evans, B. Gokden, and M. Razeghi. High-power, room-temperature, and continuous-wave operation of distributed-feedback quantum-cascade lasers at lambda 4.8 mu m. *Applied Physics Letters*, 87(4):041104, 2005.

[114] S. R. Darvish, W. Zhang, A. Evans, J. S. Yu, S. Slivken, and M. Razeghi. High-power, continuous-wave operation of distributed-feedback quantum-cascade lasers at lambda 7.8 mu m. *Applied Physics Letters*, 89(25):251119, 2006.

[115] S. R. Darvish, S. Slivken, A. Evans, J. S. Yu, and M. Razeghi. Room-temperature, high-power, and continuous-wave operation of distributed-feedback quantum-cascade lasers at lambda 9.6 mu m. *Applied Physics Letters*, 88(20):201114, 2006.

[116] Y. Bai, B. Gokden, S. R. Darvish, S. Slivken, and M. Razeghi. Photonic crystal distributed feedback quantum cascade lasers with 12 w output power. *Applied Physics Letters*, 95(3):031105, 2009.

[117] Benjamin G. Lee, Mikhail A. Belkin, Ross Audet, Jim MacArthur, Laurent Diehl, Christian Pflügl, Federico Capasso, Douglas C. Oakley, David Chapman, Antonio Napoleone, David Bour, Scott Corzine, Gloria Höfler, and Jérôme Faist. Widely tunable single-mode quantum cascade laser source for mid-infrared spectroscopy. *Applied Physics Letters*, 91(23):231101, 2007.

[118] B.G. Lee, H.A. Zhang, C. Pflugl, L. Diehl, M.A. Belkin, M. Fischer, A. Wittmann, J. Faist, and F. Capasso. Broadband distributed-feedback quantum cascade laser array operating from 8.0 to 9.8 *mu* m. *Photonics Technology Letters, IEEE*, 21(13):914–916, July1, 2009.

[119] Claire Gmachl, Deborah L. Sivco, Raffaele Colombelli, Federico Capasso, and Alfred Y. Cho. Ultra-broadband semiconductor laser. *Nature*, 415(6874):883–887, 02 2002.

[120] Richard Maulini, Arun Mohan, Marcella Giovannini, Jérôme Faist, and Emilio Gini. External cavity quantum-cascade laser tunable from 8.2 to 10.4 mu m using a gain element with a heterogeneous cascade. *Applied Physics Letters*, 88(20):201113, 2006.

[121] R. Maulini, I. Dunayevskiy, A. Lyakh, A. Tsekoun, C.K.N. Patel, L. Diehl, C. Pflügl, and F. Capasso. Widely tunable high-power external cavity quantum cascade laser operating in continuous-wave at room temperature. *Electronics Letters*, 45(2):107–108, 2009.

[122] L. S. Rothman, D. Jacquemart, A. Barbe, Chris, M. Birk, L. R. Brown, M. R. Carleer, Jr Chackerian, K. Chance, L. H. Coudert, V. Dana, V. M. Devi, J. M. Flaud, R. R. Gamache, A. Goldman, J. M. Hartmann, K. W. Jucks, A. G. Maki, J. Y. Mandin, S. T. Massie, J. Orphal, A. Perrin, C. P. Rinsland, M. A. H. Smith, J. Tennyson, R. N. Tolchenov, R. A. Toth, Vander, P. Varanasi, and G. Wagner. The hitran 2004 molecular spectroscopic database. *Journal of Quantitative Spectroscopy and Radiative Transfer*, 96(2):139–204, December 2005.

[123] I. T. Sorokina and K. L. Vodopyanov, editors. *Solid-State Mid-Infrared Laser Sources*. Springer, 2003.

[124] M. Ebrahim-Zadeh and I. T. Sorokina, editors. *Mid-Infrared Coherent Sources and Applications*. Springer, 2007.

[125] A. Kosterev, G. Wysocki, Y. Bakhirkin, S. So, R. Lewicki, M. Fraser, F. Tittel, and R. F. Curl. Application of quantum cascade lasers to trace gas analysis. *Applied Physics B: Lasers and Optics*, 90(2):165–176, 2008.

[126] B. Tuzson, M. J. Zeeman, M. S. Zahniser, and L. Emmenegger. Quantum cascade laser based spectrometer for in situ stable carbon dioxide isotope measurements. *Infrared Physics & Technology*, 51(3):198–206, 2008.

[127] B. Tuzson, J. Mohn, M. J. Zeeman, R. A. Werner, W. Eugster, M. S. Zahniser, D. D. Nelson, J. B. McManus, and L. Emmenegger. High precision and continuous field measurements of 13c and 18o in carbon dioxide with a cryogen-free qclas. *Applied Physics B: Lasers and Optics*, 92(3):451–458, 2008.

[128] R. Martini, R. Paiella, F. Capasso, C. Gmachl, H.Y. Hwang, D.L. Sivco, A.Y. Cho, E.A. Whittaker, and H.C. Liu. Absence of relaxation oscillation in quantum cascade lasers verified by high-frequency modulation. *Lasers and Electro-Optics, 2001. CLEO '01. Technical Digest. Summaries of papers presented at the Conference on*, pages CPD17–CP1–2, May 2001.

[129] N. Mustafa, L. Pesquera, C.Y.L. Cheung, and K.A. Shore. Terahertz bandwidth prediction for amplitude modulation response of unipolar intersubband semiconductor lasers. *Photonics Technology Letters, IEEE*, 11(5):527–529, May 1999.

[130] S. Blaser, D. Hofstetter, M. Beck, and J. Faist. Free-space optical data link using peltier-cooled quantum cascade laser. *Electronics Letters*, 37(12):778–780, Jun 2001.

[131] R. Martini, C. Gmachl, J. Falciglia, F.G. Curti, C.G. Bethea, F. Capasso, E.A. Whittaker, R. Paiella, A. Tredicucci, A.L. Hutchinson, D.L. Sivco, and A.Y. Cho. High-speed modulation and free-space optical audio/video transmission using quantum cascade lasers. *Electronics Letters*, 37(3):191–193, Feb 2001.

[132] R. Martini, R. Paiella, C. Gmachl, F. Capasso, E.A. Whittaker, H.C. Liu, H.Y. Hwang, D.L. Sivco, J.N. Baillargeon, and A.Y. Cho. High-speed digital data transmission using mid-infrared quantum cascade lasers. *Electronics Letters*, 37(21):1290–1292, Oct 2001.

[133] David G. Voelz and Jennifer C. Ricklin, editors. *Long-wave infrared (10-mu m) free-space optical communication system*, number 1. SPIE, 2004.

[134] J. R. Gao, J. N. Hovenier, Z. Q. Yang, J. J. A. Baselmans, A. Baryshev, M. Hajenius, T. M. Klapwijk, A. J. L. Adam, T. O. Klaassen, B. S. Williams, S. Kumar, Q. Hu, and J. L. Reno. Terahertz heterodyne receiver based on a quantum cascade laser and a superconducting bolometer. *Applied Physics Letters*, 86(24):244104, 2005.

[135] M. Hajenius, P. Khosropanah, J. N. Hovenier, J. R. Gao, T. M. Klapwijk, S. Barbieri, S. Dhillon, P. Filloux, C. Sirtori, D. A. Ritchie, and H. E. Beere. Surface plasmon quantum cascade lasers as terahertz local oscillators. *Opt. Lett.*, 33(4):312–314, 2008.

[136] Heinz-Wilhelm Hübers, S. Pavlov, A. Semenov, R. Köhler, L. Mahler, A. Tredicucci, H. Beere, D. Ritchie, and E. Linfield. Terahertz quantum cascade laser as local oscillator in a heterodyne receiver. *Opt. Express*, 13(15):5890–5896, 2005.

[137] G. Sonnabend, D. Wirtz, V. Vetterle, and R. Schieder. High-resolution observations of martian non-thermal co_2 emission near 10μm with a new tuneable heterodyne receiver. *Astronomy and Astrophysics*, 435(3):1181–1184, jun 2005.

[138] D. Weidmann, W. J. Reburn, and K. M. Smith. Ground-based prototype quantum cascade laser heterodyne radiometer for atmospheric studies. *Review of Scientific Instruments*, 78(7):073107, 2007.

[139] G. Sonnabend, M. Sornig, P. J. Krötz, R. T. Schieder, and K. E. Fast. High spatial resolution mapping of mars mesospheric zonal winds by infrared heterodyne spectroscopy of co2. *Geophys. Res. Lett.*, 33(L18201), 2006.

[140] Damien Weidmann, William J. Reburn, and Kevin M. Smith. Retrieval of atmospheric ozone profiles from an infrared quantum cascade laser heterodyne radiometer: results and analysis. *Appl. Opt.*, 46(29):7162–7171, 2007.

[141] Alan Wei Lee and Qing Hu. Real-time, continuous-wave terahertz imaging by use of a microbolometer focal-plane array. *Opt. Lett.*, 30(19):2563–2565, 2005.

[142] Barry N. Behnken, Gamani Karunasiri, Danielle R. Chamberlin, Peter R. Robrish, and Jérôme Faist. Real-time imaging using a 2.8 thz quantum cascade laser and uncooled infrared microbolometer camera. *Opt. Lett.*, 33(5):440–442, 2008.

[143] Seongsin M. Kim, Fariba Hatami, James S. Harris, Allison W. Kurian, James Ford, Douglas King, Giacomo Scalari, Marcella Giovannini, Nicolas Hoyler, Jerome Faist, and Geoff Harris. Biomedical terahertz imaging with a quantum cascade laser. *Applied Physics Letters*, 88(15):153903, 2006.

[144] Yao-Chun Shen and P.F. Taday. Development and application of terahertz pulsed imaging for nondestructive inspection of pharmaceutical tablet. *Selected Topics in Quantum Electronics, IEEE Journal of*, 14(2):407–415, March-april 2008.

[145] Mehdi Anwar, Nibir K. Dhar, and Thomas W. Crowe, editors. *Non-invasive mail inspection system with terahertz radiation*, number 1. SPIE, 2009.

[146] E. Rosencher and B. Vinter. *Optoelectronics.* Cambridge University Press, 2004.

[147] G. Bastard. *Wave Mechanics Applied to Semiconductor Heterostructures.* Les Editions de Physique. Les Ulis, France, 1988.

[148] Carlo Sirtori, Federico Capasso, Jérôme Faist, and Sandro Scandolo. Nonparabolicity and a sum rule associated with bound-to-bound and bound-to-continuum intersubband transitions in quantum wells. *Phys. Rev. B*, 50(12):8663–8674, Sep 1994.

[149] D. F. Nelson, R. C. Miller, and D. A. Kleinman. Band nonparabolicity effects in semiconductor quantum wells. *Phys. Rev. B*, 35(14):7770–7773, May 1987.

[150] M. Helm. *Intersubband transitions in quantum wells: Physics and device applications I*, chapter The basic physics of intersubband transitions. Academic Press, San Diego, 2000.

[151] Jurgen H. Smet, Clifton G. Fonstad, and Qing Hu. Intrawell and interwell intersubband transitions in multiple quantum wells for far-infrared sources. *Journal of Applied Physics*, 79(12):9305–9320, 1996.

[152] R. Ferreira and G. Bastard. Evaluation of some scattering times for electrons in unbiased and biased single- and multiple-quantum-well structures. *Phys. Rev. B*, 40(2):1074–1086, Jul 1989.

[153] A. Leuliet, A. Vasanelli, A. Wade, G. Fedorov, D. Smirnov, G. Bastard, and C. Sirtori. Electron scattering spectroscopy by a high magnetic field in quantum cascade lasers. *Physical Review B (Condensed Matter and Materials Physics)*, 73(8):085311, 2006.

[154] A. Vasanelli, A. Leuliet, C. Sirtori, A. Wade, G. Fedorov, D. Smirnov, G. Bastard, B. Vinter, M. Giovannini, and J. Faist. Role of elastic scattering mechanisms in gainas/alinas quantum cascade lasers. *Applied Physics Letters*, 89(17):172120, 2006.

[155] P. Kinsler, P. Harrison, and R. W. Kelsall. Intersubband electron-electron scattering in asymmetric quantum wells designed for far-infrared emission. *Phys. Rev. B*, 58(8):4771–4778, Aug 1998.

[156] C. Sirtori, F. Capasso, J. Faist, A.L. Hutchinson, D.L. Sivco, and A.Y. Cho. Resonant tunneling in quantum cascade lasers. *Quantum Electronics, IEEE Journal of*, 34(9):1722–1729, Sep 1998.

[157] J. Faist, F. Capasso, C. Sirtori, D. L. Sivco, and A. Y. Cho. *Intersubband transitions in quantum wells: Physics and device applications II*, volume 65 of *Semicond. Semimet.*, chapter Quantum cascade lasers. Academic Press, San Diego, 2000.

[158] Jérôme Faist. Wallplug efficiency of quantum cascade lasers: Critical parameters and fundamental limits. *Applied Physics Letters*, 90(25):253512, 2007.

[159] Fatima Toor, Deborah L. Sivco, Hao E. Liu, and Claire F. Gmachl. Effect of waveguide sidewall roughness on the threshold current density and slope efficiency of quantum cascade lasers. *Applied Physics Letters*, 93(3):031104, 2008.

[160] C.M. Herzinger, C.-C. Lu, T.A. DeTemple, and W.C. Chew. The semiconductor waveguide facet reflectivity problem. *Quantum Electronics, IEEE Journal of*, 29(8):2273–2281, Aug 1993.

[161] T. Ikegami. Reflectivity of mode at facet and oscillation mode in double-heterostructure injection lasers. *Quantum Electronics, IEEE Journal of*, 8(6):470–476, Jun 1972.

[162] Thierry Aellen, Mattias Beck, Nicolas Hoyler, Marcella Giovannini, Jerome Faist, and Emilio Gini. Doping in quantum cascade lasers. i. inalas–ingaas/inp midinfrared devices. *Journal of Applied Physics*, 100(4):043101, 2006.

[163] Stéphane Blaser, Dmitri A. Yarekha, Lubos Hvozdara, Yargo Bonetti, Antoine Muller, Marcella Giovannini, and Jérôme Faist. Room-temperature, continuous-wave, single-mode quantum-cascade lasers at lambda = 5.4 mu m. *Applied Physics Letters*, 86(4):041109, 2005.

[164] K.P. Pipe and R.J. Ram. Comprehensive heat exchange model for a semiconductor laser diode. *Photonics Technology Letters, IEEE*, 15(4):504–506, April 2003.

[165] Jérôme Faist, Federico Capasso, Carlo Sirtori, Deborah L. Sivco, Albert L. Hutchinson, and Alfred Y. Cho. Continuous wave operation of a vertical transition quantum cascade laser above t=80 k. *Applied Physics Letters*, 67(21):3057–3059, 1995.

[166] Basil W. Hakki and Thomas L. Paoli. Gain spectra in gaas double - heterostructure injection lasers. *Journal of Applied Physics*, 46(3):1299–1306, 1975.

[167] Basil W. Hakki and Thomas L. Paoli. cw degradation at 300[degree]k of gaas double-heterostructure junction lasers. ii. electronic gain. *Journal of Applied Physics*, 44(9):4113–4119, 1973.

[168] Daniel T. Cassidy. Technique for measurement of the gain spectra of semiconductor diode lasers. *Journal of Applied Physics*, 56(11):3096–3099, 1984.

[169] D. Hofstetter and J. Faist. Measurement of semiconductor laser gain and dispersion curves utilizing fourier transforms of the emission spectra. *Photonics Technology Letters, IEEE*, 11(11):1372–1374, Nov 1999.

[170] C. Gmachl, A. Soibel, R. Colombelli, D.L. Sivco, F. Capasso, and A.Y. Cho. Minimal group refractive index dispersion and gain evolution in ultra-broad-band quantum cascade lasers. *Photonics Technology Letters, IEEE*, 14(12):1671–1673, Dec 2002.

[171] M. Lerttamrab, S. L. Chuang, C. Gmachl, D. L. Sivco, F. Capasso, and A. Y. Cho. Linewidth enhancement factor of a type-i quantum-cascade laser. *Journal of Applied Physics*, 94(8):5426–5428, 2003.

[172] Zhijun Liu, C.F. Gmachl, Liwei Cheng, Fow-Sen Choa, F.J. Towner, Xiaojun Wang, and Jenyu Fan. Temperature dependence of optical gain and loss in $lambdaapprox$ 8.210.2 mum quantum-cascade lasers. *Quantum Electronics, IEEE Journal of*, 44(5):485–492, May 2008.

[173] Rudeger Kohler, Alessandro Tredicucci, Fabio Beltram, Harvey E. Beere, Edmund H. Linfield, A. Giles Davies, David A. Ritchie, Sukhdeep S. Dhillon, and Carlo Sirtori. High-performance continuous-wave operation of superlattice terahertz quantum-cascade lasers. *Applied Physics Letters*, 82(10):1518–1520, 2003.

[174] D. G. Revin, L. R. Wilson, D. A. Carder, J. W. Cockburn, M. J. Steer, M. Hopkinson, R. Airey, M. Garcia, C. Sirtori, Y. Rouillard, D. Barate, and A. Vicet. Measurements of optical losses in mid-infrared semiconductor lasers using fabry–p[e-acute]rot transmission oscillations. *Journal of Applied Physics*, 95(12):7584–7587, 2004.

[175] D. G. Revin, M. R. Soulby, J. W. Cockburn, Q. Yang, C. Manz, and J. Wagner. Dispersive gain and loss in midinfrared quantum cascade laser. *Applied Physics Letters*, 92(8):081110, 2008.

[176] E. Peter, S. Laurent, C. Sirtori, M. Carras, J. A. Robbo, M. Garcia, and X. Marcadet. Measurement of semiconductor waveguide optical properties in the midinfrared wavelength range. *Applied Physics Letters*, 92(2):021103, 2008.

[177] Daniel Hofstetter and Robert L. Thornton. Loss measurements on semiconductor lasers by fourier analysis of the emission spectra. *Applied Physics Letters*, 72(4):404–406, 1998.

[178] Josef Kroll, Juraj Darmo, Sukhdeep S. Dhillon, Xavier Marcadet, Michel Calligaro, Carlo Sirtori, and Karl Unterrainer. Phase-resolved measurements of stimulated emission in a laser. *Nature*, 449(7163):698–701, 10 2007.

[179] Wolfgang Parz, Thomas Muller, Juraj Darmo, Karl Unterrainer, Max Austerer, Gottfried Strasser, Luke R. Wilson, John W. Cockburn, Andrey B. Krysa, and John S. Roberts. Ultrafast probing of light-matter interaction in a midinfrared quantum cascade laser. *Applied Physics Letters*, 93(9):091105, 2008.

[180] Josef Kroll, Juraj Darmo, Karl Unterrainer, Sukhdeep S. Dhillon, Carlo Sirtori, Xavier Marcadet, and Michel Calligaro. Longitudinal spatial hole burning in terahertz quantum cascade lasers. *Applied Physics Letters*, 91(16):161108, 2007.

[181] W. Kuehn, W. Parz, P. Gaal, K. Reimann, M. Woerner, T. Elsaesser, T. Muller, J. Darmo, K. Unterrainer, M. Austerer, G. Strasser, L. R. Wilson, J. W. Cockburn, A. B. Krysa, and J. S. Roberts. Ultrafast phase-resolved pump-probe measurements on a quantum cascade laser. *Applied Physics Letters*, 93(15):151106, 2008.

[182] Wolfgang Parz, Thomas Müller, Juraj Darmo, Maximilian Austerer, Gottfried Strasser, Luke Wilson, John Cockburn, Andrey Krysa, John Roberts, and Karl Unterrainer. Intersubband gain-induced dispersion. *Opt. Lett.*, 34(2):208–210, 2009.

[183] S.D. McDougall and C.N. Ironside. Measurements of reverse and forward bias absorption and gain spectra in semiconductor laser material. *Electronics Letters*, 31(25):2179–2181, Dec 1995.

[184] S. Barbieri, C. Sirtori, H. Page, M. Beck, J. Faist, and J. Nagle. Gain measurements on gaas-based quantum cascade lasers using a two-section cavity technique. *Quantum Electronics, IEEE Journal of*, 36(6):736–741, 2000.

[185] Michel Rochat, Mattias Beck, Jérôme Faist, and Ursula Oesterle. Measurement of far-infrared waveguide loss using a multisection single-pass technique. *Applied Physics Letters*, 78(14):1967–1969, 2001.

[186] A. Lyakh, C. Pflügl, L. Diehl, Q. J. Wang, Federico Capasso, X. J. Wang, J. Y. Fan, T. Tanbun-Ek, R. Maulini, A. Tsekoun, R. Go, and C. Kumar N. Patel. 1.6 w high wall plug efficiency, continuous-wave room temperature quantum cascade laser emitting at 4.6 mu m. *Applied Physics Letters*, 92(11):111110, 2008.

[187] P. Yeh. *Optical Waves in Layered Media.* Wiley, New York, 1988.

[188] K. Kopitzki and P. Herzog. *Einführung in die Festkörperphysik.* Teubner GmbH, Stuttgart/Leipzig/Wiesbaden, 2002.

[189] M. Giehler P. Kleinert. Theory of free-carrier infrared absorption in gaas. *physica status solidi (b)*, 136(2):763–777, 1986.

[190] M. Giehler, H. Kostial, R. Hey, and H. T. Grahn. Effect of free-carrier absorption on the threshold current density of gaas/(al,ga)as quantum-cascade lasers. *Journal of Applied Physics*, 96(9):4755–4761, 2004.

[191] L. Diehl, D. Bour, S. Corzine, J. Zhu, G. Höfler, B. G. Lee, C. Y. Wang, M. Troccoli, and F. Capasso. Pulsed- and continuous-mode operation at high temperature of strained quantum-cascade lasers grown by metalorganic vapor phase epitaxy. *Applied Physics Letters*, 88(4):041102, 2006.

[192] C. Gmachi, F. Capasso, A. Tredicucci, D.L. Sivxo, R. Kohler, A.L. Hutchinson, and A.Y. Cho. Dependence of the device performance on the number of stages in quantum-cascade lasers. *Selected Topics in Quantum Electronics, IEEE Journal of*, 5(3):808–816, May/Jun 1999.

[193] W.W. Bewley, J.R. Lindle, Chul Soo Kim, I. Vurgaftman, J.R. Meyer, A.J. Evans, Jae Su Yu, S. Slivken, and M. Razeghi. Beam steering in high-power cw quantum-cascade lasers. *Quantum Electronics, IEEE Journal of*, 41(6):833–841, June 2005.

[194] E. Yablonovitch and E. Kane. Reduction of lasing threshold current density by the lowering of valence band effective mass. *Lightwave Technology, Journal of*, 4(5):504–506, May 1986.

[195] Chris G. Van de Walle. Band lineups and deformation potentials in the model-solid theory. *Phys. Rev. B*, 39(3):1871–1883, Jan 1989.

[196] Yu. A. Goldberg and N. M. Schmidt. *Handbook Series on Semiconductor Parameters*, volume 2. World Scientific, London, 1999.

[197] Mitsuru Sugawara, Niroh Okazaki, Takuya Fujii, and Susumu Yamazaki. Conduction-band and valence-band structures in strained in1-xgaxas/inp quantum wells on (001) inp substrates. *Physical Review B*, 48(11), 1993.

[198] J.W. Matthews and A.E. Blakeslee. Defects in epitaxial multilayers: I. misfit dislocations. *Journal of Crystal Growth*, 27:118 – 125, 1974.

[199] J. W. Matthews and A. E. Blakeslee. Defects in epitaxial multilayers : Ii. dislocation pile-ups, threading dislocations, slip lines and cracks. *Journal of Crystal Growth*, 29(3):273 – 280, 1975.

[200] J.W. Matthews and A.E. Blakeslee. Defects in epitaxial multilayers: Iii. preparation of almost perfect multilayers. *Journal of Crystal Growth*, 32(2):265 – 273, 1976.

[201] L.B. Freund. The mechanics of dislocations in strained-layer semiconductor materials. In John W. Hutchinson and Theodore Y. Wu, editors, *Advances in Applied Mechanics*, volume 30, pages 1 – 66. Elsevier, 1993.

[202] M. C. Muñoz and G. Armelles. X-point deformation potentials of iii-v semiconductors in a tight-binding approach. *Phys. Rev. B*, 48(4):2839–2842, Jul 1993.

[203] J. Massies, F. Turco, A. Saletes, and J. P. Contour. Experimental evidence of difference in surface and bulk compositions of alxga1-xas, alxin1-x as and gaxin1-x as epitaxial layers grown by molecular beam epitaxy. *Journal of Crystal Growth*, 80(2):307–314, 1987.

[204] J. M. Moison, C. Guille, F. Houzay, F. Barthe, and M. Van Rompay. Surface segregation of third-column atoms in group iii-v arsenide compounds: Ternary alloys and heterostructures. *Physical Review B*, 40(9), 1989.

[205] J. Nagle, J. P. Landesman, M. Larive, C. Mottet, and P. Bois. Indium surface segregation in strained gainas quantum wells grown on gaas by mbe. *Journal of Crystal Growth*, 127(1-4):550–554, 1993.

[206] Jean-Michel Gerard and Guy Le Roux. Growth of ingaas/gaas quantum wells with perfectly abrupt interfaces by molecular beam epitaxy. *Applied Physics Letters*, 62(26):3452–3454, 1993.

[207] K. Muraki, S. Fukatsu, Y. Shiraki, and R. Ito. Surface segregation of in atoms during molecular beam epitaxy and its influence on the energy levels in ingaas/gaas quantum wells. *Applied Physics Letters*, 61(5):557–559, 1992.

[208] Hiroshi Yamaguchi and Yoshiji Horikoshi. Replacement of group-iii atoms on the growing surface during migration-enhanced epitaxy. *Journal of Applied Physics*, 68(4):1610–1615, 1990.

[209] O. Dehaese, X. Wallart, and F. Mollot. Kinetic model of element iii segregation during molecular beam epitaxy of iii-iii'-v semiconductor compounds. *Applied Physics Letters*, 66(1):52–54, 1995.

[210] G. Gonzalez de la Cruz. The influence of surface segregation on the optical properties of quantum wells. *Journal of Applied Physics*, 96(7):3752–3755, 2004.

[211] J. R. Jensen, J. M. Hvam, and W. Langbein. Optical properties of inalgaas quantum wells: Influence of segregation and band bowing. *Journal of Applied Physics*, 86(5):2584–2589, 1999.

[212] M. Schowalter, A. Rosenauer, and D. Gerthsen. Influence of surface segregation on the optical properties of semiconductor quantum wells. *Applied Physics Letters*, 88(11):111906–3, 2006.

[213] M. Larive, J. Nagle, J. P. Landesman, X. Marcadet, C. Mottet, and P. Bois. In situ core-level photoelectron spectroscopy study of indium segregation at gainas/gaas heterojunctions grown by molecular-beam epitaxy. In *Proceedings of the 20th annual conference on the physics and chemistry of semiconductors interfaces*, volume 11, pages 1413–1417. AVS, 1993.

[214] G. S. Spencer, J. Menéndez, L. N. Pfeiffer, and K. W. West. Optical-phonon raman-scattering study of short-period gaas-alas superlattices: An examination of interface disorder. *Phys. Rev. B*, 52(11):8205–8218, Sep 1995.

[215] Kaoru Kadoiwa, Shigekazu Izumi, Yoshitsugu Yamamoto, Norio Hayafuji, and Takuji Sonoda. Novel ingaas contact layer growth for hetero-junction bipolar transistors (hbts) by using the multiple group-v source molecular beam epitaxy (mbe) system. *Journal of Crystal Growth*, 203(1-2):18–24, 1999.

[216] Toyohiro Aoki, Takahiro Kitada, Satoshi Shimomura, and Satoshi Hiyamizu. Superflat interfaces in pseudomorphic in[sub 0.72]ga[sub 0.28]as/in[sub 0.52]al[sub 0.48]as quantum wells grown on (411)a inp substrates by molecular beam epitaxy. *Papers from the 18th north american conference on molecular beam epitaxy*, 18(3):1598–1600, 2000.

[217] Romain Terazzi, Tobias Gresch, Andreas Wittmann, and Jérôme Faist. Sequential resonant tunneling in quantum cascade lasers. *Physical Review B (Condensed Matter and Materials Physics)*, 78(15):155328, 2008.

[218] L. R. Wilson, J. W. Cockburn, D. A. Carder, M. J. Steer, M. Hopkinson, C. K. Chia, R. Airey, and G. Hill. λ=8.3 μm gaas/alas quantum cascade lasers incorporating inas monolayers. *Electronics Letters*, 37(21):1292–1293, 2001.

[219] Q. K. Yang, C. Mann, F. Fuchs, R. Kiefer, K. Köhler, N. Rollbühler, H. Schneider, and J. Wagner. Improvement of lambda [approximate] 5 mu m quantum cascade lasers by blocking barriers in the active regions. *Applied Physics Letters*, 80(12):2048–2050, 2002.

[220] Felix Bloch. ber die quantenmechanik der elektronen in kristallgittern. *Zeitschrift fr Physik A Hadrons and Nuclei*, 52(7):555–600, 07 1929.

[221] C. Zener. A theory of the electrical breakdown of solid dielectrics. *Proc. R. Soc. Lond. A*, 145(855):523–529, July 1934.

[222] J. Feldmann, K. Leo, J. Shah, D. A. B. Miller, J. E. Cunningham, T. Meier, G. von Plessen, A. Schulze, P. Thomas, and S. Schmitt-Rink. Optical investigation of bloch oscillations in a semiconductor superlattice. *Phys. Rev. B*, 46(11):7252–7255, Sep 1992.

[223] Christian Waschke, Hartmut G. Roskos, Ralf Schwedler, Karl Leo, Heinrich Kurz, and Klaus Köhler. Coherent submillimeter-wave emission from bloch oscillations in a semiconductor superlattice. *Phys. Rev. Lett.*, 70(21):3319–3322, May 1993.

[224] N. Sekine and K. Hirakawa. Dispersive terahertz gain of a nonclassical oscillator: Bloch oscillation in semiconductor superlattices. *Phys. Rev. Lett.*, 94(5):057408, Feb 2005.

[225] K. Unterrainer, B. J. Keay, M. C. Wanke, S. J. Allen, D. Leonard, G. Medeiros-Ribeiro, U. Bhattacharya, and M. J. W. Rodwell. Inverse bloch oscillator: Strong terahertz-photocurrent resonances at the bloch frequency. *Phys. Rev. Lett.*, 76(16):2973–2976, Apr 1996.

[226] P. G. Savvidis, B. Kolasa, G. Lee, and S. J. Allen. Resonant crossover of terahertz loss to the gain of a bloch oscillating $inas/alsb$ superlattice. *Phys. Rev. Lett.*, 92(19):196802, May 2004.

[227] Andreas Wacker. Gain in quantum cascade lasers and superlattices: A quantum transport theory. *Phys. Rev. B*, 66(8):085326, Aug 2002.

[228] S.-C. Lee and A. Wacker. Nonequilibrium green's function theory for transport and gain properties of quantum cascade structures. *Phys. Rev. B*, 66(24):245314, Dec 2002.

[229] C. Sirtori, J. Faist, F. Capasso, D.L. Sivco, A.L. Hutchinson, and A.Y. Cho. Mid-infrared (8.5 m) semiconductor lasers operating at room temperature. *Photonics Technology Letters, IEEE*, 9(3):294–296, March 1997.

Index

Curriculum vitae

Personal information

Name	Tobias Gresch
Address	Avenue du Léman 40 1005 Lausanne Suisse Phone: +41 (0)76 526 1977 Email: tobias.gresch@gmail.com
Date of birth	November 3, 1977, Zofingen, Switzerland, unmarried, Swiss

Education

Oct. 09 – present	Employed at Alpes Lasers SA, Neuchâtel, Switzerland for process development, device modeling and system administration.
Jul. 07 – Oct. 09	PhD studies at the Quantum Optoelectronics Group, ETH Zürich, Switzerland.
Sep. 03 – Jun. 07	PhD studies at the Mesoscopic Physics Group, University of Neuchâtel, Switzerland.
2003	Diploma in physical electronics from University ofNeuchâtel, Switzerland.

Oct. 01 – Jun. 02	Lectures on advanced material sciences, given at University of Neuchâtel, University of Bern and University of Fribourg (BENEFRI).
Oct. 98 – May 03	Studies in physical electronics at Institute of Microtechnology, University of Neuchâtel, Switzerland.
May 98	Matura Typus C (mathematics & natural sciences) Kantonsschule Zofingen, Switzerland.

Educational work experience

Jul. 05 – Sep. 05	Internship at Agilent Laboratories, Palo Alto CA 94304, USA. Project consisted in designing an external cavity setup for their high performance quantum cascade lasers and under supervision by Gloria Höfler and Scott Corzine. Unfortunately project was canceled when Agilent Technologies spun-off its semiconductor division (now Avago Technologies).
Nov. 02 – May 03	Diploma thesis on quantum cascade lasers based on single quantum well active regions at the Mesoscopic Physics Group, University of Neuchâtel, Switzerland.
Summer 02	School project (14 weeks, 2 days a week) realizing a solar-powered water supply at the Thin-Film silicon and Photovoltaics Laboratory, University of Neuchâtel, Switzerland.
Winter 01/02	School project (14 weeks, 2 days a week) on micromachined gas-flow sensors at SAMLAB, University of Neuchâtel, Switzerland.
Summer 2000	Project at AlpesLasers SA, Neuchâtel, Switzerland, to develop GPIB (IEEE 488) classes for laboratory equipment in C++.

Employment

Oct. 09 – present	(full time) Employed at AlpesLasers SA, Neuchâtel, Switzerland.
Jul. 07 – Oct. 09	(full time) Employed at the Quantum Optoelectronics Group, ETH Zürich, Switzerland, as research assistant. Teaching duties consist in supervising and supporting students in course work for basic physics classes.

Aug. 03 – Jun. 07	(full time) Employed at the Mesoscopic Physics Group, University of Neuchâtel, Switzerland, as research assistant. Teaching duties consisted in supervising and training students in beginner and advanced physics labs.
Oct. 01 – Jun. 02	(part time) Work as voluntary research assistant at the Thin-Film silicon and Photovoltaics Laboratory, University of Neuchâtel, Switzerland.
Oct. 00 – Jun. 03	(part time) System administrator at AlpesLasers SA, Neuchâtel, Switzerland. Work included configuration and maintenance of different Linux distributions, Perl and C/C++ programming, system security and backup.

Languages

German	Mother tongue
French	Primary foreign language. I speak and write fluently in French.
English	I speak and write fluently in English (scientific vocabulary).
Italian	Basic understanding, limited conversations.

Lausanne, March 24, 2010

Publications

Peer-reviewed journal papers

As primary author

- T. Gresch, J. Faist, and M. Giovannini. *Gain measurements in strain-compensated quantum cascade laser.* Appl. Phys. Lett., **94**(16):161114, 2009.

- T. Gresch, R. Terazzi, J. Faist, and M. Giovannini. *Bloch gain in quantum cascade lasers at high temperature.* Appl. Phys. Lett., **94**(3):031102, 2009.

- T. Gresch, M. Giovannini, N. Hoyer, and J. Faist. *Quantum cascade lasers with large optical waveguides.* IEEE Photonics Technol. Lett., **18**(3):544546, 2006.

As co-author

- R. Terazzi, T. Gresch, M. Giovannini, N. Hoyler, N. Sekine, and J. Faist. *Bloch gain in quantum cascade lasers.* Nat. Phys., **3**(5):329333, 2007.

As contributing author

- S. Herminjard, L. Sirigu, H. P. Herzig, E. Studemann, A. Crottini, J.-P. Pellaux, T. Gresch, M. Fischer, and J. Faist. *Surface plasmon resonance sensor showing enhanced sensitivity for CO_2 detection in the mid-infrared range.* Opt. Express, **17**(1):293303, 2009.

- A. Wittmann, T. Gresch, E. Gini, L. Hvozdara, N. Hoyler, M. Giovannini, and J. Faist. *High-performance bound-to-continuum quantum-cascade lasers for broad-gain applications.* IEEE J. Quantum Electron., **44**(1):3640, 2008.

- A. Bismuto, T. Gresch, A. Bächle, and J. Faist. *Large cavity quantum cascade lasers with InP interstacks.* Appl. Phys. Lett., **93**(23):231104, 2008.

- H. Choi, T. B. Norris, T. Gresch, M. Giovannini, J. Faist, L. Diehl, and F. Capasso. *Femtosecond dynamics of resonant tunneling and superlattice relaxation in quantum cascade lasers.* Appl. Phys. Lett., **92**(12):122114, 2008.

- R. Terazzi, T. Gresch, A. Wittmann, and J. Faist. *Sequential resonant tunneling in quantum cascade lasers.* Phys. Rev. B, **78**(15):155328, 2008.

- M. S. Vitiello, T. Gresch, A. Lops, V. Spagnolo, G. Scamarcio, N. Hoyler, M. Giovannini, and J. Faist. *Influence of InAs, AlAs delta layers on the optical, electronic, and thermal characteristics of strain-compensated GaInAs/AlInAs quantum-cascade lasers.* Appl. Phys. Lett., **91**(16):161111, 2007.

Invited talks

- T. Gresch, R. Terazzi, J. Faist, M. Giovannini, and N. Sekine. *Bloch gain in quantum cascade laser structures*, Workshop on Quantum Heterostructures and THz Electronics Regensburg (Germany), Jan 24, 2008.

Talks and conference proceedings

- T. Gresch, M. Giovannini, and J. Faist. *Gain Measurements in Quantum Cascade Lasers at High Temperatures.* Conference on Lasers and Electro-Optics (CLEO08), May 04–09, 2008 San Jose CA (USA), **1–9**:1399–1400, 2008.

- T. Gresch, R. Terazzi, M. Giovannini, N. Hoyler, J. Faist, and N. Sekine. *QCL gain measurements with multi-section cavity technique.* Visit at the Alcatel Thales III-V Lab, Palaiseau CEDEX (France), Dec 13, 2006.

- T. Gresch, M. Giovannini, N. Hoyler, and J. Faist. *HIgh-power QC lasers emitting between $\lambda = 4.2$ and $\lambda = 5.2\,\mu m$.* 8th International Conference on Intersubband Transitions in Quantum Wells (ITQW 05), North Falmouth (USA), Sep 11–16, 2005.

Talks and conference proceedings (contributions)

- A. Bismuto, T. Gresch, and J. Faist. *Large cavity quantum cascade lasers with InP interstacks.* MIOMD - IX, Freiburg (Germany), Sep 7 - 11, 2008.
- S. Herminjard, L. Sirigu, H. P. Herzig, E. Studemann, A. Crottini, J.-P. Pellaux, T. Gresch, M. Fischer, and J. Faist. *Surface Plasmon Resonance Spectroscopy in the mid-infrared range.* in Conference on Lasers and Electro-Optics/Quantum Electronics and Laser Science Conference and Photonic Applications Systems Technologies, OSA Technical Digest (CD) (Optical Society of America, 2008), paper CMZ7.
- H. Choi, Z.-K. Wu, T. B. Norris, T. Gresch, M. Giovannini, J. Faist, L. Diehl, and F. Capasso. *Time-resolved studies of gain dynamics in quantum cascade laser.* AIP Conference Proceedings, 893(1):1437-1438, 2007.

Posters

- T. Gresch, R. Terazzi, and J. Faist. **Multi-section cavity gain measurements on quantum cascade laser structures**. OptETH Doctoral Student Symposium, Zürich (Switzerland), Dec 17, 2008.
- T. Gresch, R. Terazzi, and J. Faist. **Gain and Absorption Measurements on QC Lasers**. POISE Summer School 2006, Cortona (Italy), Jun 25 – 30, 2006.
- T. Gresch, R. Maulini, G. Scalari, M. Givannini, N. Hoyler, and J. Faist. **Quantum Cascade Laser Characterization**. Annual meeting of the Swiss Physical Society, Lausanne (Switzerland), 2006.

Other

- J. Faist, T. Aellen, T. Gresch, M. Beck, and M. Giovannini. *Progress in quantum cascade lasers.* in M. Ebrahim-Zadeh and I. T. Sorokina (*eds.*), *Mid-Infrared Coherent Sources and Applications*, 171–192, Springer, 2008

Acknowledgments

First of all I would like to thank the director of my thesis , Jérôme Faist for giving me the opportunity to work in his group, for his support and creative input and for his patience especially during this last year.

Furthermore, I would like to thank Carlo Sirtori for agreeing to co-advise my thesis.

In particular I would like to thank Mattias Beck, Marcella Giovannini, Nicolas Hoyler and Milan Fischer for growing the structures in the growth facility in Neuchâtel. Romain Terazzi for his support on the work related to the multi-section cavity gain measurements, scattering assisted gain and transport simulations.

In the early days in Neuchâtel I had the chance to encounter Michel Rochat, Stéphane Blaser who showed me how to measure lasers and organized unforgettable ski-weekends in the alps and Harald Willenberg[2] who was supposed to overview my diploma thesis but unfortunately it came otherwise.

During my PhD work in Neuchâtel I spent much enjoyable time with members of the group; either in the cleanroom fabricating devices, in the laboratories measuring them or during leisure time activities. I would like to thank them for the creative discussions and the pleasant time I could spend with them. In particular these members are (in arbitrary order): Giacomo Scalari, Thierry Aellen, Christophe Walther, Richard Maulini, Maria Amanti-Bismuto, Milan Fischer, Andreas Hugi, Andreas Wittmann, Dimitri Yarekha, Lorenzo Sirigu, Lassaad Ajili, Laurent Diehl, Maxi Scheinert, Yargo Bonetti and the members of the group of Daniel Hofstetter: Marcel Graf, Esther Baumann and Fabrizio Giorgetta. In Neuchâtel we also shared the cleanroom with people working at AlpesLasers SA and I would like to thank them for their support and discussion. These people are: Lubos Hvozdara, Guillaume Vandeputte and Sophie Brunner.

For the time I was employed at the Institute of Physics at the University of Neuchâtel I also would like to thank particularly the staff at the local machine shop and electronics shop. They supported my work in every way

---

[2] 17.11.1972–5.11.2002

they could and showed a high degree of loyalty with respect to the institute and the groups even once it was known that the group was going to leave the University of Neuchâtel. In particular I would like to thank Mr. Delhove for helping to fix all the problems related to our cleanroom and helped to keep this facility running what would not have been possible without him. Mr. Scacchi[3] in the electronics shop teached me to delegate work as he was much better in realizing small electronic projects than I was. Mr. Varidel and Mr. Bart were always there for us when computers or laboratory equipment made trouble and Mr. Hèche and his team in the machine shop fabricated complicated mechanical parts in the shortest delays.

During and after the move to the Institute of Quantum Electronics at ETH Zürich I had the chance to encounter many other people, including: Laurent Nevou, James Lloyd-Hughes, Valeria Liverini, Samuel Wiesendanger, Antal van Kolck and Erna Hug. I would like to thank them for the interesting discussions and their support although I was not around so much.

In particular I would like to thank Fabrizio Castellano who jumped-in to do the exercise work with the students when I was unavailable. I also owe special thanks to Alfredo Bismuto who continued the work on lasers with large optical cavity waveguides and helped me in many ways during all that time.

On the non-scientific side I would like to thank my parents, Ruth and Richard Gresch, for giving me the opportunity to study at the University of Neuchâtel and for all the moral support they gave me during all this time; my brothers Christoph and Dominik with his family for the enjoyable time I could spend with them on weekends at my parents' place. Special thanks also to my brother Dominik for proofreading the manuscript.

Last but not least I would like to thank my fiancee, Belinda de Souza, for all the support and motivation she gave me since we met. I would like to thank her especially for staying at my side when I was in the hospital and it was not clear if and how I would recover from my stroke.

---

[3] –29.06.2004